NASA CONTRACTOR REPORT

NASA CR-66897-1

NASA CR-66897-1

SUBSTANTIATION DATA FOR

HYPERSONIC CRUISE VEHICLE WING STRUCTURE EVALUATION

Volume 1, Sections 1 through 10

by P. P. Plank, I. F. Sakata, G. W. Davis, and C. C. Richie

Prepared by
LOCKHEED MISSILES & SPACE COMPANY
Sunnyvale, California
for Langley Research Center

NATIONAL AERONAUTICS AND SPACE ADMINISTRATION · WASHINGTON, D.C.
FEBRUARY 1970

NASA CONTRACTOR REPORT

NASA CR-66897-1

NASA CR-66897-1

SUBSTANTIATION DATA FOR

HYPERSONIC CRUISE VEHICLE WING STRUCTURE EVALUATION

Volume 1, Sections 1 through 10

by P. P. Plank, I. F. Sakata, G. W. Davis, and C. C. Richie

Prepared by
LOCKHEED MISSILES & SPACE COMPANY
Sunnyvale, California
for Langley Research Center

NATIONAL AERONAUTICS AND SPACE ADMINISTRATION · WASHINGTON, D.C.
FEBRUARY 1970

NASA CONTRACTOR REPORT

NASA CR-66897-1

NASA CR-66897-1

SUBSTANTIATION DATA FOR

HYPERSONIC CRUISE VEHICLE WING STRUCTURE EVALUATION

Volume 1, Sections 1 through 10

by P. P. Plank, I. F. Sakata, G. W. Davis, and C. C. Richie

Prepared by
LOCKHEED MISSILES & SPACE COMPANY
Sunnyvale, California
for Langley Research Center

NATIONAL AERONAUTICS AND SPACE ADMINISTRATION · WASHINGTON, D.C.
FEBRUARY 1970

NASA CR-66897-1

SUBSTANTIATION DATA FOR

HYPERSONIC CRUISE VEHICLE

WING STRUCTURE EVALUATION

Volume 1, Sections 1 through 10

15 February 1970

by

P. P. Plank, I. F. Sakata, G. W. Davis, and C. C. Richie

Prepared under Contract No. NAS 1-7573
Lockheed Missiles & Space Company
Sunnyvale, California

for Langley Research Center

NATIONAL AERONAUTICS AND SPACE ADMINISTRATION

CONTENTS

SUMMARY

An analytical and experimental evaluation was performed for several promising structural concepts to provide the basis of minimum total-system-cost for selection of the best concepts for the design of a hypersonic vehicle wing.

Results, procedures, and principal justification of results are presented in reference 1. Detailed substantiation data are given herein. Each major analysis is presented in a separate section. Vehicle loads and temperatures are given with each structural analysis that influences weight. In addition to the weight analysis, fabrication cost, performance penalties (surface roughness drag), reliability, and total-system-cost analyses are presented.

Reference 1. Plank, P. P.; Sakata, I. F.; Davis, G. W.; and Richie, C. C.: Hypersonic Cruise Vehicle Wing Structure Evaluation, NASA CR-1568, 1970.

INTRODUCTION

The utility of a hypersonic cruise vehicle depends upon a low structural mass fraction in a high-temperature environment. Unfortunately, this requirement exceeds the limits of state-of-the-art structures. The only hypersonic structures flown to date have been the X-15 research airplane and the ASSET unmanned lifting reentry test vehicle, both of which are unsuitable for cruising flight.

For the past several years, the NASA Langley Research Center and other agencies have been investigating promising structural concepts, such as those discussed in references 2, 3, and 4, and the 1967 Conference on Hypersonic Aircraft Technology (ref. 5) was devoted to the subject.

An evaluation was performed of promising wing structure concepts to the same in-depth analyses, including all known environmental structural considerations that could affect the four evaluation factors: weight, cost, performance, and reliability. These factors were then interacted in a total-system-cost study for a system range-payload capability of 205 billion ton-miles to provide the basis for selecting the best structural concept for the wing structure of minimum total-system-cost.

Results of this structural evaluation are reported in reference 1. This reference also includes the procedures and principal justification of results, whereas this report gives detailed substantiation of the results in reference 1. Principal analytical and test efforts are presented in separate sections. This report is bound as three separate volumes.

REFERENCES

2. Heldenfels, R. R.: Structural Prospects for Hypersonic Air Vehicle ICAS paper, 1966.

3. Plank, P. P.; and MacMiller, C. I.: Analytical Investigation of Candidate Thermal-Structural Concepts Applicable to Wing, Fuselage, and Inlet Structure of a Manned Hypersonic Vehicle. AFFDL-TR-66-15, 1966 (conf).

4. Plank, P. P.: Hypersonic Thermal-Structural Concept Trends. SAE paper 660678, 1966.

5. NASA-SP-148 (Conf). Conference on Hypersonic Technology, Ames Research Center, 1967.

ACKNOWLEDGEMENT

This investigation was conducted under NASA Contract No. NAS1-7573, Research and Development Program for Development and Validation of Structural Concepts for a Hypersonic Cruise Vehicle Wing Structure. The study was originated at the Lockheed-California Company, Burbank, California and completed at Lockheed Missiles & Space Company, Sunnyvale, California. P. P. Plank was the Program Technical Manager, I. F. Sakata and G. W. Davis the Project Engineers, and C. C. Richie was head of structural concept optimization. The other contributors to the program are acknowledge at each section.

Four Lockheed-California Company personnel acted in an advisory capacity. They are L. W. Nelson, Structure Division Engineer, Structures Division; E. J. Himmel, Department Manager, Stress Analysis; W. J. Crichlow, Department Manager, Advanced Materials and Structural Mechanics; and M. G. Childers, Manager, Physical Sciences Laboratory Development Engineer.

Dr. M. S. Anderson, L. R. Jackson, and J. C. Robinson of the Structures Research Division, NASA Langley Research Center, Hampton, Virginia, were the Program Manager, Technical Representative of the Contracting Officer (TRCO), and Assistant TRCO, respectively, for the project.

Section 1

TRAJECTORY ANALYSIS

by

B. C. Wollner, C. F. Ehrlich, R. S. Peyton,
J. E. Hames, H. F. Harper

TABLES

ILLUSTRATIONS

SYMBOLS

a	Acceleration
C_D	Drag coefficient
C_L	Lift coefficient
D	Drag
g	Gravitational acceleration
H	Altitude
I_{sp}	Specific impulse
$L_{/D}$	Lift to drag ratio
M	Mach number
M_∞	Free stream Mach number
n_x, n_y, n_z	Load factors expressed in Cartesian coordinate system
q	Dynamic pressure
T	Thrust
W	Weight
α	Angle of attack
ΔC_D	Incremental drag coefficient

Section 1

TRAJECTORY ANALYSIS

The detailed structural concept analyses were conducted for the relatively large wing section of the Mach 8 hypersonic cruise airplane, shown in figure 1-1.

The configuration of figure 1-1 is a discrete wing-body airplane with a low wing that is continuous under the fuselage. A structural arrangement consisting of an integral hot fuselage and hot wing structure with separate liquid hydrogen tanks and pressurized compartments suspended within the fuselage was considered for the structural concept evaluation. Although only the section of the wing shown in figure 1-1 was thoroughly analyzed, load and temperature criteria were determined in a gross sense for the entire airplane. These calculations were required to ensure that representative thermal, aerodynamic and inertia loads were applied to the wing section and to ensure that considerations of rib and spar spacings were included in the wing design.

The following data are used for the hypersonic cruise vehicle:

1.	Total wing area	10000 ft^2
2.	Reference area (rear delta-wing area)	8330 ft^2
3.	Vertical tail area	574 ft^2
4.	Engine capture area	306 ft^2
5.	Zero-lift line (degrees to FRL)	3 deg

Masses assigned to the various base-line airplane components are listed below as fractions of the gross takeoff weight, which is 550,000 pounds:

Component	Mass fraction
Fuel	0.40
Structure	0.27
Landing gear	0.03
Propulsion	0.15
Equipment	0.05
Payload	0.10

The hypersonic cruise airplane utilizes the flight schedule outlined in figures 1-2 through 1-4. Altitude versus velocity is presented in figure 1-2, indicating the resulting dynamic pressures. In addition, acceleration and specific impulse data, figures 1-3 and 1-4, are required for determination of time dependent trajectory data.

Forward accelerations for the cruise airplane, as shown in figure 1-3, are for the ascent period. A maximum forward acceleration of 0.2-g is imposed on the trajectory analysis. At initiation of cruise, a normal climb at constant Mach 8 occurs until maximum L/D is approached, followed by a 1-g flight attitude at maximum L/D. A constant deceleration of 0.2-g caused by drag augmentation is used for descent flight. The altitude at termination of cruise is that which provides the required fuel for descent. For life analyses, it is assumed that 90 percent of the flights are with this trajectory. For determination of limit loads due to pressure, inertial, and thermal effects, a trajectory perturbation (10 percent of the flights) is assumed to occur at constant Mach 8. This perturbation is a -0.5-g acceleration normal to the plane of the wing, which is assumed to exist at the initiation of cruise (Mach 8, q = 1500 psf) resulting from a -1.5-g (-1.5 + 1.0 gravity = -0.5-g) nose-down maneuver. This -0.5-g condition is followed by 2.0-g pull-up maneuver(which does not exceed q = 2200 psf) and is held at constant acceleration until maximum L/D is approached with a smooth transition to maximum L/D, followed by 1-g nominal flight condition at maximum L/D for the remainder of the cruise period. Negative limit loads are the critical combination of temperatures and loads occurring during the nose-down maneuver, and positive limit loads are the critical combination of temperatures and loads occurring during the pull-up maneuver. For life analyses, this limit load trajectory is used for every tenth flight.

Aerodynamic data were determined in the form of $C_L = F(M,\alpha)$ and $C_D = F(M, C_L)$. Incremental drag effects (ΔC_D) due to scale effects, engine cowls and vertical tail were also generated. These data were based on extensive aerodynamic analysis of a geometrically similar vehicle (reference 1-1). It was necessary to apply the appropriate wing area, engine capture area, and vertical tail area to obtain the proper C_D. The C_L data were used without change.

The aerodynamic data are referenced to the zero-lift line. Negative lift coefficients, required for the analysis of negative g maneuver at Mach 8, were obtained.

The flight trajectory characteristics of the vehicle were determined, utilizing the established aerodynamic data, by using the mission analysis automated procedure of reference 1-2. Given a mathematical model of the airplane, the program simulates a complete mission within the range of a given flight profile. A time history of the simulated flight and a final performance summary are provided for each mission. The following time-based trajectory parameters were developed: altitude, velocity, Mach number, dynamic pressure, angle of attack, flight path angle, thrust, drag, vehicle weight, range and L/D.

Using the aerodynamic data, both a basic cruise mission and maneuver perturbation trajectory were developed. The resulting time history of the trajectory parameters of dynamic pressure, angle of attack, altitude and Mach number is presented in figure 1-5. The thrust and drag schedule for ascent and descent is presented in figure 1-6. The thrust and drag schedule reflects a power-on descent from end of cruise (q = 470 psf) following a varying dynamic pressure path to an altitude of 40 000 feet. Drag augmentation, as indicated, was provided to result in a constant deceleration of -0.2-g. The baseline vehicle weight schedule is presented in figure 1-7. Both total vehicle weight including fuel and the fuel consumption schedule are presented. Figure 1-8 indicates the longitudinal acceleration schedule during ascent, cruise and descent with resulting load factors of $\pm$0.2-g. The baseline vehicle's range in the cruise mission and variation of lift to drag are presented in figure 1-9. The aforementioned vehicle design trajectory data were used to provide time data per mission for the various vehicle trajectory phases of ascent, maneuver, cruise, and descent. As indicated in table 1-1, 1.23 hours are required for the basic trajectory and 1.25 hours are required for the basic trajectory plus the maneuver perturbation. Using the data of table 1-1, 8110 flights were established per 10 000 hours of life for the basic trajectory and basic trajectory plus perturbation, as presented in table 1-2. The basic trajectory requires 8978.4 hours and the basic trajectory plus perturbation requires 1013.75 hours providing an accumulative total of 9992.15 hours, as shown in table 1-2. However, as indicated in table 1-2, 9000 (basic trajectory), 1000 (basic trajectory plus perturbation) and 10 000 hours (life) were assumed for design. Therefore, using the data of tables 1-1 and 1-2, time data per the 8110 flights for the various trajectory phases were established, as shown in table 1-3. Table 1-3 indicates that the maneuver perturbation requires only 16 hours of a total 10 000 hour vehicle life while the cruise condition requires 4460 hours.

REFERENCES

1-1. Rising, J. J.: Aerodynamic Performance Coefficients for a Proposed Delta Wing - Body, Manned Hypersonic Vehicle, Lockheed-California Company Aerodynamic Memorandum Report No. 40, 1966.

1-2. Fully Automatic Computer Technique of Sizing for Manned Hypersonic Vehicles. Lockheed California Company Computer Control No. 2802, 1966.

TABLE 1-1

TIME DATA PER MISSION FOR VARIOUS VEHICLE TRAJECTORY PHASES

Trajectory phase	Basic trajectory	Basic trajectory plus perturbation
Ascent	21.0 min (0.35 hr)	21.0 min
Maneuver	--	0.9 min (0.02 hr)
Cruise	33.0 min (0.55 hr)	33.0 min
Descent	20.0 min (0.33 hr)	20.0 min
Total	74.0 min (1.23 hr)	74.9 min (1.25 hr)

TABLE 1-2

NUMBER OF FLIGHTS PER 10 000 HOURS OF LIFE

Number of flights	Hours		
	Basic trajectory	Basic trajectory plus perturbation	Accumulative
8110	8978.4	1013.75	9992.15
For design assume	(9000)	(1000)	(10 000)

TABLE 1-3

TIME DATA PER 8110 FLIGHTS FOR VARIOUS TRAJECTORY PHASES

Trajectory phase	Basic trajectory (hr)	Basic trajectory plus perturbation (hr)	Total (hr)
Ascent	2560	280	2 840
Maneuver	0	16	16
Cruise	4020	440	4 460
Descent	2420	264	2 684
Total	9000	1000	10 000

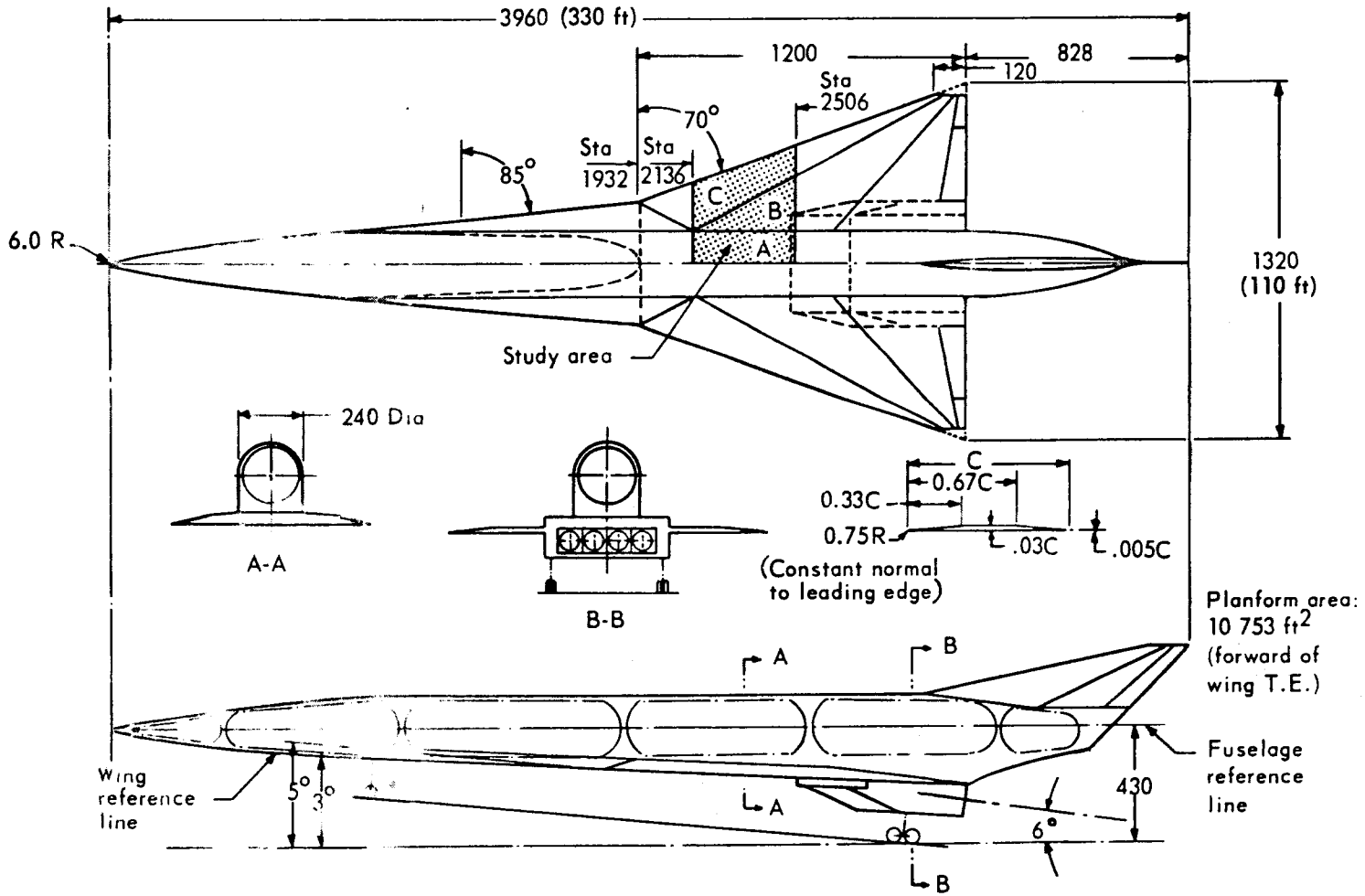

Figure 1-1 Hypersonic cruise vehicle

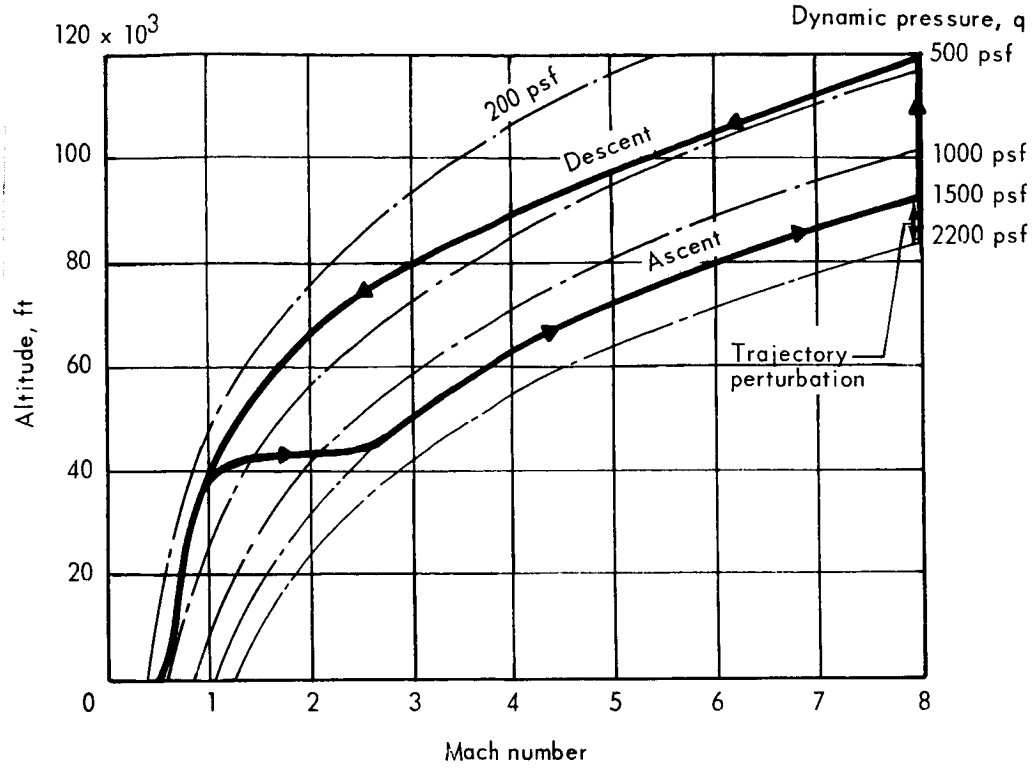

Figure 1-2. Hypersonic cruise airplane design trajectory

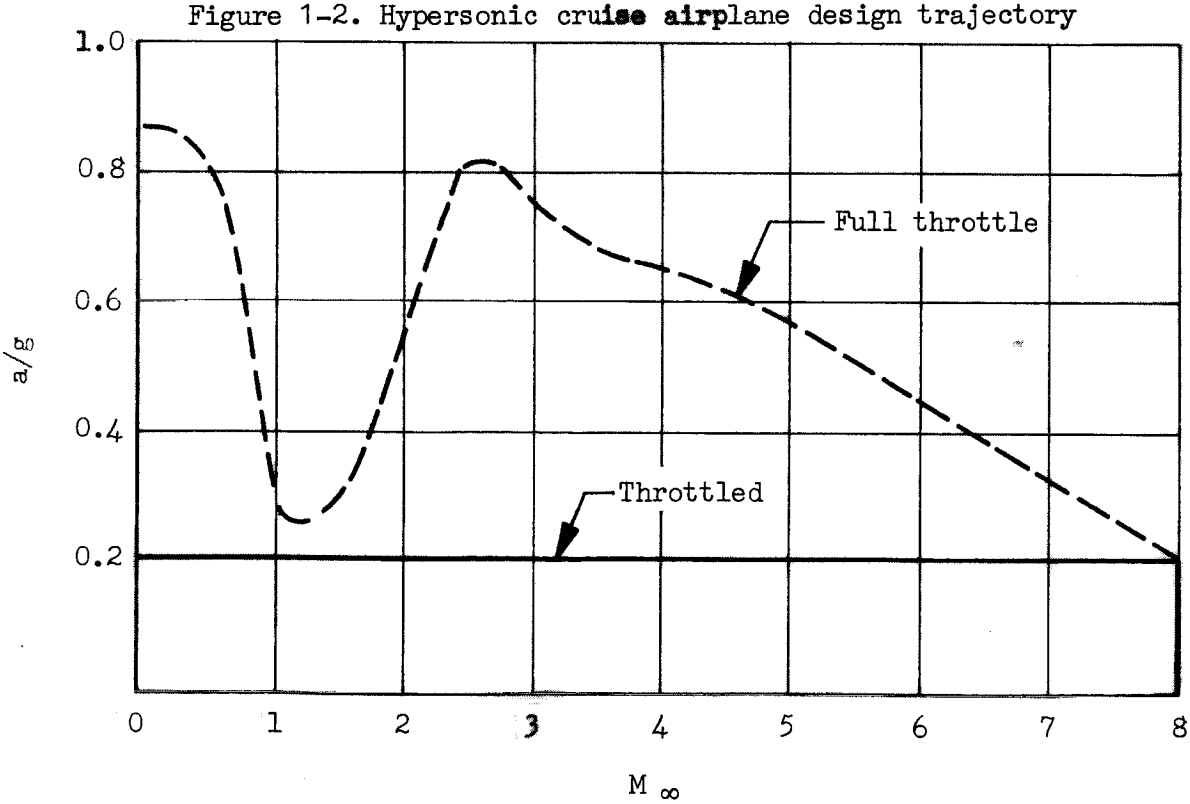

Figure 1-3. Forward acceleration of cruise airplane

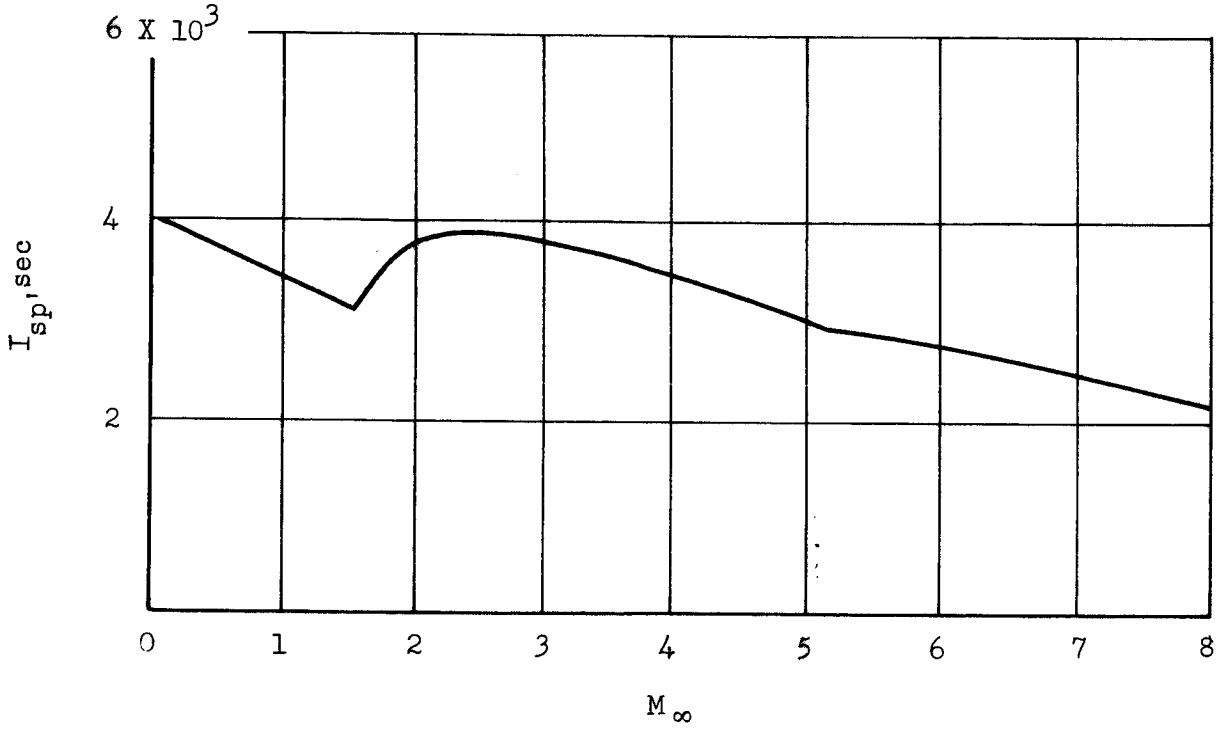

Figure 1-4. Specific impulse data

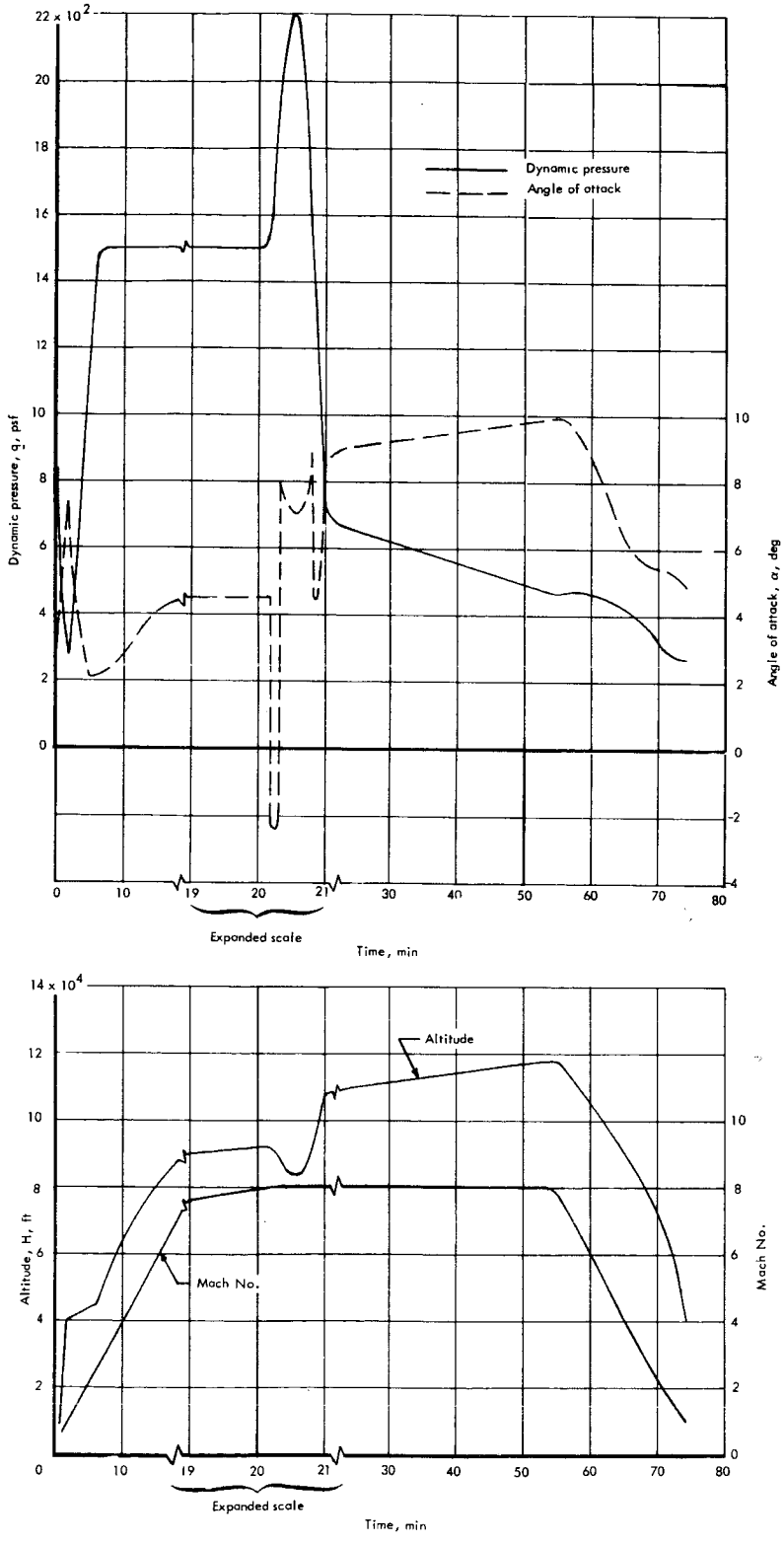

Figure 1-5. Trajectory data for cruise airplane - basic trajectory plus trajectory perturbation

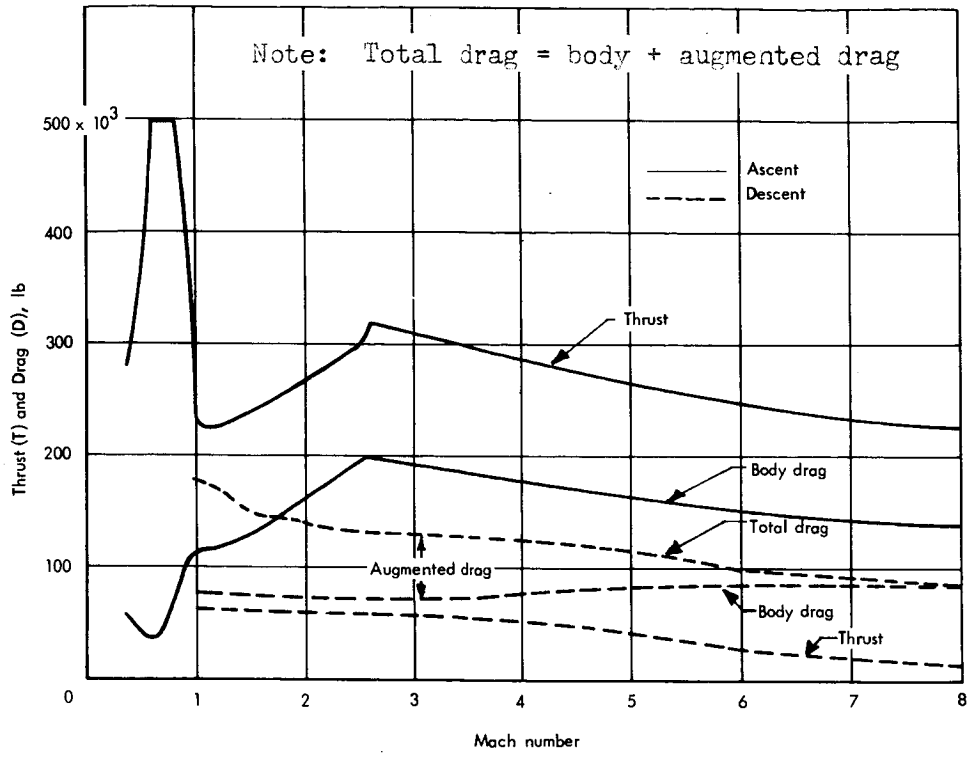

Figure 1-6. Cruise airplane thrust and drag schedule - basic trajectory

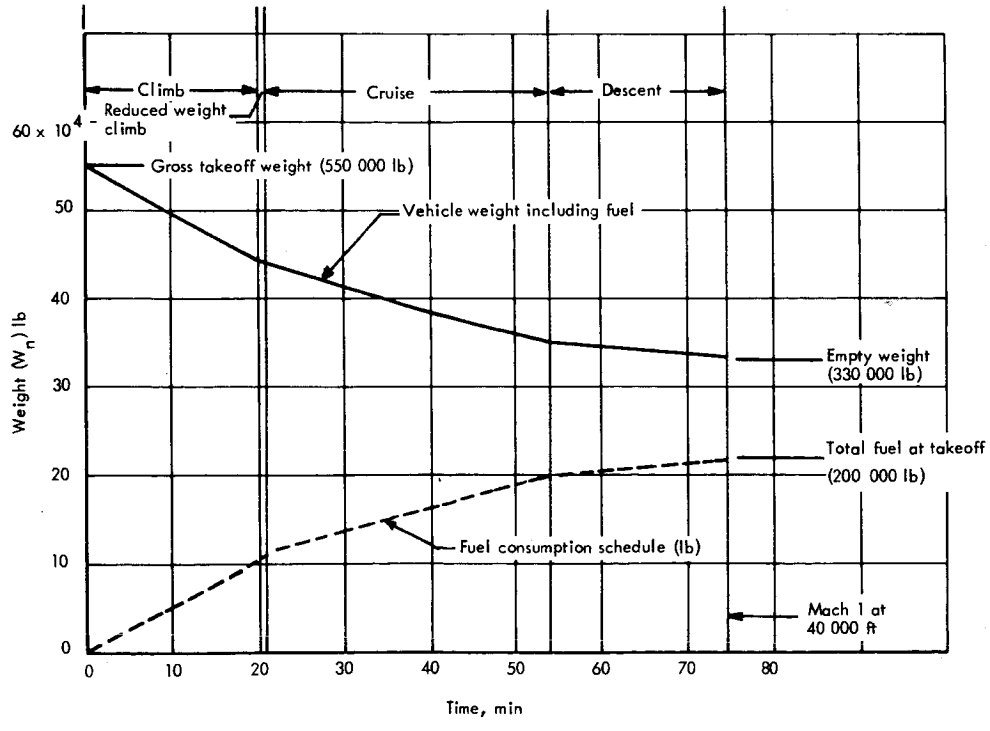

Figure 1-7. Cruise airplane weight schedule - basic trajectory

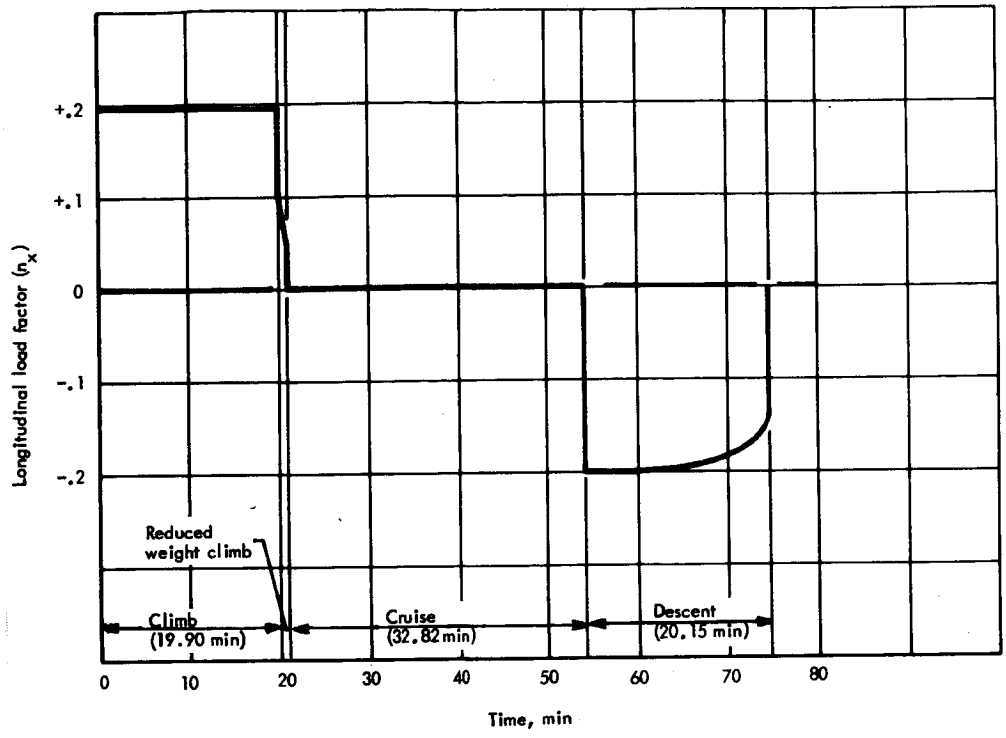

Figure 1-8. Cruise airplane longitudinal acceleration schedule - basic trajectory

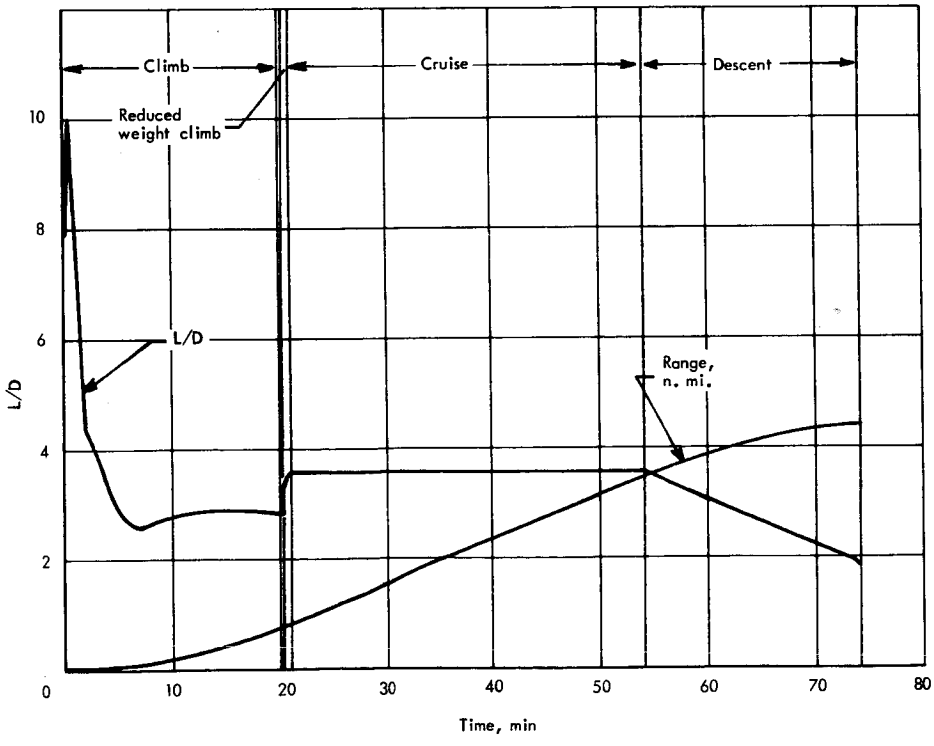

Figure 1-9. Range and L/D data for cruise airplane - basic trajectory

Section 2

VEHICLE LOADS

by

B.C. Wollner, J.L. Benson, and F.L. Falconer

CONTENTS

TABLES

ILLUSTRATIONS

SYMBOLS

BL	Butt line
c.g.	Center of gravity
c.p.	Center of pressure
D	Drag force
F_A, F_N	Engine stream thrust resolved into axial (subscript A) and normal (subscript N) components.
F_x, F_y, F_z	Forces in x, y, and z axes
F_1, F_2, F_3, F_g	Engine stream thrusts
FS	Fuselage station
g	Gravitational acceleration
L	Lift force
L_α	Total airload
L_δ	Total elevon load
M_x, M_y, M_z	Moments taken about the x, y, and z axes
n_xW, N_yW, n_zW	Total inertia loads in the x, y, and z axes
p	Pressure
q	Dynamic pressure
R	Radius
T	Thrust
WRL	Wing reference line
α	Angle of attack
Δp	Pressure differential
ψ	Vector angle

Section 2

VEHICLE LOADS

Net vehicle loads, using the airplane configuration and trajectory, were determined in a general sense for the entire airframe to ensure that representative net loads were applied to the wing section and that realistic spar and rib spacings were included in the wing section design.

Unit load distributions were developed for the hypersonic cruise vehicle to represent the following influence functions:

1. Aerodynamic loading – Aerodynamic loadings over the vehicle at the design condition at Mach 8.0 (-.5g, 2.0g and cruise conditions) were determined based on oblique shock and Prandtl-Meyer expansion relationships, references 2-1 and 2-2. Newtonian impact theory was used for estimating loadings on the nose of the vehicle, reference 2-3. Load panel points for application of these theories were established with consideration to vehicle contours. The resultant rigid loading distributions were transformed to a network model for application to the stress analysis and the aeroelastic loads analysis.

2. Inertia loading – Vehicle weights were distributed to provide an inertia loading distribution for use in determining design loads. Appropriate fuel burn-off was considered in deriving the weights consistent with design loading conditions (-.5g, 2g and cruise).

3. Elevon loading – Loads due to elevon displacement were concentrated on the control surface. Longitudinal control displacement serves as a trim device to balance vehicle pitching moments.

4. Thrust loading – To obtain the loads imposed on the vehicle by the propulsion system, the following assumptions were made:

   a. The propulsion system is integral with the vehicle

   b. The inlet is two-dimensional

   c. The engine employs a lifting two-dimensional plus nozzle.

   d. The vehicle forebody drag is included in the aerodynamic drag buildup; therefore, the net propulsive thrust is based upon the change in total momentum from the station at the inlet ramp to the aft vehicle station.

The network model for application to the stress analysis and aeroelastic loads analysis is shown in figure 2-1. In addition to the assumptions presented, it was also determined that the required net propulsive thrust for the engine at a q = 2200 psf was 318 000 pounds at Mach 8 to provide a vertical acceleration of 2g. Based on the assumptions made, the stream thrusts at the various defined stations (figure 2-2) were computed and are shown below:

Stream thrust	Magnitude	Vector angle,
F_1	1 027 000 lb	$\psi 1 = 0^o$
F_2	849 000 lb	$\psi 2 = 20^o$
F_3	1 017 000 lb	$\psi 3 = 0^o$
F_g, Gross thrust	1 357 000 lb	$F_g = 2{,}7k2^o$

The stream thrust is defined as:

$$F = \dot{m}V + (P - P\infty)\, A = PA\,(1 + \gamma M^2) - P\infty A$$

The stream thrust vector angle, ψ, is positive and is measured in the clockwise direction from the wing reference line. Resolution of these engine stream thrust levels into components parallel to and normal to the wing reference line provides the following:

	Station Location			
Force	1-2	2-3	3-4	Net
F_A (lb)	-229 000	219 000	338 000	328 000
F_N (lb)	290 000	-290 000	64 200	64 200

which result in a net axial force of 328 000 pounds (propulsive) and a net normal force of 64 200 pounds (lifting). From a systems analysis, it was established that the vehicle angle of attack was 7 degrees (freestream flow) direction with respect to the wing reference line) during the 2g maneuver. Therefore, resolution of the axial and normal propulsive system forces provides a thrust of 318 000 pounds and a contribution of 104 000 pounds to the vehicle lifting force.

The 2g vehicle trim requirement is 62 676 pounds. Vehicle trim associated with the cruise condition (q = 750 psf) is 17 635 pounds, as shown in the tabulation below:

Conditions		Loads		
		2g	1g	-0.5g
$L\alpha$,	total airload, lb	831 250	389 372	-236 930
c.p.	feet	176.0	176.9	176.9
$L\delta$,	total elevon load to trim, lb	62 676	17 635	12 160
cp,	feet	256	256	256
$n_z W$	total inertia load, lb	-893 926	-407 007	224 770
cg,	feet	176.8	176.8	176.8

VEHICLE BALANCE

Vehicle balance was obtained under the system of forces discussed in the preceding paragraph. Both normal and axial balance were effected with the resultant thrust vector approximately through the vehicle center-of-gravity. (In view of the range of cg motion as fuel is expended, the line of action of the thrust vector is maintained within this region.) Both normal and axial balance requirements were observed. A summary of these forces for all design conditions is contained on figures 2-3 through 2-5. These forces are listed in the body axis systems.

The individual forces contributing to total loads on the vehicle are listed on tables 2-1 and 2-2. These forces are listed in both wind and body axis systems.

The total loads at the cg for the three flight conditions are shown diagrammatically on figures 2-6 through 2-8. Forces are listed in the body axis system. These loadings are distributed, as previously discussed, to provide a loading function for determination of elastic load distributions. Vehicle balance is inherent in the elastic load solution.

A matrix solution is employed to balance the vehicle under the elastic loadings. The basic representation includes all external forces contributing to vehicle attitude and is as follows:

$$\left\{P_z\right\}_{air} = (\alpha)\left\{A\right\} + [A]\left[D_\theta\right]\left[[E]\left\{P_z\right\}_{net} + \left\{E_T\right\}\right] + \left[A_\alpha\right]\left\{\alpha_\delta\right\}(\delta_e)$$

where

$\left\{A\right\}$ = rigid aerodynamic loading

$\left[A_\alpha\right]$ = aerodynamic influence coefficient matrix

D_θ = differentiating matrix

$[E]$ = structural influence coefficient matrix

$\left\{E_T\right\}$ = thermal deflection

$\left\{\alpha_\delta\right\}$ = elevon effectiveness

(α) = vehicle angle of attack

(δ_e) = elevon deflection

Net load is equal to

$$\left\{P_z\right\}_{net} = \left\{P_z\right\}_{air} + n_z\left\{W\right\} + (T)\left\{P_T\right\}$$

where

n_z = load factor

$\left\{W\right\}$ = inertia loading

T = net thrust

$\left\{P_T\right\}$ = unit thrust loading

Vehicle balance is maintained through the relations

$$[1]\left\{P_z\right\}_{net} = 0$$

$$[x]\left\{P_z\right\}_{net} = 0$$

where $[x]$ represents the distance of each panel load centroid from the cg.

In the foregoing solution, the differentiating matrix, $[D_\theta]$, relates vertical deflections at each panel point to the angular deflection of the panel. The aerodynamic influence coefficient matrix was developed considering a one-degree increment in angle-of-attack on each panel using oblique-shock and Prandtl-Meyer expansion relations.

NET DESIGN LOADS

Rigid-body load analyses were conducted for the 0.5g, 2g and cruise conditions and net panel point loads are presented in tables 2-3 through 2-6.

In addition, aeroelastic analyses were conducted for both the positive maneuver (2g) and cruise conditions. The lower loadings experienced during the negative maneuver condition (-0.5g) were not significantly changed because of flexibility effects.

Net panel point loads (2g and cruise) for both the rigid and elastic wing computations are presented in tables 2-4 and 2-3, which contain wing loads; and table 2-5, which compares loads for the fuselage. As indicated in tables 2-4 and 2-5, elastic loads were obtained for the monocoque, semimonocoque spanwise, semimonocoque chordwise and statically determinant concepts.

The fuselage data of table 2-6 are shown as combined loads on the body at each longitudinal station to indicate that the longitudinal distribution of loading is but little influenced by elastic considerations. Distribution of the net loads between the double panel points at each station was included in the redundant analysis.

Evaluation of the elastic load distribution indicates that the magnitude of the loads at the main wing area does not vary significantly from the rigid load values. The effect of elasticity is to deflect the trailing edge, aft of station 2580, upward, thus inducing a negative angle of attack upon the affected panels. The attendant incremental negative loading necessitates additional trailing edge down elevon deflection (positive load) for trim. Significant changes in loading due to elastic effects are noted in the area of trailing edge and tip region as well as fuselage nose. Net loads in the tip area decrease in local angle of attack. This loss in lift is made up by additional elevon deflection required for trim which further increases trailing edge deflection.

The wide variation evidenced in fuselage loadings (table 2-6) is due in part to the need for trimming the vehicle under the elastic loading; whereas, the chordwise semimonocoque structural concept demonstrates the most flexibility in the spanwise direction (table 2-5).

Resultant net shear and bending moment distribution for the specified cruise and maneuver conditions are shown in figures 2-9 and 2-10 as a function of longitudinal station. Discontinuities evident over the aft portion of the vehicle are due to the concentrated thrust and elevon loads.

Average pressure loadings over the wing investigation area are listed for upper and lower surfaces for each design condition on table 2-7, where lower surface pressures are further defined in terms of the airload pressure and ramp (propulsion system). The pressure loading for the entire wing is shown in table 2-9. For the detailed evaluation of structural concepts, the pressure loadings of table 2-8 were used. The upper surface shields for aerodynamic smoothness requirements and lower surface heat shield panels were designed for a limit Δp of ± 0.5 psi.

A history of leading edge pressures during the cruise mission is shown on figure 2-11. Variations in these loadings during the defined maneuver excursion are shown on figure 2-12. The lower surface primary load-carrying panels are designed for the calculated aerodynamic pressures. These pressures are uniformly distributed over the primary-structure panels (based on complete venting through the heat-shield panels) or with 0.5 psi applied to the heat shield and introduced at the heat-shield support interface, with the balance of the pressure uniformly distributed over the structure panels.

REFERENCES

2-1 NACA Report 1135; Equations, Tables and Charts for Compressible Flow, 1955.

2-2 NASA Report R-171: The Correlation of Oblique Shock Parameters for Ratios of Specific Heats from 1 to 5/3 With Application to Real Gas Flows, 1963.

2-3 Cole, J. D.: Newtonian Flow Theory for Slender Bodies, Journal Aero. Science, Vol. 24, No. 6, June 1957, pp 448-455.

TABLE 2-1

SUMMARY OF STATIC BALANCE – M8

NORMAL TO WING REFERENCE LINE

Loads, lb	Flight condition		
	-0.5g	2g	Cruise 1g nominal (.92g)
Force			
Airload	-258 830	767 150	367 502
cp	174.1	169.3	172.3
Forward ramp	35 400	51 900	17 700
cp	197.1	197.1	197.1
Inlet ramp	162 300	238 000	81 160
cp	217.0	217.0	217.0
Duct	-197 700	-290 000	-98 890
cp	233.0	233.0	233.0
Aft body	21 900	64 200	21 900
cp	277.0	277.0	277.0
Elevon	12 160	62 676	17 635
cp	256.0	256.0	256.0
Inertia			
n_zW	224 770	-893 920	-407 010
cg	176.8	176.8	176.8

Note: All loads are limit. All stations in feet.

TABLE 2-2

SUMMARY OF NORMAL AND AXIAL BALANCE AT CG – M8

Reference system		Flight condition	Maneuver n'_z = -0.5g	Maneuver n'_z = +2.0g	Cruise n_z = 1.0 nominal (.92g)
		α, deg.	-2.6	7.0	9.2
		q, psf	1 500	2 200	
Wind		Drag, D	-114 880	-325 550	-111 520
		Lift, L	-240 880	860 660	394 170
		Thrust, T	114 880	325 550	111 520
		Inertia $n'_x W$	0	0	0
		Inertia $n'_z W$	225 000	-900 630	-412 430
Wing reference line	Normal	D sinα	-5 170	39 670	18 020
		L cosα	-241 500	790 050	367 090
		T_N	21 900	64 200	21 900
		$n_z W$	224 770	-893 920	-407 000
	Axial	D cosα	-113 765	-323 130	-110 050
		L sinα	9 970	104 890	63 700
		T_A	114 000	328 000	113 000
		$n_x W$	-10 205	-109 760	-66 650

Note: All loads are limit.

TABLE 2-3

NET VEHICLE LOADS – LIMIT (-0.5G MANEUVER LIMIT, RIGID)

Panel number	Load, lb	Panel number	Load, lb	Panel number	Load, lb
1	-2 198	16	-1 441	32	-1 700
2	1 770	17	-1 308	33	-1 637
3	-2 151	18	-1 194	34	3 572
4	-3 350	19	-782	35	-227
5	-875	20	-734	36	-381
6	-442	21	921	37	-595
7	661	22	9 861	38	-730
8	5 537	23	-9 423	39	-1 487
9	4 815	24	-6 878	40	-1 611
10	12 723	25	1 484	41	3 244
11	-7 685	26	-398	42	-405
12	-35 192	27	-522	43	-693
13	-25 123	28	-468	44	-948
14	4 389	29	-592	45	2 908
15	4 959	30	-1 008	46	-723
		31	-1 520	47	2 255

[a] Includes points 48 – 57 (fig. 2-1)

TABLE 2-4

NET WING LOADS – LIMIT
(2G MANEUVER)

Panel number	Rigid, lb	Elastic, lb			
		Monocoque	Semimonocoque (spanwise)	Semimonocoque (chordwise)	Statically determinate
16	3 718	655	3 730	3 494	3 741
17	3 385	3 310	3 386	3 181	3 409
18	3 236	3 175	3 252	3 085	3 333
19	3 294	3 281	3 351	3 224	3 454
20	3 002	3 013	3 101	2 971	3 199
21	6 311	6 354	6 519	6 331	6 656
22	20 677	20 738	21 083	20 778	21 401
23	-17 885	-17 998	-17 551	-17 961	-17 145
24	-15 154	-15 848	-15 315	-15 572	-15 211
25	-1 629	-1 648	-1 361	-1 223	-1 698
26	877	841	860	765	888
27	1 265	1 211	1 225	1 101	1 288
28	1 088	1 038	1 055	935	1 118
29	1 443	1 402	1 440	1 291	1 510
30	2 444	2 392	2 511	2 234	2 640
31	3 711	3 595	3 841	3 403	4 238
32	4 131	3 620	3 898	3 461	4 485
33	3 891	2 553	2 784	2 577	2 942
34	12 254	15 415	14 375	15 141	12 953
35	506	478	488	425	527
36	890	847	865	701	941
37	1 407	1 331	1 366	1 191	1 513
38	1 608	1 491	1 538	1 288	1 822
39	3 721	2 951	2 948	2 597	3 601
40	4 035	2 325	2 211	2 146	2 382
41	12 238	14 613	13 261	14 138	11 745
42	925	693	649	587	808
43	1 550	688	453	423	907
44	2 292	999	657	739	795
45	11 869	13 490	11 818	12 920	10 220
46	1 719	510	215	481	2
47	9 161	10 651	9 069	10 306	7 838

TABLE 2-5

NET WING LOADS – LIMIT
CRUISE (1G)

Panel number	Rigid, lb	Elastic, lb			
		Monocoque	Semimonocoque (spanwise)	Semimonocoque (chordwise)	Statically determinate
16	1 875	1 831	1 858	1 796	1 809
17	1 705	1 666	1 681	1 640	1 651
18	1 627	1 582	1 581	1 571	1 580
19	1 592	1 548	1 545	1 540	1 551
20	1 455	1 408	1 412	1 399	1 418
21	2 679	2 597	2 611	2 582	2 636
22	7 695	7 569	7 614	7 544	7 683
23	-6 280	6 526	6 467	6 581	6 368
24	-5 432	-5 847	-5 797	-5 911	-5 724
25	-838	-785	-710	-700	-706
26	461	446	449	435	441
27	648	631	627	620	627
28	565	540	536	528	540
29	739	699	695	681	705
30	975	1 164	1 162	1 124	1 191
31	1 398	1 712	1 721	1 631	1 809
32	2 116	1 774	1 775	1 631	1 908
33	2 005	1 428	1 418	1 245	1 489
34	4 396	6 341	6 358	6 705	6 111
35	265	250	247	241	250
36	461	423	421	410	431
37	725	658	645	620	670
38	869	751	729	682	783
39	1 891	1 532	1 455	1 350	1 540
40	2 050	1 404	1 315	1 164	1 368
41	4 480	6 130	6 074	6 382	5 795
42	482	373	343	325	376
43	812	508	398	359	488
44	1 175	704	396	525	631
45	4 435	5 720	5 595	5 907	5 288
46	885	465	388	345	341
47	3 366	4 467	4 311	4 651	4 022

TABLE 2-6

NET FUSELAGE LOADS – LIMIT

Cond.	Panel number	Rigid, lb	Elastic, lb			
			Monocoque	Semimonocoque (spanwise)	Semimonocoque (chordwise)	Static determinate
2G Maneuver	1	-3 021	-2 482	-2 540	-2 240	-3 240
	2	-12 800	-12 848	-12 933	-12 826	-13 128
	3	-2 754	-3 071	-3 421	-3 107	-3 775
	4	447	791	338	695	164
	5 + 48	-2 070	-1 785	-2 001	-1 655	-1 935
	5 + 49	-2 258	-2 069	-2 126	-1 990	-2 048
	7 + 50	-518	-441	-361	-317	-240
	8 + 51	6 938	6 497	6 607	1 664	6 768
	9 + 52	5 666	5 737	5 905	5 901	6 082
	10 + 53	15 845	15 875	16 061	16 081	16 401
	11 + 54	64 300	64 723	65 330	65 178	65 669
	12 + 55	-81 531	-80 980	-80 029	-80 325	-79 799
	13 + 56	-68 215	-63 378	-67 521	-67 778	-67 091
	14 + 57	-23 606	-24 231	-23 168	-23 565	-22 596
	15	12 023	11 530	12 260	12 004	12 465
Cruise (1G)	1	-3 335	-3 016	-2 981	-2 931	-2 627
	2	-5 382	-5 305	-5 301	-5 281	-5 276
	3	-307	-125	-127	-71	-406
	4	1 341	1 718	1 660	1 793	1 138
	5 + 48	-481	-505	-565	-463	-620
	6 + 49	-694	-698	-725	-698	-763
	7 + 50	-132	-165	-165	-167	-167
	8 + 51	2 202	2 144	2 155	2 160	2 168
	9 + 52	1 951	1 383	1 903	1 890	1 921
	10 + 53	5 341	5 204	5 223	3 208	5 287
	11 + 54	21 679	21 524	21 618	2 158	21 639
	12 + 55	-30 082	-32 275	-30 128	-30 152	-30 063
	13 + 56	25 650	-26 077	-25 938	-25 969	-25 793
	14 + 57	-10 300	-10 919	-10 741	-10 825	-10 528
	15	1 875	1 441	1 520	1 483	1 650

TABLE 2-7

WING LIMIT PRESSURE LOADINGS

Panel number	Limit pressure loading, psi					
	-0.5-g		+2.0-g		1.0-g	
	Upper surface	Lower surface	Upper surface	Lower surface	Upper surface	Lower surface
1–4	0.1623	0.0320	0.0929	0.4692	0.0454	0.2300
5	0.1892	0.0172	0.0500	0.5492	0.0245	0.2685
6–8	0.1461	0.0124	0.0359	0.9615	0.0175	0.4692
9	0.1892	0.0172	0.0500	0.5492	0.0245	0.2685
10–12	0.1461	0.0124	0.0359	0.9615	0.0175	0.4692
13–22	0.1646	0.0368	0.1065	0.4754	0.0521	0.2331

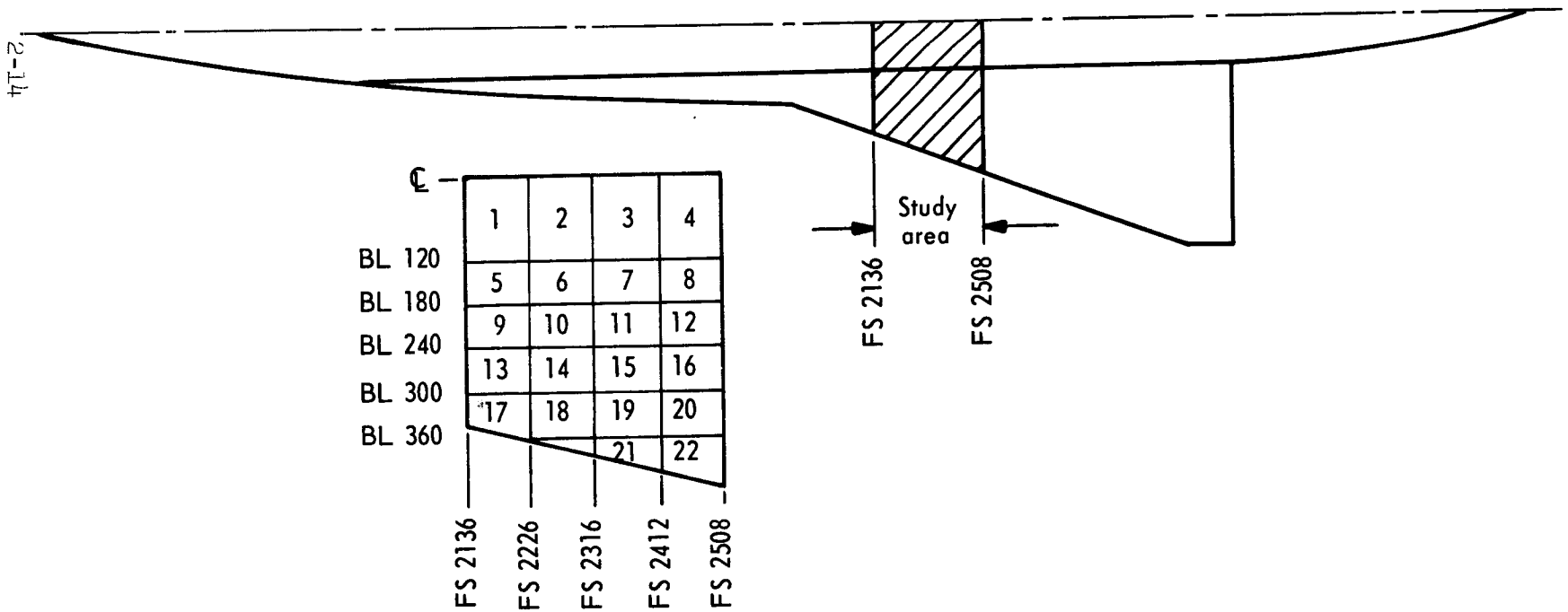

TABLE 2-8

HYPERSONIC CRUISE VEHICLE WING PRESSURES

Location \ Condition	Limit pressure Δp, psi [a, b, c]								
	BL 0-120			BL 120-212			BL 212-350		
	-0.5-g	+2.0-g	Cruise	-0.5-g	+2.0-g	Cruise	-0.5-g	+2.0-g	Cruise
Lower surface structural panels	-0.53	-0.97	-0.73	-0.51	-1.46	-0.97	-0.54	-0.98	-0.73
All heat shields & upper surface panels	←——— ±0.50 ———→								

[a]For ultimate design pressures, multiply (1.3) (1.5) by limit pressures shown.
[b]Negative values indicate inward-acting pressures;positive values indicate outward-acting pressures.
[c]Sta. 2274-2366.

TABLE 2-9

PRESSURE LOADINGS FOR ENTIRE WING

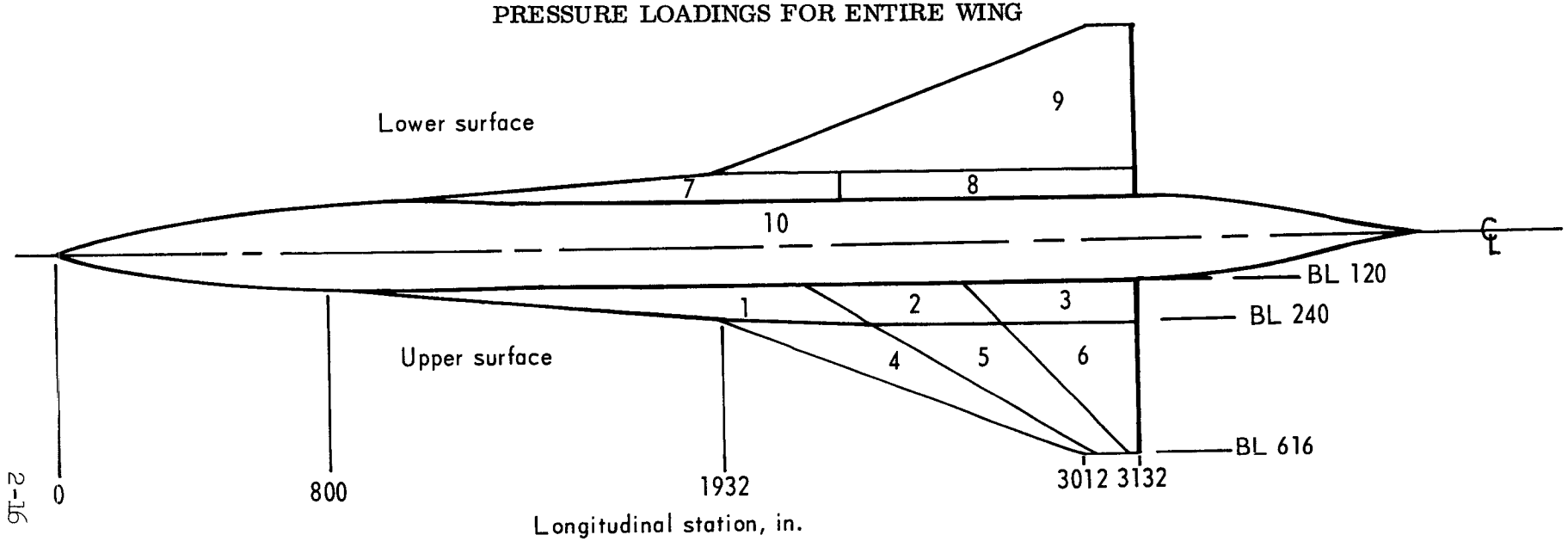

Wing area	Limit aerodynamic pressure[a], psi		
	Design condition		
	-0.5-g	+2.0 g	+1.0 g
1	0.1892	0.0500	0.0245
2	0.1461	0.0359	0.0175
3	0.0549	0.0097	0.0038
4	0.1646	0.1065	0.0521
5	0.1243	0.0358	0.0168
6	0.0463	0.0096	0.0037
7	0.0172	0.5492	0.2685
8	0.0124	0.9615	0.4692
9	0.0368	0.4754	0.2331
10	0.0320	0.4692	0.2300

[a]Ramp pressure not included.

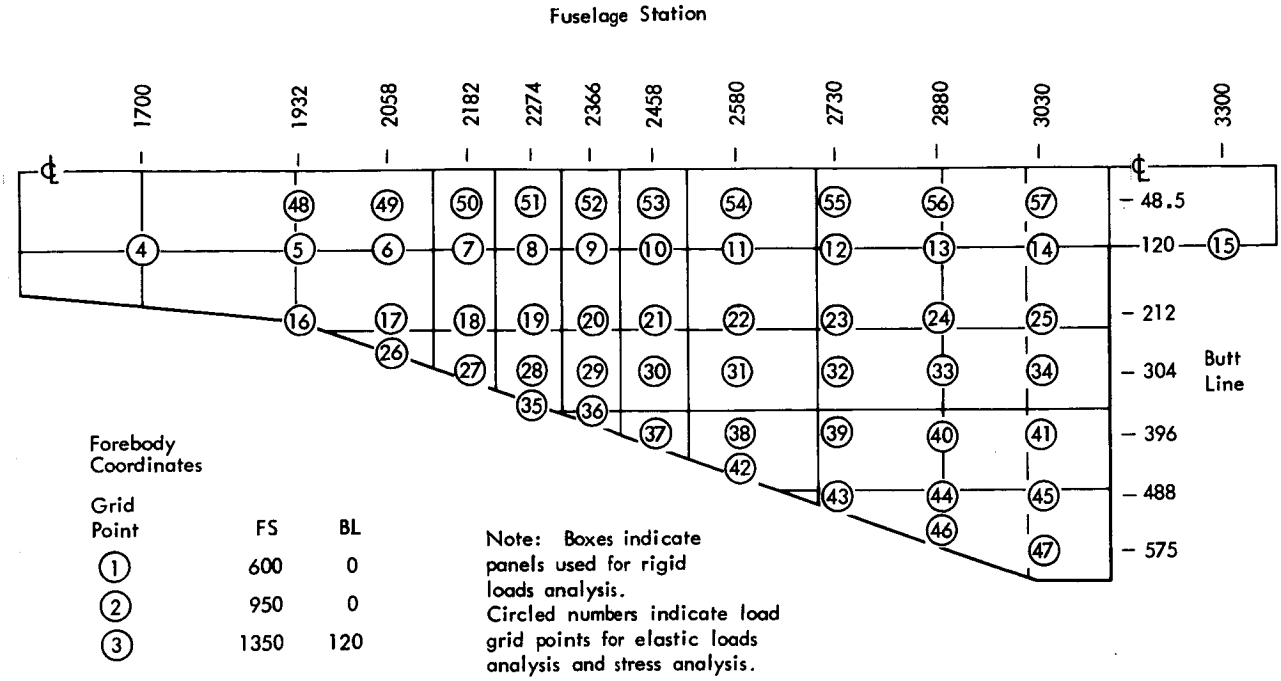

Figure 2-1. Loads network wing model

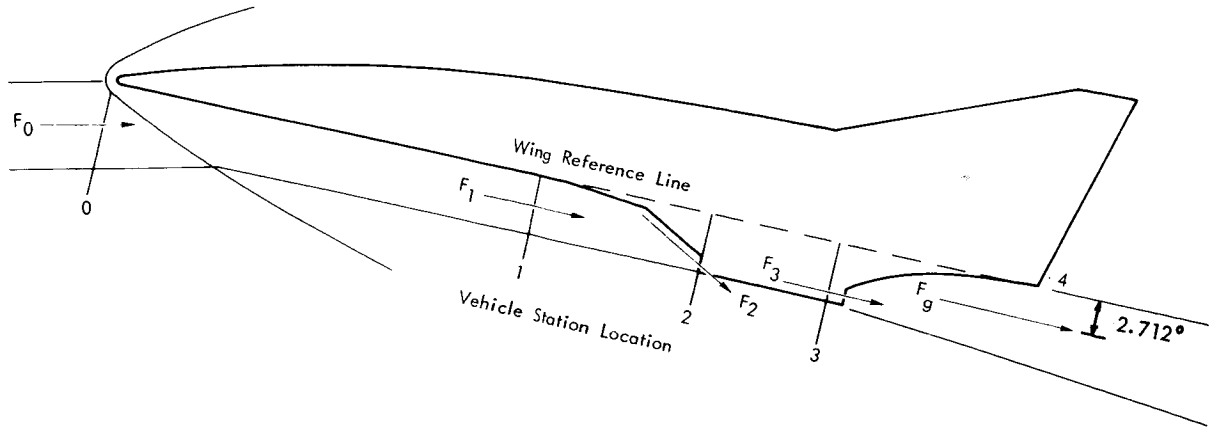

Figure 2-2. Integral engine: Hypersonic cruise vehicle

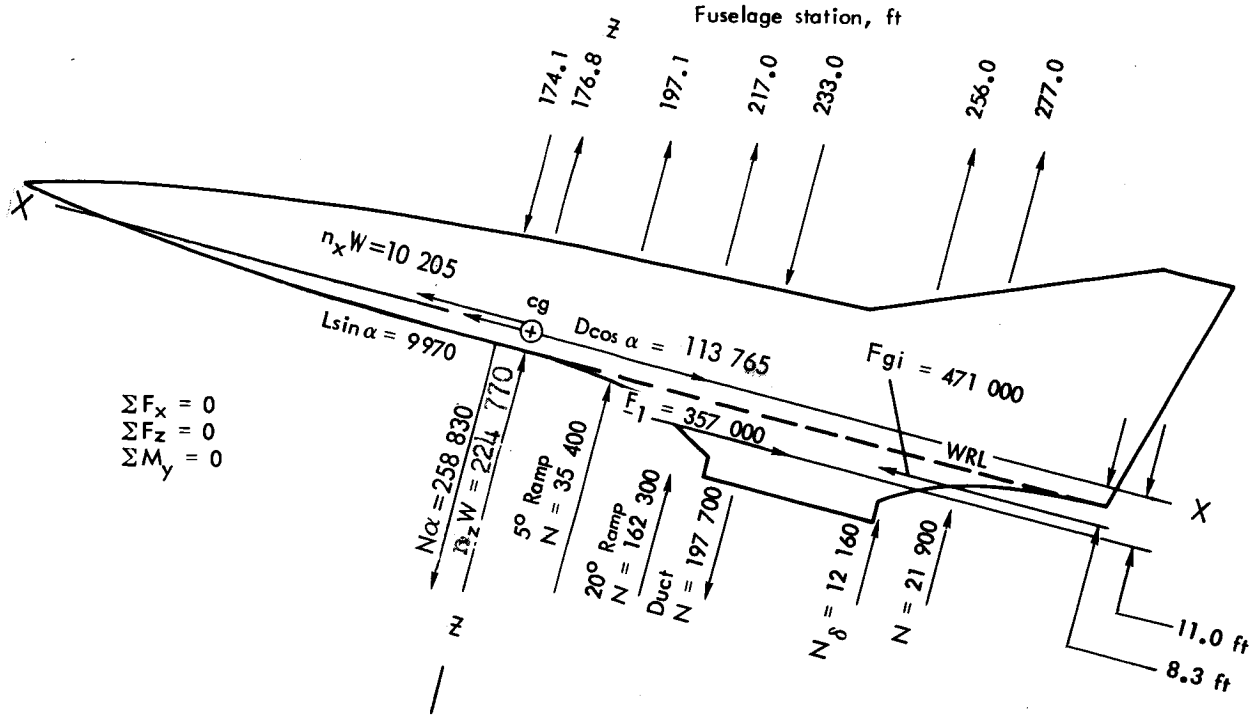

Figure 2-3. Static balance: -0.5g maneuver condition

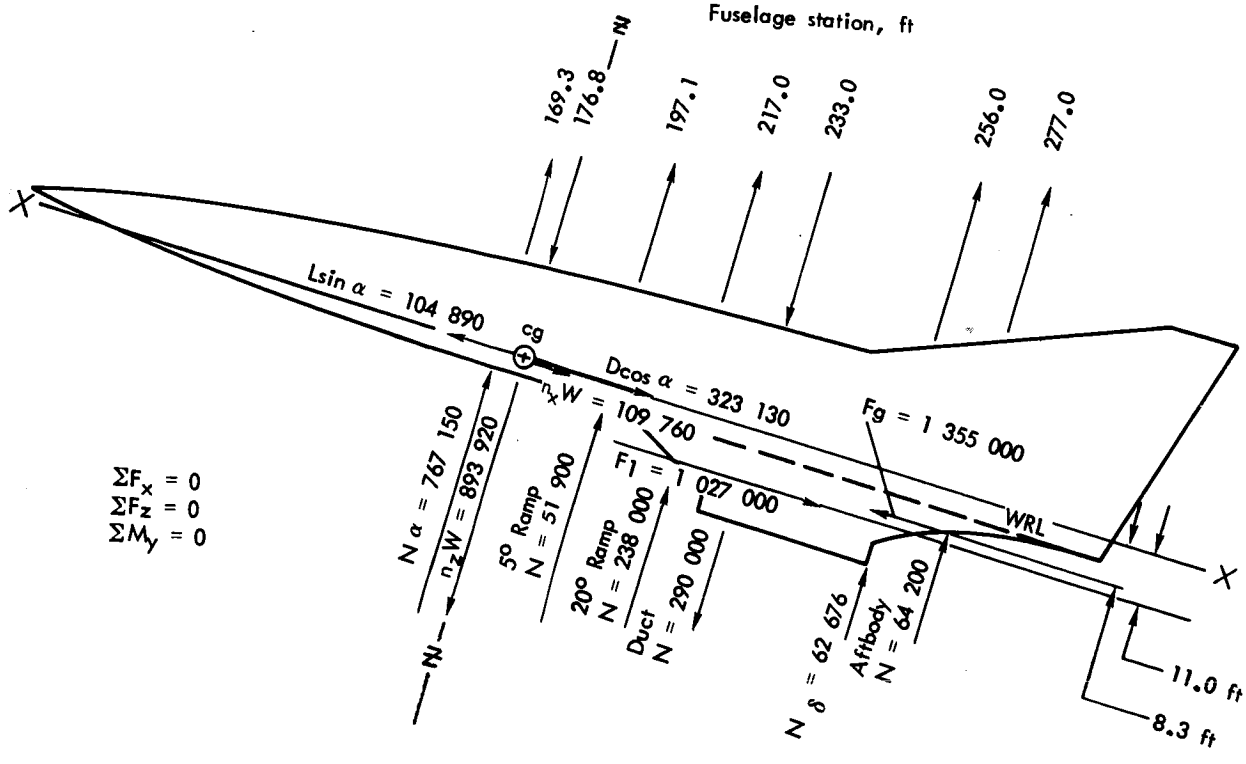

Figure 2-4. Static balance: +2.0g maneuver condition

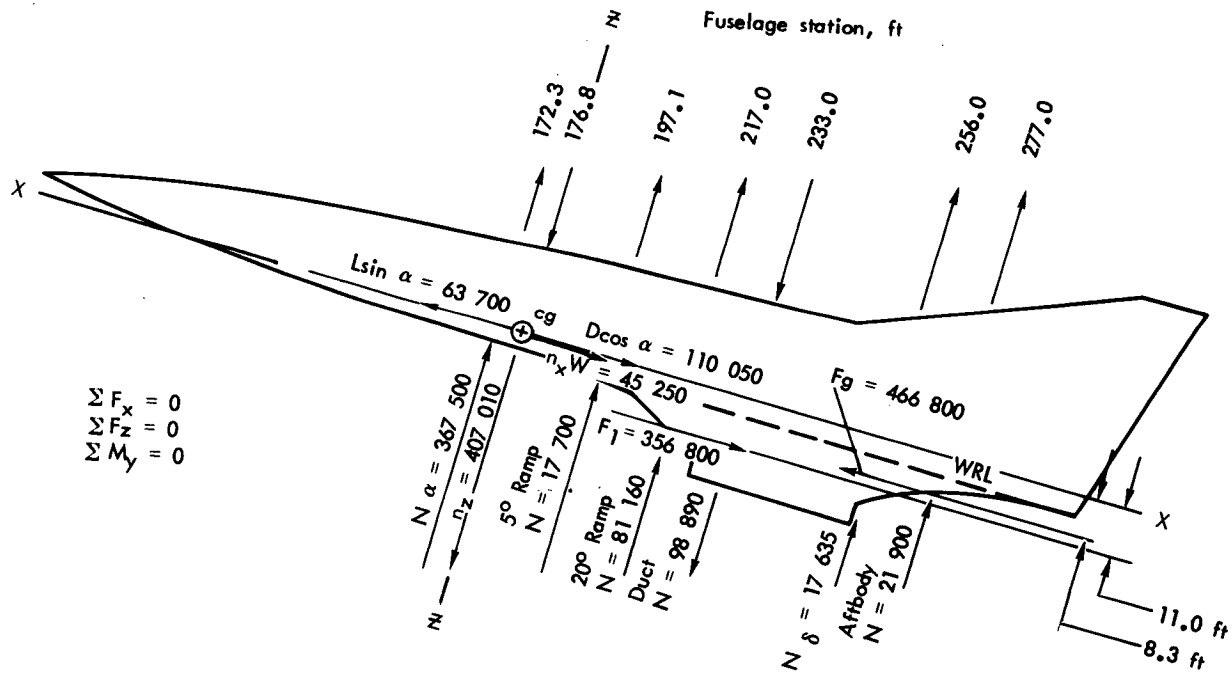

Figure 2-5. Static balance: cruise condition (1g nominal)

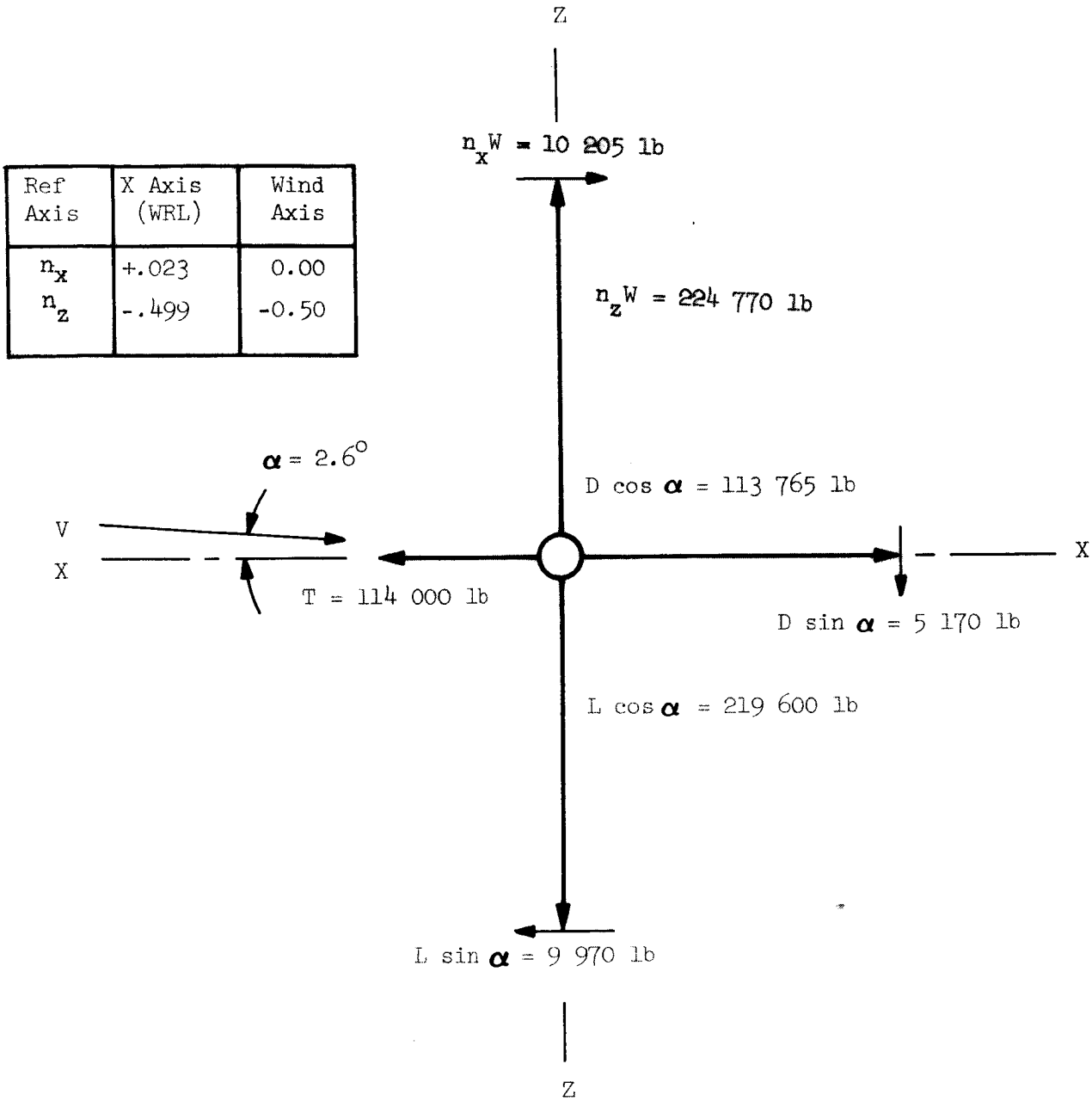

Ref Axis	X Axis (WRL)	Wind Axis
n_x	+.023	0.00
n_z	-.499	-0.50

Figure 2-6. -0.5g maneuver condition: static balance at cg

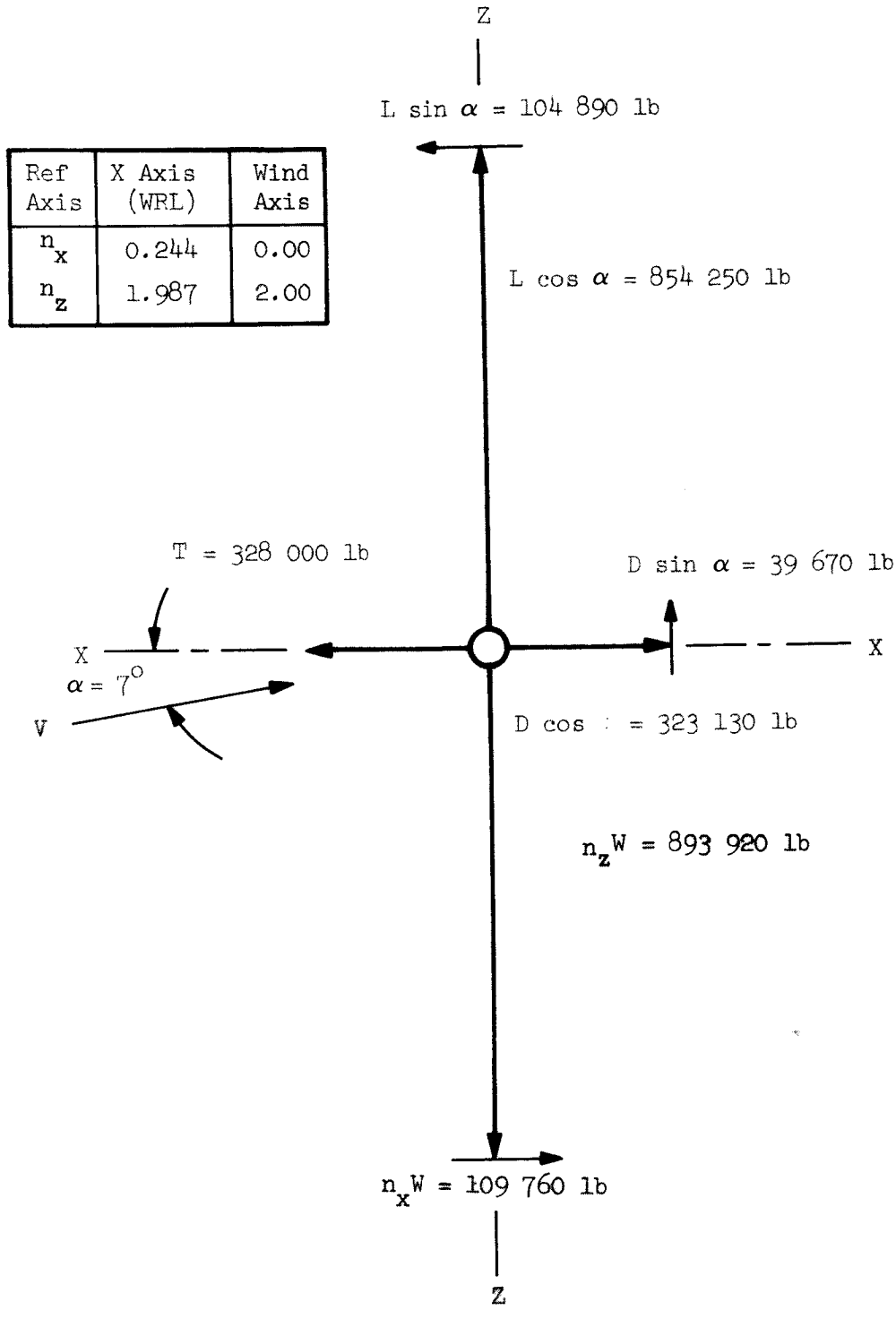

Ref Axis	X Axis (WRL)	Wind Axis
n_x	0.244	0.00
n_z	1.987	2.00

Figure 2-7. 2g maneuver condition: static balance at cg

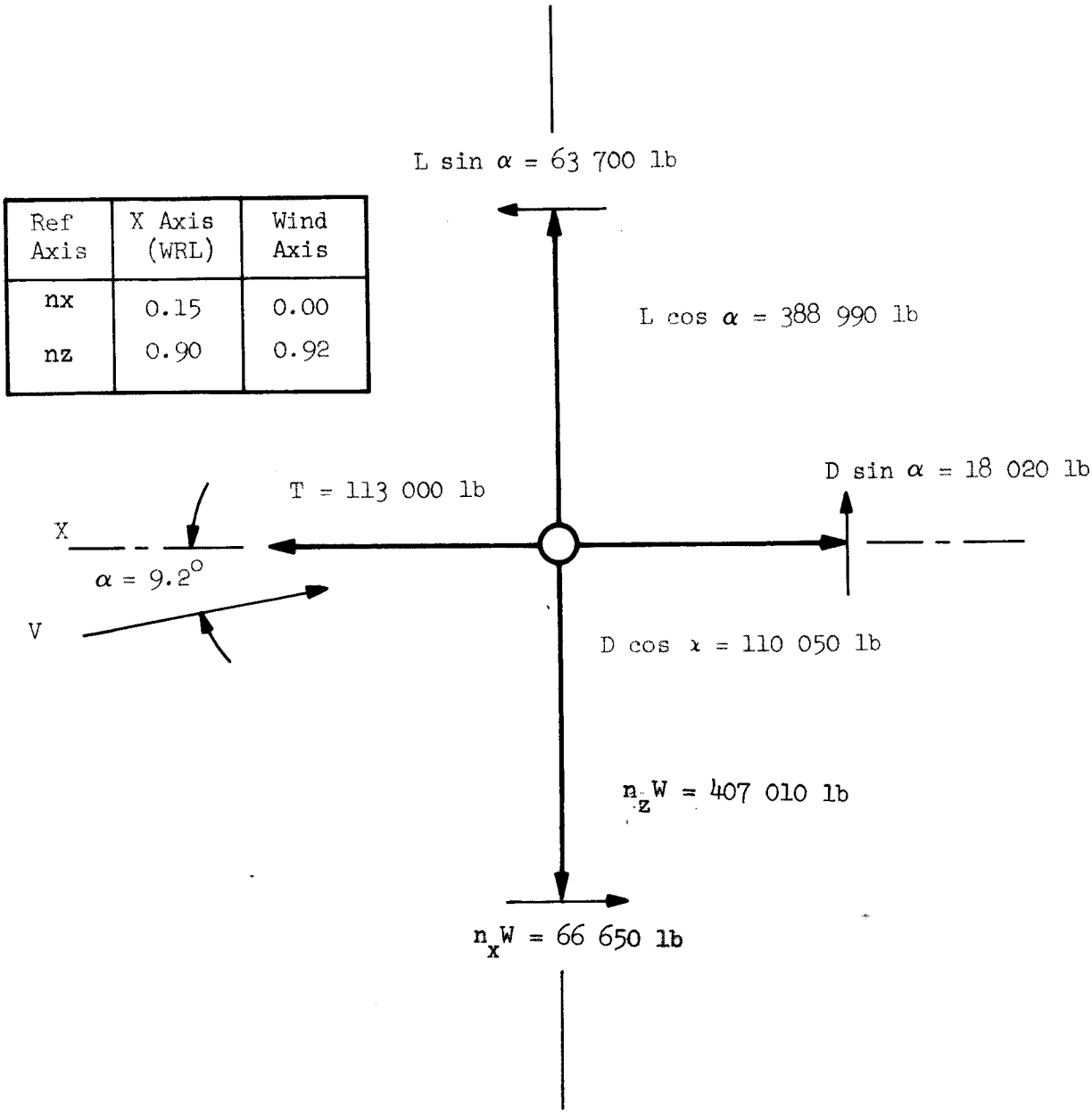

Ref Axis	X Axis (WRL)	Wind Axis
nx	0.15	0.00
nz	0.90	0.92

Figure 2-8. 1g cruise condition: static balance at cg

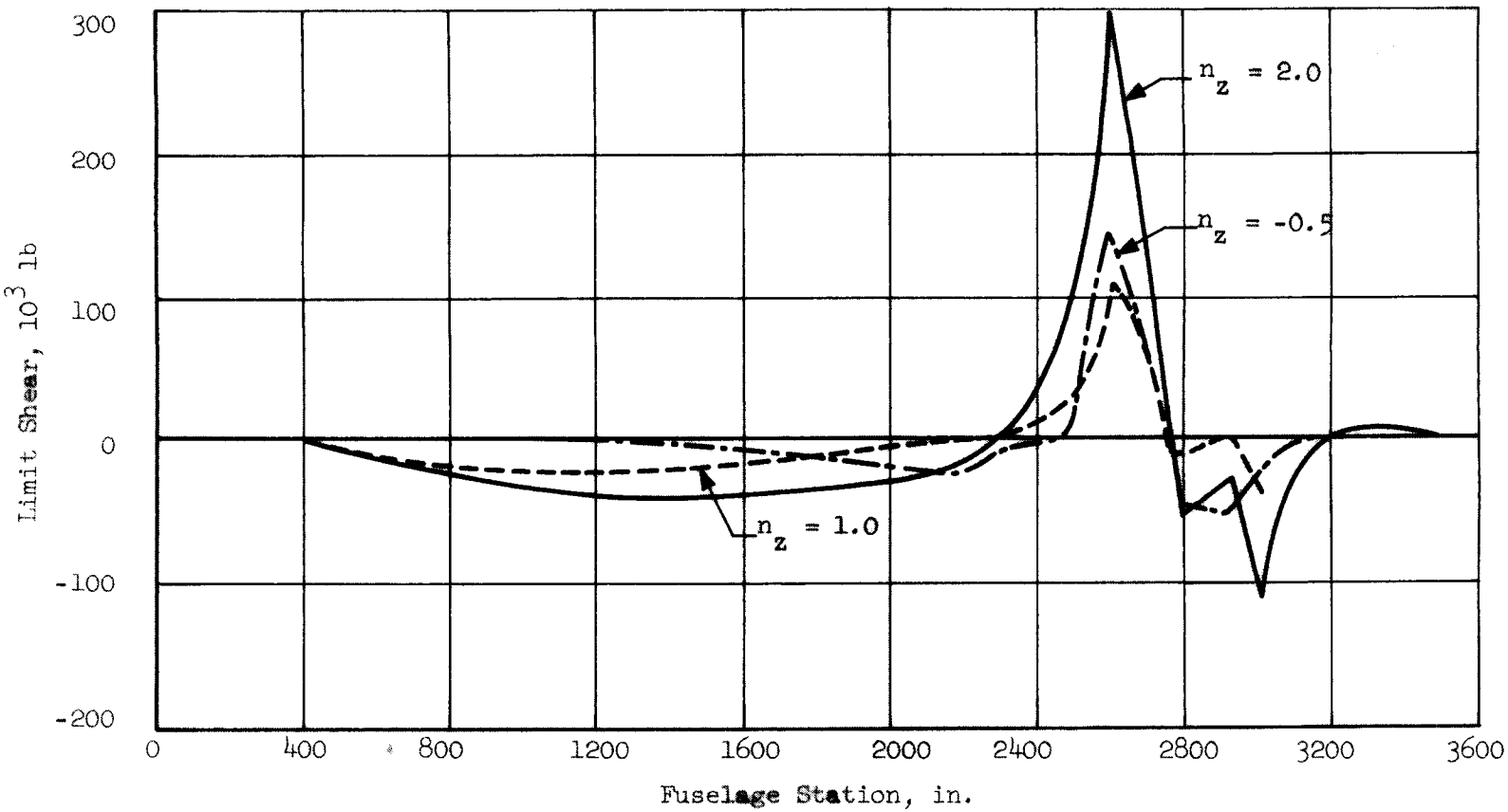

Figure 2-9. Vehicle longitudinal shear distribution (limit)

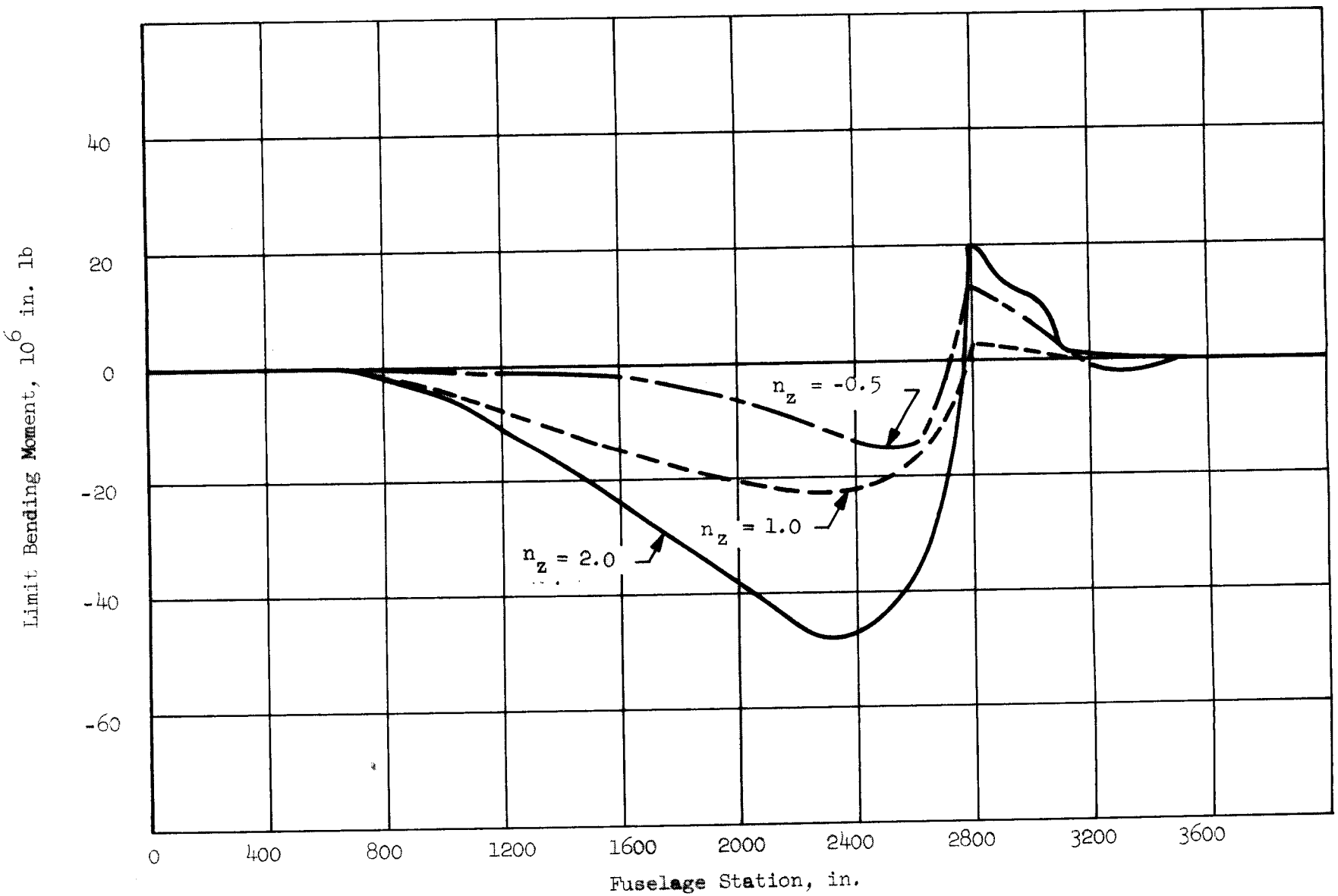

Figure 2-10. Vehicle longitudinal bending moment (limit)

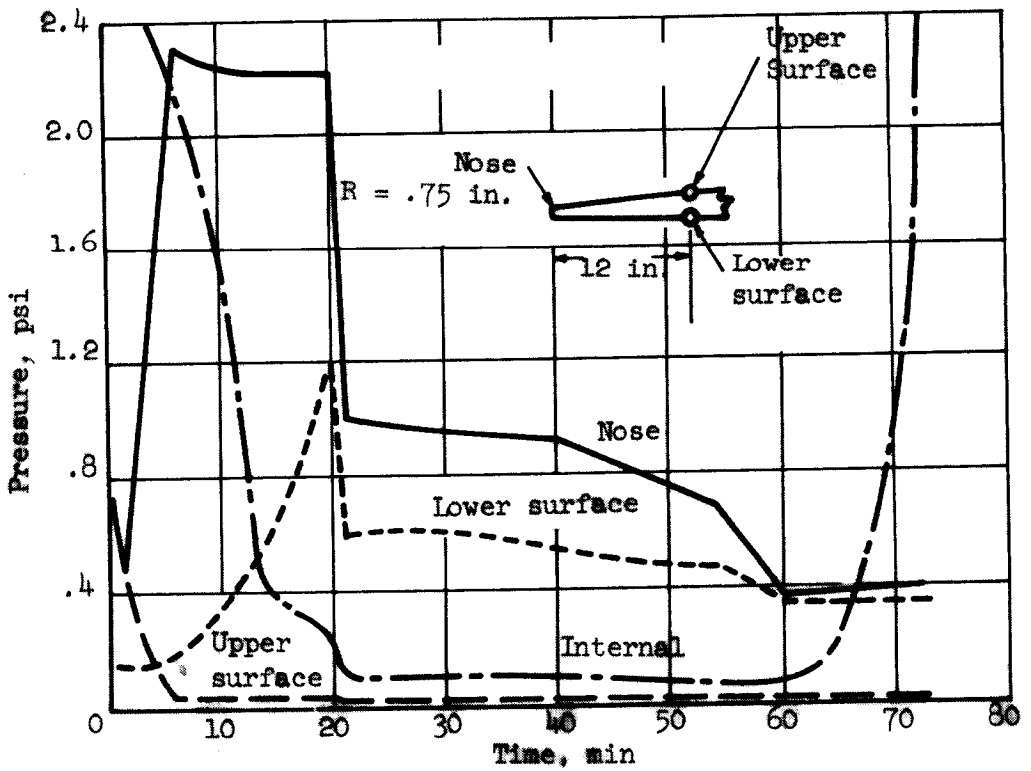

Figure 2-11. History of wing leading edge pressure vairations for cruise mission

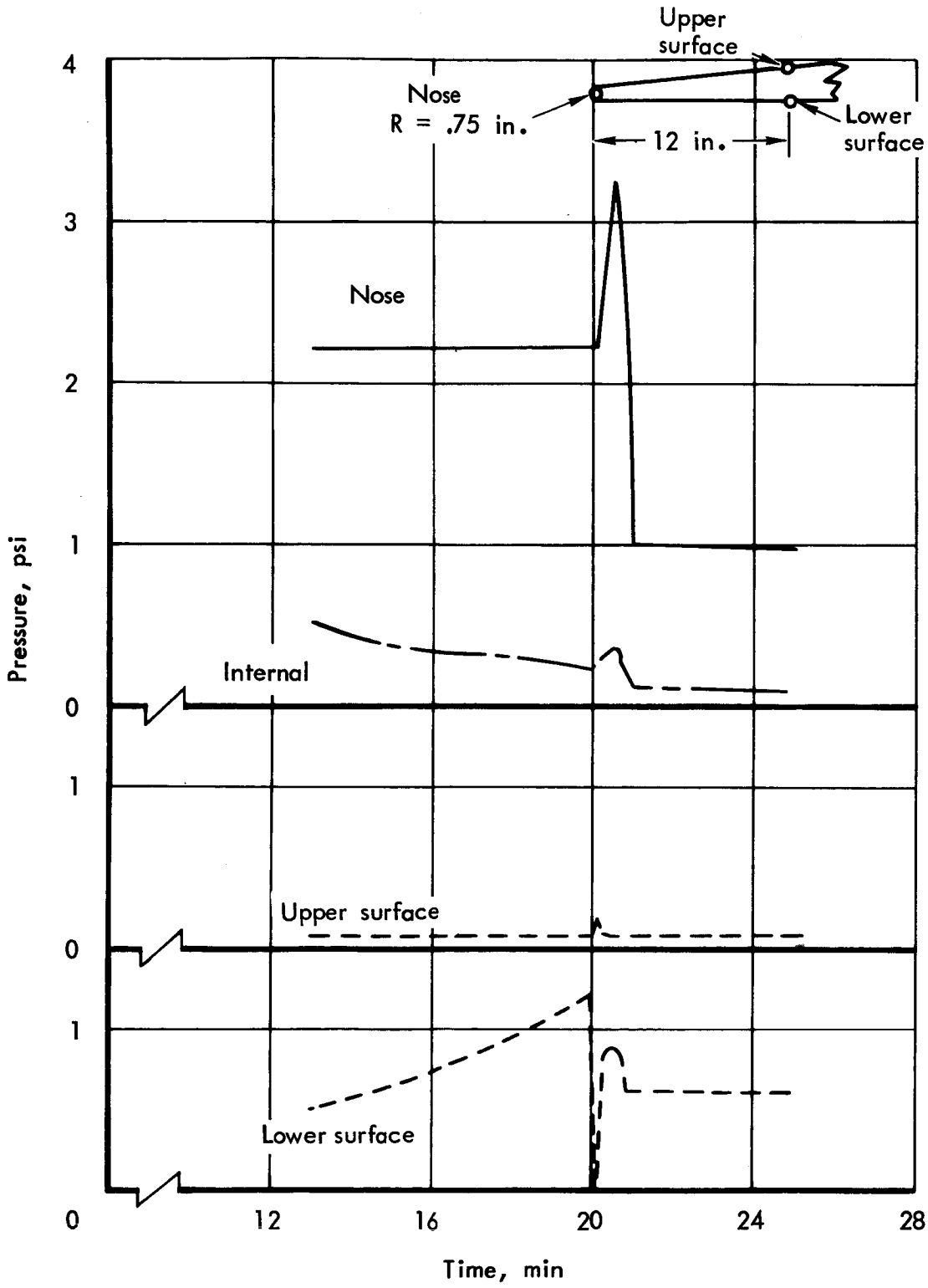

Figure 2-12. Wing leading edge pressure (limit) variations during maneuver

Section 3

AERODYNAMIC HEATING ANALYSIS

by

D. A. Brogan, F. L. Guard

CONTENTS

ILLUSTRATIONS

SYMBOLS

BL	Butt line
$\mathcal{F}_{ls}$, $\mathcal{F}_{lu}$, $\mathcal{F}_{us}$	Configuration factors for determining the radiation heat transfer from lower surface to space, from lower surface to upper surface, and from upper surface to space, respectively
g	Gravitational acceleration
h	Local heat transfer coefficient
M_e	Local Mach number
Re_e	Reynolds number evaluated at the boundary layer edge
T	Temperature
T_{aw}	Adiabatic wall temperature
ϵ	Emittance
σ	Stefan-Boltzmann constant

Section 3

AERODYNAMIC HEATING ANALYSIS

GENERAL

Accurate prediction of aerodynamic heating and resulting temperatures is required for proper materials selection, structural design, and determination of insulation requirements. Theoretical and empirical methods were employed to predict aerodynamic heating rates during this investigation. Also, prediction techniques were required for structural temperature determination using transient structural heating analyses.

Aerodynamic heating requirements were established at various vehicle locations as summarized below. In all cases, Hansen's equilibrium air properties (ref. 3-1) and 1962 Standard Atmosphere data were used in theory evaluation.

Leading Edge Heating

Wing leading edge heating rates were computed by the swept cylinder theory of Beckwith for laminar flow (ref. 3-2) and the Beckwith and Gallagher theory for turbulent flow (ref. 3-3).

Leading edge transition from laminar to turbulent flow was based on the criterion proposed by Bushnell (ref. 3-4) and was assumed to occur at a free-stream Reynolds number of 130000 based on leading edge diameter. Circumferential leading edge heating was determined from reference 3-5.

Wing Lower Surface Heating

The flow field over the wing lower surface as positive angle of attack (windward surface) was obtained from a real gas computer solution (ref. 3-6) assuming local conditions to be those behind a single oblique shock produced by a flow deflection equal to the local effective angle of attack. Laminar and turbulent heat transfer coefficients were computed from two-dimensional theory using Eckert's reference enthalpy method (ref. 3-7), and the theory of Spalding and Chi (ref. 3-8), respectively.

Flow over both the wing lower and upper surfaces was assumed turbulent whenever the leading edge flow was turbulent. For laminar leading edge flow,

the transition criteria used in analyses resulted from flight heating data obtained on the ASSET test program (ref. 3-9); however, two other transition criteria were also evaluated but not used. The second criterion was based on recent wind tunnel and ballistic range flat plate transition data which were correlated by Lockheed (ref. 3-10). The third transition criterion evaluated is by Jillie and Hopkins (ref. 3-11).

Wing Upper Surface Heating

The prediction of heating rates on the leeward wing upper surface is subject to large unknowns, due to the limited amount of theoretical and experimental work in this area. For the present study, upper surface flow field and heating methods were used which yielded good agreement with data obtained from the X-15 flight test program (ref. 3-12). For leeward upper surface flow, a Prandtl-Meyer expansion was assumed to the local expansion angle up to a total flow deflection angle of 8 degrees. For larger expansion angles, constant flow properties equal to those for an 8-degree expansion were assumed. Turbulent flow was assumed for all flight conditions. For windward flow on the upper surface, flow field and transition criteria were employed identical to those used on the lower surface.

Fuselage Heating

Inviscid flow properties on the fuselage were obtained from a computer solution of the method of characteristics (ref. 3-13). Pressures along the upper surface centerline were assumed equal to freestream static, and heating rates were determined from the theories discussed previously (vis., Eckert, Spalding and Chi). Flow behind the bow shock along the bottom of the fuselage area was assumed identical to wedge flow behind a leading edge oblique shock.

The method of characteristics flow field solution was also used to provide flow properties upstream of the wing leading edge which were used in evaluating the freestream Reynolds number for leading edge transition.

Radiation Equilibrium Temperatures

Initial calculations of the vehicle external surface temperature distributions used for the initial structural concept and material screening were made assuming radiation equilibrium conditions; i.e., the convective heating rate to the vehicle surface is balanced by radiation to space. This assumption is reasonable since the various structural concepts are thin metal skins with little capability for storing heat internally. For the wing, where

appreciable heat may be transferred from the lower to upper surface by radiation, configuration factors were calculated with a formula developed by Hottel (ref. 3-14). Radiation relief to space was included for all surfaces, with an appropriate view factor determined by Nusselt's unit sphere method.

Transient Thermal Analysis

Temperatures developed by the radiation equilibrium analysis neglected thermal capacities of the structure and accounted for radiation within the wing by a simple two-surface network, neglecting the effects of intervening structure. As such, the analysis defined the general thermal environment and probable maximum temperatures for the vehicle external surfaces. To aid in the selection of the optimum structural concepts with the given thermal environment capability, thermal analyses accounting for transient effects and the necessary structure detail were used to examine in detail the comparative structural temperature and thermal gradients for each candidate concept. The analyses were performed using the Thermal Analyzer IBM-360 (ref. 3-6) computer program, which affords direct solution of three-dimensional transient problems involving conduction, convection, radiation, and heat storage under impressed arbitrary boundary conditions (temperatures and/or heating rates). The transient heat transfer solution is obtained by converting the physical system into one consisting of lumped thermal capacities (nodes) connected by thermal resistors, and then using the lumped parameter, or finite differences, approach to solve for the temperature history of the system. Boundary conditions included the convective heat fluxes imposed on external surfaces according to the heating theories outlined above, as well as radiation relief to the surroundings assumed at $0^{\circ}F$. All internal radiation was assumed to originate from gray diffusely reflecting surfaces of constant emittance. Reflected radiation was accounted for by using configuration factors determined from the matrix method of Hottel (ref. 3-15). This method, in combination with a discrete dissection of the internal structure into assumed constant temperature nodes, provides the most sophisticated approach to the radiation/convection heat transfer problem currently available for solution on the computer. Conduction heat transfer was accounted for in these analyses whenever applicable. However, for a thin skinned structure at very high temperatures, radiation heat transfer within a structure is usually at least an order of magnitude greater than conduction heat transfer, and the latter may be neglected.

ANALYSIS RESULTS

The laminar-turbulent flow transition criteria were evaluated, and the corresponding lower surface temperature computed. The chordwise temperature distributions during cruise from the leading edge through the transition region are shown superimposed in figure 3-1 for wing location BL 304.

One criterion was based on recent wind tunnel and ballistic range flat plate transition data which were correlated by Lockheed (ref. 3-10). The

following empirical equations were recommended for estimating the locations of the start and end of transition:

$$\text{LOG}_{10}\left[\frac{\text{Re}_{e,\ \text{start}}}{\left(\frac{\text{Re}_e/\text{ft}}{10^6}\right)^{0.70}}\right] = 5.30 + 0.10\ M_e$$

$$\text{LOG}_{10}\left[\frac{\text{Re}_{e,\ \text{end}}}{\left(\frac{\text{Re}_e/\text{ft}}{10^6}\right)^{0.35}}\right] = 5.95 + 0.08\ M_e$$

where:

Re_e/ft = unit Reynolds number per foot

$\text{Re}_{e,\text{start}}$ = Reynolds number evaluated at start of transition

$\text{Re}_{e,\text{end}}$ = Reynolds number evaluated at end of transition

M_e = local Mach number

Subscript e denotes evaluation at the boundary layer edge. Flow properties on the lower wing surface were computed by wedge theory and also by isentropically expanding leading edge stagnation line properties to the wedge pressure. The two flow field solutions resulted in transition locations which agreed within seven percent.

The transition criterion proposed by Jillie and Hopkins (ref. 3-11) is based on the assumption that the change in transition location produced by variations in Mach number and sweep angle is associated entirely with changes in local unit Reynolds number. The latter is evaluated assuming an isentropic expansion of leading edge stagnation line properties to the inviscid flat plate pressure. The zero-sweep freestream transition Reynolds number (27 million) was obtained from figure 3 of reference 3-11 and is based on extrapolation of test data obtained at a freestream Mach number of 2.5. Jillie and Hopkins do not present a method for estimating the location of the end of transition. The temperature distribution shown in figure 3-1 assumes that end of transition Reynolds number is twice the start of transition value.

Comparison of the wing surface temperatures resulting from the three transition criteria, plotted in figure 3-1, indicates small differences in transition location compared to the total chord length of 80 feet at this wing location. For all three criteria, transition starts within the first 10 feet

after the leading edge. Peak temperatures at the start of fully turbulent flow fall within a 100°F range for the three methods, indicating a flat portion of the curve and good predictability for peak temperatures in this region of the wing.

Radiation Equilibrium Temperatures

Initial calculations of the vehicle external surface temperature distribution were made assuming radiation equilibrium conditions. Radiation relief to space was included for all surfaces, with an appropriate view factor determined by Nusselt's unit sphere method. Computed view factors for the wing upper surface are shown in figure 3-2.

A schematic of a typical wing location is shown below:

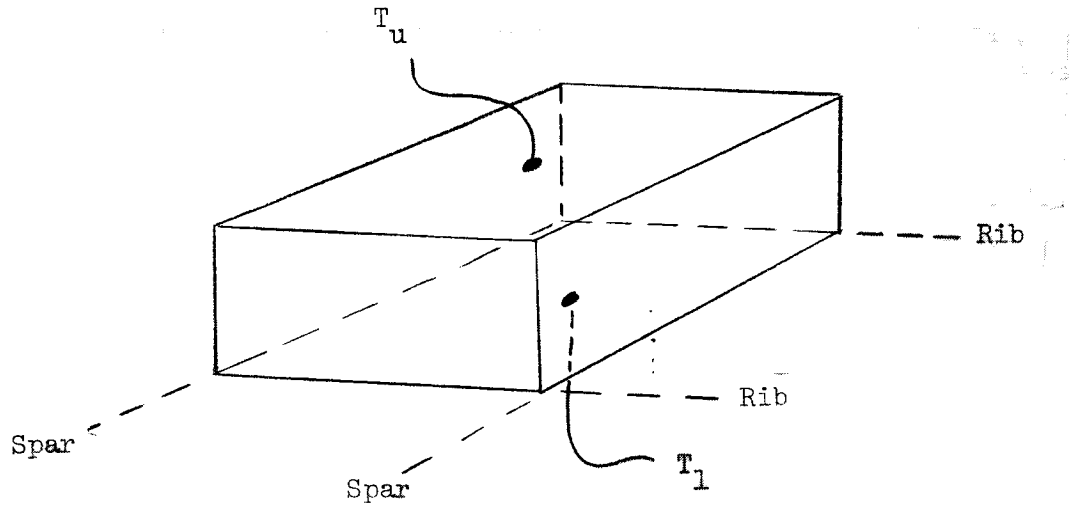

An energy balance results in two equations for the two unknown surface temperatures:

$$h_l (T_{aw,l} - T_l) - \sigma\epsilon\mathfrak{F}_{ls} T_l^4 - \sigma\epsilon\mathfrak{F}_{lu}(T_l^4 - T_u^4) = 0$$

$$h_u (T_{aw,u} - T_u) - \sigma\epsilon\mathfrak{F}_{us} T_u^4 + \sigma\epsilon\mathfrak{F}_{lu}(T_l^4 - T_u^4) = 0$$

Methods for computing the local heat transfer coefficients (h) and adiabatic wall temperatures (T_{aw}) were discussed previously. The configuration

factors, $\mathcal{F}_{ls}$, $\mathcal{F}_{lu}$, and $\mathcal{F}_{us}$, determine the radiation heat transfer from lower surface to space, from lower surface to upper surface, and from upper surface to space, respectively.

Results of the radiation equilibrium analysis are shown in figure 3-3, 3-4, and 3-5 for the -0.5g, 2.0g and cruise conditions, respectively. The trajectory perturbations at the end of climb show the effects of peak heating rates on the upper surface (-0.5g condition) and on the lower surface (2.0g condition). Temperatures for the transient 2.0g condition average 400°F higher than at the cruise condition. For the -0.5g condition, upper wing surface temperatures are hotter than lower surface temperatures because of a negative flight angle of attack. However, expansion of the flow over the upper surface results in decreasing temperatures such that at the aft portion of the wing, upper and lower surface temperatures are almost identical. The effect of radiation heat transfer between the wing surfaces may be seen in the unusual temperature patterns on the lower wing surface, which reflect the different temperature levels on the differently sloped portions of the upper surface.

REFERENCES

3-1 Hansen, C.F.: Approximations for the Thermodynamic and Transport Properties of High Temperature Air. NASA TR R-50, 1959

3-2 Beckwith, I.E.: Similar Solutions for the Compressible Boundary Layer on a Yawed Cylinder with Transpiration Cooling. NASA TR R-42, 1959.

3-3 Beckwith, I.E.; and Gallagher, J. J.: Local Heat Transfer and Recovery Temperatures on a Yawed Cylinder at a Mach Number of 4.15 and High Reynolds Numbers. NASA TR R-104, 1961.

3-4 Bushnell, D. M.: Interference Heating on a Swept Cylinder in Regions of Intersection with a Wedge at Mach Number 8. NASA TN D-3094, December 1965.

3-5 Thomas, A. C.: Perlbachs, A.; and Nagel, A.L.: Advanced Reentry System Heat Transfer Handbook for Hypersonic Flight. AFFDL-TR-65-195, June 1966.

3-6 Schultz, H.D.: Thermal Analyzer Computer Program for the Solution of General Heat Transfer Problems. Lockheed-California Company, LR 18902, July 1965.

3-7 Eckert, E. R. G.: Survey of Heat Transfer at High Speeds. WADC TR-54-70, April 1954.

3-8 Spalding, D. B.; and Chi, S. W.: The Drag of a Compressible Turbulent Boundary Layer on a Smooth Flat Plate With and Without Heat Transfer. Journal of Fluid Mechanics, Vol, 18, January 1964.

3-9 Pagel, L.; et al: ASSET, Correlative Analysis of Heat Transfer Data. AFFDL-TR-65-31, Vol. IV, April 1966 (Confidential).

3-10 Schultz, H. D.: Hypersonic Boundary Layer Transition. Lockheed-California Company, LR 21245, December 1967.

3-11 Jillie D. W.; and Hopkins, E. J.: Effects of Mach Number, Leading-Edge Bluntness, and Sweep on Boundary-Layer Transition on a Flat Plate. NASA TN D-1071, 1961.

3-12 Personal Communication. F. L. Guard, Lockheed-California Company and R. D. Banner, NASA Flight Research Center, Edwards Air Force Base, California, November 1967.

3-13 Benson, J. L.: Computer Program for the Design and Analysis of Hypersonic Inlets. Lockheed-California Company, LR 18079, August 1964.

3-14 Jakob, M: Heat Transfer. Volume II, Wiley, New York, 1949.

3-15 McAdams, W. H.: Heat Transmission. McGraw-Hill, New York, 1933.

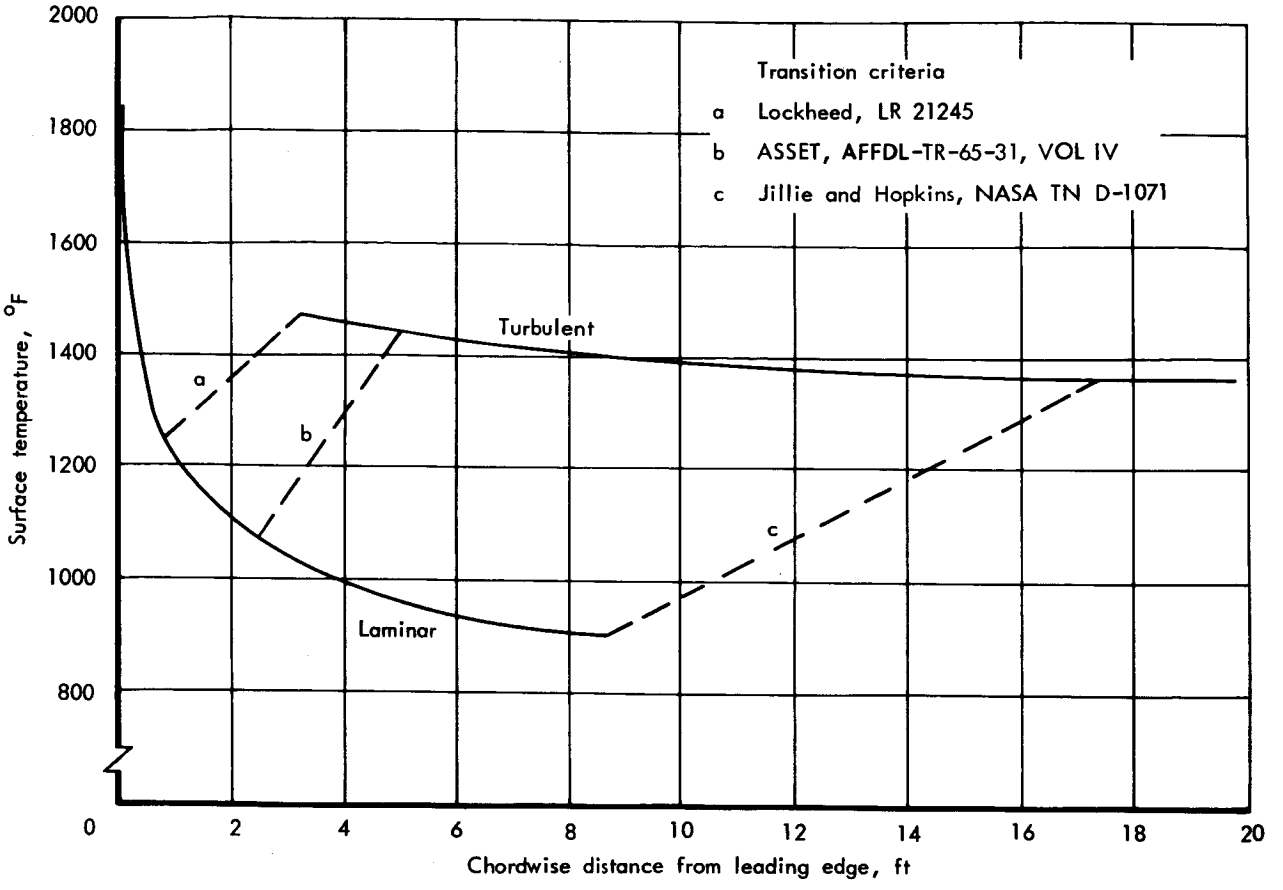

Figure 3-1. Wing lower surface laminar to turbulent transition comparison, cruise condition

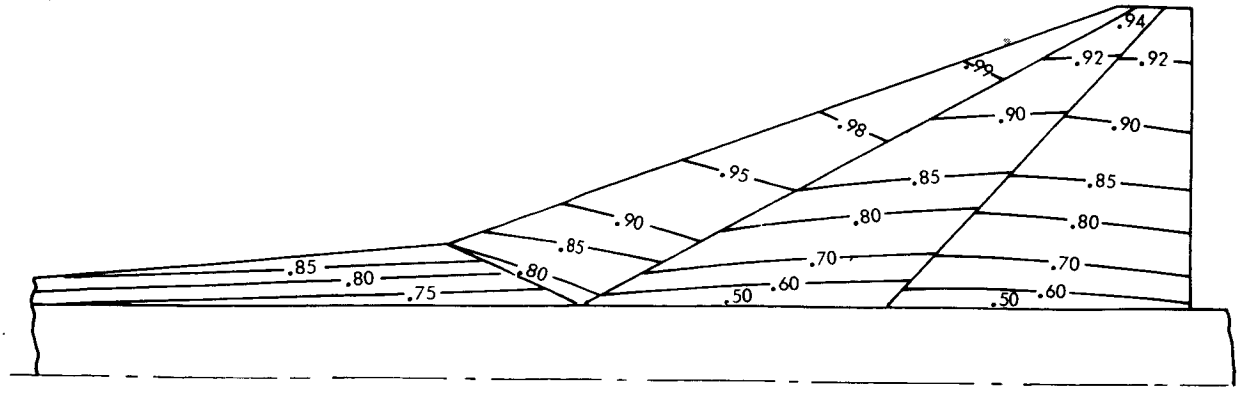

Figure 3-2. Wing upper surface view factors to space

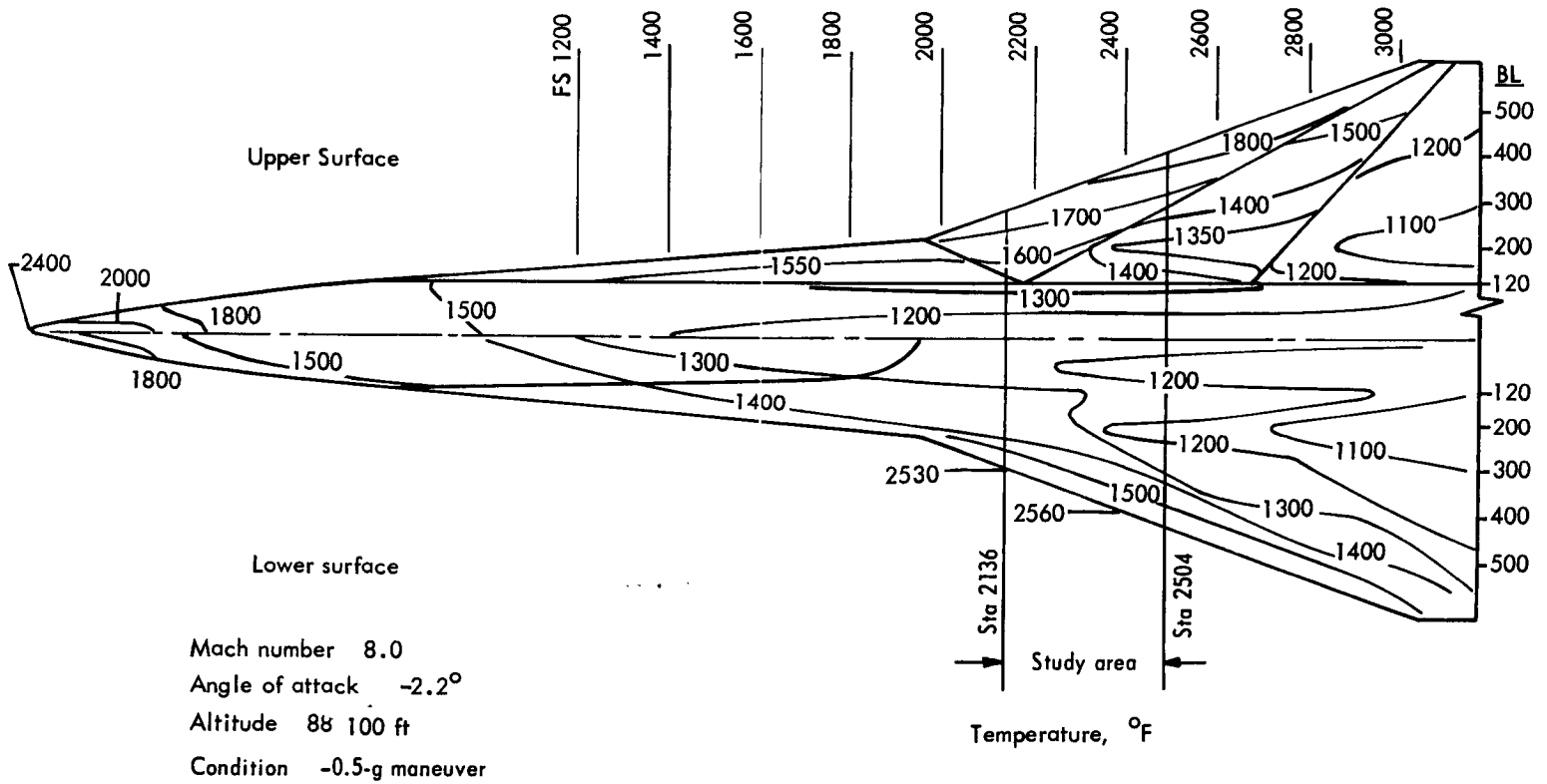

Figure 3-3. Radiation equilibrium temperature distribution for -0.5-g maneuver

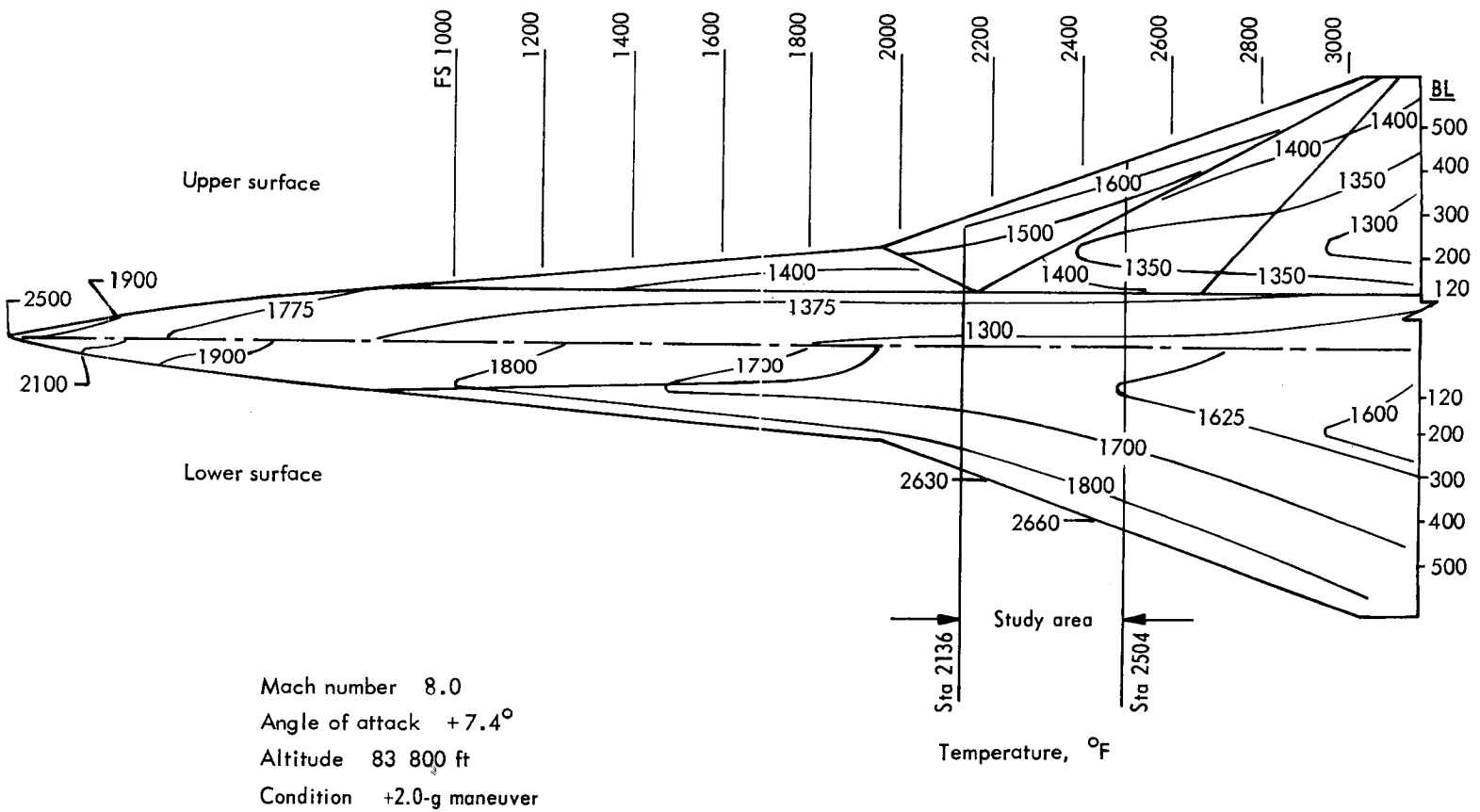

Figure 3-4. Radiation equilibrium temperature distribution for 2.0-g maneuver

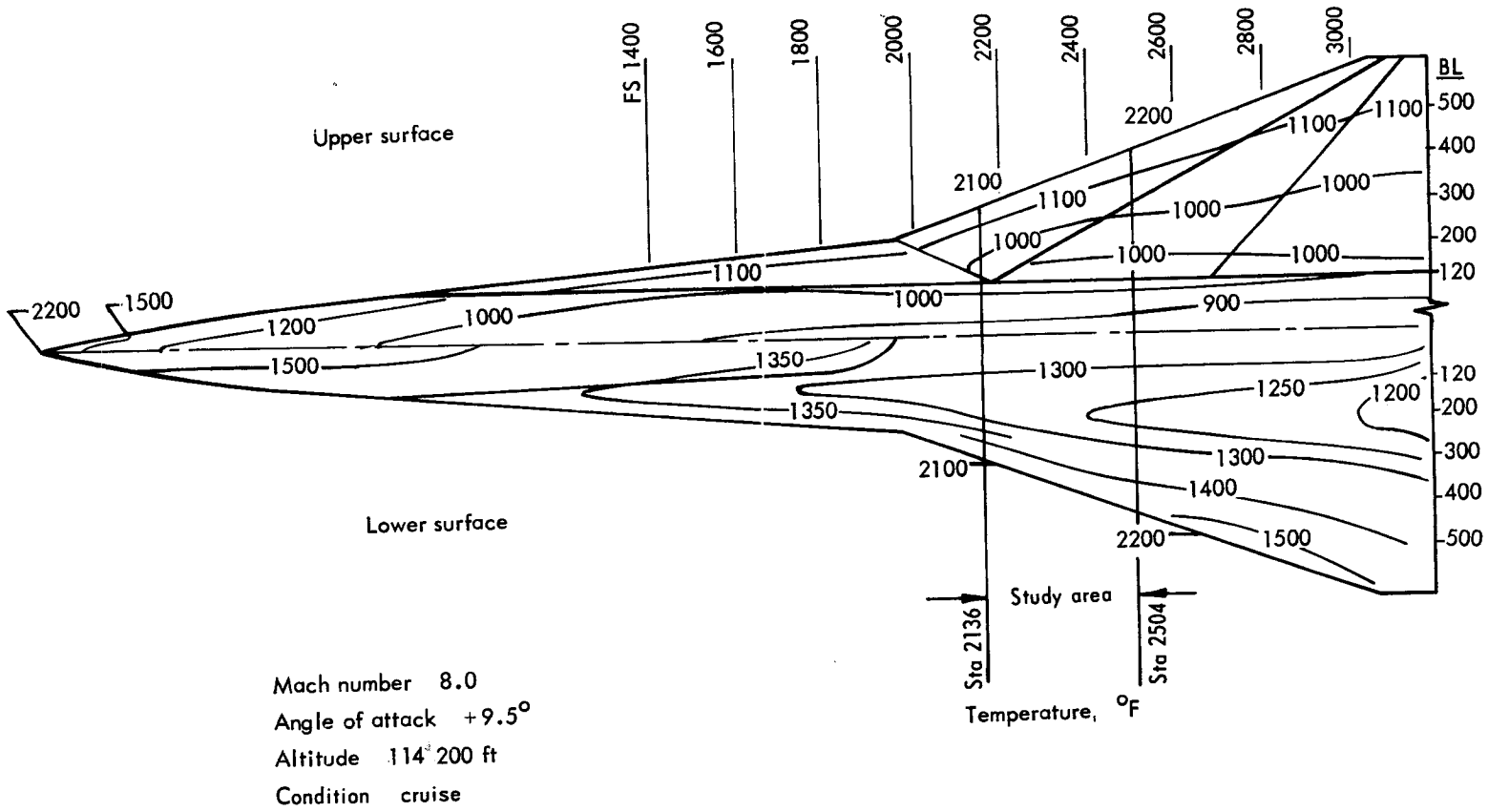

Figure 3-5. Radiation equilibrium temperature distribution for cruise

Section 4

MATERIAL ANALYSIS

by

J. W. Lewis, L. F. Tenn, I. F. Sakata

CONTENTS

TABLES

ILLUSTRATIONS

ILLUSTRATIONS (Cont.)

SYMBOLS

C_p	Specific heat
E	Modulus of elasticity
E_c	Compression modulus of elasticity
$E_{e\ell}$	Elastic modulus of elasticity
e	Strain
F_{cy}	Compression – yield strength
F_{tu}	Ultimate tensile strength
$F_{0.7}$	Stress corresponding to modulus of $0.7\ E_{e\ell}$
f_a, f_m	Alternating and mean stress used when defining cyclic stresses
K	Thermal conductivity
K_t	Stress concentration factor
n	Shape factor
P_L	Larson-Miller parameter
T	Temperature
t	Thickness
t_m	Minimum gage thickness
α	Mean coefficient of thermal expansion
ρ	Density

Section 4

MATERIAL ANALYSIS

GENERAL

Considering the load-temperature environment and vehicle life characteristics, candidate superalloys and refractory metal materials were evaluated. At elevated temperatures the usefulness of a material system is limited by its strength, oxidation resistance, and metallurgical stability. The primary consideration for a candidate alloy, in this program, is its ability to maintain strength at its service temperature and perform without serious degradation in properties throughout cyclic exposures.

Superalloys (nickel and cobalt base) were considered for wing primary structure application. Dispersion-strengthened alloys, as well as the nickel and cobalt base superalloys, were considered for heat shield application. For leading edge requirements, dispersion-strengthened, and refractory alloys were evaluated. Fibrous quartz materials were considered for the lower surface thermal protection aspects.

A materials survey was conducted encompassing all available materials, resulting in a parametric evaluation of several leading candidate alloys. It is important to utilize the correct properties of candidate materials when comparisons are made. Comparing tensile and creep strength alone is often misleading when the failure mode is buckling or minimum gage requirements are imposed. The most significant material property factors were considered in this parametric analysis. These factors are presented as merit indices for the leading candidate alloys. Merit indices, as listed below, are devised to relate materials to various design parameters that provide an efficient index for materials comparison.

- Physical properties (α, K, C_p, and emissivity)
- Mechanical properties (F_{tu}/ρ, F_{cy}/ρ, and creep)
- Structural stability during cyclic exposure $\left(\bar{\eta} E_c \right)^{1/2}$
- Fabricability
- t_m - material minimum gage
- Oxidation characteristics
- Metallurgical stability

In addition to using existing data for the evaluation of leading candidate alloys and final material selection, 176 material screening, 330 joining technique, and 576 formability tests were conducted (see section 5).

The material screening tests were for oxidation and thermal stability (tensile properties after exposure to elevated temperatures for various periods of time and metallurgical examination), and emittance.

The joining technique test evaluation encompassed resistance spotwelding, spot diffusion bonding, brazing (spot and continuous), TIG welding, electron beam welding and mechanical fasteners for the various leading candidate materials and a range of gage thicknesses.

The formability evaluation consisted of bend, flanging-shrink, flanging-stretch, beading-stretch, and draw form tests for the various leading candidate materials.

After the final selection of alloys, design-allowable data were established and used for the structural concept analyses.

MATERIAL CHARACTERISTICS

Materials evaluation and selection were heavily influenced by the general characteristics of superalloys and refractory metals.

Characteristics of Superalloys

The term superalloy applies to the nickel and cobalt base alloys, which are intended for structural use in the temperature range of 1000° to 2000°F. Generally, the cobalt base alloys are more chemically and metallurgically stable at higher temperatures than are the nickel base alloys. Superalloys display good weldability with the exception of the thoria-dispersed strengthened alloys, and are oxidation resistant except at high temperatures. Oxidation resistance is dependent not only on velocity, density, and composition and flow pattern of the oxidizing environment but also on structure, state of stress, and geometry of the part. Therefore, alloys designed for strength may not have maximum oxidation resistance. When maximum strength is desired, protective coatings should be considered, usually a light surface oxide for high emittance; however, intergranular oxidation in small amounts can have a serious effect on thin sections. Intergranular oxidation not only reduces the cross section, but can act as a notch in notch-sensitive materials. Of the superalloys, the precipitation hardenable nickel base alloys, such as Rene' 41, are the most susceptible to intergranular oxide penetration above 1600°F.

Characteristics of Refractory Metals

For structures to be used at temperatures above 2000°F, refractory metals must be considered. For example, columbium possesses several properties that make it attractive for high temperature structural applications. This metal

and most of its alloys possess excellent fabricability, and its density is less than that of most of the refractory materials. However, the use of columbium at temperatures greater than 1000°F requires an oxidation protective system, since unprotected columbium reacts with oxygen to form a nonadherent oxide at a rate dependent on alloy composition, temperature, and environment. At temperatures greater than 2700°F, the rate is great enough to produce an exothermic reaction, called autoignition. At lower temperatures, the diffusion of oxygen causes embrittlement.

Columbium retains structural strength up to temperatures approaching 3000°F, but the autoignition restricts its maximum useful temperature to approximately 2700°F on a short time basis. Reuse of coated columbium should be limited to temperatures up to 2500°F wherein creep is significant. Two fused slurry coating systems, R512A (Si-20Cr) and R512E (Si-20Cr-20Fe), have been shown to be effective for high-temperature columbium applications.

Tantalum is useful in the greatest temperature range of any metal because of its high melting point, retention of ductility at room temperatures, and excellent fabricability. Its greatest potential as a structural material lies in the temperature range greater than that possible with columbium.

However, like columbium, unprotected tantalum oxidizes at a high rate. For this reason, a protective coating must be employed when service temperatures exceed 1000°F in oxidizing environments. This coating would also inhibit autoignition, which would occur at some high temperature ($T \approx 3000°F$).

Two practical coating systems to protect tantalum at 3000°F are Sylcor R512C (So-20Ti-10Mo) and R505 (Sn-25Al).

PARAMETRIC ANALYSIS

The materials listed below were evaluated for structural application by parametric analysis based on published property data and were selected for additional screening tests.

Leading candidates	ρ, Density (lb/in^3)	Application
Rene' 41	0.298	Primary structure
Haynes 25	0.330	
Rene' 41	0.298	Heat shields
Haynes 25	0.330	
TD NiCr	0.306	
Ta-10W	0.608	Leading edge
Cb-752	0.326	
TD NiCr	0.306	

Merit indices relating materials to various design parameters provide an efficient index for comparison as shown in figures 4-1 through 4-9. Figures 4-1 and 4-2 show density-compensated tensile and compressive-yield stresses versus temperature for the leading candidate materials. The allowable stresses divided by the density ρ show advantages for Rene 41 in the temperature ranges 1200° to 1600°F of the major portion of the wing structure.

The compressive buckling weight index, $\frac{\rho}{\bar{\eta}(E_c)^{\frac{1}{2}}}$, is plotted in figure 4-5 versus the applied compressive stress f_c for temperatures of 1200°, 1300°, and 1400°F. The index $\frac{\rho}{\bar{\eta}\ (E_c)^{\frac{1}{2}}}$ is an expression of a material's structural stability characteristic in relation to weight (ref. 4-1). The terms of the expression are: ρ is density, E_c is compression modulus , and $\bar{\eta}$ is the plasticity correction factor.

The curves of figure 4-3 indicate that for a given compressive load, panels would weight considerably less if constructed of Rene 41 rather than Haynes 25, provided minimum gage does not constrain the results.

Other factors considered included fabrication, physical properties, (, K, Cp, and emissivity), creep, fatigue, minimum gages, oxidation characteristics, and metallurgical stability. Coefficient of thermal expansion, thermal conductivity, specific heat, emissivity, and modulus data are given in figures 4-4 through 4-9.

As an example of elevated temperature considerations, figure 4-10 shows Rene 41 constant-life fatigue diagrams at 1400°F for various stress levels. Variations of mechanical properties of Rene 41 from room temperature to 1600°F are shown in table 4-2 for both A and B probability values (ref. 4-2). Mechanical properties for Haynes 25 and TD NiCr are presented in tables 4-3 and 4-4 (ref. 4-3).

A typical isochronous stress-strain diagram used for creep analysis is shown in figure 4-11. The temperature environment is 1300°F for the Rene 41 sheet material in the 1400°F aged condition. The 4460 hours corresponds to the cruise condition at the low level of reliability; the other 2 curves correspond to nominal and high reliability levels. F_{cy} (0.2 percent strain) and the 0.5 percent strain for tensile creep are indicated in figure 4-11. Tensile creep data for Inconel 625, Haynes 25, Rene 41, 90 Ta-10W, Cb-752, and TD NiCr are presented in figures 4-12 through 4-17.

MATERIALS TESTING

Material screening tests were performed in conjunction with parametric analysis. Existing data, supplemented by data generated under this test investigation, provided the design allowables used in the structural analysis (see section 5).

Material Property Tests

Oxidation and thermal stability, tensile property, emittance, and metallurgical examination tests were conducted for Rene' 41, Haynes 25, and TD NiCr during the materials screening (176 tests). Emittance tests were conducted for the Cb-752 and Ta-10W alloys.

Tensile test data for Rene' 41 and Haynes 25 included room temperature tests of solution heat-treated (annealed) material after exposure to the thermal environment. The normal aging response to annealed Rene' 41 as well as Hayes 25 causes a sharp increase in strength, followed by a drop in strength, as shown in figure 5-5 of Section 5, indicating an overaged condition. Therefore, it was found that Rene' 41 is the most favorable material to satisfy elevated temperature strength requirements, provided it is aged after fabrication to provide predictable allowables required for design.

Emittance test data obtained over expected temperature ranges for Rene' 41, Hayes 25, TD NiCr, Cb-752 and Ta-10W, were used in the thermal structural analyses. Rene' 41 emittance test data are shown in figure 5-41 of section 5, and as a result, an emittance of 0.8 was used for designing with Rene' 41.

Coating Tests for Leading Edge

Initial radiation equilibrium temperature predictions (see figure 3-4 of section 3) indicated that refractory metals would be required for leading-edge applications. Accordingly, screening tests for coated refractory-metal systems were performed. Two leading-edge material candidates were fabricated and tested in a plasma-arc under simulated flight conditions. The first (porous metal), a 50-percent dense porous powder-metallurgy product of Ta-10W, was sintered to a Ta-10W backing sheet. A protective coating of Sylcor R505 (Al-25Sn) was applied to the assembly and vacuum fired at 1900°F for 1 hour. The second candidate fabricated and tested was a Ta-10W sheet leading-edge specimen, disilicide, coated with Sylcor R512C (Si-20Ti-10Mo). This coating was diffused in a vacuum 2580°F for 1 hour.

The two leading-edge material arrangements (porous and sheet) were tested at 2800°, 3000°, and 3100°F for cyclic conditions of temperature to determine the failure point of each. Six-minute cycles were selected to correspond with earlier leading-edge tests, ref. 4-4. The leading-edge test results are shown in figure 5-55 of section 5.

As shown, the sheet concept did not fail after 37 six-minute cycles at 2800°F. Although the porous metal failed after 12 six-minute cycles at 2800°F, there were indications of improvements by a factor of 2 over earlier tests with the same type of coating (ref. 4-4). The mode of oxidation that occurs in the porous Ta-10W/R505 concept produces a considerable number of local hot spots. Failure is a combination of progressive Ta oxidation and thermal stress. The results indicate that adequate oxidation protection at 3100°F is not practical with either of the concepts tested, whereas limited oxidation protection is afforded at 3000°F with the monolithic 90 Ta-10W/R512C concept (37 six-minute cycles).

Structural Joint Tests

Representative structural joints and splices were selected for evaluation (330 tests). Resistance spotwelding and diffusion spot-bonding were evaluated for René 41. For Haynes 25, resistance spotwelding was investigated. Diffusion spot-bonding, brazed-spot, continuous-braze, and riveted techniques were used for TD NiCr.

The joint technique evaluation results, shown in table 5-10 of section 5, indicated that higher joint strengths at elevated temperatures are possible for the resistance spotwelded specimens than for the diffusion-bonded specimens. X-ray inspection of the René 41 spots indicated crackfree welds; therefore, resistance spotwelding was selected for use in panel fabrication of René 41. For the TD NiCr materials, the riveted specimens provided the highest strengths at elevated temperatures, as shown in table 5-13 of section 5.

Formability Tests

Four types of formability tests (bend, flanging, stretch bending, and draw form) were conducted to establish fabrication limits and procedures for the manufacture of the panel-element and structure designs. In the tests of the leading candidate materials, various gages were considered. Procedures resulting from these tests were defined for design, manufacturing panels, and costing exercises (see section 5).

MINIMUM GAGE SELECTION

Minimum gage for fabrication of acceptable structural elements, sheet-thickness availability, and sheet-thickness variation were considered in the structural concept optimization. Table 4-5 presents minimum metallic material thicknesses that were selected for the concepts evaluation. The basis of selection was suitability to fabrication processes involved and to damage resistance.

MATERIAIS SELECTION

Final selections were Rene' 41 for the primary structure and the heat shields (below 1800°F), and TD NiCr for heat shields (above 1800°F) and the leading edge.

Primary Structure and Heat Shield

Rene' 41 was selected for use in the detailed evaluation of the primary structure and heat shields (below 1800°F) because of its excellent high-temperature buckling strength and acceptable fabricability. As indicated in figures 4-1, 4-2, and 4-3, Rene' 41 is the most efficient superalloy at the elevated temperature range in which the structure must operate. Because of oxidation, additional material weight was considered for depth of attack for the operational temperatures and flight times of this program.

Static oxidation behavior at one atmosphere is used for alloy comparison and is shown in figure 4-18 (refs. 4-5, 4-6 and 4-7). Depth of penetration per side for the candidate superalloys is presented, assuming (1) uniform oxide attack, (2) depth of penetration, extrapolated from current data, is uniform and linear with respect to time and temperature to the extrapolated points, and (3) at no stress. These published data have been substantiated by static thermal stability tests conducted in this program. These data are shown in figure 4-18 and discussed in detail in section 5.

TD NiCr was selected for heat shield application above 1800°F, because it is lower in weight than Rene' 41, as discussed in section 20.

Leading Edge

For leading edges, Ta-10W was originally considered the leading candidate on the basis of radiation equilibrium temperatures. However, the two-dimensional thermal analysis described in the section on leading-edge weight indicated a maximum operating temperature of 2200°F, allowing use of TD NiCr without the oxidation coating requirement of refractory metals. For service temperatures from 2300°F, the Cb-752/R512E material was selected; for service from 2500°F to 3000°F, the Ta-10W/R512C material system was chosen.

Figure 4-19 shows the predicted coating life of the Cb-752/R512E system under cyclic exposure. These data represent a composite of tests performed at Lockheed and those reported by the supplier, under various reentry conditions of time, temperature, and pressure. The majority of these tests were for a one-hour time-temperature cycle.

Insulation Materials

Several materials were considered for the insulation required as a part of the lower surface (outboard) thermal-protection system with heat shields. Of the three leading candidate low-density silica fibrous materials, two (Micro-Quartz and Dyna-Flex) are feltlike materials and one, Dyna-Quartz, is a block-tile material. The following tabulation shows the leading candidate insulation material characteristics:

Insulation	Density, lb/ft^3	Maximum utilization temperatures, ^{o}F
Micro-Quartz	3.5 (3.0 nominal)	1600
Dyna-Quartz (heat-stabilized Micro-Quartz)	4.5	2750
Dyna-Flex	6.0	2800

Dyna-Flex was selected because it was the only insulation material that satisfied the requirements for the application. Micro-Quartz does not satisfy the maximum temperature requirement for this program (about 2000°F), and Dyna-Quartz is brittle and therefore has doubtful resistance to vibration loads. Thermal conductivity of Dyna-Flex is shown in figure 4-20.

REFERENCES

4-1 Plank, P. P.: Hypersonic Thermal-Structural Concept Trends. SAE paper 660678, October 1966.

4-2 Lemcoe, M. M.,; and Trevino, Jr., A.: Determination of the Effect of Elevated Temperature Material Properties of Several High Temperature Alloys. ASD-TDR-61-529, June 1962.

4-3 Lockheed California Company, Advanced Material Handbook, LR 18456, December 1964.

4-4 Stein, B. A.; and Vickorek, G. R.: Results of Current Studies on Coated Alloy Sheet at NASA Langley Research Center, July 1967.

4-5 DMIC Report 153: Physical Metallurgy of Nickel Base Superalloys, Battelle Memorial Institute, Defense Metals Information Center, May 1961.

4-6 DMIC Report 214: Oxidation of Nickel-and Cobalt-base Superalloys, Batelle Memorial Institute, Defense Metals Information Center, March 1965

4-7 TD NiCr Data based on information supplied by E. I. DuPont Nemours & Co., dated Sept 20, 1967.

4-8 MIL-HDBK-5: Metallic Materials and Elements for Aerospace Vehicle Structures, December 1968.

4-9 High Temperature High Strength Alloys, American Iron and Steel Institute, Feb 1968.

4-10 Tensile and Creep Properties of .010 & .050 in. René 41 Alloy Sheet from RT to 2000°F, The Marquardt Corp., Report PR 281-1Q-1, AF 33(657)-8706, Sept 1962.

TABLE 4-1

CANDIDATE MATERIALS FOR HYPERSONIC WING STRUCTURES

Temp. range	Wing structural application	Candidate material	Leading candidate materials	Remarks
To 1800°F	Wing surfaces, primary structure, heat shield	Cobalt base alloy: Haynes 25	Haynes 25	Annealed material with moderate tensile properties; good oxidation resistance to 1800°F
		Nickel base alloy: Inco 625		
		Inco 718		
		Hastelloy X		
		Rene' 41	Rene' 41	Fair weldability, but excellent in all other aspects. Primary structure: 1600°F; heat shields; 1800°F
		TD Nickel		
		TD NiCr	TD NiCr	Candidate uncoated material for heat shield application
1800°-2500°F	Lower wing surface leading edge, and heat shield	Chrome 30		
		TD Nickel		
		TD NiCr	TD NiCr	Candidate uncoated material for heat shield and leading edge application to 2200°F
		Columbium Alloy: D-43 B-66 FS-85 C-219Y Cb-752	Cb-752	Candidate for leading edge application to 2500°F. Moderately high mechanical properties preferred. Coating system is a fused slurry silicide (Si-20 CR-20 Fe)
2500°-3500°F	Leading edge	Tantalum alloy: 90Ta-10W	90Ta-10W	Moderate mechanical properties; very good with respect to fabricability. Requires oxidation protective system
		T-222		

TABLE 4-2

MECHANICAL PROPERTIES OF RENE' 41 MATERIAL[a]

Rene' 41 sheet and strip (1400°F aged); t ≤ 0.187 inches						
Temp., °F	Grain	Basis	n (b)	$F_{0.7}$ ksi (b)	E_c 10^6 psi	F_{cy} ksi
75	L	A	25	134.5	31.6	135.0
75	T	A	25	140.7	31.6	141.0
75	L	B	25	139.7	31.6	140.0
75	T	B	25	147.0	31.6	147.0
1200	L	A	15	130.7	24.6	129.6
1200	T	A	15	137.0	24.6	135.4
1200	L	B	15	135.9	24.6	134.4
1200	T	B	15	143.2	24.6	141.1
1400	L	A	15	108.1	22.8	108.0
1400	T	A	15	113.3	22.8	112.8
1400	L	B	15	112.4	22.8	112.0
1400	T	B	15	118.4	22.8	117.6
1500	L	A	10	79.3	20.9	81.0
1500	T	A	10	83.3	20.9	84.6
1500	L	B	10	82.6	20.9	84.0
1500	T	B	10	87.2	20.9	88.2
1600	L	A	10	55.8	17.7	58.0
1600	T	A	10	58.5	17.7	60.6
1600	L	B	10	58.1	17.7	60.2
1600	T	B	10	61.3	17.7	63.2

[a] Reference 4-3.

[b] Ramberg Osgood Parameters, NACA-TN 902.

TABLE 4-3

DESIGN PARAMETERS FOR HAYNES 25 (L-605) SHEET AT ELEVATED TEMPERATURE[a]

Material	Thickness ins.	Temp F	Grain	Basis	n	$F_{0.7}'$ ksi	E_c' 10^6 psi	F_{cy}' ksi
Haynes 25 solution treated sheet (L-605)	0.020 - 0.187	Room	L	B	9	30.82	34.20	37.00
			T	B	9	55.09	34.20	62.00
		1200	L	B	11	21.84	24.60	25.40
			T	B	11	34.42	24.60	38.40
		1300	L	B	11	21.72	23.90	25.20
			T	B	11	32.05	23.90	35.90
		1400	L	B	11	21.08	22.60	24.40
			T	B	11	29.28	22.60	32.90
		1500	L	B	10	16.77	20.90	20.00
			T	B	10	26.12	20.90	29.80
		1600	L	B	10	13.89	18.80	16.70
			T	B	10	22.71	18.80	26.00
		1700	L	B	8	11.84	16.80	15.00
			T	B	8	19.88	16.80	23.60
		1800	L	B	7	10.92	14.00	14.10
			T	B	7	16.90	14.00	20.50

[a]Reference 4-3.

TABLE 4-4

DESIGN PARAMETERS FOR TD NiCr SHEET AT ELEVATED TEMPERATURE

Material	Condition	Temp., °F	Grain	Basis	n (a)	$F_{0.7}$, ksi	E_c, 10^6 psi	F_{cy}, ksi
TD NiCr dispersion strengthened DuPont Ni-20Cr-2ThO_2	Long life @ 2000°F exposure	Room	T	A	10	71.7	21.0	74.0
		500	T	A	10	65.8	19.5	68.0
		1000	T	A	10	49.5	17.3	52.0
		1500	T	A	10	21.7	12.7	24.0
		1800	T	A	10	14.4	9.0	16.0
		2000	T	A	10	10.7	7.0	12.0
		2200	T	A	10	7.0	5.5	8.0
		2400	T	A	10	5.2	5.0	6.0
	Long life @ 2200°F exposure	Room	T	A	10	59.6	21.0	62.6
		500	T	A	10	54.6	19.5	57.5
		1000	T	A	10	41.0	17.3	43.9
		1500	T	A	10	17.8	12.7	20.1
		1800	T	A	10	11.7	9.0	13.3
		2000	T	A	10	8.7	7.0	9.9
		2200	T	A	10	5.6	5.5	6.5
		2400	T	A	10	4.0	5.0	4.8

[a]Estimated.

TABLE 4-5

MATERIAL MINIMUM GAGE FOR STRUCTURAL CONCEPTS

Structural concept	Element	Min. Thickness, in.	
Monocoque panels			
Waffle grid	Skin	.020	.015[a]
Stiffened plate $0^\circ \times 90^\circ$ and $45^\circ \times 45^\circ$	Stiffener	.020	.015[a]
Honeycomb-core Sandwich plate	Skin (exterior)	.015	
	Skin (interior)	.010	
	Core	.002	
Truss-core Sandwich	Skin (exterior)	.015	
	Skin (interior)	.010	
	Core	.006	
Semimonocoque panels			
Tubular	Skin	.010	
Beaded	Skin	.015	
Trapezoidal Corrugation	Skin	.015	
Corrugation-stiffened skin	Skin (exterior)	.015	
	Skin (interior)	.010	
Convex beaded	Skin (exterior)	.015	
	Skin (interior)	.010	
Ribs & spars			
Caps	Flanged sheet metal	.030	
Webs	Corrugation	.015	
Heat shields			
Corrugation	Skin	.010	
Dimpled stiffened	Skin (exterior)	.015	
	Skin (interior)	.010	
Modular	Skin	.010	

[a]These gages applicable to bonded construction.

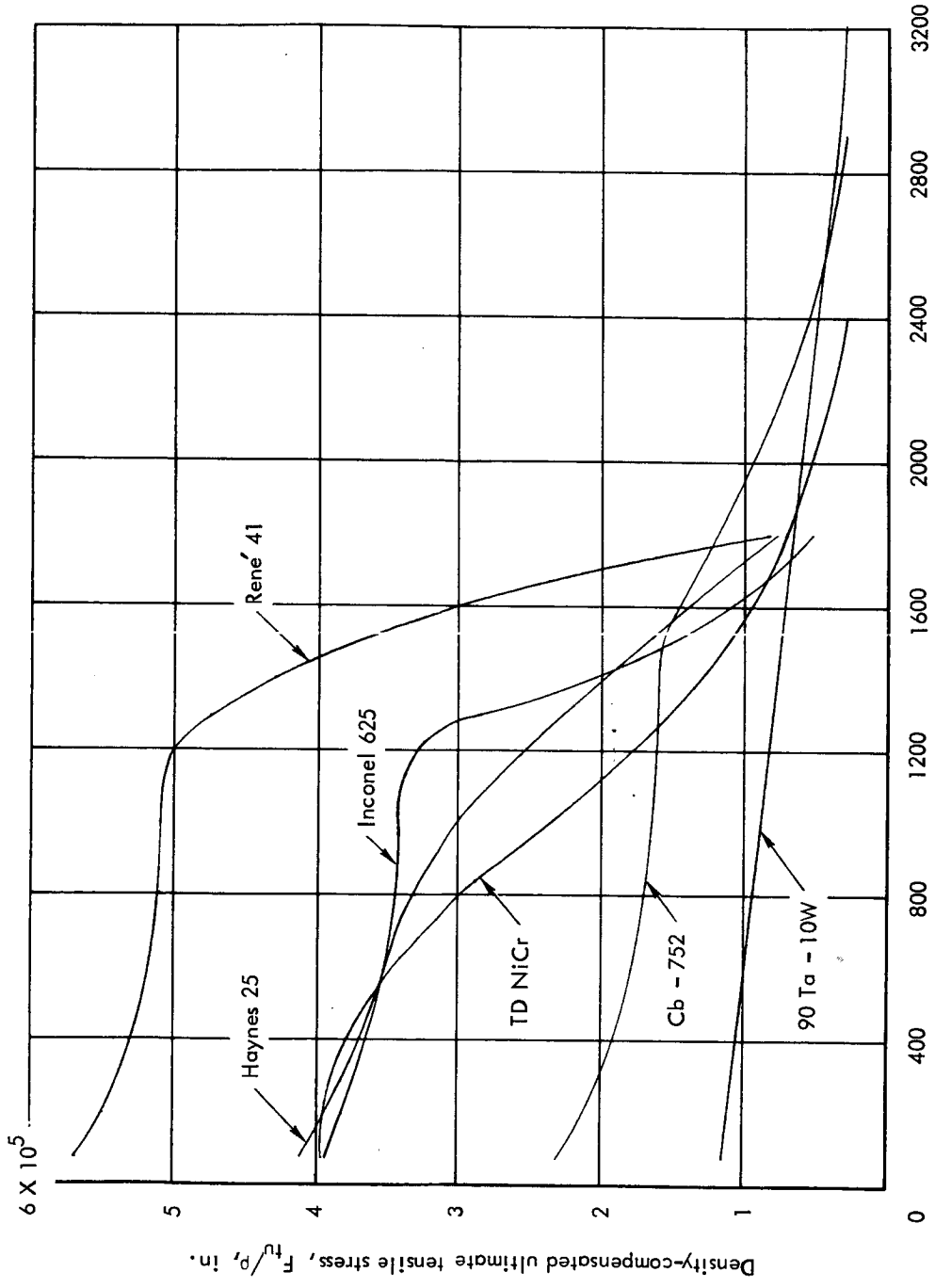

Figure 4-1. Density compensated ultimate tensile stress vs temperature of candidate high temperature materials

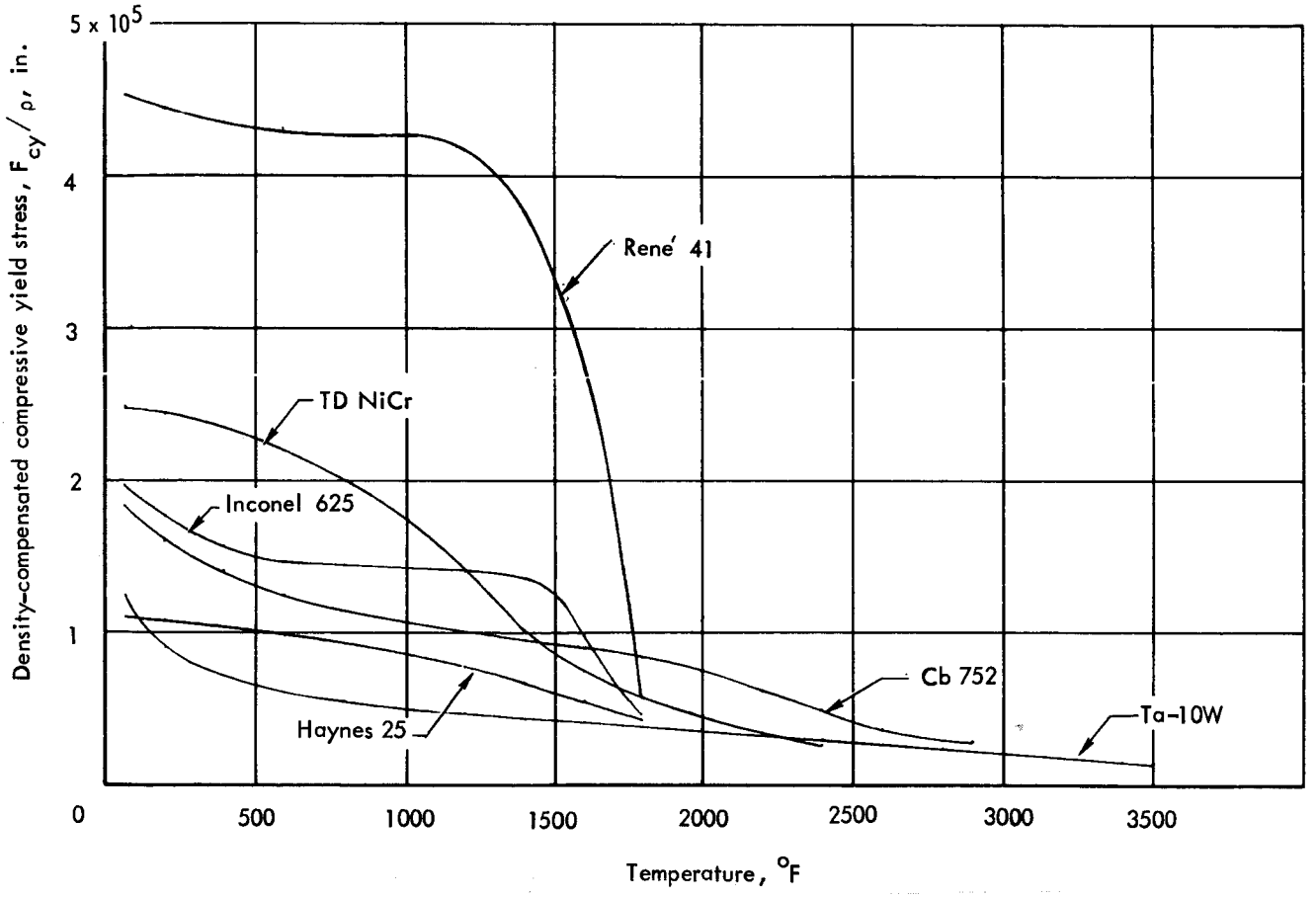

Figure 4-2. Density compensated compressive yield stress vs temperature of candidate high temperature materials

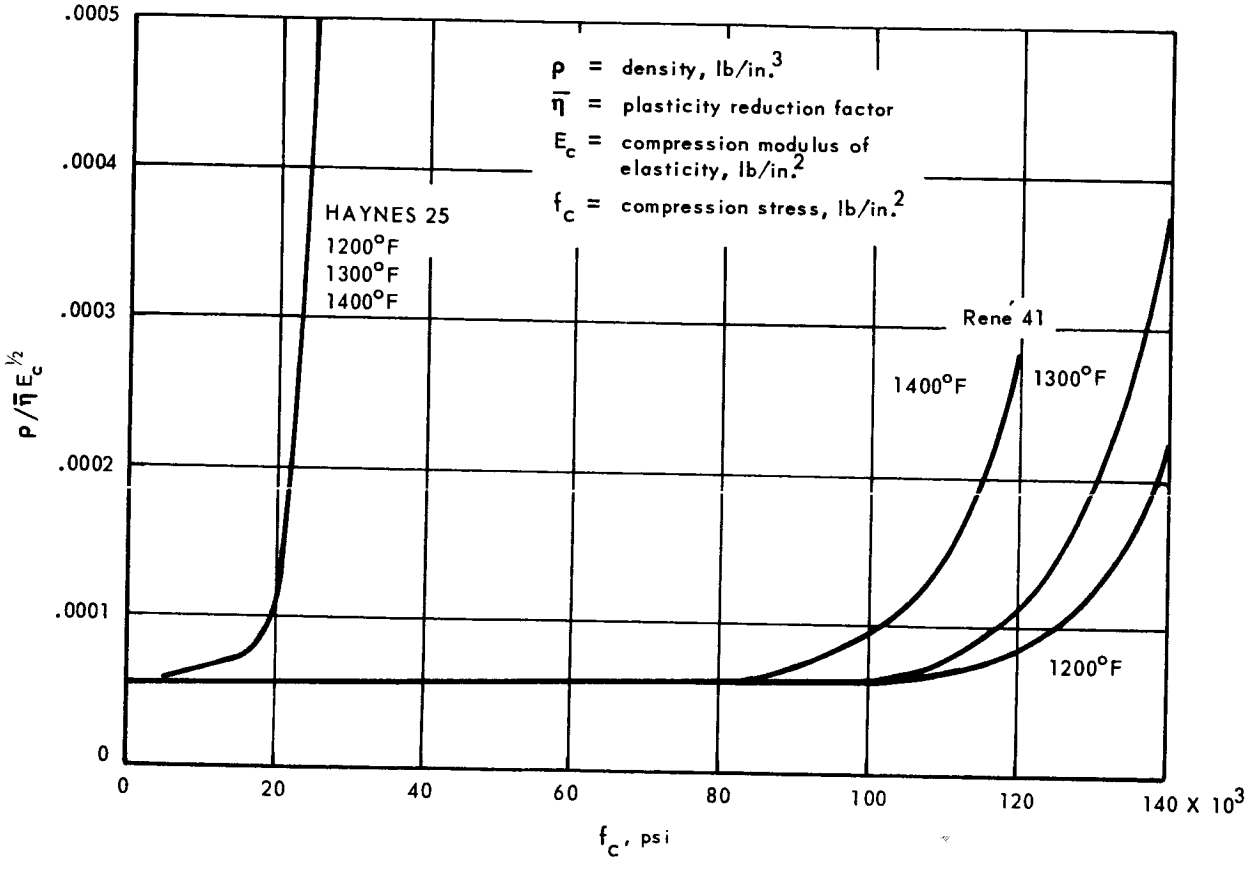

Figure 4-3. Compression loads vs weight index for René 41 and Haynes 25

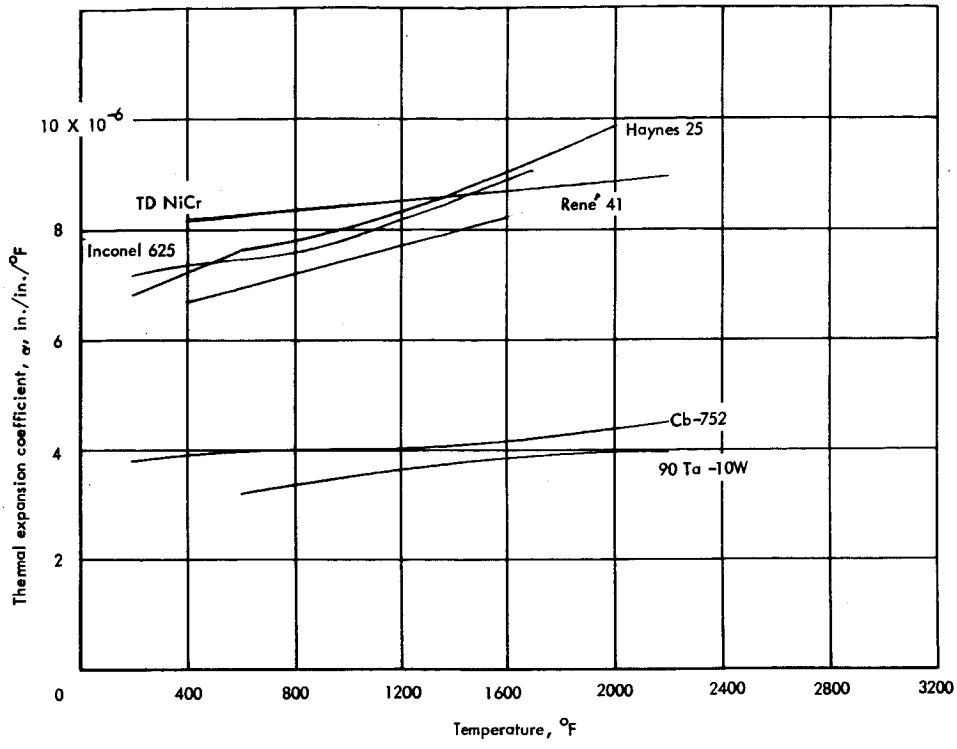

Figure 4-4. Coefficient of thermal expansion vs temperature of candidate materials

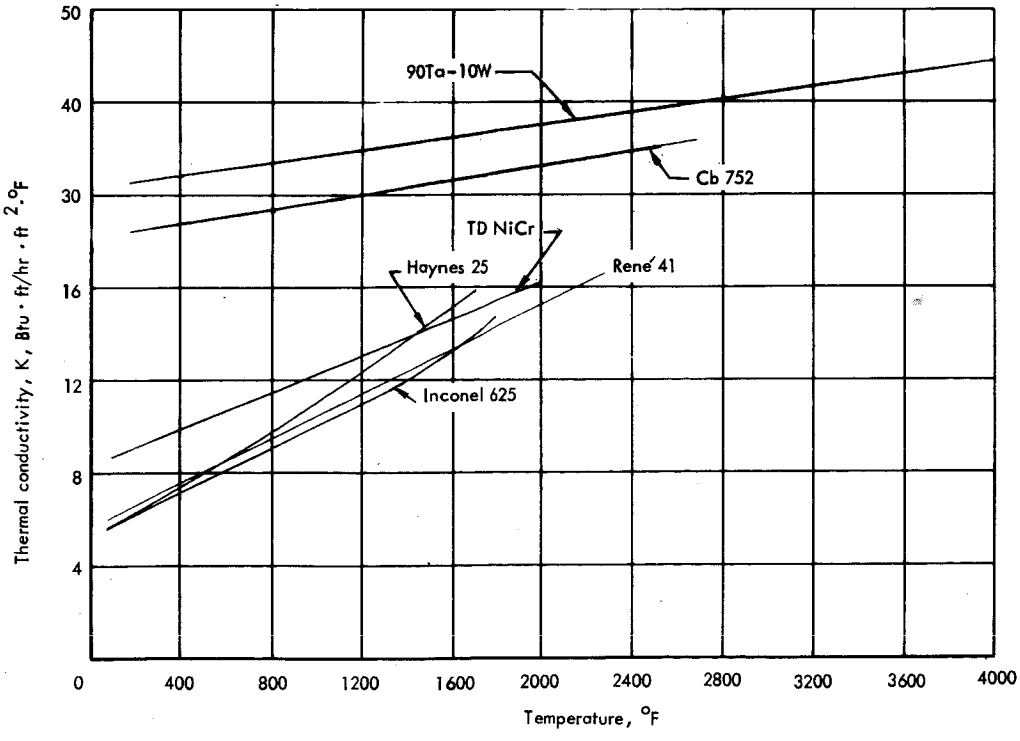

Figure 4-5. Thermal conductivity vs temperature of candidate materials

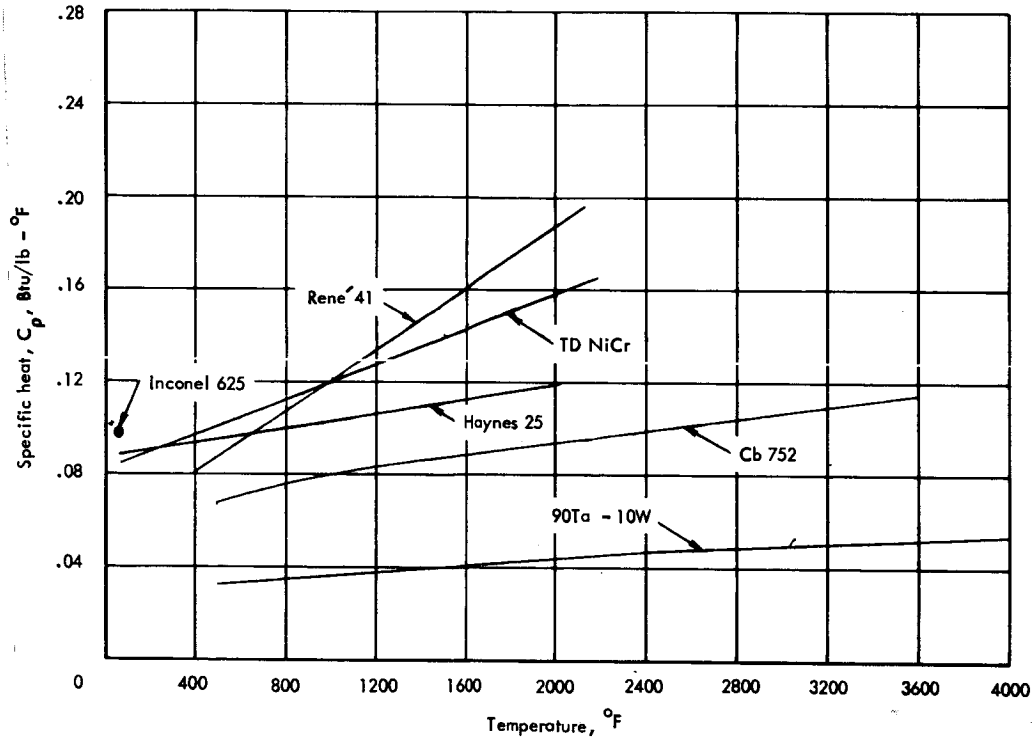

Figure 4-6. Specific heat vs temperature of candidate materials

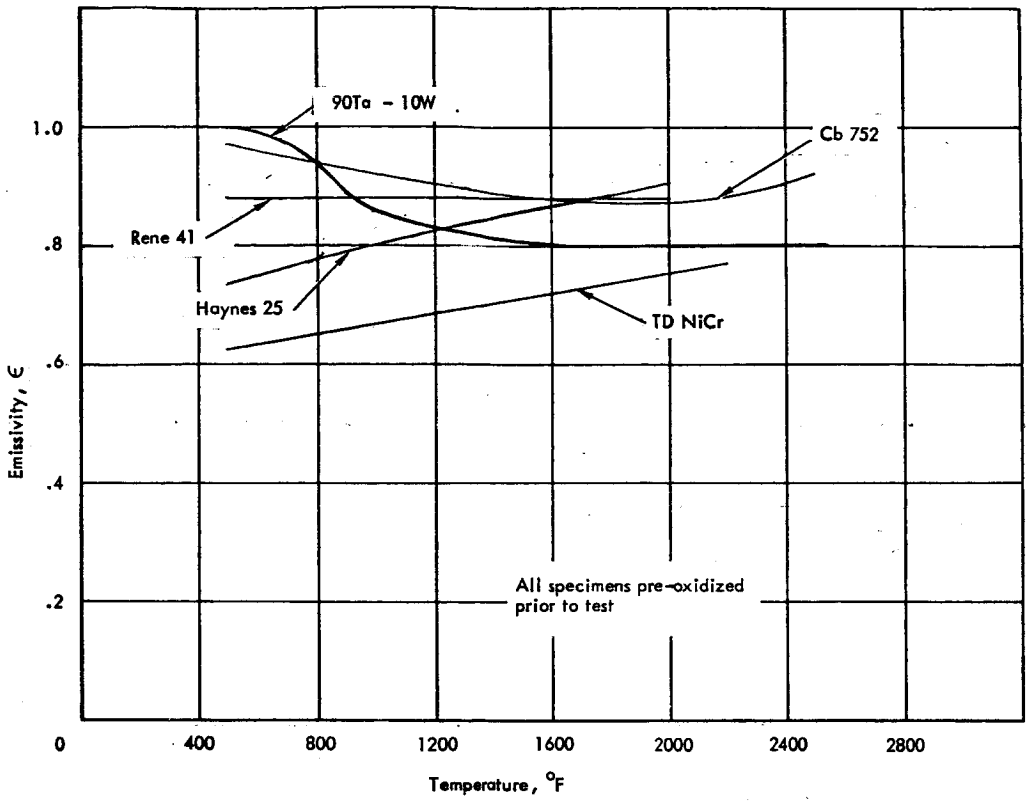

Figure 4-7. Emissivity vs temperature of candidate materials

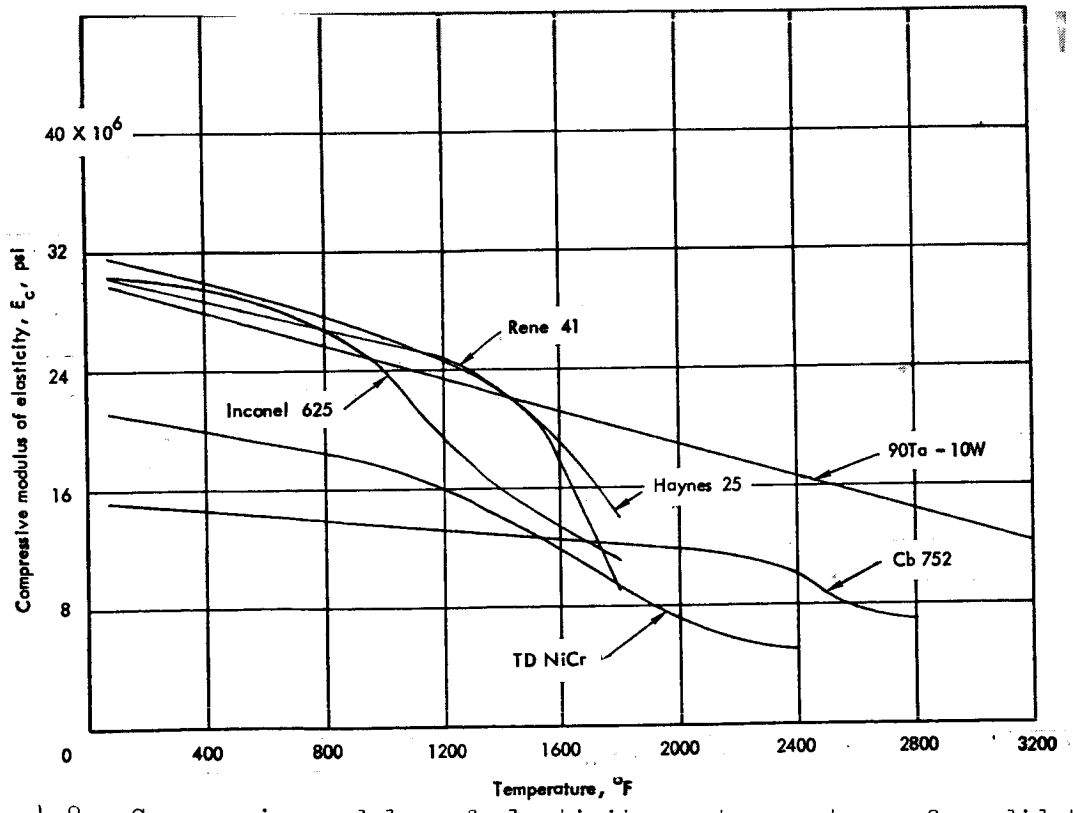

Figure 4-8. Compressive modulus of elasticity vs temperature of candidate high temperature materials

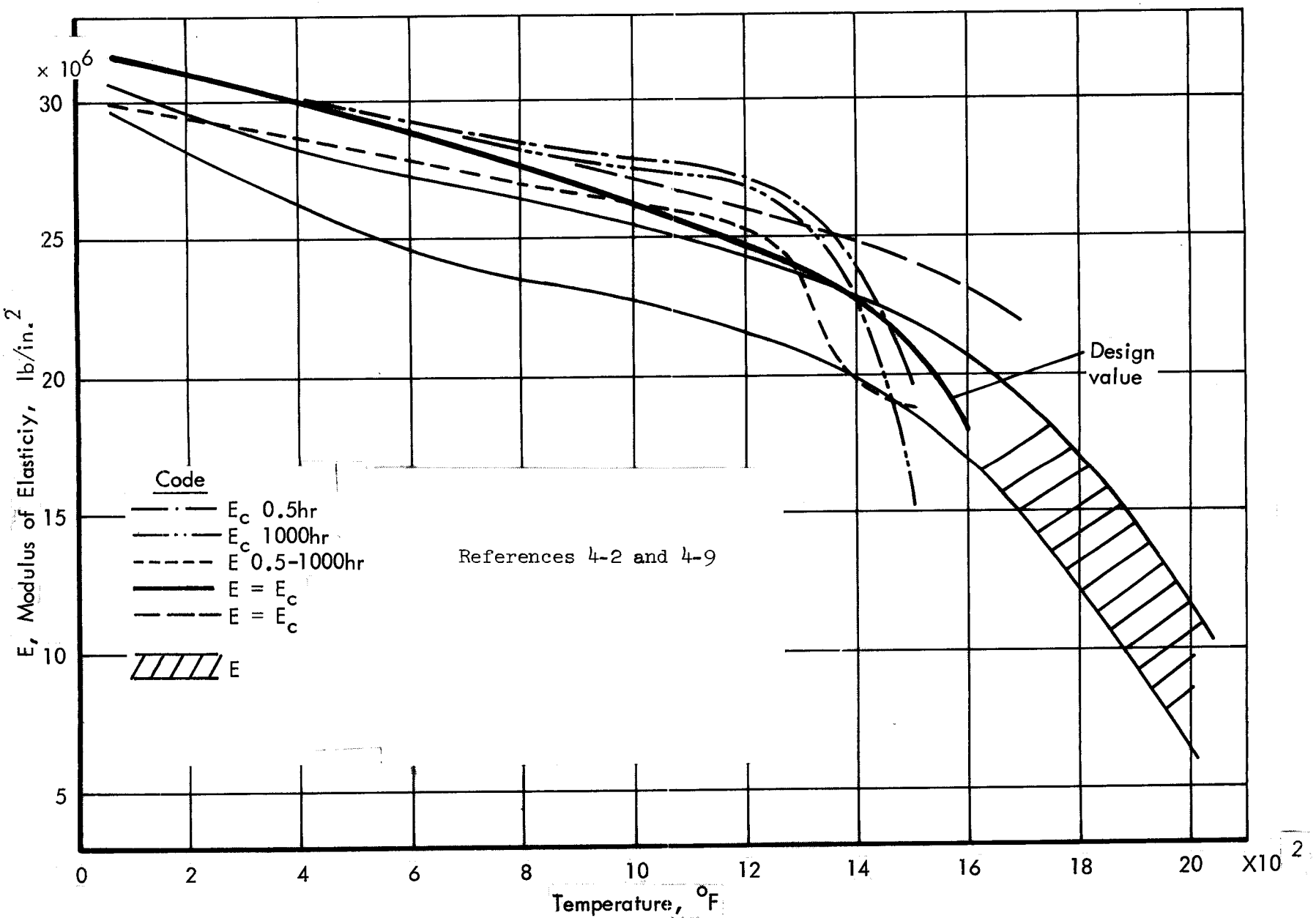

Figure 4-9. Modulus of elasticity (E and E_c) - René 41

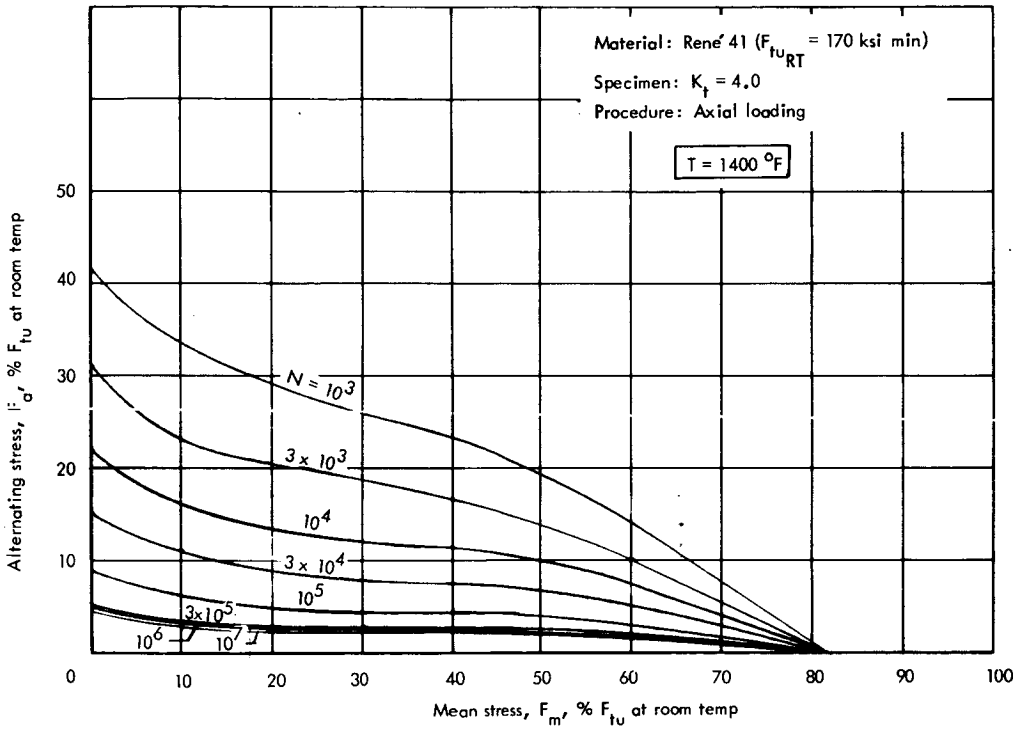

Figure 4-10. Constant life diagram, Rene' 41 (K_t = 4.0) - 1400°F

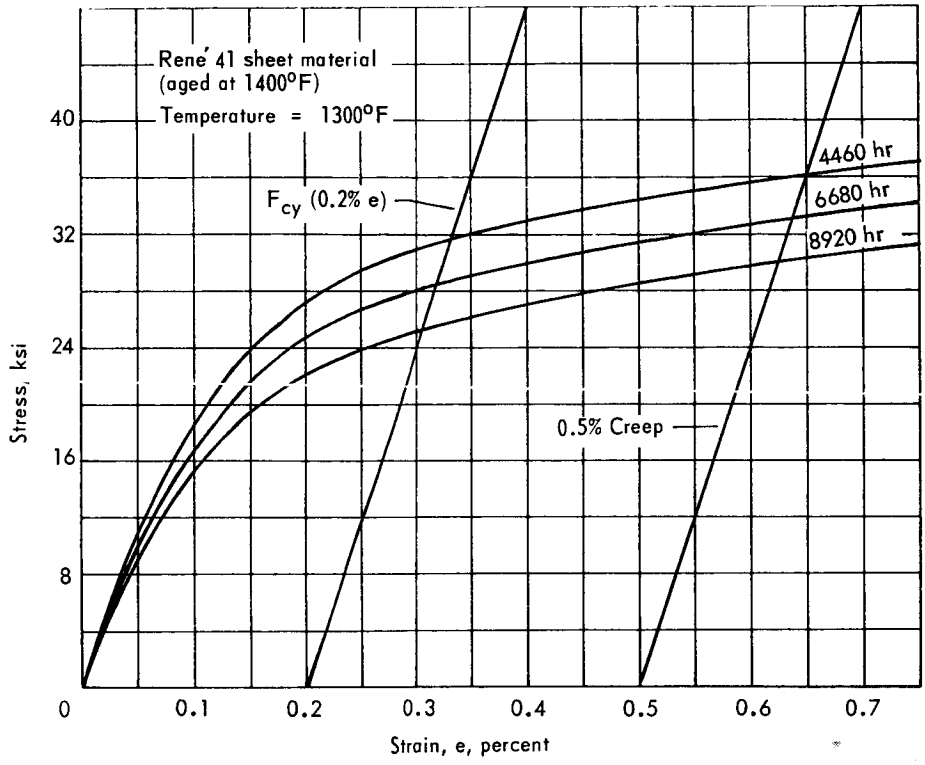

Figure 4-11. Typical isochronous stress-strain diagram for Rene' 41 at 1300°F

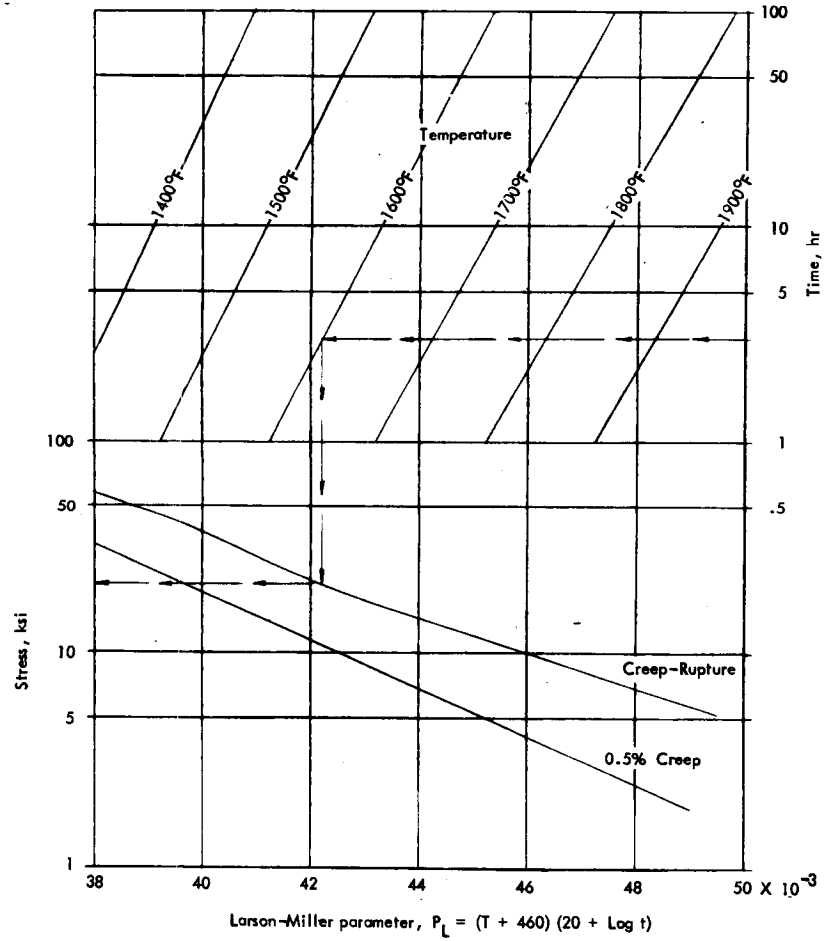

Figure 4-12. Creep design data for Inconel 625

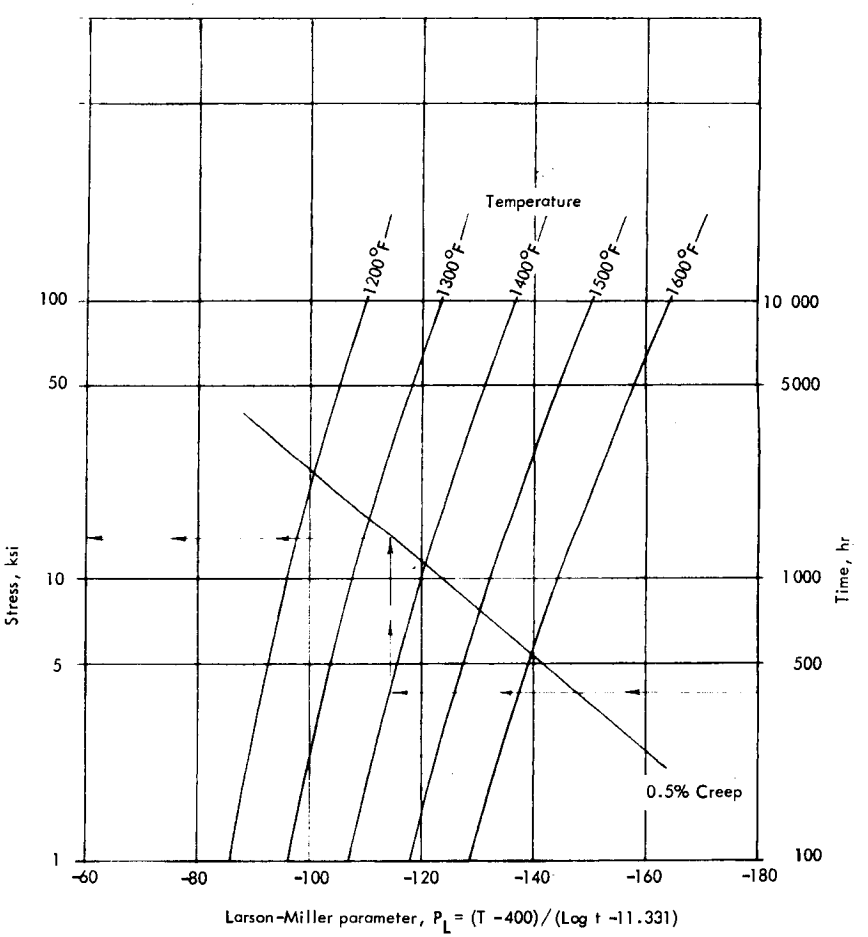

Figure 4-13. Creep design data for Haynes 25

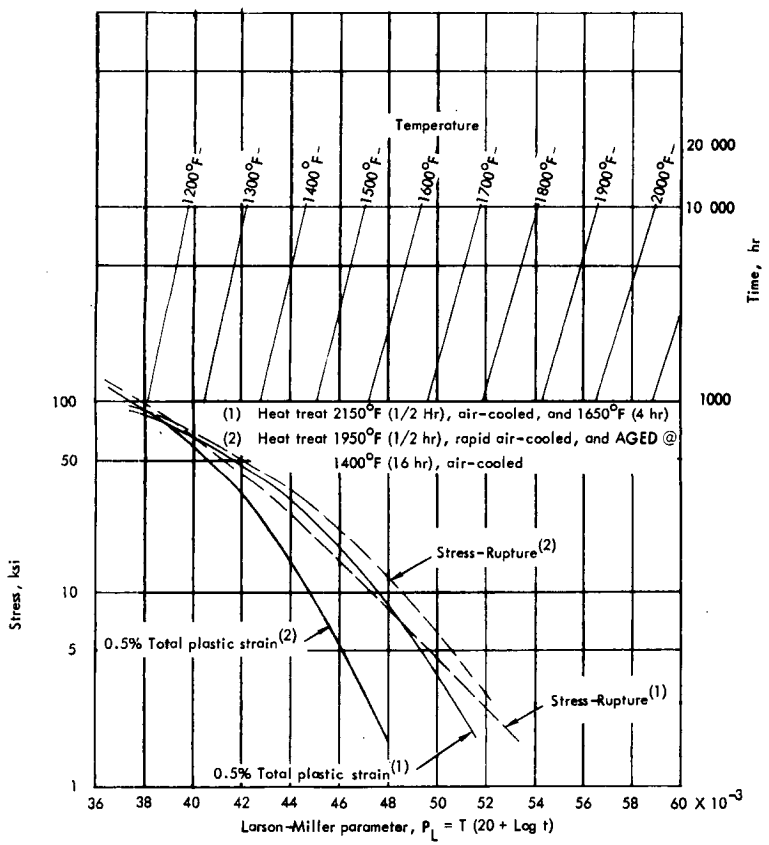

Figure 4-14. Creep design data for Rene' 41

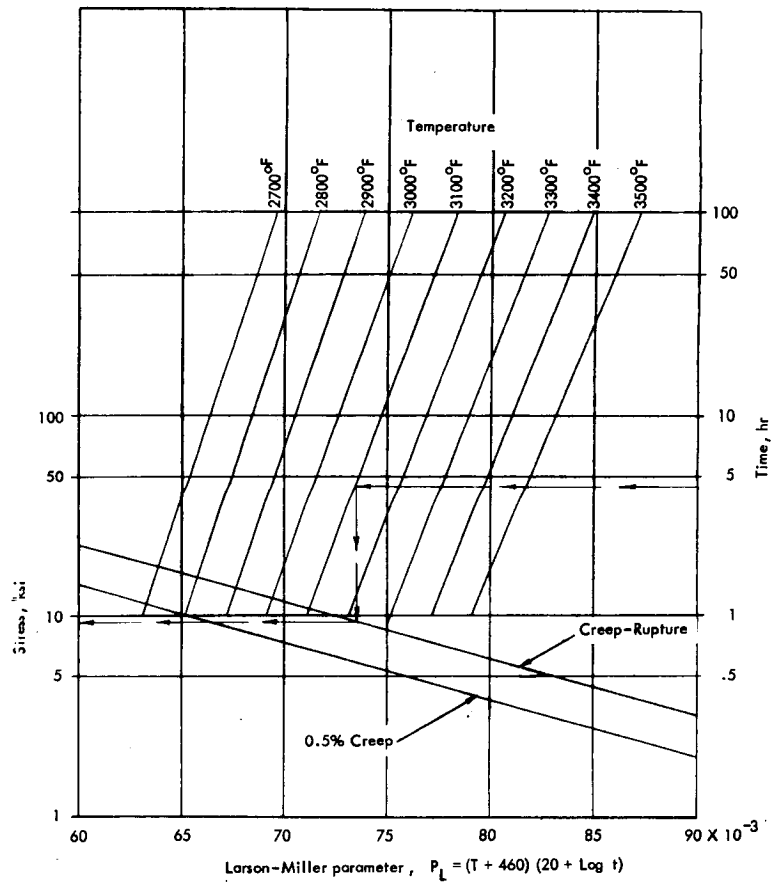

Figure 4-15. Creep design data for 90Ta-10W

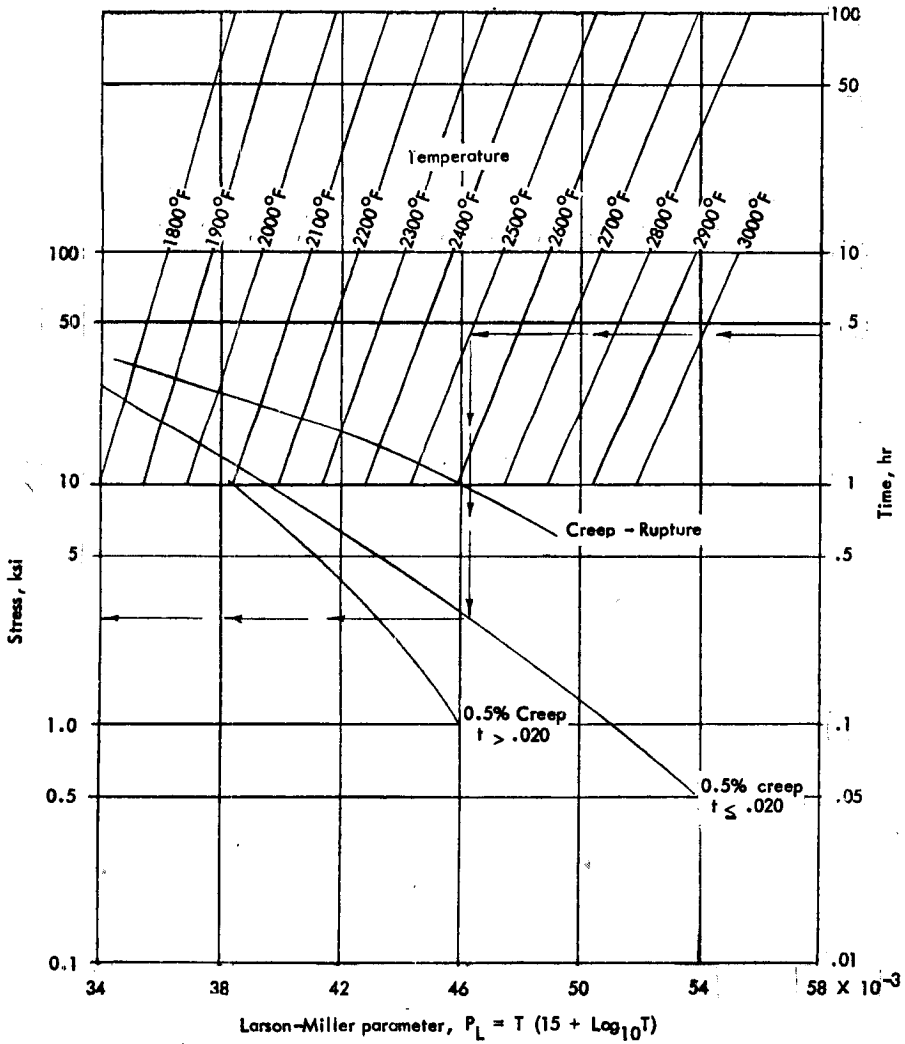

Figure 4-16. Creep design data for Cb-752

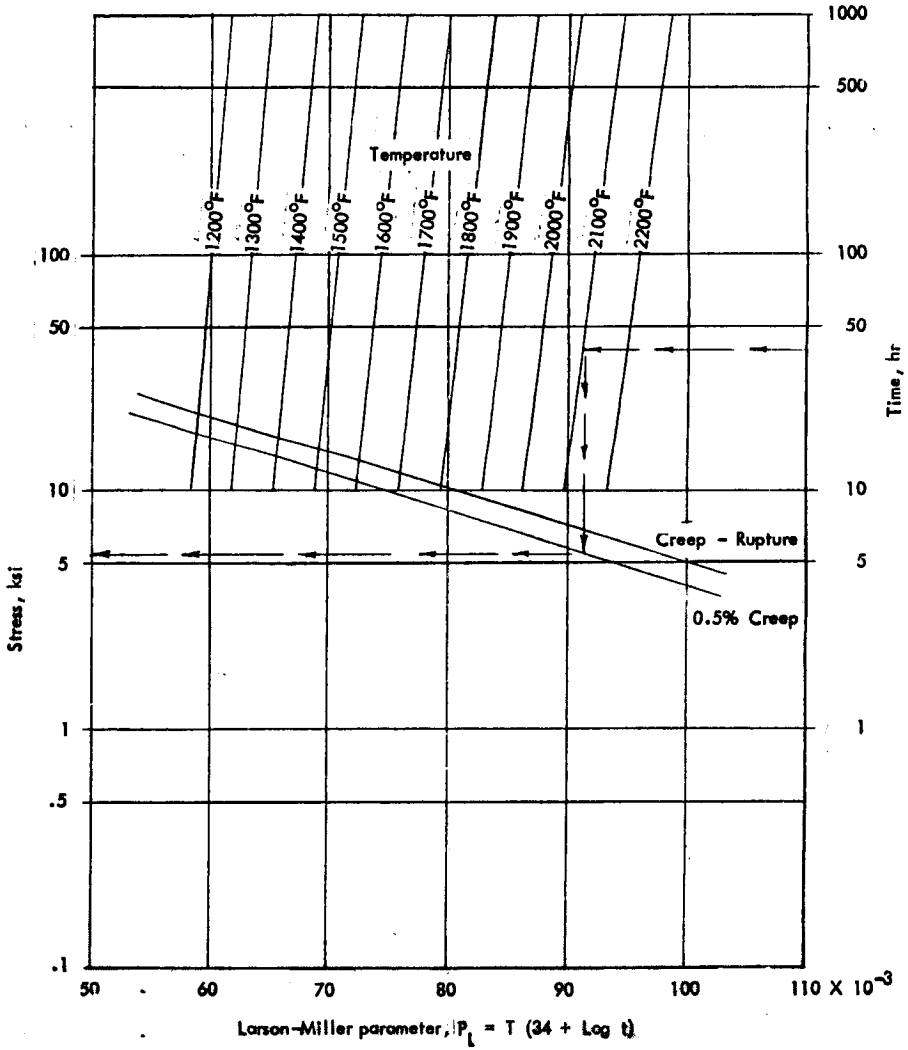

Figure 4-17. Creep design data for TD NiCr

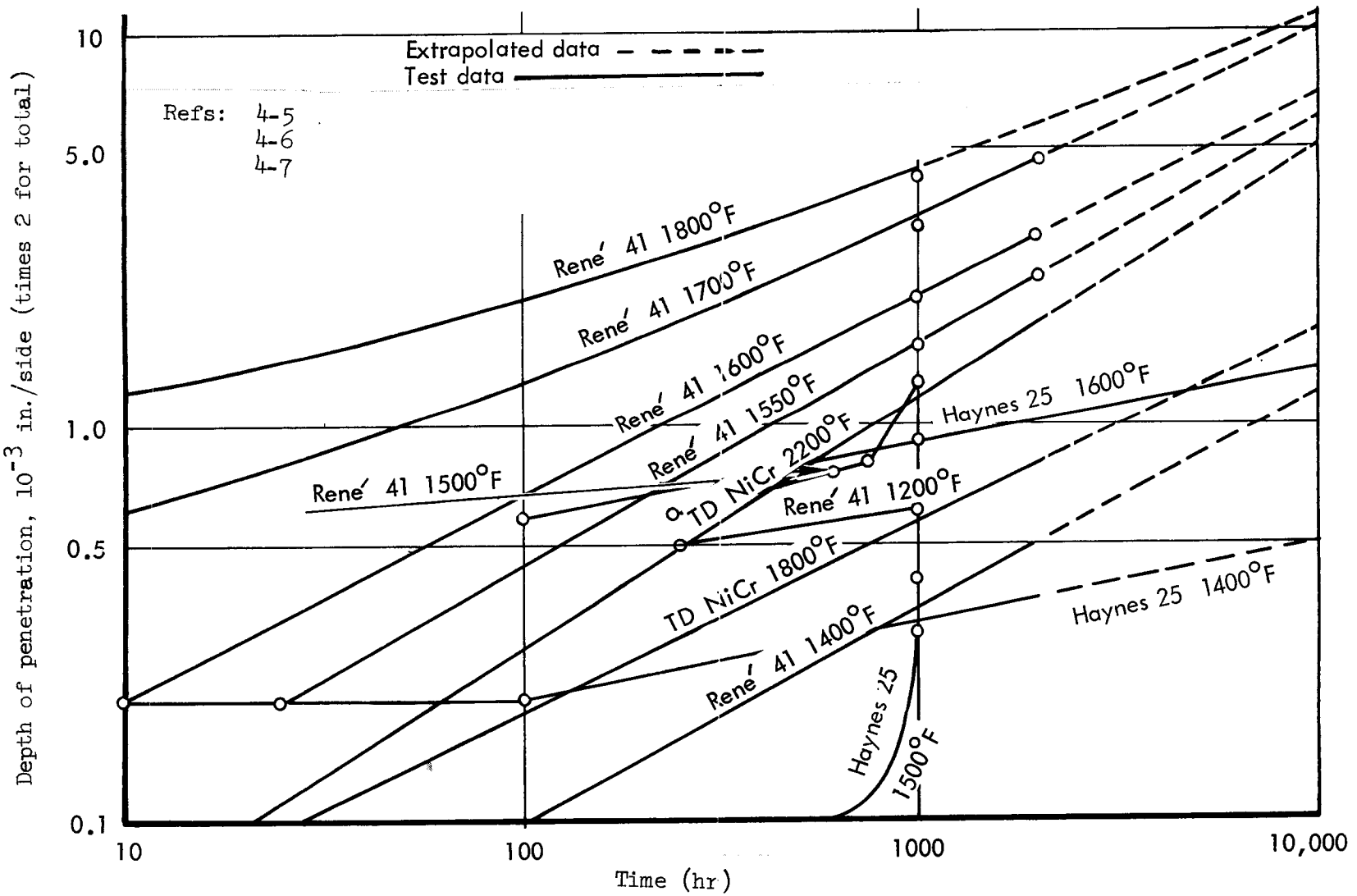

Figure 4-18. Depth of oxidation vs temperature for Rene' 41, TD NiCr, and Haynes 25

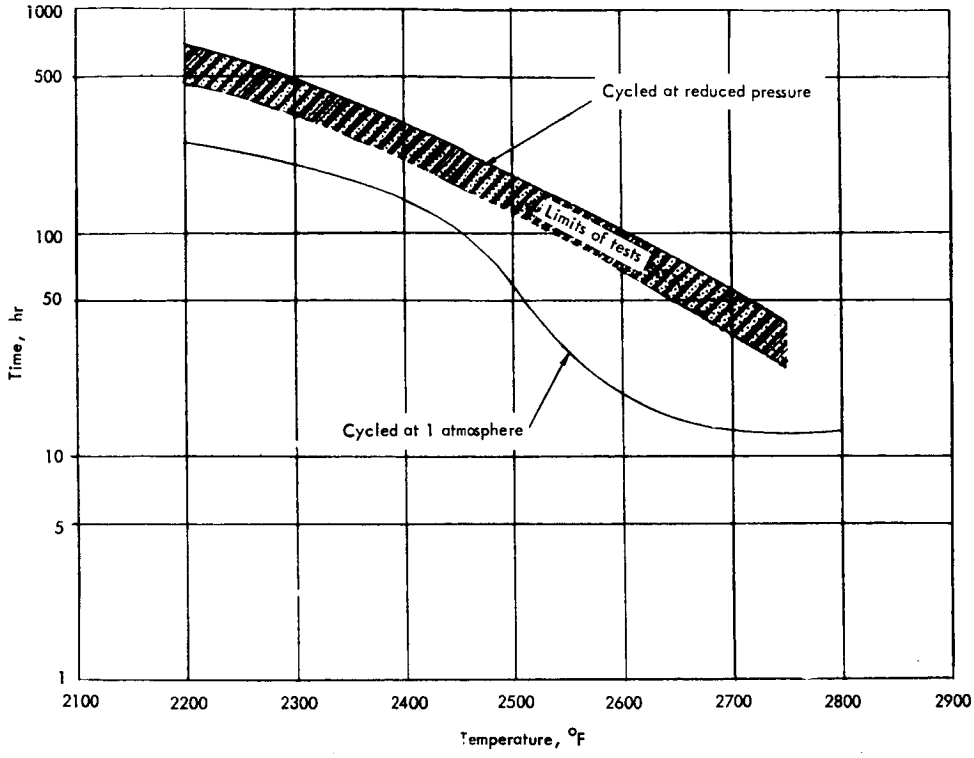

Figure 4-19. R512E coating life — Cb-752

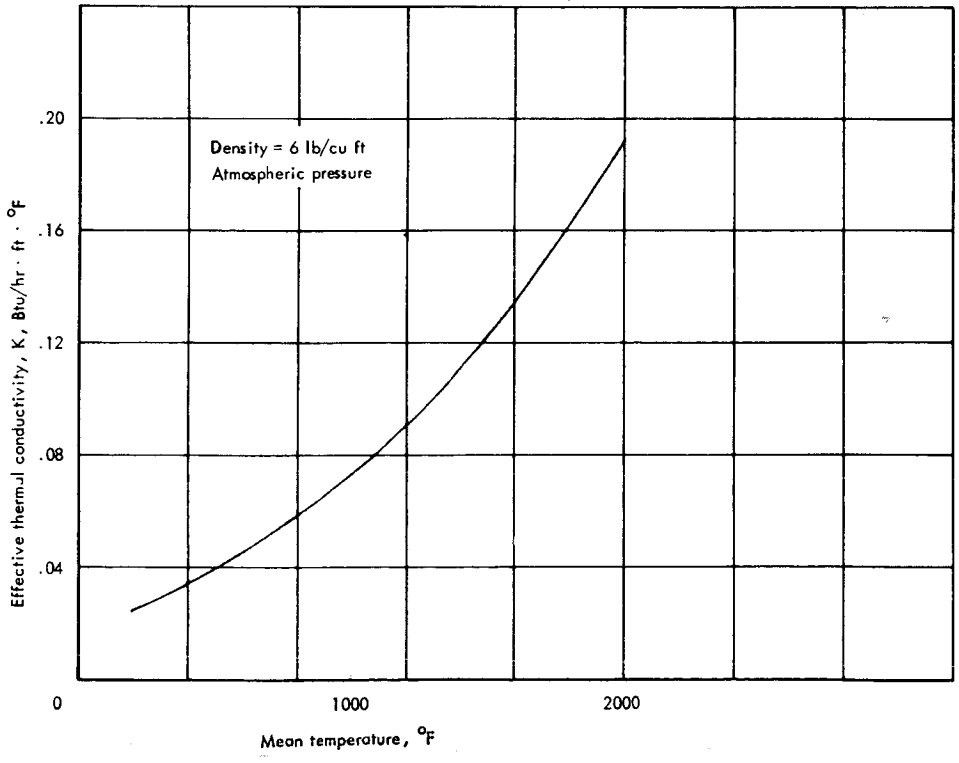

Figure 4-20. Effective thermal conductivity vs temperature — Dyna-Flex (atmospheric pressure)

Section 5

MATERIAL AND PROCESS DEVELOPMENT TESTING

by

K. A. Wilhelm, R. C. Dickason, J. J. Panik, I. F. Sakata, J. W. Lewis,
R. S. Jusko, R. Schwartz, and C. B. Stuhlman

CONTENTS

TABLES

ILLUSTRATIONS

ILLUSTRATIONS (Cont.)

ILLUSTRATIONS (Cont.)

ILLUSTRATIONS (Cont.)

ILLUSTRATIONS (Cont.)

SYMBOLS

C_2	Second radiation constant
E_a	Apparent modulus of elasticity
F_{tu}	Ultimate tensile strength
F_{ty}	Tensile yield strength
I	Current in Amperes
l	Distance between potential leads
R,r	Radius
RT	Room temperature
S	Spectral or apparent
T	Temperature; temperature of blockbody
V	Voltage drop between potential leads
ϵ_{ht}	Hemispherical total emittance
$\epsilon_{n\lambda}$	Normal spectral emittance at the measured wave length
λ	Wave length
σ	Boltzmann's radiation constant

SECTION 5

MATERIAL AND PROCESS DEVELOPMENT TESTING

MATERIAL SCREENING TESTS

Material Screening Test Plan

Table 5-1 outlines the material screening test program performed in support of this contract. Existing data, supplemented by data generated under this test plan, were used in establishing the design allowables used in the final analysis.

Description of Tensile Specimen

Room and elevated temperature tensile properties of exposed René 41, Haynes 25 and TD NiCr material alloy systems tensile coupons were machined to obtain mechanical properties data in the transverse grain (or transverse to the rolling) direction.

Tensile Test Setup and Procedure

Mechanical properties data for the exposed material alloy systems were determined using accepted standard laboratory testing procedures and equipment. A 5000-pound capacity Baldwin Universal Testing Machine (in compliance with ASTM E-4 designation) and a Baldwin B3M Differential Transformer Extensometer (in compliance with ASTM E-83 and E-21 designations for calibration, accuracy, and attachment) were used to obtain autographic tensile load-strain curves. The tensile tests were conducted at a head separation rate equivalent to a straining rate of 0.0005 in./in. per minute. Figure 5-1 is a standard one-inch gage length tensile specimen. A typical tensile test arrangement is shown in figures 5-2 and 5-3. The method of gripping the tensile specimen shown includes combined pin and friction clamp attachment at the specimen ends.

Tensile Properties, Oxidation, and Thermal Stability Test Results

Tensile test data for René 41, Haynes 25, and TD NiCr, including the effects of thermal exposure on these materials, are presented in table 5-2.

These data reflect room temperature tests of solution heat-treated (annealed) material after exposure to the environment indicated. The normal aging response of annealed René 41 and Haynes 25 is noted with a sharp increase in strength, followed by a drop in strength indicating an overaged condition. The apparent moduli presented are the "best fit" of the autographic load-deflection curves. It is obvious that René 41 is the most favorable material to satisfy the elevated temperature strength requirements of this program. It is also obvious that René 41 must be aged after fabrication to provide predictable allowables required for design. Typical tensile stress-strain curves for Haynes 25 and René 41 after 1000 hours static exposure at 1500°F are shown in figures 5-4 and 5-5.

The tensile test data for TD NiCr, presented in table 5-2, were determined at room temperature after exposure to the indicated thermal environments. The 0.2 percent offset yield strengths reported were determined from the autographic load strain curves using a room-temperature modulus value of 22 x 10^6 psi. Typical tensile stress-strain curves for 0.010 and 0.030 gage TD NiCr for various exposure times and temperatures are shown in figures 5-6 and 5-7.

Metallurgical Examination

Figures 5-8 through 5-18 show microsections of René 41 and Haynes 25 before and after static thermal exposure at 1200°F and 1500°F for various times. It is noted that these data agree well with published data (ref. 5-1). The René 41 specimens exposed at 1200°F did not show any appreciable amount of oxide penetration. However, René 41 specimens exposed at 1500°F for periods up to 1000 hours showed evidence of intergranular oxidation and apparent alloy-depleted areas. The Haynes 25 specimens showed a negligible effect due to thermal exposure at 1200°F and 1500°F for periods up to 1000 hours.

The TD NiCr tensile coupons were exposed to temperatures of 1500°F, 2000°F, and 2200°F for 500, 750 and 1000 hours as indicated in the schedule shown in table 5-3. After thermal exposure, the specimens were tested in tension, and representative coupons were selected for metallographic sectioning in both the longitudinal and transverse grain directions. The depth of the oxide surface contamination due to the thermal exposure was measured. These data are presented in table 5-4. Photomicrographs depicting the condition of the TD NiCr after exposure at 1500°F, 2000°F, and 2200°F are presented in figures 5-19 through 5-34.

During the thermal exposure of the TD NiCr specimens at 2200°F, a fluxing reaction between the coupon and the support rack (high temperature fire brick) was noted (see fig. 5-35). A chemical analysis (ref. 5-2) was made to determine the composition of the material at the area of contact between the coupon and the support rack. The results of the chemical analysis indicated that the contaminated area of the TD NiCr specimen exhibited a loss of 4 percent chromium, whereas the contaminated area of the fire brick exhibited an increase of 3 percent chromium and a depletion of 5 percent aluminum and 2 percent silicon.

Metallurgical analyses of specimen sections taken through the areas in contact with the brick indicated the affected area to be approximately 50 percent of the original thickness of the material (see fig. 5-36).

An alternate heat treat rack was constructed using high purity aluminum oxide (Al_2O_3) as the base and TD NiCr as the specimen support. This rack was used to continue the thermal exposure of the 0.010 in. thick TD NiCr specimens at 2200°F for 750 and 1000 hours. Visual examination of the rack and specimens after thermal exposure disclosed some discoloration of the rack base and that a chemical reaction had taken place in the tensile coupon grip area (see fig. 5-37). Note that the contamination in the grip area extended approximately 2 inches beyond the point of contact between the specimen and support.

Emittance Test Results

Spectral (6500°A) and total hemispherical emittance data were obtained as a part of this study by Marquardt Corporation over the temperature ranges indicated in table 5-1.

The Marquardt test apparatus, figure 5-38, uses the hole-in-tube or indirect method of measuring spectral (6500°A) and total hemispherical emittance as described in reference 5-3. The specimen material is formed into a long, thin walled tube per Marquardt drawing X21182 (figure 5-39). A small hole is drilled through one wall of the tube near the center for optical viewing. Water cooled copper electrodes are clamped at each end of the tube for resistance heating to the desired temperature. Two 0.010-inch diameter wires are spotwelded to the tube, 0.020 inch apart opposite the small hole, to act as voltage probes. The preoxidized sample is placed inside a bell jar with optical quality quartz parts for optical temperature measurements. The bell jar is then evacuated to the indicated partial pressure prior to two stabilization runs (at maximum temperature) before any optical measurements are recorded. The blackbody temperature is measured through the small hole in the tube with a calibrated automatic photomatic pyrometer. Sighting the pyrometer on the outside of the wall of the tube will give the apparent temperature, which is a function of the emittance of the outer wall.

The following relationships were used to obtain the normal spectral emittance at 6500°A:

$$\ln \epsilon_{n_\lambda} = \frac{C_2}{\lambda}\left(\frac{1}{T} - \frac{1}{S_\lambda}\right)$$

where:

ϵ_{n_λ} = the normal spectral emittance at the measuring wave length

C_2 = the second radiation constant

λ = the wave length at which the detector measures (in microns)

T = the blackbody temperature (K)

S_λ = the spectral or apparent temperature (K)

The total hemispherical emittance will be calculated from the relationship:

$$\frac{IV}{2\pi r l} = \epsilon_{ht} \sigma T^4$$

where:

I = current through the tube (amperes)

V = voltage drop between potential leads (volts)

r = the radius of the tube (cm)

l = the distance between potential leads (cm)

ϵ_{ht} = the hemispherical total emittance

σ = Boltzmann's radiation constant

T = the blackbody temperature of the tube (K)

The emittance curves for the tested materials are shown in figures 5-40 through 5-44. It should be noted that the emittance curve for 90Ta-10W/R512C material system does not reflect the maximum test temperature as indicated in table 5-1. This was due to an interruption of voltage control through the attached probes by eutectic melting (alloy formation between free silicon and the voltage probes). Several runs were made, using various contact probes (including Ta). All results were identical. The chemically aggressive free silicon in the coating reacted with the probes, resulting in a loss of voltage control to the specimen.

Figure 5-44 is the total and spectral emittance of preoxidized TD NiCr. It is well to note that this data is comparable with emittance data published on TD Ni but does not agree with data published on TD NiCr contained in reference 5-4.

Leading Edge Testing

Two leading edge concepts were fabricated and tested in a plasma arc under simulated flight conditions.

Porous metal concept.- The first concept, a 50-percent dense porous powder metallurgy product of 90Ta-10W was sintered to a 0.040-inch thick 90Ta-10W backing sheet to which a 90Ta-10W tube was electron beam welded to facilitate attachment to the fixture. A protective coating of Sylcor R505 (Al-25Sn) was applied to the assembly and vacuum fired at 1900°F for one hour. The coated assemblies are shown in figure 5-45. One additional specimen was fabricated and sectioned after coating to observe coating penetration by destructive testing. Figure 5-46 illustrates the general structure of the impregnated porous leading edge sample. The upper photomicrograph shows the Al-Sn alloy on the surface with the aluminide below it and the infiltrated porous 90Ta-10W below the aluminide. The lower picture shows a portion of the infiltrated 90Ta-10W and the substrate.

Sheet concept. - The second concept fabricated and tested was a sheet leading edge specimen disilicide coated with Sylcor R512C (Si-20Ti-10Mo) coating. This coating was diffused in vacuum at 2580°F for one hour. A typical example of this concept is shown in figure 5-47.

Element testing facility.- The plasma arc test facility at Space General Corporation (fig. 5-28) was selected to evaluate the two leading edge concepts under simulated flight conditions. The test facility projected a supersonic (Mach 2.5), hyperthermal environment that was accurately controlled. A 3-inch nozzle was used to input a gas flow of 79-percent nitrogen and 21-percent oxygen.

Test plan.- The following test plan was formulated for evaluation of the two leading edge material system concepts (porous and sheet) for cyclic conditions of temperature to determine the failure point of each material - coating system at specific levels of temperature. Six-minute cycles were selected to correspond with earlier work performed at the NASA Langley Research Center (ref. 5-5).

Test 1

a. Heat to 3100°F within 30 seconds

b. Stabilize temperature and hold for 6 minutes

c. Cool for 10 minutes (to approximately 300°F)

d. Repeat a through c until visual indication of failure is observed

Test 2

a. Heat to 2800°F within 30 seconds

b. Stabilize temperature and hold for 6 minutes

c. Cool for 10 minutes (to approximately 300°F)

d. Repeat a through c until visual indication of failure is observed.

Test results.- A summary of test results, identified by model number coating system, and pertinent test data, are given in table 5-5. A detailed history of all test parameters is given in tables 5-6 through 5-8.

The results indicate that adequate oxidation protection at 3100°F is not practical with either of the concepts tested, whereas limited oxidation protection is offered at 3000°F utilizing the sheet 90Ta-10W/R512C concept (37 six-minute cycles). Although the porous metal concept failed after 12 six-minute cycles at 2800°F, there were indications of improvements (factor of two) over previously tested concepts. The mode of oxidation that occurs in the porous 90Ta-10W/R505 concept produces considerable local hot spots. Failure is a combination of progressive Ta oxidation and thermal stress. The sheet concept did not fail after 37 six-minute cycles at 2800°F.

Figures 5-49 through 5-54 are photographs of the two leading edge concepts before and after cyclic thermal exposure. A comparison of similar tests conducted by NASA (ref. 5-5) on a modified Al-Sn coating and those completed under this contract are shown in figure 5-55. Although a direct comparison cannot be made due to the difference in stagnation pressures at the specimen-jet interface, marked improvements over previously tested concepts are indicated. (The low pressure tests conducted at Space General are considered more severe for coatings than those conducted at or near one atmosphere.)

Additional studies were made in an attempt to upgrade the porous metal concept by the impregnation of the porous material with a disilicide coating. Results from Sylcor indicated that the R512C disilicide coating system is too chemically aggressive to be feasible in this proposed application.

JOINT EVALUATION

Test Plan

Four representative joint-type specimens were selected for evaluation which encompass those joints needed for the design of subsequent test components, leading edge test specimens, and representative hypersonic wing structure components. The joint types, methods of joining, materials, gages, and test temperatures are outlined in table 5-9.

Description of Specimens

The resistance spotweld and diffusion spot bond specimen configuration is shown in figure 5-56. The riveted lap joint specimen is shown in figure 5-57. The brazed lap joint specimen is shown in figure 5-58. The resistance spotweld and diffusion spot bond tension specimen is shown in figure 5-59. The electron beam weld tee joint and butt joint specimens are shown in figures 5-60 and 5-61. The fabrication and joining techniques for these specimens are described below.

Specimen Fabrication and Joining Techniques

Lap joint specimens.- The lap joint specimens were made by shearing 2.0-in. by 4.0-in. coupons and 1.0-in. by 2.0-in. doublers (as required), deburring, cleaning, and packaging for joining.

The cleaning procedure consisted of:

Trichlorethylene degrease

Demineralized water rinse

Clean air dry

Chromic-sulfuric acid immersion

Demineralized water rinse

Clean air dry

Seal in polyethylene.

Rene' 41 aged specimens were aged after assembly. All coupons passed X-ray inspection. Aging treatment consisted of heating in air to 1400°F, holding at temperature for 16 hours, then cooling in air to room temperature.

Riveted lap joint coupons required 0.125-in. and 0.188-in. diameter, flush head rivets. These rivets were cold headed in plant from TD nickel wire, due to unavailability of TD NiCr, as follows:

Rivet size	Wire diam., in.	Finished shank diam., in.	Grip length, in.
1/8	0.123 - 0.1235	0.1245 - 0.1255	0.25
3/16	0.185 - 0.186	0.1870 - 0.1878	0.40

Head configuration - MS20426

Rivets were formed from "as-received" wire, annealed condition, then stress relieved after heading (2000°F for 5 minutes). Upsetting was accomplished in one-stroke squeeze riveter. Holes were drilled, countersunk, and reamed before assembly using T15 high speed steel tools.

Coupons and rivets were cleaned before assembly, white glove handled in clean room and packaged after assembly in polyethylene bags. The cleaning procedure used was outlined above.

Spot tension specimens. - The resistance spotweld and diffusion bond spot tension joint specimens were made by shearing square coupons 2.0-in. by 2.0-in. and die piercing a 4-hole pattern.

Doublers (0.030 in.) were required to minimize deflection and to verify tensile spot strength values. Doublers consisted of 0.030-in. by 2.0-in. square coupons with normal 4-hole pattern but with 3/8-in. diameter center hole. These doublers were resistance spotwelded to the 0.015-in. gage coupons.

Aged specimens were made by aging (1400°F for 16 hours) after joining; solution treated (annealed material) coupons were X-rayed before and after aging.

Tee and butt joint specimens. - The electron beam welded 90Ta-10W tee and butt joint specimens were made by shearing coupons (1.0 in. by 12.0 in. and 4.0 in. by 4.0 in.). The cleaning procedure used was the same as that outlined for the lap joint specimens. All welds passed X-ray inspection.

Test Setup Equipment and Procedures

Lap shear tests. - The lap shear joint specimens were tested at room and elevated temperatures. A typical elevated temperature joint test arrangement is shown in figure 5-62. The room temperature setup was essentially the same. Both the room and elevated temperature joint specimens were loaded by means of combined pin and friction gripping. A loading rate of 5000 pounds per minute was used for these tests. Specimen test temperatures were achieved by means of radiant heating (Tungsten filament quartz lamps, type 1000T3/CL/HT, and gold plated reflectors, Research Incorporated Type AU5-212). Power to the heat lamps was supplied by a 100-ampere, 480-volt Thermac ignitron power controller unit. Chromel-alumel thermocouples were attached to the test specimens by the capacitance discharge method. One control thermocouple was used to regulate the power to the radiant heat lamps for maintaining specimen test temperatures. The remaining thermocouples were used for monitoring and recording specimen temperature by means of a Brown strip chart recorder.

A typical test arrangement for the riveted joint specimens is shown in figure 5-63. A Class B-1 averaging differential transformer type extensometer is shown attached to the specimen for the purpose of establishing the joint yield strength. The yield load for this specimen configuration was determined by repeatedly loading and unloading the specimen to successively greater load levels until a permanent joint deformation of 0.005 in. was obtained. These data were obtained from the reduction of autographic load-deflection curves produced by a standard drum type recorder in accordance with the MIL-H-5 committee guidelines.

Spot tension tests. - A typical spot tension test setup is shown in figure 5-64. The specimen is shown mounted in the compression bay of a 5000-pound capacity Baldwin Universal Testing Machine. The test fixtures, located on either side of the specimen, consist of a base and four posts which apply a bearing load to the specimen face sheet opposite the test fixture. This arrangement produces a tensile load at the weld located in the center of the specimen. Test loading was applied at a rate of approximately 5000 pound per minute.

Joint test results. - A summary of the lap joint test data for René 41 and Haynes 25 material alloy systems is given in table 5-10. The values listed in this table are an average of the results of five specimen tests. A listing of each test specimen result is presented in tables 5-11 and 5-12 which show the scatter in the test data obtained for these two material alloy systems.

A summary of the lap joint test data for TD NiCr is given in table 5-13, and represents averaged values for five specimen tests per condition. A listing of each test specimen result is presented in table 5-16.

The joint technique evaluation results, shown in table 5-10, indicated that higher joint strengths at elevated temperatures are possible for the resistance spotwelded specimens than for the diffusion-bonded specimens. X-ray inspection of the René 41 spots indicated crackfree welds; therefore, resistance spotwelding was selected for use in panel fabrication of René 41. For the TD NiCr materials, the riveted specimens provided the highest strengths at elevated temperatures, as shown in table 5-13.

FORMABILITY TESTS

Four types of forming tests were conducted to establish fabrication limits for the manufacture of the panel element and structure designs. The forming test schedule is outlined in table 5-17 and lists the materials, gages, test conditions, and total number of tests conducted. A detailed description of each of the forming tests is given below along with recommended procedures resulting from these tests.

Room Temperature Bend Tests

Room temperature bend coupons (fig. 5-65) were sheared to 1.0-in. by 3.0-in. rectangular blanks. Edges were left as-sheared. Half of the coupons were cut with length parallel to rolling direction of sheet; the other half of the coupons were cut with length normal to rolling direction of sheet. Bends were formed in conventional mechanical brake with strain rate control using radius punch and open channel die. Each coupon was bent in two places in opposite directions. Minimum bend radius, effect of grain direction, edge and surface effect, and spring back for each condition of forming were determined, as follows:

Punch radii - 0.010, 0.015, 0.031, 0.045, 0.061, 0.076, 0.090, 0.125 inch
Channel die width - punch diameter plus 2-1/2 times metal thickness
Channel die radii - 2-1/2 times metal thickness
Rate - from 0.05 to 1.50 in. per minute
Bend angle - 110° closed before spring back

Material Alloy	Gage, in.	Recommended Minimum Bend Radius	
		Longitudinal[a]	Transverse[b]
Haynes 25	0.010 - 0.125	1.0 t	1.0 t
René 41	0.010 - 0.025	1.5 t	1.5 t
René 41	0.030 - 0.100	2.0 t	2.0 t
TD NiCr	0.010	2.0 t	2.5 t
TD NiCr	0.030	2.5 t	3.0 t
Cb-752	0.010 - 0.060	1.5 t	2.0 t
Ta-10W	0.010 - 0.060	1.5 t	1.5 t

[a]Normal to rolling direction of sheet.
[b]Parallel to rolling direction of sheet.

All "good" bends were dye penetrant inspected, sectioned, and examined for microscopic cracking at 120 x magnification.

Room Temperature Flanging Tests

Room temperature flanging specimens (figs. 5-66 and 5-67) were prepared by shearing 3.50-in. wide strips, rough blanking contour, drilling pin holes, then trace milling final size shrink and strength flange coupons. All coupons were cut so that bend would be parallel to rolling direction of sheet (transverse bend). Forming was done on standard flanging tools made of hardened steel and with bend radii to match bend radii determined from bend tests. Edges of coupon blanks were deburred but not polished. Forming was accomplished using 3/8-in. thick Adiprene LD 167A urethane elastomer vulcanizate sheet as a cover, form blocks LC 31-4741-6703-115 and -116 for tooling, and in a 41 kiloton, 10 ksi Verson-Wheelon forming press. Forming pressures ranged from 4500 to 7500 psi. Coupons were photo gridded (0.100 in. line spacing at 45 deg and 90 deg) before forming and elongations were measured from inner mold line to edge of flange. Specimens were prepared as follows:

Material alloy	Gage, in.	Bend radius	Recommended elongation limits, percent	
			Shrink	Stretch
Ta-10W	0.010 - 0.060	1.5 t	1.5	14.0
Rene' 41	0.010 - 0.025	1.5 t	1.0	22.5
Rene' 41	0.030 - 0.060	2.0 t	1.5	30.0
Haynes 25	0.010 - 0.060	1.0 t	2.0	45.0
TD NiCr	0.010	2.5 t	1.0	10.5
TD NiCr	0.030	3.0 t	1.0	12.5

Room Temperature Draw Forming Tests

Coupons were made by shearing 2.5-in. by 2.5-in. squares from sheet stock (fig. 5-68). Corners were removed as required by hand shearing. Edges of blanks were deburred. Draw forming results were obtained by Lockheed Aircaaft Corporation-modified Ericson cup tests. Previous values were substantiated for single draw operations.

Summary of draw forming:

Material alloy	Gage, in.	Draw depth to blank diam. ratio, %
Ta-10W	0.010 - 0.030	90
Cb-752	0.010 - 0.030	80
Rene' 41	0.010 - 0.020	60
Rene' 41	0.025 - 0.030	80
Haynes 25	0.010 - 0.060	100

Room Temperature Stretch Beading Tests

Room temperature stretch beading test coupons were prepared by shearing 3.0-in. by 5.0-in. blanks, deburring edges, and forming by high pressure in forming tool equipped with positive lock draw ring (fig. 5-69). Limits of forming in annealed condition were established; parts were then interstage annealed and second forming, third forming, and fourth forming stage limits determined. Annealing was accomplished in two different methods. One method involved encasing blank in a sealed stainless steel envelope so that annealing in air furnace could be accomplished without oxidation of coupon; the envelope was removed for final forming stage. A second method utilized hydrogen atmosphere bright annealing furnace (not a production facility). No appreciable forming differences between the two methods was noted.

Forming - See room temperature flanging tests above.

Tooling - LC 31-4741-6703-117 (Tungsten carbide facing applied to provide positive grip at interfaces under draw ring).

Summary of stretch beading:

Material alloy	Gage, in.	No. of process anneals[a]	Recommended total max. elong., percent
Haynes 25	0.010 - 0.025	1	50.0
Haynes 25	0.030 - 0.050	1	58.0
Rene' 41	0.010 - 0.020	1	17.0
Rene' 41	0.010 - 0.020	2	25.0
Rene' 41	0.010 - 0.020	3	30.0
Rene' 41	0.025 - 0.030	1	20.0
Rene' 41	0.025 - 0.030	2	30.0
Rene' 41	0.025 - 0.030	3	36.0
Rene' 41	0.025 - 0.030	4	40.0

[a] 1950° - 1975°F - 15 minutes; cool to 1000°F within 3 seconds.

REFERENCES

5-1 Oxidation of Nickel- and Cobalt-base Superalloys, Battele Memorial Institute, Defense Metals Information Center, DMIC Report 214, May 1961.

5-2 Metallurgical Service Lab. Reports 88270-1, -2 and -3, August 19, 1968.

5-3 Thermal Radiative Properties of Selected Materials. Battelle Memorial Institute, Defense Metals Information Center, DMIC Report 177, Volume 1, November 1962.

5-4 Dispersion-Strengthened Metal Structural Development. DAC 60647, Douglas Missile and Space Systems. Interim Technical Report No. 1, 1 Feb to 1 May 1967 (Contract F33 615-67-C-1319, BPSN 7 (61136873-6240533h)).

5-5 Wichorek, Gregory R; and Stein, Bland A.: Experimental Investigation of Aluminide-Coated Ta-10w for Heat-Shield Applications. NASA TN D-5524, 1969.

TABLE 5-1

MATERIAL SCREENING TEST PLAN

Test		Material					Number of Tests
		Rene' 41	Haynes 25	TD Nicr	Cb 752 R512E	90Ta-10W R512C	
Oxidation and thermal stability	Time, hr	250, 500, 750, 1000	250, 500, 750, 1000	500, 750, 1000			
	Temp, °F	1200, 1500	1200, 1500	1500, 2000, 2200			
	Gage, in.	0.015, 0.060	0.016, 0.030 0.060	0.010, 0.030			
	Coupons, No.	38	57	42			137
Tensile properties; F_{tu}, F_{ty}, E, e		(Tensile properties after exposure to elevated temperatures will be obtained from oxidation and thermal stability test coupons)					137 (b)
Emittance(a)	Temp. °F Gage, in. Specimen	1800 0.015 2	1800 0.015 2	2200 0.015 2	2600 0.015 2	2800 0.015 2	10
Metallurgical examination	Coupons, No.	9	9	11			29
						TOTAL	176

[a] Emittance tests were conducted to the limitation of test equipment. Specimens were preoxidized or coated (refractory metal)

[b] Same coupons as oxidation and thermal stability test coupons

TABLE 5-2

MECHANICAL PROPERTIES TESTS OF THERMALLY EXPOSED MATERIALS

Material	Gage, in.	Heat no.	Thermal exposure		F_{tu}, ksi	F_{ty}, ksi	% elong. (1 in.)	E_a, psi
			hr	°F				
Rene' 41	.015	2490-6-8512	As received		143	72	44	29×10^6
			250	1200	192	148	12	29
			500	↓	204	158	12	29
			750	↓	203	157	14	30
			1000	↓	197	159	10	30
			250	1500	166	114	7	29
			500	↓	152	108	4	28
			750	↓	143	105	4	32
			1000	↓	140	102	2	32
	.060	TV361	As received		149	75	38	27
			250	1200	188	150	10	30
			500	↓	197	152	9	35
			750	↓	189	162	4	33
			1000	↓	191	162	6	31
			250	1500	179	134	5	34
			500	↓	168	131	2	35
			750	↓	161	123	3	33
			1000	↓	157	120	2	31

TABLE 5-2.- Continued

MECHANICAL PROPERTIES TESTS OF THERMALLY EXPOSED MATERIALS

Material	Gage, in.	Heat no.	Thermal exposure		F_{tu}, ksi	F_{ty}, ksi	% elong. (1 in.)	E_a, psi
			hr	°F				
Haynes 25	.016	B16506	As received		139	71	34	36×10^6
			250	1200	114	85	10	33
			500	↓	119	97	6	32
			750	↓	132	114	4	34
			1000	↓	133	117	4	31
			250	1500	119	94	9	37
			500	↓	113	72	4	26
			750	↓	121	76	4	34
			1000	↓	126	75	5	35
	.030	51795	As received		151	75	36	33
			250	1200	115	86	7	35
			500	↓	128	99	8	33
			750	↓	140	117	5	37
			1000	↓	148	126	3	32
			250	1500	148	79	13	34
			500	↓	154	83	8	34
			750	↓	152	83	5	33
			1000	↓	150	89	5	36
	.060	186-6-1931	As received		148	69	57	32
			250	1200	131	86	18	35
			500	↓	132	98	7	33
			750	↓	124	110	4	35
			1000	↓	143	121	6	36
			250	1500	125	86	9	35
			500	↓	132	79	5	32
			750	↓	130	78	4	31
			1000	↓	130	79	3	31

TABLE 5-2. - Continued

MECHANICAL PROPERTIES TESTS OF THERMALLY EXPOSED MATERIALS

Material	Gage, in.	Heat no.	Thermal exposure		F_{tu}, ksi	F_{ty}, ksi	% elong. (1 in.)	E_a, psi	Coupon no.
			hr	°F					
TD NiCr	.010	2870	As received		132	87.7	14	22×10^6	33-1
			As received		133	88.9	14		-2
			As received		133	88.3	14		-3
			500	1500	126	87.6	14		-4
			500		126	87.3	17		-5
			750		122	83.0	16		-6
			750		118	81.9	14		-7
			1000		122	84.0	15		-8
			1000		120	83.6	14		-9
			500	2000	119	82.9	10		-10
			500		114	82.5	7		-11
			750		108	66.7	5		-12
			750		108	73.4	9		-13
			1000		102	72.9	5		-14
			1000		75.9	71.2	NA		-15
			500	2200	115	71.1	10		-16
			500		113	72.7	9[a]		-17
			750		86.6	48.2	6		X-3
			750		92.1	51.4	12[a]		-4
			750		89.7	52.6	10		-5
			1000		47.5	41.0	(1)		-13
			1000		81.3	43.6	9		-14
			1000		80.9	48.0	4		-15

[a]Failed outside specimen gage length.

TABLE 5-2.- Concluded

MECHANICAL PROPERTIES TESTS OF THERMALLY EXPOSED MATERIALS

Material	Gage, in.	Heat no.	Thermal exposure		F_{tu}, ksi	F_{ty}, ksi	% elong. (1 in.)	E_a, psi	Coupon no.
			hr	°F					
TD NiCr	.030	2855	As received		131	86.2	15	22×10^6	30-1
			As received		130	85.0	17		-2
			As received		132	85.8	16		-3
			500	1500	125.6	100.9	16		-4
			500		124.2	81.3	17		-5
			750		125.2	82.2	17		-6
			750		125.2	81.8	19		-7
			1000		126.8	82.4	19		-8
			1000		126.9	83.9	17		-9
			500	2000	125.5	79.9	19		-10
			500		124.7	80.1	18		-11
			750		123.1	80.1	12		-12
			750		123.8	79.2	17		-13
			1000		(b)	(b)	(b)		-14
			1000		(b)	(b)	(b)		-15
			500	2200	121.1	78.6	18		-16
			500		121.2	78.6	16		-17
			750		(c)	(c)	(c)		-18
			750		(c)	(c)	(c)		-19
			1000		(c)	(c)	(c)		-20
			1000		(c)	(c)	(c)		-21

[b]No data - specimens failed during test.

[c]No data - excessive degradation due to thermal exposure; specimens impossible to test.

TABLE 5-3

THERMAL EXPOSURE SCHEDULE FOR TD NiCr TENSILE SPECIMENS

Alloy code	Thickness, in.	Specimen identification			Exposure Temp., °F
		Exposure time, hrs			
		500	750	1000	
33	0.010	33-4, 5	33-6, 7	33-8, 9	1500
		33-10, 11	33-12, 13	33-14, 15	2000
		33-16, 17	33-18, 19	33-20, 21	2200
30	0.030	30-4, 5	30-6, 7	30-8, 9	1500
		30-10, 11	30-12, 13	30-14, 15	2000
		30-16, 17	30-18, 19	[a]30-20, 21	2200

[a] Specimens of 0.030-in. thick material that were contaminated from the brick supporting rack were not exposed at 2200°F for 1000 hours.

TABLE 5-4

THICKNESS OF SURFACE OXIDE ON TD NiCr SPECIMENS AFTER THERMAL EXPOSURE

Specimen identification	Thermal exposure		Surface oxide thickness, in.
	Time, hrs	Temp., ^{o}F	
33-1	As received		-
33-9	1000	1500^{o}F	0.0002
33-13	750	2000^{o}F	0.0002
33-15	1000	2000^{o}F	0.0002
33-16	500	2200^{o}F	0.0003
33-19	750	2200^{o}F	0.0003
33-21	1000	2200^{o}F	0.0005
30-1	As received		-
30-8	1000	1500^{o}F	NIL
30-14	1000	2000^{o}F	0.00005

TABLE 5-5

LEADING EDGE TEST DATA

Model No.	Coating	Exposure time, sec	Pre-weight, grams	Post-weight, grams	Weight loss, grams	Change in thickness[a], in.	Remarks
1	R512C	430	334.0	334.0	0	0	Six-minute cycle plus 1 min 10 sec. at T = 3100°F - Failure
2	R505	95	272.9	272.4	0.5	-0.010	Six-minute cycle plus 1 min 35 sec. at T = 3100°F - Failure
2A	R505	360	272.4	270.5	1.9	-0.014	
3	R505	1,800	264.9	264.9	0	+0.011	5 six-minute cycles plus an additional 1-hour cycle at T = 2800°F - Failure
3A	R505	3,600	264.9	264.0	0.9	+0.050	
4	R512C	11,160	336.9	336.9	0	0	31 six-minute cycles plus 6 additional 6-minute cycles at T = 2800°F - No Failure
4A	R512C	2,160	336.9	336.9	0	-0.006	
5	R505	720	269.1	269.0	0.1	-0.003	2 six-minute cycles plus 10 additional six-minute cycles at T = 2800°F - Failure
5A	R505	3,600	269.0	268.6	0.4	-0.009	
6	R512C	13,320	339.0	339.0	0	-0.003	37 six-minute cycles at T = 3000°F - Failure

[a] Change in thickness obtained at center of specimen.

TABLE 5-6

LEADING EDGE CALIBRATION DATA

Model No.	Gas stagnation enthalpy, btu/lb	Model stagnation pressure, atm	Nozzle stagnation pressure, atm	Nozzle static pressure, atm	Gas flow rate[a], lb/sec
1	4,000	0.063	0.308	0.00585	0.0161
2	2,570	0.052	0.257	0.00477	0.0161
2A	2,600	0.043	0.259	0.00394	0.0161
3	1,498	0.041	0.245	0.00366	0.0185
3A	1,450	0.039	0.243	0.00348	0.0185
4	1,720	0.044	0.262	0.00398	0.0185
4A	1,720	0.042	0.262	0.00378	0.0185
5	1,630	0.041	0.257	0.00370	0.0185
5A	1,630	0.042	0.257	0.00378	0.0185
6	4,400	0.064	0.380	0.00595	0.0185

[a] Gas flow comprised of 79% Nitrogen and 21% Oxygen - mixed in arc chamber.

TABLE 5-7

LEADING EDGE MODEL TEST DATA

Model No.	Coating	Exposure time, sec	Pre-weight, grams	Post-weight, grams	Weight loss, grams	Change in thickness[a], in.	Type of heating cycle
1	R512C	430	334.0	334.0	0	0	6-minute cycles at T = 3100°F
2	R505	95	272.9	272.4	0.5	-0.010	1 cycle at T = 3100°F
2A	R505	360	272.4	270.5	1.9	-0.014	6-minute cycles at T = 3100°F
3	R505	1800	264.9	264.9	0	+0.011	6-minute cycles at T = 2800°F
3A	R505	3600	264.9	264.0	0.9	+0.050	1-Hour cycle at T = 2800°F
4	R512C	11,160	336.9	336.9	0	0	6-minute cycles at T = 2800°F
4A	R512C	2160	336.9	336.9	0	-0.006	6-minute cycles at T = 2800°F
5	R505	720	269.1	269.0	0.1	-0.003	6-minute cycles at T = 2800°F
5A	R505	3600	269.0	268.6	0.4	-0.009	6-minute cycles at T = 2800°F
6	R512C	13,320	339.0	339.0	0	-0.003	6-minute cycles at T = 3000°F

[a] Change in thickness obtained at center of model.

TABLE 5-8

LEADING EDGE TEMPERATURE-TIME HISTORIES

Model 1

Temp.-°F	Time
3,020	0 - 4 min
2,930	6 min
3,000	1 min
3,100	Failure at 1 min 10 sec

Total Time = 7 min 10 sec

Model 2

Temp.-°F	Time
2700-3,000	0 - 1 min 30 sec
3,000	1 min 35 sec

Total Time = 1 min 35 sec

Model 3

Temp.-°F	Time
2700	0 - 6 min
2700	6 - 12 min
2700	12 - 18 min
2700	18 - 24 min
2700	24 - 30 min

Total Time:30 min 00 sec

Model 2A

Temp.-°F	Time
3,000	0 - 6 min; hot spot:

Total Time = 6 min 00 sec

3,280 at 1 min
3,310 at 2 min
2,980 at 3 min
3,020 at 4 min
3,120 at 5 min
3,170 at 6 min

Model 3A

Temp.-°F	Time
2700	0 - 60 min; hot spot:

Total Time 60 min 00 sec

2,820 at 10 min
2,800 at 15 min
3,015 at 26 min
3,055 at 28 min
3,035 at 31 min
3,010 at 33 min
3,010 at 45 min
3,010 at 60 min

TABLE 5-8.- Continued

LEADING EDGE TEMPERATURE-TIME HISTORIES

Model 4			Model 4A	
Temp.-°F	Time		Temp.-°F	Time
2700	0 - 6 min		2700	0 - 6 min
2700	6 - 12 min		2700	6 - 12 min
2700	12 - 18 min		2700	12 - 18 min
2705	18 - 24 min		2700	18 - 24 min
2705	24 - 30 min		2700	24 - 30 min
2700	30 - 36 min		2700	30 - 36 min
2705	36 - 42 min			
2705	42 - 48 min		Total Time = 36 min 00 sec	
2705	48 - 54 min			
2700	54 - 60 min			
2700	60 - 66 min			
2700	66 - 72 min			
2700	72 - 78 min			
2700	78 - 84 min			
2700	84 - 90 min			
2700	90 - 96 min			
2700	96 - 102 min			
2700	102 - 108 min			
2700	108 - 114 min			
2700	114 - 120 min			
2700	120 - 126 min			
2700	126 - 132 min			
2700	132 - 138 min			
2700	138 - 144 min			
2700	144 - 150 min			
2700	150 - 156 min			
2700	156 - 162 min			
2700	162 - 168 min			
2700	168 - 174 min			
2700	174 - 180 min	Total Time =		
2700	180 - 186 min	186 min 00 sec		

TABLE 5-9

JOINT EVALUATION TEST PLAN

Joint type	Material	Joining method	Material gage, in.	Number of heats	Thermal exposure	Number of specimens per test temperature					Total number of specimens		Total number of specimens tested
						RT	1200°F	1500°F	2000°F	2200°F	Aged[a]	Annealed	
Lap	René 41	Resistance spotweld	.015	2	None	20	20	20	--	--	30	30	60
				2	250 hr @ 1500°F	20	--	--	--	--	10	10	20
		Diffusion spot bond	.015	1	None	10	10	10	--	--	15	15	30
				1	250 hr @ 1500°F	10	--	--	--	--	5	5	10
	Haynes 25	Resistance spotweld	.010	1	None	5	5	5	--	--	--	15	15
			.030	1	None	5	5	5	--	--	--	15	15
			.060	1	None	5	5	5	--	--	--	15	15
	TD Ni Cr	Diffusion spot bond	.010	1	None	5	--	--	5	5	--	15	15
			.030	1	None	5	--	--	5	5	--	15	15
		Brazed spot	.010	1	None	5	--	--	5	5	--	15	15
			.030	1	None	5	--	--	5	5	--	15	15
		Riveted	.030	1	None	5	--	--	5	5	--	15	15
			.060	1	None	5	--	--	5	5	--	15	15
		Continuous braze	.010	1	None	5	--	--	5	5	--	15	15
Spot tension	René 41	Resistance spotweld	.015	2	None	20	--	--	--	--	10	10	20
				2	250 hr @ 1500°F	20	--	--	--	--	10	10	20
		Diffusion spot bond	.015	1	None	10	--	--	--	--	5	5	10
				1	250 hr @ 1500°F	10	--	--	--	--	5	5	10
Tee / Butt	Ta-10W	Electron beam welded	.060	1	None	Specimens fabricated but not tested.[b]							0
												Total	330
												Total + EB Spec =	350

[a] Aging treatment: heated in air to 1400°F, held at temp for 16 hrs, air cooled

[b] 5 specimens (8 x 5) were fabricated but not cut into the 1-in. widths required for test

TABLE 5-10

SUMMARY OF LAP JOINT TEST DATA

Material	Heat No.	Gage, in.	Condition	Method of joining	Thermal exposure		Ultimate load, lb/spot		
					hr	°F	RT	1200°F	1500°F
René 41	2490-6-8512	.015	Aged	Resistance spot	None		612 532	405 442	294 234
			Annealed						
			Aged		250	1500	632 629	--- ---	--- ---
			Annealed						
	2490-7-8513		Aged		None		682 579	516 461	301 286
			Annealed						
			Aged		250	1500	560 586	--- ---	--- ---
			Annealed						
	2490-6-8512		Aged	Diffusion spot	None		557 524	313 420	181 163
			Annealed						
			Aged		250	1500	548 559	--- ---	--- ---
			Annealed						
Haynes 25	51795	.010 .030 .060	Annealed Annealed Annealed	Resistance spot	None		277 1573 3329	150 982 2216	109 750 1440

TABLE 5-11

LAP JOINT TEST DATA FOR 0.015 RENE' 41

Specimen identification	Method of joining	Gage, in.	Heat No.	Condition	Thermal exposure		Ultimate load, lb/spot		
					hr	°F	RT	1200°F	1500°F
1-1	Resistance spot	.015	2490-6-8512	Aged	None	None	623	401	306
1-2							619	361	302
1-3							642	398	279
1-4							605	408	284
1-5							569	455	301
Avg							612	405	294
2-1				Annealed			533	440	261
2-2							533	447	225
2-3							532	451	231
2-4							529	434	226
2-5							531	440	225
Avg							532	442	234
24-1				Aged	250	1500	619		
24-2							643		
24-3							645		
24-4							661		
24-5							591		
Avg							632		
25-1				Annealed			635		
25-2							597		
25-3							638		
25-4							640		
25-5							634		
Avg							629		

TABLE 5-11. - Continued

LAP JOINT TEST DATA FOR 0.015 RENÉ 41

Specimen identification	Method of joining	Gage, in.	Heat No.	Condition	Thermal exposure		Ultimate load, lb/spot		
					hr	°F	RT	1200°F	1500°F
3-1	Resistance spot	.015	2490-7-8513	Aged	None	None	685	516	317
3-2							661	521	300
3-3							699	509	314
3-4							685	506	285
3-5							679	530	291
Avg							682	516	301
4-1				Annealed			578	459	271
4-2							597	477	280
4-3							567	470	278
4-4							567	451	302
4-5							586	447	297
Avg							579	461	286
26-1		.015	2490-7-8513	Aged	250	1500	587		
26-2							570		
26-3							515		
26-4							563		
26-5							563		
Avg							560		
27-1				Annealed			590		
27-2							555		
27-3							623		
27-4							625		
27-5							537		
Avg							586		

TABLE 5-12

LAP JOINT TEST DATA FOR HAYNES 25

Specimen identification	Method of joining	Gage, in.	Condition	Heat No.	Thermal exposure		Ultimate load, lb/spot		
					hr	°F	RT	1200°F	1500°F
21-1	Resistance spot	.010	Annealed	L1635	None	None	271	162	115
21-2							267	164	117
21-3							277	160	112
21-4							280	137	93
21-5							289	128	110
Avg							277	150	109
22-1		.030		51795			1577	965	777
22-2							1573	973	730
22-3							1560	1012	733
22-4							1573	993	743
22-5							1583	966	767
Avg							1573	982	750
23-1		.060		186-6-1931			3360	2193	1393
23-2							3360	2300	1475
23-3							3307	2246	1480
23-4							3373	2246	----
23-5							3247	2093	1413
Avg							3329	2216	1440

TABLE 5-13

SUMMARY OF TD NiCr LAP JOINT TEST DATA

Material	Heat No.	Material gage, in.	Material condition	Method of joining	Test temperature			
					RT	RT	2000°F	2200°F
					Ultimate, lb/spot	Yield	Ultimate, lb/spot	Ultimate, lb/spot
TD NiCr	2862-1	.010	Annealed	Diffusion spot bond	247	-	38	31
	2862-1	.030	Annealed	Diffusion spot bond	942	-	63	40
	2862-1	.010	Annealed	Brazed spot	488	-	52	39
	2862-1	.030	Annealed	Brazed spot	1098	-	92	67
	2901	.030	Annealed	Riveted	[a] 596	[a] 367	[a] 84	[a] 73
	2891	.060	Annealed	Riveted	[a] 1730	[a] 915	[a] 220	[a] 176
	2862-1	.010	Annealed	Continuous braze	[b] 1910	-	[b] 180	[b] 118

[a]Pounds per rivet.

[b]Total load on specimen (brazed area 1 in. x 2 in.).

TABLE 5-14

LAP JOINT TEST DATA FOR TD NiCr

Specimen identification	Method of joining	Gage, in.	Condition	Heat No.	Thermal exposure		Ultimate load, lb/spot		
					hr	°F	RT	2000°F	2200°F
31-1	Diffusion spot bond	.010	Annealed		None	None	219	37	33
31-2							285	53	36
31-3							220	-	33
31-4							273	33	26
31-5							239	27	25
Avg							247	38	31
32-1		.030					963	93	24
32-2							987	45	57
32-3							920	-	30
32-4							907	20	26
32-5							933	95	65
Avg							942	63	40
33-1	Brazed spot	.010					520	49	35
33-2							465	63	40
33-3							523	51	45
33-4							453	55	41
33-5							480	43	36
Avg							488	52	39
34-1		.030					965	89	47
34-2							1112	130	103
34-3							1152	131	53
34-4							1163	27	86
34-5							1100	84	44
Avg							1098	92	67
							Ult / yield		
35-1	Rivets	.030					598 / 370	89	70
35-2							600 / 357	89	67
35-3							560 / 375	79	74
35-4							619 / 352	74	80
35-5							601 / 380	90	73
Avg							596 / 367	84	73
38-1		.060					1763 / 916	229	173
38-2							1700 / 900	222	167
38-3							1708 / 933	216	169
38-4							1702 / 925	209	185
38-5							1767 / 900	224	176
Avg							1730 / 915	220	176
37-1	Continuous braze	.010	As rec'd	2862-1			1425	148	116
37-2							2000	182	108
37-3							2140	244	104
37-4							2115	166	118
37-5							1885	160	144
Avg							1910	180	118

TABLE 5-15

SUMMARY OF SPOT TENSION TEST DATA

Method of joining	Heat no.	Condition	Thermal exposure		Ultimate load, lb (a)
			hr	°F	
Resistance spot	2490-7-8513	Aged	None		190
		Annealed	None		373
		Aged	250	1500	115
		Annealed	250	1500	124
	2490-6-8512	Aged	None		164
		Annealed	None		310
		Aged	250	150	99
		Annealed	250	1500	106
Diffusion spot bond	2490-7-8513	Aged	None		64
		Annealed	None		176
		Aged	250	1500	106
		Annealed	250	1500	112

[a]All values are the average of five specimens.

TABLE 5-16

SPOT TENSION TEST DATA FOR .015 RENE' 41

Specimen identification	Method of joining	Condition	Heat no.	Thermal exposure		Ultimate load, lb
				hr	°F	
9-1	Resistance spot	Aged	2490-7-8513	None	None	166
9-2						221
9-3						205
9-4						172
9-5						184
Avg						190
10-1		Annealed				385
10 2						376
10-3						354
10-4						376
10-5						376
Avg						373
13-1		Aged		250	1500	124
13-2						122
13-3						122
13-4						94
13-5						112
Avg						115
14-1		Annealed				120
14-2						126
14-3						NA
14-4						128
14-5						124
Avg						124
11-1		Aged	2490-6-8512	None	None	174
11-2						166
11-3						168
11-4						163
11-5						147
Avg						164
12-1		Annealed				288
12-2						338
12-3						310
12-4						306
12-5						NA
Avg						310

TABLE 5-16. - Concluded

SPOT TENSION TEST DATA FOR .015 RENÉ 41

Specimen identification	Method of joining	Condition	Heat no.	Thermal exposure		Ultimate load, lb
				hr	°F	
15-1	Resistance spot	Aged	2490-6-8512	250	1500	91
15-2						105
15-3						93
15-4						105
15-5						100
Avg						99
16-1		Annealed				104
16-2						98
16-3						110
16-4						108
16-5						110
Avg						106
17-1	Diffusion spot bond	Aged	2490-7-8513	None	None	60
17-2						49
17-3						34
17-4						109
17-5						68
Avg						64
18-1		Annealed				162
18-2						194
18-3						156
18-4						190
18-5						178
Avg						176
19-1		Aged		250	1500	103
19-2						103
19-3						121
19-4						93
19-5						112
Avg						106
20-1		Annealed				80
20-2						115
20-3						112
20-4						116
20-5						135
Avg						112

Section 6

STRUCTURAL ANALYSIS MODEL

by

G. W. Haggenmacher, R. S. Lahey, G. W. Davis,
M. J. Blaha, and W. R. Easter

CONTENTS

TABLES

ILLUSTRATIONS

SYMBOLS

BL	Butt line
g	Gravitational acceleration
P_x, P_y, P_z	Forces in Cartesian coordinate system
T	Temperature
t	Thickness
t_e	Equivalent extensional thickness
t_s	Equivalent shear thickness
t_w	Web thickness
α	Mean coefficient of thermal expansion
ΔT	Temperature differential

Section 6

STRUCTURAL ANALYSIS MODEL

This section provides a description of the redundant structural analysis model, summarizes redundant model input data, and discusses uses of redundant model output.

REDUNDANT MODEL DESCRIPTION

Internal loads, displacements, and influence coefficients for the wing structure were determined by a mechanized redundant-structure analysis solution based on the matrix force method (ref. 6-1). The lumped element model used for this analysis represented one-half of the structure on one side of the symmetry plane of the vehicle. The analysis for influence coefficients and internal loads was necessary only for symmetrical boundary conditions at the symmetry-plane of the model, since only symmetrical maneuver loads were evaluated. For the analysis of design conditions, the external loads were transformed into the nodes of the structural model. Only loads normal to the wing surface were considered. A drawing of the model is shown in figure 6-1. It consisted of three parts:

1. The center wing model was a fairly well-detailed representation of the region of primary interest and was used for the evaluation of structural concepts. This model consisted of cap members and shear panels for both wing cover surfaces, and had typical spar spacings to satisfy requirements for conducting the stress analysis.

2. The aft wing plate representation (with increasing spacing away from the center area) served to provide realistic restraint and load transfer to the center area and to a number of deflection points sufficient for load computation purposes. Also, this part of the analysis model consisted of a mesh of spanwise and chordwise bending members and torsion box elements.

3. The fuselage model was a highly idealized representation of the fuselage shell and could be coupled to the wing model in several ways to analyze the effect of various fuselage wing attachment methods. The fuselage consisted of a number of longeron, panel, and frame elements to represent the bending and shear stiffness of the fuselage.

The redundant-structure analysis solution determined thermal stresses and thermoelastic deflections due to the average thermal expansion of axial elements. Stresses due to thermal gradients within elements of the redundant analysis model were computed separately by means of a thermal-stress computer program, and were superimposed on redundant model stresses. These elements were analyzed for simple boundary conditions (usually no axial restraint and full rotational restraint), and their cross sections were subdivided into many small subelements, for each of which the free thermal expansion was specified in terms of local temperatures.

The wing considered for the Hypersonic Cruise Vehicle was a multispar, multirib structure. For the purpose of structural analysis, it was represented by a grid of spanwise and chordwise beams and ribs which consisted of upper and lower cap area and vertical shear web. The grid was completed by cover-shear-panels in each surface. This beam-rib system of the analysis model represented lumped areas of the actual structure, since model grid distances were different from actual beam and rib spacings.

The beam-rib gridwork of the analysis model in the investigation region had approximately twice as fine a mesh than fore and aft.

This model was used in analyzing various types of structural panels and two main structural arrangements:

1. Arrangement 1 – Full spanwise and chordwise bending continuity for all beams and ribs of the model within the wing was provided. Wing-fuselage connection for both P_X and P_Y loads was located at each spar along the BL 120 rib. This arrangement was analyzed for various sets of section properties representing lumped values of chordwise, spanwise, and shear-stiffness characteristics of monocoque and semimonocoque structures.

2. Arrangement 2 – Represented the statically determinate wing; a typical configuration is shown in figure 6-2. Its main characteristic was the absence of any chordwise bending continuity from one box beam to the next. The same basic model network was used as in arrangement 1, each spanwise beam of the model representing lumped beam properties. For this arrangement, this single model beam represented two adjacent parallel beams which were connected to have the same vertical deflection. The continuity of chordwise cap forces was interrupted at each beam so that no chordwise bending continuity exists in the model. This was accomplished by a technique of calculating the redundant force units in two sets on two sets of alternating box beams (figure 6-2). Each box beam was independently connected to the fuselage vertically (P_Z) at both beams and horizontally (P_X), only at the top of the front spar of each box. In this fashion no force system was set up which can express continuity of chordwise strains between one box and the next and between wing and fuselage.

External loads were introduced at node points. Effects of differential thermal expansion were accounted for by introducing free thermal expansions of axial elements as initial strains. The load point network for both versions of the redundant model is presented in figure 6-3. This load point network was used to introduce air, inertia, and ramp loads into the wing structure. Fuel tank inertia loads were introduced at the wing-fuselage intersection (BL 120).

SUMMARY OF REDUNDANT MODEL INPUT DATA

The evaluation matrix for redundant model loads is presented in table 6-1. Initial internal loads were based on a nominal panel configuration representative of both monocoque and semimonocoque structure concepts. Equivalent extensional and shear thicknesses of the primary structural panels used for determining initial loads are shown in table 6-2. Thermal data ($\alpha\Delta T$) were input for each flight condition, and temperatures were from preliminary isotherm data. These isotherms were constructed from radiation equilibrium temperature data at five stations and approximately twenty discrete points per wing surface.

Final and intermediate internal loads were based on the panel dimension flexibilities and actual thermal input data described in tables 6-3 through 6-8, respectively, for the monocoque (waffle and honeycomb), semimonocoque (spanwise and chordwise), and statically determinate primary structure concepts. The element flexibility matrix for the waffle version of the redundant model was adjusted to account for Poisson's effect. Two redundant analyses were required for the chordwise concept (intermediate and final).

USES OF REDUNDANT MODEL OUTPUT

For this program, the redundant model output data were used in the following areas:

1. Internal load distributions, particularly in the main area of interest, as a basis for the stress analysis and evaluation of the various structural concepts. Initial redundant model loads are presented in the evaluation results section of this document as well as the final redundant model internal loads for the monocoque, semimonocoque (spanwise and chordwise), and statically determinate primary structure concepts.

2. Structural influence coefficients for vehicle flutter evaluation.

3. Vehicle deflections for evaluating aeroelastic effects on panel pressure distributions and cruise performance (drag change).

REFERENCES

6-1 Haggenmacher, G. W.: Preparation of Data for the Redundant Structures Analysis Programs. Lockheed-California Company, LR 13091, February 1964.

TABLE 6-1

EVALUATION MATRIX FOR REDUNDANT MODEL LOADS

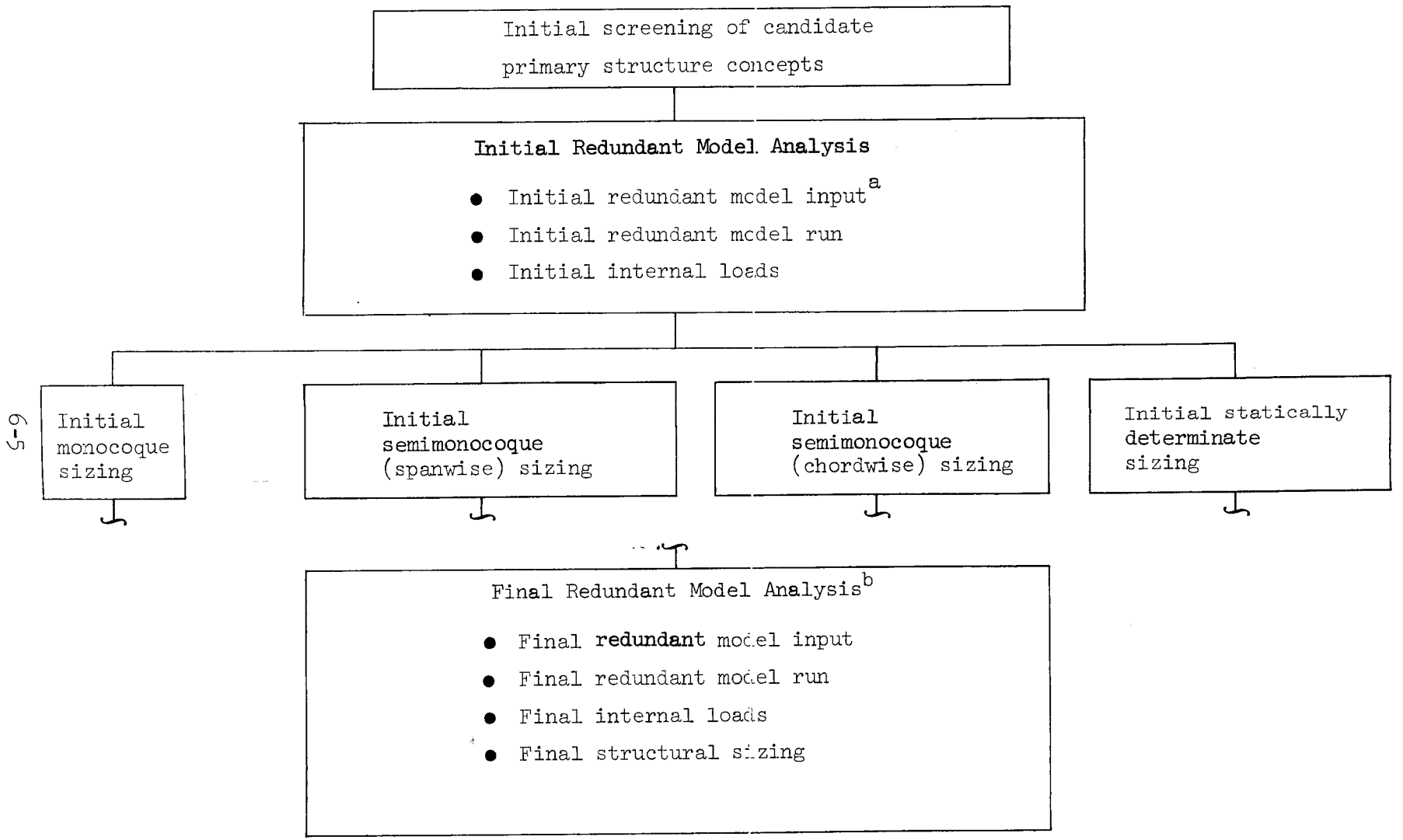

[a]Based on nominal panel configuration representative of both monocoque and semimonocoque primary structure concepts.

[b]Five cases (two monocoque concepts, and one each for the following concepts: semimonocoque spanwise, semimonocoque chordwise, and statically determinate) with two iterations as required.

TABLE 6-2

REDUNDANT MODEL INPUT DATA FOR INITIAL INTERNAL LOADS

Panel concept: nominal panel configuration representative of both monocoque and semimonocoque concepts.

Panel orientation: chordwise

Material:

a. primary structural panels - René 41
b. rib and spar webs - Haynes 25

Thermal protection system: no heat shields or insulation

Rib and spar webs: 60° circular-arc corrugation, minimum gage web thickness, t_w = 0.015 in.

Equivalent extensional (t_e) and shear (t_s) thickness of the primary structural panels:

Location	t_e in.	t_s in.
Upper Surface	0.038	0.020
Lower Surface	0.038	0.020

Panel size: spanwise direction = 46 in.
chordwise direction = 92 in.

Rib spacing: 46 in.

Spar spacing: 92 in.

Effective cap areas (includes closeout effects):

spar caps = 0
rib caps = 0

Thermal data: $(\alpha \Delta T)$ input for each flight condition.

Modulus: extensional and shear modulus based on average temperatures for the 2g maneuver condition.

TABLE 6-3

MONOCOQUE WAFFLE REDUNDANT MODEL INPUT DATA
FOR FINAL INTERNAL LOADS

Panel concept: -45° x 45° unflanged waffle grid plate

Panel orientation: chordwise

Material: Panels, ribs, ans spars material René 41, solution treated and aged at 1400°F

Thermal protection system: partial heat shields at outboard area lower surface

Rib and spar webs: 60° circular-arc corrugation, minimum gage web thickness, t_w = 0.015 in.

Equivalent extensional (t_e) and shear (t_s) thicknesses of the primary structural panels:

Location	t_e, in.	t_s, in.
Upper Surface	0.020	0.040
Lower Surface		
BL 0-120	0.025	0.046
BL 120-212	0.025	0.046
BL 212-350	0.030	0.053

Panel size: spanwise direction = 20 in.
chordwise direction = 43 in.

Rib spacing - 23 in.
Spar spacing - 46 in. } from cap ℄ to cap ℄

Effective cap areas (includes closeout effects):

spar caps = 0.16 $in.^2$
rib caps = 0.12 $in.^2$

Thermal data: ($\alpha\Delta T$) input for each flight condition

Modulus: extensional and shear modulus based on temperatures for the 2g maneuver condition

TABLE 6-4

MONOCOQUE HONEYCOMB-CORE SANDWICH REDUNDANT MODEL
INPUT DATA FOR FINAL INTERNAL LOADS

Panel concept: Honeycomb-core sandwich

Panel orientation: chordwise

Material: René 41, solution-treated and aged at 1400°F

Thermal protection system: partial heat shields at outboard area lower surface

Rib and spar webs: 60° circular-arc corrugation, minimum gage web thickness, t_w = 0.015 in.

Equivalent extensional (t_e) and shear (t_s) thicknesses of the primary structural panels:

Location	t_e, in.	t_s, in.
Upper Surface	0.029	0.029
Lower Surface		
BL 0-120	0.033	0.033
BL 120-212	0.042	0.042
BL 212-350	0.027	0.027

Panel size: spanwise direction = 40 in.
chordwise direction = 80 in.

Rib spacing: 40 in.

Spar spacing: 80 in.

Effective cap areas (includes closeout effects):

spar caps = 0.315 $in.^2$
rib caps = 0.315 $in.^2$

Thermal data: ($\alpha\Delta T$) input for each flight condition

Modulus: extensional and shear modulus based on temperatures for the 2g maneuver condition

TABLE 6-5
SEMIMONOCOQUE SPANWISE REDUNDANT MODEL INPUT DATA
FOR FINAL INTERNAL LOADS

Panel concept: Tubular panels (upper and lower surfaces)

Panel orientation: spanwise

Material: Panels, ribs, and spars material Rene' 41, solution treated and aged at 1400°F.

Thermal protection system: heat shields, both upper and lower, with partial insulation (1/4 inch Dyna-Flex) on the lower surface outboard area

Rib and spar webs: 60° circular-arc corrugation configuration with minimum gage thickness, t_w = 0.015 in.

Equivalent extensional (t_e) and shear (t_s) thicknesses of the primary structural panels:

Location	t_e in.	t_s in.
Upper surface	0.028	0.016
Lower surface		
BL 0-120	0.026	0.015
BL 120-212	0.030	0.018
BL 212-350	0.028	0.016

Panel size: spanwise direction = 43.0 in.
chordwise direction = 89.0 in.

Rib spacing: 46.0 in.
Spar spacing: 92.0 in.
} from cap ℄ to cap ℄

Effective cap areas (includes closeout effects):

spar caps = 0.22 $in.^2$
rib caps = 0.34 $in.^2$

Thermal data: ($\alpha\Delta T$) input for each flight condition

Modulus: extensional and shear modulus based on temperatures for the 2g maneuver condition.

TABLE 6-6
SEMIMONOCQUE CHORDWISE REDUNDANT MODEL INPUT DATA
FOR INTERMEDIATE RUN

Panel concept: Convex beaded panels for exposed upper surfaces; tubular lower surface panels

Panel orientation: chordwise

Material: Panels, ribs, and spars material René 41, solution-treated and aged at 1400°F

Thermal protection system: heat shield lower surface with partial insulation of the outboard lower surface

Rib and spar webs: 60° circular-arc corrugation configuration with minimum gage thickness, t_w = 0.015 in.

Equivalent extensional t_e and shear t_s thicknesses of the primary structural panels:

Location	$t_{e,x}$ in.	t_s in.
Upper Surface	0.029	0.022
Lower Surface	0.044	0.028

Panel size: spanwise direction = 89.0 in.
chordwise direction = 43.0 in.

Rib spacing: 92.0 in.
Spar spacing: 46.0 in.
} from cap ℄ to cap ℄

Effective cap areas (including closeout effects):

spar caps = 0.34 $in.^2$
rib caps = 0.24 $in.^2$

Thermal data: $(\alpha\Delta T)$ input for each flight condition

Modulus: extensional and shear modulus based on temperatures for the 2g maneuver condition

TABLE 6-7

SEMIMONOCOQUE CHORDWISE REDUNDANT MODEL
INPUT DATA FOR FINAL INTERNAL LOADS

Panel concept: Convex beaded panels for upper exposed surfaces; tubular lower surface panels

Panel orientation: chordwise

Material: Panels, ribs, and spars material Rene' 41, solution-treated and aged at 1400°F

Thermal protection system: heat shield lower surface with partial insulation on outboard lower surface.

Rib and spar webs: 60° circular-arc corrugation configuration with minimum gage thickness, t_w = 0.015 in.

Equivalent extensional t_e and shear t_s thicknesses of the primary structural panels:

Location	$t_{e,x}$ in.	t_s in.
Upper surface		
℄ - BL 120	0.025	0.016
BL 120 - OUTBOARD	0.031	0.025
Lower surface		
℄ - BL 120	0.026	0.015
BL 120 - BL 212	0.033	0.020
BL 212 - BL 350	0.028	0.017

Panel size:
57 x 21 in. (span x chord), ℄ - BL 120
75 x 21 in., BL 120 - OUTBOARD

Rib spacing:
60 in., ℄ - BL 120
78 in., BL 120 - OUTBOARD } from cap ℄ to cap ℄

Spar spacing: 24.0 in. } from cap ℄ to cap ℄

TABLE 6-7 - Concluded

SEMIMONOCOQUE CHORDWISE REDUNDANT MODEL
INPUT DATA FOR FINAL INTERNAL LOADS

Effective cap areas (includes closeout effects):

spar caps:

Location	Upper	Lower
℄ - BL 120	0.34	0.25
BL 120 - BL 212	0.40	0.21
BL 212 - OUTBOARD	0.31	0.20

rib caps: 0.19 $in.^2$

Thermal data: $(\alpha \Delta T)$ for each flight condition

Modulus: extensional and shear modulus based on temperatures for the 2g maneuver condition

TABLE 6-8

STATICALLY DETERMINATE REDUNDANT MODEL
INPUT DATA FOR FINAL INTERNAL LOADS

Panel concept: Beaded both surfaces

Panel orientation: spanwise

Material: Panels, ribs, and spars material
René 41, solution treated and aged at 1400°F

Thermal protection system: heat shield both surfaces no insulation

Rib and spar webs: 60° circular-arc corrugation configuration with minimum gage thickness, t_w = 0.015 in.

Equivalent extensional (t_e) and shear (t_s) thicknesses of the primary structural panels:

Location	t_e in.	t_s in.
Upper Surface	0.028	0.016
Lower Surface		
BL 0 - 120	0.026	0.015
BL 120 - 212	0.030	0.018
BL 212 - 350	0.028	0.016

Panel size: 43 x 89 in. (span x chord)

Rib spacing: 46 in. | from cap ℄ to cap ℄ |
Spar spacing: 92 in.

Effective cap areas (includes closeout effects):

spar caps = 0.15 $in.^2$
rib caps = 0.12 $in.^2$

Thermal data: ($\alpha \Delta T$) input for each flight condition

Modulus: extensional and shear modulus based on temperatures for the 2g maneuver condition

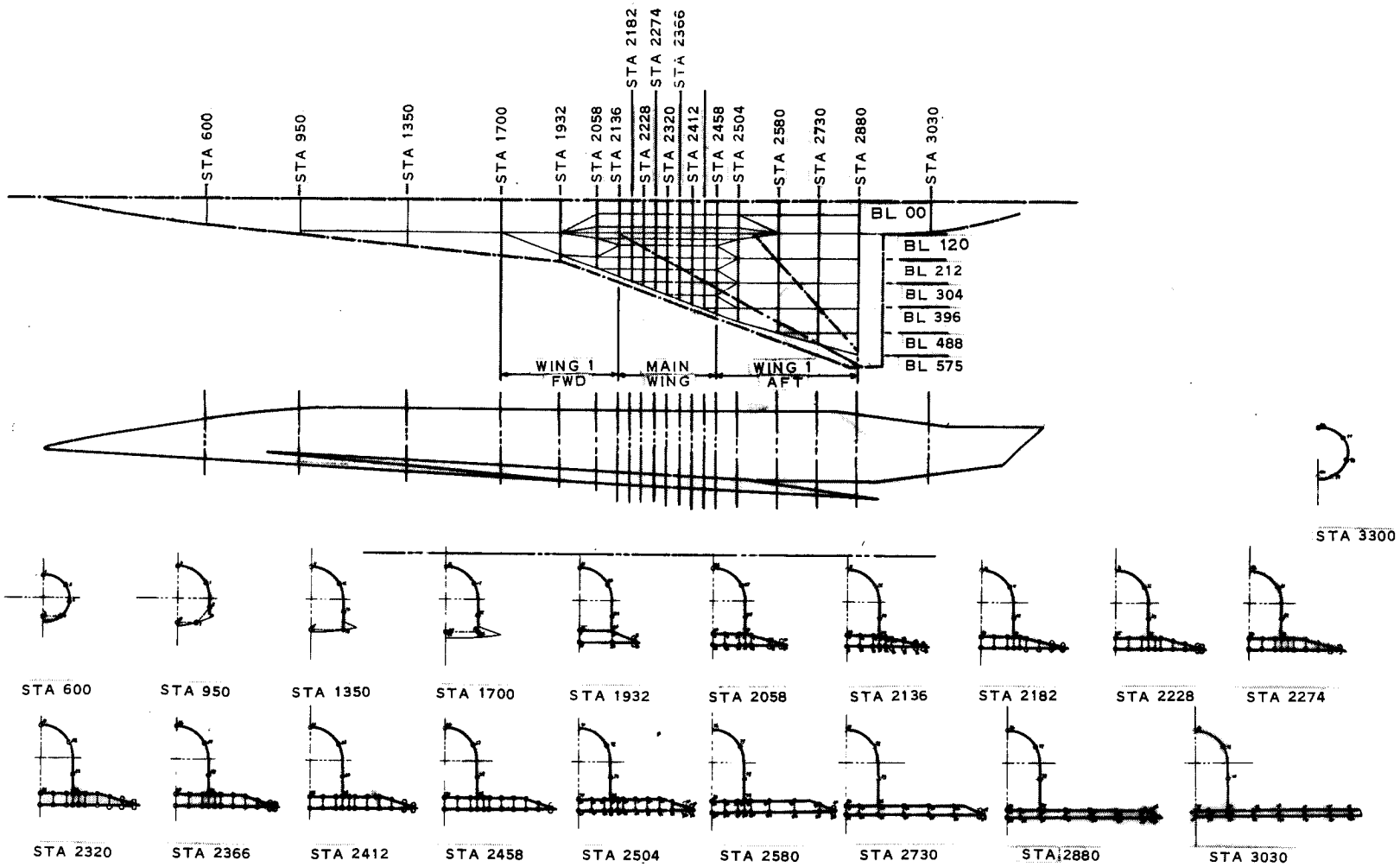

Figure 6-1. Master Model drawing

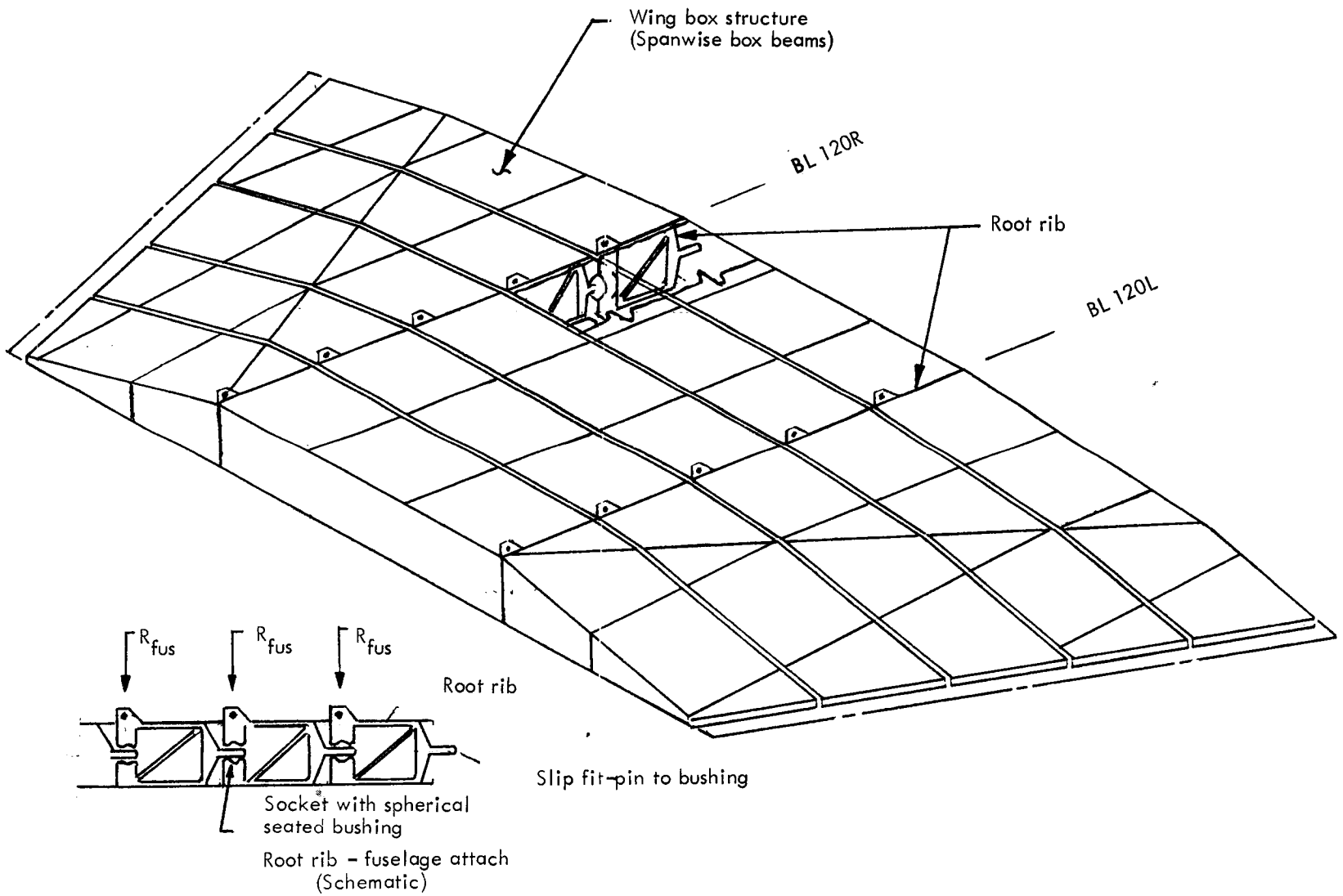

Figure 6-2. Statically determinate wing structure

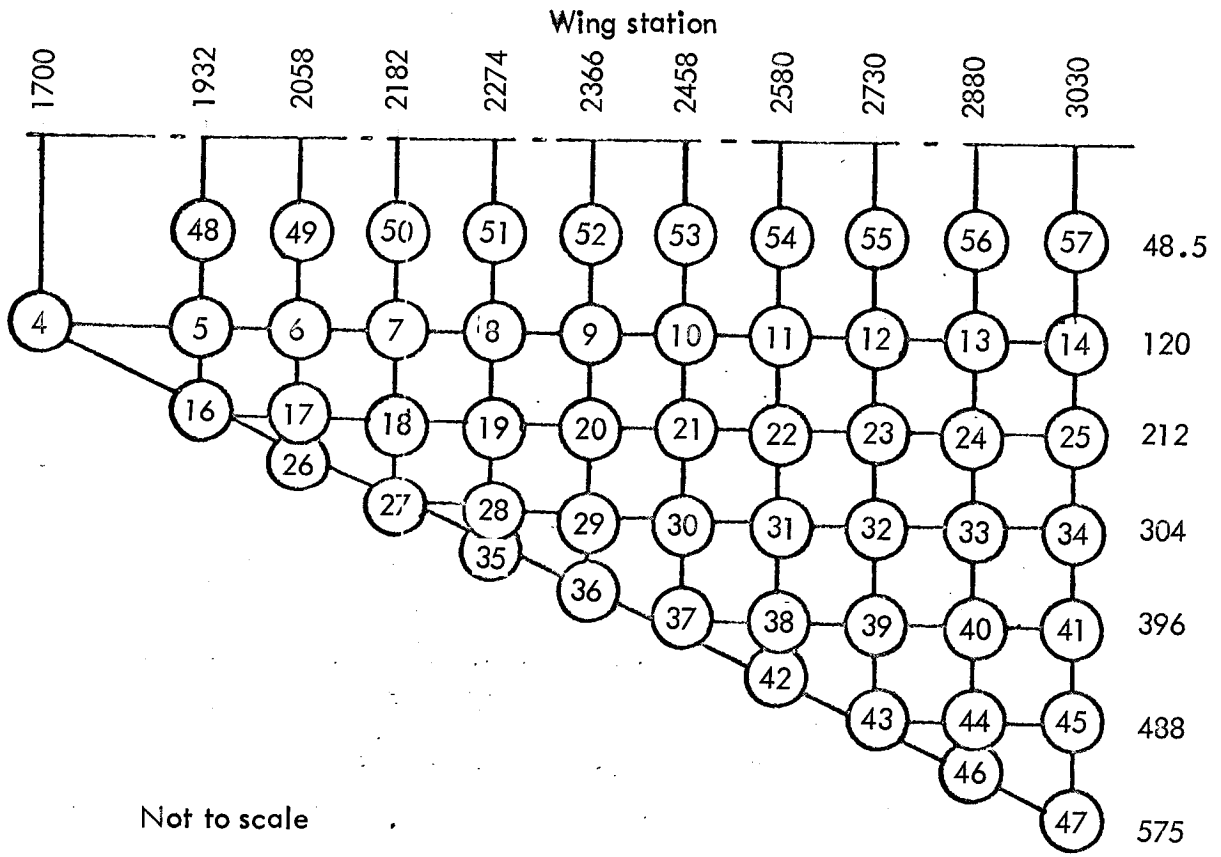

Additional network coordinates not shown

NO.	Sta.	Bl
1	600	00
2	950	00
3	1350	120
15	3300	120

Figure 6-3. Loads network model

Section 7

A PLANE STRAIN ANALYSIS FOR DETERMINING THERMAL STRESSES

by

C. C. Richie

CONTENTS

SYMBOLS

A	Area of lumped element, Δst
a,b,c	Rectangular Cartesian coordinates
E	Modulus of elasticity
L	Length
M	Bending moment
N	Extensional force in xy coordinates
T	Temperature
t	Average thickness of lumped element
u	Axial displacement
α	Mean coefficient of thermal expansion
Δs	Average width of lumped element
ϵ	Strain
σ	Stress

Subscripts

a,b,c	Denotes relationship to a,b, and c axes
j	Denotes number of lumped element
m,n	Denotes first and last number of lumped elements, respectively; also, m denotes mean value
o	Denotes temperature at which the thermal stress of all elements is zero

Section 7

A PLANE-STRAIN ANALYSIS FOR DETERMINING THERMAL STRESSES

A plane-strain analysis of thermal stresses is presented in this section. For many applications, the procedure provides an adequate estimate of stresses due to temperature gradients. It is especially useful for determining approximate stresses of high-temperature structures during the preliminary phase of design.

ANALYSIS

Consider the lumped structural model shown in figure 7-1. When the structure is subjected to external loading of N_a, M_b, and M_c, and to transient heating, a plane located originally at $a' = 0$ is translated parallel to the a' axis and rotated about the b'' and c'' axes. This analysis was conducted using the methods of references (7-1) and (7-2). The Bernoulli-Euler assumption was used for the axial displacement equation. This requires the axial displacement component be a linear function of the coordinates in the plane of the cross section. Denoting the axial coordinate by a', and letting b' and c' be the centroidal cross section. The axial displacement u may be written as

$$u_j = F_0(a') + c'_j F_1(a') + b'_j F_2(a') \qquad (7\text{-}1)$$

where

F_0, F_1 and F_2 = linear functions of the axial coordinate

a', b' and c' = coordinates measured from centroidal axes of cross section

j = subscript denotes number of lumped elements

The corresponding strain can be written as

$$\epsilon_j = \frac{\partial u}{\partial a'} = \dot{F}_0 + c'_j \dot{F}_1 + b'_j \dot{F}_2 \qquad (7\text{-}2)$$

where dots indicate differentiation with respect to a'.

The stress component is

$$\sigma_j = E_j \left[\epsilon_j - \alpha m_j (T_j - T_o) \right] = E_j (\dot{F}_0 + c'_j \dot{F}_1 + b'_j \dot{F}_2) - \alpha m_j E_j (T_j - T_o) \tag{7-3}$$

where

α_m = mean coefficient of thermal expansion based on T_o, in./in.
T_o = temperature at which the thermal stress of all elements is zero, ^oF

The last term on the right-hand side of equation (7-3) is entirely a function of temperature for a given material; hence, it is convenient to express it simply as

$$f(T)_j = -\alpha_{m_j} f E_j (T_j - T_o) \tag{7-4}$$

The functions F_0, F_1, and F_2 are determined so as to satisfy the following equations of equilibrium.

$$\sum_{j=m}^{j=n} \sigma_j \Delta A_j = N_a \tag{7-5}$$

$$\sum_{j=m}^{j=n} \sigma_j \Delta A_j c'_j = M_b - N_a \bar{c} \tag{7-6}$$

$$\sum_{j=m}^{j=n} \sigma_j \Delta A_j b'_j = -(M_c + N_a \bar{b}) \tag{7-7}$$

in which

$\bar{b}$ and $\bar{c}$ = coordinates of centroid, in.
N_a = axial load acting parallel to a axis, lb
M_b = moment about b axis, in.-lb
M_c = moment about c axis, in.-lb
A = $\Delta s \; t$ = area of lumped element, $in.^2$

t = average thickness of lumped element

Δs = average width of lumped element

m and n = subscripts denoting first and last number of lumped elements, respectively

The coordinates of the centroid are

$$\bar{b} = \frac{\sum_{j=m}^{j=n} E_j \Delta A_j b_j}{\overline{EA}} \tag{7-8}$$

$$\bar{c} = \frac{\sum_{j=m}^{j=n} E_j \Delta A_j c_j}{\overline{EA}} \tag{7-9}$$

where

$$\overline{EA} = \sum_{j=m}^{j=n} E_j \Delta A_j \tag{7-10}$$

The coordinates in the $b'c'$ system can now be expressed in terms of the reference coordinate system, $b\ c$.

$$b' = b - \bar{b} \tag{7-11}$$

$$c' = c - \bar{c} \tag{7-12}$$

Substituting equation (7-3) into equations (7-5), (7-6), and (7-7) and noting that

$$\sum_{j=m}^{j=n} E_j \Delta A_j b'_j = \sum_{j=m}^{j=n} E_j \Delta A_j c'_j = 0$$

yields

$$\dot{F}_o = \frac{N_{a'}}{\overline{EA}} \tag{7-13}$$

$$(\overline{EI})_b \dot{F}_1 + (\overline{EI})_{bc} \dot{F}_2 = M_b' \tag{7-14}$$

$$(\overline{EI})_{bc} \dot{F}_1 + (\overline{EI})_c \dot{F}_2 = M_c' \tag{7-15}$$

where

$$N_a' = N_a - \sum_{j=m}^{j=n} f(T)_j \Delta A_j \tag{7-16}$$

$$M_b' = M_b - N_a \bar{c} - \sum_{j=m}^{j=n} f(T)_j \Delta A_j c_j' \tag{7-17}$$

$$M_c' = M_c + N_a \bar{b} + \sum_{j=m}^{j=n} f(T)_j \Delta A_j b_j' \tag{7-18}$$

$$(\overline{EI})_b = \sum_{j=m}^{j=n} E_j \Delta A_j c_j'^2 \tag{7-19}$$

$$(\overline{EI})_{bc} = \sum_{j=m}^{j=n} E_j \Delta A_j b_j' c_j' \tag{7-20}$$

$$(\overline{EI})_c = \sum_{j=m}^{j=n} E_j \Delta A_j b_j'^2 \tag{7-21}$$

Solving equations (7-14) and (7-15) for $\dot{F}_1$ and $\dot{F}_2$ and then substituting the resulting expressions and equation (7-13) into equation (7-3) gives the following final stress equation:

$$\sigma_j = f(T)_j + \frac{N_a'}{\overline{EA}} E_j$$

$$+ E_j \frac{\left[M_b' (\overline{EI})_c + M_c' (\overline{EI})_{bc}\right] c_j' - \left[M_c' (\overline{EI})_b + M_b' (\overline{EI})_{bc}\right] b_j'}{(\overline{EI})_b (\overline{EI})_c - (\overline{EI})^2_{bc}} \qquad (7\text{-}22)$$

The stress of all fibers on the principal axes is equal to zero when only the moment loads are considered; hence, the following expression can be obtained from equation (7-22) for the angle between the principal axes, b" and c" coordinate axes, and the centroidal axes, b' and c' coordinate axes.

$$\tan \beta = \frac{c_j'}{b_j'} = \frac{M_c'(\overline{EI})_b + M_b'(\overline{EI})_{bc}}{M_b'(\overline{EI})_c + M_c'(\overline{EI})_{bc}} \qquad (7\text{-}23)$$

The above equation is not required to perform a stress analysis with the equations presented herein; however, for some applications, it may be desirable to know the position of the principal axes.

SUMMARY OF EQUATIONS

The equations thus far presented are specifically formulated for the case of complex bending about two axes with axial loading included. For problems of simple bending about two axes with axial loading, bending about one axis with axial loading, and axial loading only, the equations are of simpler form. A summary of all of the equations is presented.

Case 1. Complex bending about two axes and axial loading:

$$\sigma_j = f(T)_j + \frac{N_a'}{\overline{EA}} E_j$$

$$+ E_j \frac{\left[M_b'(\overline{EI})_c + M_c'(\overline{EI})_{bc}\right] c_j' - \left[M_c'(\overline{EI})_b + M_b'(\overline{EI})_{bc}\right] b_j'}{(\overline{EI})_b (\overline{EI})_c - (\overline{EI})^2_{bc}}$$

$$N_a' = N_a - \sum_{j=m}^{j=n} f(T)_j \Delta A_j$$

$$M_b' = M_b - N_a\bar{c} - \sum_{j=m}^{j=n} f(T)_j \Delta A_j c_j'$$

$$M_c' = M_c + N_a\bar{b} + \sum_{j=m}^{j=n} f(T)_j \Delta A_j b_j'$$

$$\overline{EA} = \sum_{j=m}^{j=n} E_j \Delta A_j \qquad (\overline{EI})_b = \sum_{j=m}^{j=n} E_j \Delta A_j c_j'^2$$

$$(\overline{EI})_{bc} = \sum_{j=m}^{j=n} E_j \Delta A_j b_j' c_j' \qquad (\overline{EI})_c = \sum_{j=m}^{j=n} E_j \Delta A_j b_j'^2$$

$$\bar{b} = \frac{\sum_{j=m}^{j=n} E_j \Delta A_j b_j}{\overline{EA}} \qquad \bar{c} = \frac{\sum_{j=m}^{j=n} E_j \Delta A_j c_j}{\overline{EA}}$$

$$\Delta A_j = t_j \Delta s_j \qquad b_j' = b_j - \bar{b} \qquad c_j' = c_j - \bar{c}$$

$$\tan \beta = \frac{M_c'(\overline{EI})_b + M_b'(\overline{EI})_{bc}}{M_b'(\overline{EI})_c + M_c'(\overline{EI})_{bc}}$$

Case 2. Simple bending about two axes and axial loading:

$$\sigma_j = f(T)_j + \frac{N_a'}{\overline{EA}} E_j + \frac{M_b' c_j'}{(\overline{EI})_b} E_j - \frac{M_c' b_j'}{(\overline{EI})_c} E_j$$

$$N_a' = N_a - \sum_{j=m}^{j=n} f(T)_j \Delta A_j$$

$$M_b' = M_b - N_a\bar{c} - \sum_{j=m}^{j=n} f(T)_j \Delta A_j c_j'$$

$$M_c' = M_c + N_a\bar{b} + \sum_{j=m}^{j=n} f(T)_j \Delta A_j b_j'$$

$$\overline{EA} = \sum_{j=m}^{j=n} E_j \Delta A_j \qquad (\overline{EI})_b = \sum_{j=m}^{j=n} E_j \Delta A_j c_j'^2$$

$$(\overline{EI})_c = \sum_{j=m}^{j=n} E_j \Delta A_j b_j'^2 \qquad \bar{b} = \frac{\sum_{j=m}^{j=n} E_j \Delta A_j b_j}{\overline{EA}}$$

$$\bar{c} = \frac{\sum_{j=m}^{j=n} E_j \Delta A_j c_j}{\overline{EA}} \qquad \Delta A_j = t_j \Delta s_j$$

$$b_j' = b_j - \bar{b} \qquad c_j' = c_j - \bar{c}$$

Case 3. Bending about one axis and axial loading:

$$\sigma_j = f(T)_j + \frac{N_a'}{\overline{EA}} E_j + \frac{M_b' c_j'}{(\overline{EI})_b} E_j$$

$$N_a' = N_a - \sum_{j=m}^{j=n} f(T)_j \Delta A_j$$

$$M_b' = M_b - N_a\bar{c} - \sum_{j=m}^{j=n} f(T)_j \Delta A_j c_j'$$

$$\overline{EA} = \sum_{j=m}^{j=n} E_j \Delta A_j \qquad (\overline{EI})_b = \sum_{j=m}^{j=n} E_j \Delta A_j c_j'^2$$

$$\bar{c} = \frac{\sum_{j=m}^{j=n} E_j \Delta A_j c_j}{\overline{EA}} \qquad \Delta A_j = t_j \Delta s_j$$

$$c_j' = c_j - \bar{c}$$

Case 4. Axial loading only:

$$\sigma_j = f(T)_j + \frac{N_a'}{\overline{EA}} E_j \qquad N_a' = N_a - \sum_{j=m}^{j=n} f(T)_j \Delta A_j$$

$$\overline{EA} = \sum_{j=m}^{j=n} E_j \Delta A_j \qquad \Delta A_j = t_j \Delta s_j$$

REFERENCES

7-1 Hubka, R. E.: Effects of Physical Factors and Analytical Procedures on Predicted Temperatures and Thermal Stresses. Lockheed Report 12777, Lockheed-California Company, 1959.

7-2 Boley, B. A., Weiner, J. H.: Theory of Thermal Stresses, John Wiley & Sons, Inc., 1960.

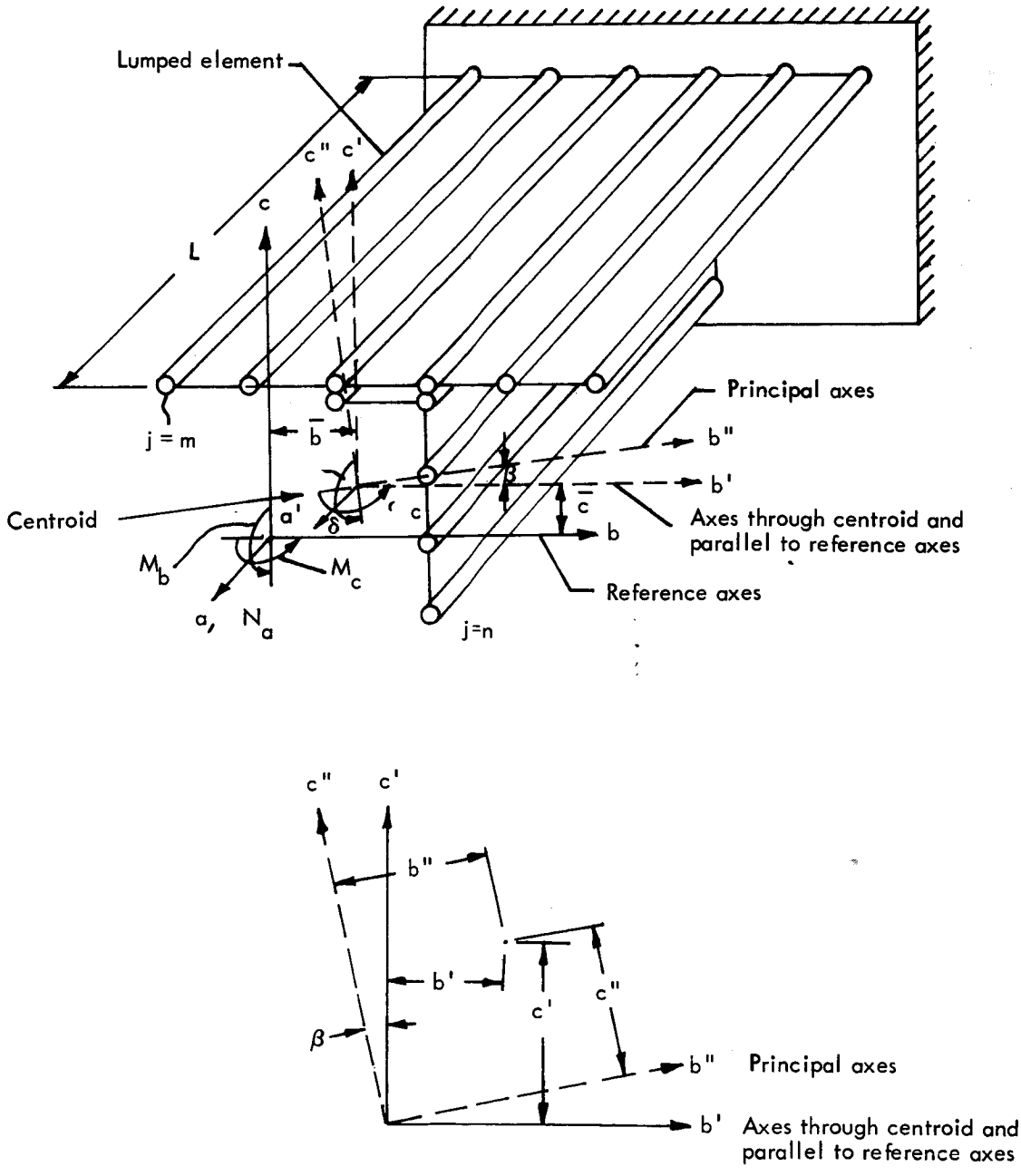

Figure 7-1 Structural Model

Section 8

STRUCTURAL INTERNAL LOADS

by

C. C. Richie, G. W. Davis, W. A. Claus, and D. G. Watson

CONTENTS

TABLES

TABLES (CONT.)

TABLES (CONT.)

TABLES (CONT.)

ILLUSTRATIONS

ILLUSTRATIONS (CONT.)

ILLUSTRATIONS (CONT.)

ILLUSTRATIONS (CONT.)

SYMBOLS

a, b	x and y distances between simply supported edges of panel
a/b	Panel aspect ratio
Area A	Area between $\mathbb{C}_L$ and BL 120 of wing investigation area
Area B	Area between BL 120 and BL 212 of wing investigation area
Area C	Area between BL 212 and BL 350 of wing investigation area
BL	Butt line
f_x, f_y, f_{xy}	Extensional stresses and shear stress in xy coordinate system
g	Gravitational acceleration
N_x, N_y, N_{xy}	Extensional forces and shear force in xy coordinate system per unit length of section
p	Pressure
T	Temperature
T(av)	Average panel temperature
t_e	Equivalent extensional thickness
t_s	Equivalent shear thickness
α	Mean coefficient of thermal expansion
ΔT	Temperature difference
ϵ_x, ϵ_y, ϵ_{xy}	Extensional strains and shear strain in xy coordinate system

Section 8

STRUCTURAL INTERNAL LOADS

The structural analysis model discussed in section 6 was used for determining internal loads for the initial panel weight screening, intermediate weight screening, and final structural weight evaluation. The plane-strain analysis of section 7 was used to obtain chordwise thermal stresses for the various thermal-protection systems.

INITIAL PANEL WEIGHT SCREENING LOADS

Table 8-1 shows the loads used for the initial panel weight screening. The loads resulted from preliminary redundant analyses using an extensional (bending) stiffness of 0.055 inch and a shear stiffness of .070 inch for the wing surface panels. These stiffnesses were based on panel geometry for a typical monocoque waffle wing structure.

INTERMEDIATE WEIGHT SCREENING LOADS

The redundant-model internal loads (based on the data contained in table 6-20)are shown in table 8-2 and were used for the intermediate screening. Equivalent extensional and shear thicknesses of the primary structural panels were based on a nominal panel configuration representative of both monocoque and semimonocoque primary-structure concepts. Poisson's effect was not included in this redundant model. Thermal data ($\alpha\Delta T$) were input for each flight condition. Temperatures were obtained from preliminary isotherm data. The isotherms were constructed from radiation-equilibrium temperature data at five stations and approximately 20 discrete points per wing surface.

A survey of the preliminary transient-temperature data for the three flight conditions (-0.5-g, +2.0-g, and cruise) and the loads of table 8-2 led to the choice of the +2.0-g maneuver condition as the controlling design for the intermediate screening. The thermal strains of table 8-3 rather than the thermal loads of table 8-2 were combined with the airloads and the temperatures of the preliminary transient analysis for each concept.

DETAIL INTERNAL LOADS (USED FOR FURTHER INTERMEDIATE SCREENING AND FINAL STRUCTURAL LOADS)

MONOCOQUE WAFFLE LOADS

Redundant-model internal loads and thermal strains for the monocoque waffle primary-structure concept are shown in tables 8-4 and 8-5. Comparison of these internal loads with the initial loads shown in tables 8-2 and 8-3

shows a marked reduction in the final spanwise and chordwise thermal loads and a considerable increase in the final spanwise airloads.

Comparison of surface panel equivalent extensional and shear thicknesses for the redundant model and the sized waffle primary-structure concept is shown in table 8-6. Best correlation is obtained in the inboard and outboard area lower surface. However, considerable increase in the panel equivalent shear thickness occurs in the highly loaded inboard area.

A comparison of redundant-model and plane-strain thermal stresses is presented in figures 8-1, 8-2, and 8-3 for the -0.5-g maneuver, 2-g maneuver, and cruise conditions, respectively. As indicated, good agreement was obtained, except near the leading edge. In the leading-edge area, the redundant-model stresses are higher than the plane-strain stresses. These higher stresses are probably the result of shear lag effect of the leading-edge member resulting from sweepback and the difference in temperature gradients between the redundant-model and plane-strain analysis. The plane-strain analysis considers the ΔT in the spanwise direction only; whereas, the redundant model considers both spanwise and chordwise gradients.

Detail internal loads encompass airloads and thermal strains for the five candidate thermal-protection arrangements that follow:

Heat-shield arrangment	Insulation arrangement
1. Lower surface heat shields outboard of one-third wing chord	No insulation
2. Lower surface heat shields outboard of one-third wing chord	Insulation
3. Heat shields on entire lower surface	No insulation
4. Heat shields on entire lower surface	Insulation outboard of one-third wing chord
5. No heat shields	No insulation

However, the redundant-model loads were determined only for the first arrangement. For the remaining four concepts, internal loads were evaluated by assuming that:

> The airloads are constant for all monocoque waffle primary-structure concepts

Redundant-model thermal strains are proportional to chordwise thermal strains obtained from a plane-strain analysis; i.e.,

$$(\epsilon_1)\ \text{Arrangement i} = (\epsilon_1)\ \underset{\text{model}}{\text{Redundant}} \left[\frac{\epsilon_x,\ \text{Arrangement i}}{\epsilon_x,\ \text{Arrangment 1}}\right] \underset{\text{analysis}}{\text{plane-strain}}$$

where: 1 = x, y, xy

The first assumption states that airloads are based mainly on equilibrium and vary little with perturbations in panel stiffness. The second assumption is supported by the close correlation (see figs. 8-1, 8-2, and 8-3) of chordwise thermal strains obtained from redundant-model and the plane-strain analyses.

Average thermal strains used for final structural sizing of the five monocoque primary-structure concepts are shown in table 8-7. Average values for the chordwise thermal strains for each arrangement were obtained from the plane-strain analyses and are shown in figures 8-4 through 8-8.

MONOCOQUE HONEYCOMB SANDWICH LOADS

The honeycomb sandwich primary structure was evaluated with lower surface heat shields and insulation outboard of the one-third wing chord, since this arrangement has the lowest weight for the monocoque waffle concept. Using the results of the intermediate screening, extensional and shear stiffnesses were input into the final redundant-model analysis. Thermal data ($\alpha\Delta T$) for each flight condition were based on the temperatures obtained from a detailed transient thermal analysis. Table 8-8 shows the final internal loads, resulting from the redundant-model analysis, used for the final structural sizing.

Comparison of the surface panel equivalent extensional and shear thicknesses for the redundant model and the sized honeycomb sandwich is shown in table 8-8. Good correlation is obtained in all areas with the exception of the lower inboard area where a considerable decrease is noted.

Average thermal strains used for the final structural sizing are shown in table 8-9 for the three flight conditions.

SEMIMONOCOQUE SPANWISE LOADS

Following the intermediate screening, the equivalent extensional and shear stiffnesses of the tubular concept (representative of the spanwise concepts), as shown in section 6, were input into the final redundant-model analysis. Thermal data ($\alpha\Delta T$) for each flight condition were based on the temperatures obtained from a detailed transient thermal analysis at 30 wing locations with insulation at the lower surface outboard area. The internal loads resulting from the spanwise redundant-model analysis are shown in table 8-10.

A comparison between the surface panel stiffnesses input into the final redundant model and those obtained by analysis for the two better concepts using the final redundant model internal loads is shown in table 8-12. Good agreement in extensional and shear stiffness is obtained. A comparison between redundant model and plane-strain thermal stresses for identical stiffnesses and thermal data input is shown in figures 8-11, 8-12, and 8-13.

For all thermal-protection arrangements, except that used in the redundant model, the thermal strains were calculated by using the mathematical relationship stated on page 6-2.

The plane-strain limit chordwise thermal stresses for each of the flight conditions for the two thermal-protection arrangements are shown in figures 8-14 through 8-19. The airloads, which are least susceptible to slight changes in extensional and shear stiffnesses, were considered to be invariant for all thermal-protection arrangements. Based on the thermal-strain ratio and constant airloads, the internal airloads and thermal strains for the various arrangements for each flight condition can be obtained. Tables 8-13 through 8-18 contain the inplane loads (N_x, N_y, and N_{xy}), the chordwise axial thermal strains (ϵ_x and ϵ_y), thermal shear strain (ϵ_{xy}), pressure, and average panel temperature.

Insulation was placed to maintain the 1600°F material limit, to minimize thermal gradients in the spanwise direction, and to provide a match between the gradients through the wing and the fuselage. Figure 8-18 shows the reductions in thermal stresses that result from proper insulation placement.

SEMIMONOCOQUE CHORDWISE LOADS

The results of the initial structural sizing were reviewed, and the convex beaded upper/tubular lower arrangement was selected for input into the chordwise redundant-model analyses. This arrangement was considered representative of the candidates to be carried to the detail sizing analysis. The extensional and shear stiffnesses, panel dimensions, cap areas, and basic description of the model input are presented in section 6.

The temperature data ($\alpha\Delta T$) were input for each flight condition. These data were based on radiation-equilibrium isotherm temperatures, obtained from a detailed gross model thermal analysis performed at 30 wing locations. The ultimate loads resulting from this chordwise redundant-model run are shown in table 8-19 for the three flight conditions. A comparison between the stiffnesses of the structure sized by using the redundant-model loads is shown in table 8-20. However, the stiffnesses resulting from the minimum-weight chordwise structural arrangement were observed to differ from the stiffenesses used for the redundant-model analysis. The primary differences encompassed the shear stiffnesses, the extensional stiffnesses for the upper and lower surface spanwise direction (effecting spar-cap geometry), and the extensional stiffnesses for the lower surface chordwise direction (affecting lower surface panel shape). Therefore, a new redundant analysis was conducted with the actual stiffnesses of the minimum-weight chordwise structural arrangement (provided later in this discussion).

The following combinations of tubular convex-beaded primary-structure and thermal-protection arrangements were assessed:

Primary structure and heat-shield arrangement [a]	Insulation arrangement
Upper: tubular Lower: tubular	No Yes[b]
Upper: convex beaded Lower: tubular	No Yes[b]
Upper: convex beaded Lower: convex beaded	No No
Upper: convex beaded Center lower: convex beaded Inboard and Outboard lower: tubular	No Yes[b]

[a] Tubular upper surface under fuselage for all arrangements.
Convex beaded: no heat shields
Tubular: Heat shields required

[b] Insulation on lower surface outboard.

The plane-strain thermal stresses for all flight conditions for the candidate thermal-protection arrangements are presented in figures 8-19 through 8-39.

Using the same assumption as stated in the semimonocoque spanwise section, invariant airloads and the thermal-strain ratio, the loads and strains for all the flight conditions for each candidate arrangement can be determined. Tables 8-21 through 8-41 contain the inplane loads (N_x, N_y, and N_{xy}) as well as the chordwise axial thermal strains (ϵ_x) and the thermal shear strains (ϵ_{xy}). The pressure and average panel temperature are also listed.

As shown in figure 8-29 and table 8-31, the tubular lower/convex beaded upper surface arrangement with insulation at the lower surface outboard area provides the lowest thermal stresses and strains.

The load results of the new and final chordwise redundant analysis for the three flight conditions, presented in table 8-40, indicate lower airloads in the spanwise direction when compared to the loads of table 8-19. For example, the lower surface spanwise loads for the inboard area B (BL 120 to 212) were reduced from -1122 lb/in. to -965 lb/in., at the +2.0-g flight condition. The chordwise panel airloads remained approximately the same for both surfaces at the three flight conditions. In general, the shear and thermal loads were reduced.

Tables 8-43 through 8-45 contain the final airloads, thermal strains, pressures, and average panel temperatures for the three flight conditions.

A stiffness comparison between the final sized structure and the input into the redundant model, shown in table 8-46, shows good correlation in almost all areas.

STATICALLY DETERMINATE LOADS

Based on the results of the semimonocoque spanwise initial structural sizing, the tubular concept was input into the statically determinate redundant model. The extensional and shear stiffnesses, panel dimensions, cap areas, and basic description of the model input are presented in section 6.

Thermal data ($\alpha\Delta T$) were input for each flight condition. These data were based on the final temperature isotherms. The internal loads resulting from this redundant model run are shown in table 8-48. A comparison between the final-model internal loads for the selected beaded concept is shown in table 8-49.

Good agreement in extensional stiffness is obtained in the center and inboard regions, while a variation of approximately 30 percent is recorded in the outboard region. This same trend is obtained in shear stiffness. The airloads and thermal strains used for the final sizing were the final redundant-model loads. These loads are presented in tables 8-49 through 8-51.

TABLE 8-1

LOADS USED FOR INITIAL PANEL WEIGHT SCREENING

		Wing surface		
		Upper	Lower	
N_X	lb/in.	-84	-1000	Chordwise
N_Y	lb/in.	-300	±325	Spanwise
N_{xy}	lb/in.	-132	-32	Shear[(a)]

[a]Used for monocoque only.

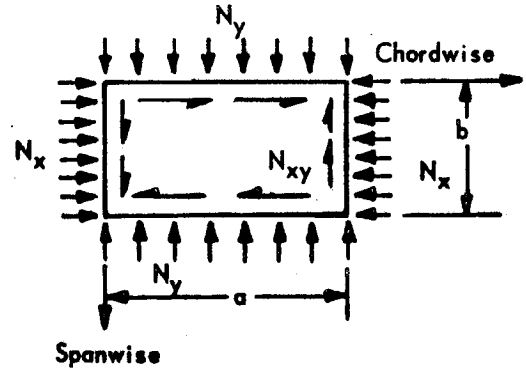

TABLE 8-2

PRELIMINARY REDUNDANT-MODEL LOADS FOR WING INVESTIGATION AREA
(Average Loads Between Sta. 2274 and 2366)

Wing panel location	Load Vector	Ultimate loads, lb/in.[a]					
		-0.5g maneuver		2g maneuver		Cruise condition	
		Upper	Lower	Upper	Lower	Upper	Lower
℄ to BL 120 Area A	N_x	-64 (-1659)	-182 (-737)	-330 (2120)	-555 (-1400)	-158 (-1659)	-251 (-737)
	N_y	168 (-62)	-118 (-29)	-510 (46)	550 (143)	-251 (-62)	268 (-29)
	N_{xy}	-2 (14)	-13 (-36)	-34 (13)	-5 (-35)	-18 (14)	-5 (-36)
BL 120 to BL 212 Area B	N_x	-42 (1635)	-170 (-363)	-270 (1380)	-495 (-900)	-131 (1635)	-222 (-363)
	N_y	116 (-112)	-78 (26)	-375 (-72)	420 (165)	-180 (-112)	-194 (26)
	N_{xy}	-7 (112)	-28 (-39)	-156 (118)	89 (-71)	-66 (112)	41 (-39)
BL 212 to BL 350 Area C	N_x	-26 (1136)	-111 (-1097)	-120 (910)	-210 (-1600)	-69 (1136)	-99 (-1097)
	N_y	44 (-127)	-32 (72)	-173 (-357)	195 (169)	-77 (-127)	87 (72)
	N_{xy}	-5 (80)	-30 (-99)	-106 (-92)	95 (-225)	-48 (80)	42 (-99)

[a]Values within parentheses are thermal loads; values not within parentheses are airloads; negative values indicate compression, positive values indicate tension.

TABLE 8-3

ULTIMATE THERMAL STRAINS AND STRESSES, +2.0-g MANEUVER CONDITION[a]

(Preliminary Redundant-Model Analysis for Intermediate Weight Screening)

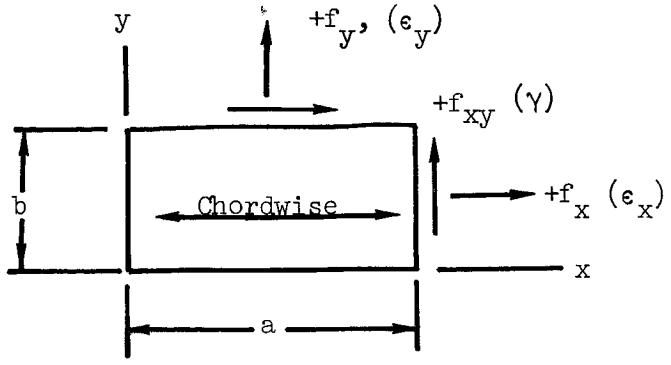

	Stresses, psi		Strains, in./in.	
Surface	Upper	Lower	Upper	Lower
Panels Between BL 120-220	f_x=36.3 x 10^3 f_y=-1.89 f_{xy}=5.9	f_x=-23.7 x 10^3 f_y= 4.1 f_{xy}=-3.55	ϵ_x=1.59 x 10^{-3} ϵ_y=-0.0831 γ = 0.672	ϵ_x=-1.315 x 10^{-3} ϵ_y= 0.228 γ =-0.512
Panels between BL 220-outboard	f_x = 23.9 f_y = -6.75 f_{xy} = -4.6	f_x = -42.1 f_y = 4.45 f_{xy} = -11.25	ϵ_x = 1.05 ϵ_y =-0.412 γ =-0.524	ϵ_x = -2.02 ϵ_y = 2.13 γ = -1.4

[a] Positive values indicate tension; negative values indicate compression.

TABLE 8-4

WAFFLE REDUNDANT MODEL LOADS
(Average Loads Between Sta. 2274– 2366)

Wing panel location	Direction	Ultimate loads, lb/in.[a,b]					
		-0.5-g condition		+2.0-g condition		Cruise condition	
		Upper	Lower	Upper	Lower	Upper	Lower
$\mathcal{L}$ to BL 120 Area A	N_x	-24 (+216)	-152 (+341)	-152 (+468)	-508 (-376)	-75 (-567)	-234 (-540)
	N_y	+140 (+62)	-110 (+150)	-857 (-65)	+804 (+59)	-387 (-81)	+369 (-58)
	N_{xy}	-24 (+4)	+42 (-18)	-56 (0)	+20 (+9)	-20 (-50)	+2 (-34)
BL 120 to BL 220 Area B	N_x	-22 (+220)	-131 (+156)	-144 (+801)	-459 (-641)	-71 (572)	-213 (-376)
	N_y	+62 (+43)	-34 (+123)	-807 (-115)	+768 (+52)	-364 (-137)	+340 (-30)
	N_{xy}	-12 (+108)	-48 (+42)	-414 (+154)	+278 (-23)	-176 (+106)	+143 (-12)
BL 220 to BL 350 Area C	N_x	-68 (-650)	-145 (-255)	-25 (+513)	-226 (-568)	-34 (710)	-134 (-294)
	N_y	+107 (-231)	-19 (+135)	-396 (-198)	+384 (+128)	-160 (-108)	+166 (+90)
	N_{xy}	-16 (+431)	-31 (+156)	-349 (-67)	+318 (-15)	-150 (+139)	+132 (-12)

[a] Design ultimate loads are { air = 1.5 x 1.3 x limit; thermal = 1.3 x limit } lb/in.

[b] Values within parenthesis are thermal loads; values not within parenthese are airloads; negative values indicate compression; positive values indicate tension.

TABLE 8-6

COMPARISON OF SURFACE PANEL EQUIVALENT EXTENSIONAL AND SHEAR THICKNESSES FOR THE REDUNDANT MODEL AND SIZED MONOCOQUE PRIMARY-STRUCTURE CONCEPT

		Center		Inboard		Outboard	
		Upper	Lower	Upper	Lower	Upper	Lower
Final redundant model	t_e [b]	0.020	0.025	0.020	0.025	0.020	0.030
	t_s [c]	0.040	0.046	0.040	0.046	0.040	0.053
Monocoque primary structure concept, (a/b = 2.0, b = 20 in.)	t_e [b]	0.0246	0.0261	0.0245	0.0316	0.0240	0.0301
	t_s [c]	0.0557	0.0451	0.0612	0.0603	0.0544	0.0530

[a] Partial heat shield at outboard area lower surface, a = 40 in., b = 20 in.

[b] t_e = Equivalent extensional thickness

[c] t_s = Equivalent shear thickness

TABLE 8-8

FINAL REDUNDANT-MODEL LOADS FOR MONOCOQUE HONEYCOMB-CORE SANDWICH PANELS
(Average Loads Between Sta. 2274 and 2366)

Wing panel location	Direction	Design ultimate loads,[a,b] lb/in.					
		-0.5g maneuver		2g maneuver		Cruise condition	
		Upper	Lower	Upper	Lower	Upper	Lower
$\mathcal{C}_L$ to BL 120 Area A	N_x	6 (161)	-186 (470)	-400 (674)	-297 (-771)	-187 (-1174)	-142 (-658)
	N_y	211 (47)	-178 (293)	-651 (-85)	587 (74)	-307 (-205)	285 (-230)
	N_{xy}	15 (20)	34 (41)	26 (-16)	3 (-45)	7 (65)	-24 (64)
BL 120 to BL 212 Area B	N_x	11 (51)	-177 (461)	-331 (899)	-387 (-959)	-152 (894)	-185 (-397)
	N_y	88 (57)	-78 (261)	-589 (-96)	559 (100)	-266 (-129)	258 (-162)
	N_{xy}	12 (63)	-50 (186)	-302 (109)	-193 (181)	-130 (47)	84 (-92)
BL 212 to BL 350 Area C	N_x	-49 (-1080)	-96 (-16)	-101 (452)	-64 (-235)	-42 (1376)	-40 (558)
	N_y	33 (-214)	-31 (141)	-242 (-156)	242 (174)	-111 (40)	109 (142)
	N_{xy}	-2 (-614)	-39 (141)	-192 (-127)	-148 (171)	86 (346)	73 (286)

[a] Design Ultimate Loads are: $\begin{cases} \text{air} & = 1.5 \times 1.3 \times \text{limit} \\ \text{thermal} & = 1.3 \times \text{limit} \end{cases}$ lb/in.

[b] Values within paretheses are thermal loads; values not within parentheses are airloads; negative values indicate compression; positive values indicate tension.

TABLE 8-9

COMPARISON OF EXTENSIONAL AND SHEAR THICKNESSES FOR THE HONEYCOMB SANDWICH REDUNDANT MODEL AND FINAL HONEYCOMB SANDWICH PANEL EVALUATION

		Center		Inboard		Outboard	
		Upper	Lower	Upper	Lower	Upper	Lower
[a] Final redundant model	t_e [b]	0.029	0.033	0.029	0.042	0.029	0.027
	t_s [c]	0.029	0.033	0.029	0.042	0.029	0.027
[a] Final panel width and aspect ratio	t_e [b]	0.0289	0.030	0.0291	0.0336	0.0359	0.0272
Evaluation	t_s [c]	0.0289	0.030	0.0291	0.0336	0.0359	0.0272

[a] Partial heat shield at outboard area lower surface, a = 80 in., b = 40 in.

[b] t_e = Equivalent extensional thickness.

[c] t_s = Equivalent shear thickness.

TABLE 8-10

HONEYCOMB SANDWICH REDUNDANT-MODEL THERMAL STRAINS[a]
(Average Strains Between Sta. 2274 and 2366)

Wing location	Design ultimate thermal strains, in./in.					
	-0.5 g Maneuver		2 g Maneuver		Cruise Condition	
	Upper	Lower	Upper	Lower	Upper	Lower
℄ - BL 120	ϵ_x 216x10^{-6}	554x10^{-6}	1029x10^{-6}	-1150x10^{-6}	-1637x10^{-6}	-854x10^{-6}
	ϵ_y -2	220	-423	442	217	44
	γ 77	155	-61	-170	249	241
BL 120 - 212	ϵ_x 16	448	1330	-1176	1337	-414
	ϵ_y 60	142	-524	461	569	-51
	γ 235	567	406	559	175	-284
BL 212 - 350	ϵ_x -1518	-99	746	-487	2039	874
	ϵ_y 164	247	-436	414	-557	-43
	γ -2386	621	-494	754	1345	1260

[a]Negative values indicate compression, positive values indicate tension.

TABLE 8-11

FINAL REDUNDANT-MODEL LOADS FOR SEMIMONOCOQUE SPANWISE-STIFFENED PANELS
(Average Loads Between Sta. 2274 and 2366)

Wing panel location	Load Vector	Ultimate loads, lb/in.[a]					
		-0.5-g condition		+2.0-g condition		Cruise condition	
		Upper	Lower	Upper	Lower	Upper	Lower
$\mathcal{L}$ to BL 120 Area A	N_x	-72 (319)	-117 (46)	-269 (174)	-385 (39)	-129 (-344)	-179 (-364)
	N_y	210 (-34)	-177 (76)	-563 (-23)	644 (49)	-269 (-65)	309 (-4)
	N_{xy}	-4 (2)	23 (3)	-15 (-3)	19 (19)	-7 (-10)	3 (-13)
BL 120 to BL 212 Area B	N_x	-74 (83)	-116 (-24)	-269 (127)	-385 (10)	-128 (-50)	-181 (-192)
	N_y	98 (-40)	-72 (63)	-496 (-32)	576 (51)	-231 (-64)	265 (24)
	N_{xy}	-8 (-5)	-38 (21)	-176 (-11)	139 (14)	-77 (9)	64 (4)
BL 212 – Outboard Area C	N_x	-55 (-79)	-84 (-73)	-135 (-27)	-210 (-40)	-65 (210)	-102 (122)
	N_y	78 (-85)	-33 (59)	-197 (-67)	215 (106)	-92 (-57)	72 (29)
	N_{xy}	-7 (-107)	-35 (56)	-138 (-92)	112 (49)	-63 (67)	48 (62)

[a] Average load between stations 2274 and 2366; values within parentheses = thermal loads; value not within parentheses = air loads; negative values indicate compression; positive values indicate tension.

[b] Ultimate loads are: $\left\{ \begin{array}{l} \text{Air} = 1.5 \times 1.3 \times \text{Limit} \\ \text{Thermal} = 1.3 \times \text{Limit} \end{array} \right\}$ lb/in.

TABLE 8-12

COMPARISON OF SURFACE PANEL EQUIVALENT EXTENSIONAL AND SHEAR THICKNESSES FOR THE REDUNDANT MODEL AND SIZED SEMIMONOCOQUE SPANWISE PRIMARY STRUCTURE CONCEPT

		Center		Inboard		Outboard		Spacing	
		Upper	Lower	Upper	Lower	Upper	Lower	Rib	Spar
Final redundant model (input)	(a) t_{e_x}	0.007	0.007	0.007	0.007	0.007	0.007	46	92
	(a) t_{e_y}	0.028	0.026	0.028	0.030	0.028	0.028		
	(b) t_s	0.016	0.015	0.016	0.018	0.016	0.016		
Beaded	(a) t_{e_x}	0.0045	0.0050	0.0051	0.0057	0.0054	0.0051	(c) 50	90
	(a) t_{e_y}	0.026	0.020	0.026	0.022	0.022	0.020	40	
	(b) t_s	0.0152	0.0114	0.0152	0.0129	0.0131	0.0114	40	
Tubular	(a) t_{e_x}	0.0045	0.0050	0.0051	0.0057	0.0054	0.0051	(c) 50	90
	(a) t_{e_y}	0.029	0.026	0.029	0.028	0.026	0.025	40	
	(b) t_s	0.0165	0.0155	0.0169	0.0170	0.0155	0.0158	40	

[a] t_e = Equivalent extensional thickness, x denotes spanwise and y denotes chordwise

[b] t_s = Equivalent surface panel shear thickness

[c] Denotes center, inboard and outboard area rib spacing

TABLE 8-13

LOADS FOR SEMIMONOCOQUE SPANWISE - STIFFENED PANEL FOR -0.5-g CONDITION: EXPOSED SURFACES SHIELDED[a]

Item	Units	A		B		C	
		Upper surface	Lower surface	Upper surface	Lower surface	Upper surface	Lower surface
N_x	lb/in.	-72	-117	-74	-116	-55	-84
N_y	lb/in.	210	-177	98	-72	78	-33
N_{xy}	lb/in.	-4	23	-8	-38	-7	-35
ϵ_x	in./in.	$1131(10)^{-6}$	$-752(10)^{-6}$	$-465(10)^{-6}$	$-1099(10)^{-6}$	$-1956(10)^{-6}$	$-1836(10)^{-6}$
ϵ_y	in./in.	$-31.9(10)^{-6}$	$-329.4(1)^{-6}$	$59.4(10)^{-6}$	$765.2(10)^{-6}$	$-557.6(10)^{-6}$	$383.7(10)^{-6}$
ϵ_{xy}	in./in.	24×10^{-6}	555×10^{-6}	58×10^{-6}	355×10^{-6}	5312×10^{-6}	2765×10^{-6}
p	psi	± 0.975	-0.975	± 0.975	-0.975	± 0.975	-0.975
T (av)	$^{\circ}F$	1220	1260	1300	1330	1430	1430

[a]All loads and strains are design ultimate.

TABLE 8-14

LOADS FOR SEMIMONOCOQUE SPANWISE – STIFFENED PANEL FOR +2.0-g CONDITION: EXPOSED SURFACES SHIELDED[a]

Item	Units	A		B		C	
		Upper surface	Lower surface	Upper surface	Lower surface	Upper surface	Lower surface
N_x	lb/in.	-269	-385	-269	-385	-135	-210
N_y	lb/in.	-563	644	-496	576	-197	215
N_{xy}	lb/in.	-15	19	176	139	138	112
ϵ_x	in./in.	1193×10^{-6}	870×10^{-6}	572×10^{-6}	221×10^{-6}	-1323×10^{-6}	-1898×10^{-6}
ϵ_y	in./in.	-42×10^{-6}	278×10^{-6}	-38×10^{-6}	289×10^{-6}	-850×10^{-6}	1284×10^{-6}
ϵ_{xy}	in/in.	24×10^{-6}	555×10^{-6}	58×10^{-6}	355×10^{-6}	5312×10^{-6}	2765×10^{-6}
p	psi	±0.975	-1.89	±0.975	-2.85	±0.975	-1.91
$T_{(av)}$	°F	1220	1350	1300	1420	1430	1550

NOTE: All loads and strains are ultimate.

TABLE 8-15

LOADS FOR SEMIMONOCOQUE SPANWISE – STIFFENED PANEL FOR CRUISE CONDITION: EXPOSED SURFACES SHIELDED[a]

Item	Units	A		B		C	
		Upper surface	Lower surface	Upper surface	Lower surface	Upper surface	Lower surface
N_x	lb/in.	-129	-179	-128	-181	-65	-102
N_y	lb/in.	-269	309	-231	265	-92	72
N_{xy}	lb/in.	-7	3	-77	64	-63	48
ϵ_x	in./in.	$-1048(10)^{-6}$	$-919(10)^{-6}$	$924(10)^{-6}$	$-225(10)^{-6}$	$513(10)^{-6}$	$919(10)^{-6}$
ϵ_y	in./in.	$-52.3(10)^{-6}$	$-2.7(10)^{-6}$	$315(10)^{-6}$	$7.5(10)^{-6}$	$-36.8(10)^{-6}$	$56.1(10)^{-6}$
ϵ_{xy}	in./in.	24×10^{-6}	555×10^{-6}	58×10^{-6}	355×10^{-6}	5312×10^{-6}	2765×10^{-6}
p	psi	± 0.975	-1.423	± 0.975	-1.89	± 0.975	-1.43
$T_{(av)}$	^{o}F	1320	1330	1130	1260	1170	1310

[a]All loads and strains are ultimate.

TABLE 8-16

LOADS FOR SEMIMONOCOQUE SPANWISE – STIFFENED PANEL FOR -0.5-g CONDITION: EXPOSED SURFACES SHIELDED, INSULATION OUTBOARD[a]

Item	Units	A		B		C	
		Upper surface	Lower surface	Upper surface	Lower surface	Upper surface	Lower surface
N_x	lb/in.	-72	-117	-74	-116	-55	-84
N_y	lb/in.	210	-177	98	-72	78	-33
N_{xy}	lb/in.	-4	23	-8	-38	-7	-35
ϵ_x	in./in.	$1789(10)^{-6}$	$258(10)^{-6}$	$467(10)^{-6}$	$-135(10)^{-6}$	$-456(10)^{-6}$	$-421(10)^{-6}$
ϵ_y	in./in.	$-50.4(10)^{-6}$	$113(10)^{-6}$	$-59.7(10)^{-6}$	$94(10)^{-6}$	$-130(10)^{-6}$	$88(10)^{-6}$
ϵ_{xy}	in./in.	20×10^{-6}	140×10^{-6}	73×10^{-6}	90×10^{-6}	625×10^{-6}	336×10^{-6}
p	psi	± 0.975	-0.975	± 0.975	-0.975	± 0.975	-0.975
$T_{(av)}$	^{o}F	1220	1260	1300	1330	1330	1350

[a]All loads and strains are ultimate.

TABLE 8-17

LOADS FOR SEMIMONOCOQUE SPANWISE – STIFFENED PANEL FOR +2.0-g CONDITION: EXPOSED SURFACES SHIELDED, INSULATION OUTBOARD[a]

Item	Units	A		B		C	
		Upper surface	Lower surface	Upper surface	Lower surface	Upper surface	Lower surface
N_x	lb/in.	-269	-385	-269	-385	-135	-210
N_y	lb/in.	-563	644	-496	576	-197	215
N_{xy}	lb/in.	-15	19	-176	139	-138	112
ϵ_x	in./in.	976×10^{-6}	219×10^{-6}	716×10^{-6}	56×10^{-6}	-1558×10^{-6}	-231×10^{-6}
ϵ_y	in./in.	-34.4×20^{-6}	70.1×10^{-6}	-47.6×10^{-6}	73.2×10^{-6}	-100×10^{-6}	156×10^{-6}
ϵ_{xy}	in./in.	20×10^{-6}	140×10^{-6}	73×10^{-6}	90×10^{-6}	625×10^{-6}	336×10^{-6}
p	psi	+0.975	-1.89	±0.975	-2.85	±0.975	-1.91
$T_{(av)}$	°F	1220	1350	1300	1420	1330	1350

[a]All loads and strains are design ultimate.

TABLE 8-18

LOADS FOR SEMIMONOCOQUE SPANWISE – STIFFENED PANEL FOR CRUISE CONDITION: EXPOSED SURFACES SHIELDED, INSULATION OUTBOARD[a]

Item	Units	A		B		C	
		Upper summary	Lower summary	Upper summary	Lower summary	Upper summary	Lower summary
N_x	lb/in.	-129	-179	-128	-181	-65	-102
N_y	lb/in.	-269	309	-231	265	-92	72
N_{xy}	lb/in.	-7	3	-77	64	-63	48
ϵ_x	in./in.	$-1929(10)^{-6}$	$-2040(10)^{-6}$	$-280(10)^{-6}$	$-1075(10)^{-6}$	$1212(10)^{-6}$	$704(10)^{-6}$
ϵ_y	in./in.	$-96.3(10)^{-6}$	$-5.9(10)^{-6}$	$-95.5(10)^{-6}$	$35.8(10)^{-6}$	$-87(10)^{-6}$	$43(10)-6$
ϵ_{xy}	in./in.	20×10^{-6}	140×10^{-6}	73×10^{-6}	90×10^{-6}	625×10^{-6}	336×10^{-6}
p	psi	± 0.975	-1.423	± 0.975	-1.89	± 0.975	-1.43
$T_{(av)}$	^{o}F	1320	1330	1130	1260	1130	1250

[a]All loads and strains are design ultimate.

TABLE 8-19

INTERMEDIATE CHORDWISE DESIGN ULTIMATE LOADS
(Average Loads Between Sta. 2274 and 2366)

Location \ Condition	Direction	-5.0-g condition		+2.0-g condition		Cruise condition	
		Upper	Lower	Upper	Lower	Upper	Lower
$\mathcal{L}$ – BL 120	N_x	-32(581)	-166(262)	-243(360)	-624(-650)	-113(-1306)	-301(-1242)
	N_y	149(115(	-127(164)	-114(64)	966(111)	-504(-192)	434(-213)
	N_{xy}	-8(30)	8(44)	-80(70)	0(-360)	-35(23)	-14(-26)
BL 120-212	N_x	-44(-150)	-166(160)	-362(482)	-625(-590)	-155(1061)	-295(-161)
	N_y	42(75)	-17(152)	-1122(44)	971(110)	-497(-134)	422(-131)
	N_{xy}	-16(121)	-52(82)	-758(191)	580(-54)	-315(153)	249(-92)
BL 212 – Outboard	N_x	-58(-568)	-112(-186)	-187(-195)	-200(-236)	-94(1016)	-158(114)
	N_y	7(-114)	15(80)	-537(-137)	524(62)	-289(-48)	223(28)
	N_{xy}	-26(-292)	11(-78)	-457(-166)	557(63)	-189(234)	228(99)

TABLE 8-20

INTERMEDIATE REDUNDANT MODEL COMPARISON SEMIMONOCOQUE CHORDWISE – STIFFENED PRIMARY-STRUCTURE CONCEPT

		Center		Inboard		Outboard		Spacing	
		Upper	Lower	Upper	Lower	Upper	Lower	Rib	Spar
Final redundant model (input)	(a) t_e x	0.029	0.044	0.029	0.044	0.029	0.044	92	46
	(a) t_e y	0.007	0.007	0.007	0.007	0.007	0.007		
	(b) t_s	0.022	0.028	0.022	0.028	0.022	0.028		
Minimum weight structural arrangement	(a) t_e x	0.025	0.026	0.030	0.033	0.031	0.028	75	24
	(a) t_e y	0.0139	0.0103	0.0168	0.0089	0.0131	0.0085		
	(b) t_s	0.0155	0.0153	0.0248	0.0202	0.0231	0.0174		

[a] t_e = Equivalent extensional thickness, x denotes spanwise direction and y denotes chordwise direction

[b] t_s = Equivalent surface panel shear thickness.

TABLE 8-21

LOADS FOR SEMIMONOCOQUE CHORDWISE TUBULAR PANELS BOTH SURFACES; EXPOSED SURFACES SHIELDED; NO INSULATION; -0.5-g CONDITION[a]

Item	Units	A		B		C	
		Upper surface	Lower surface	Upper surface	Lower surface	Upper surface	Lower surface
N_x	lb/in.	- 32	- 166	- 44	- 166	- 58	- 112
N_y	lb/in.	149	- 127	42	- 17	7	15
N_{xy}	lb/in.	- 8	8	- 16	- 52	- 26	11
ϵ_x	in./in.	$1363(10)^{-6}$	$936(10)^{-6}$	$763(10)^{-6}$	$431(10)^{-6}$	$-470(10)^{-6}$	$-1116(10)^{-6}$
ϵ_{xy}	in./in.	$185(10)^{-6}$	$287(10)^{-6}$	$741(10)^{-6}$	$297(10)^{-6}$	$-422(10)^{-6}$	$-634(10)^{-6}$
p	$lb/in.^2$	±0.975	-0.975	±0.975	-0.975	±0.975	-0.975
$T_{(av)}$	^oF	1210	1259	1254	1302	1442	1450

[a]All loads and strains are ultimate

TABLE 8-22

LOADS FOR SEMIMONOCOQUE CHORDWISE TUBULAR PANELS BOTH SURFACES; EXPOSED SURFACES SHIELDED, NO INSULATION; +2.0-g CONDITION[a]

Item	Units	A		B		C	
		Upper surface	Lower surface	Upper surface	Lower surface	Upper surface	Lower surface
N_x	lb/in.	- 243	- 624	- 362	- 625	- 187	- 200
N_y	lb/in.	-1143	966	-1122	971	- 537	524
N_{xy}	lb/in.	- 80	0	- 758	580	- 457	557
ϵ_x	in./in.	$1616(10)^{-6}$	$564(10)^{-6}$	$1084(10)^{-6}$	$- 17(10)^{-6}$	$- 584(10)^{-6}$	$-1811(10)^{-6}$
ϵ_{xy}	in./in.	$599(10)^{-6}$	$- 521(10)^{-6}$	$870(10)^{-6}$	$- 10(10)^{-6}$	$- 533(10)^{-6}$	$895(10)^{-6}$
p	$lb/in.^2$	±0.975	-1.89	±0.975	-2.85	±0.975	-1.91
$T_{(av)}$	^oF	1254	1363	1297	1398	1466	1538

[a]All loads and strains are ultimate

TABLE 8-23

LOADS FOR SEMIMONOCOQUE CHORDWISE FOR TUBULAR PANELS BOTH SURFACES; EXPOSED SURFACES SHIELDED, NO INSULATION; CRUISE CONDITION[a]

Item	Units	A		B		C	
		Upper surface	Lower surface	Upper surface	Lower surface	Upper surface	Lower surface
N_x	lb/in.	- 113	- 301	- 155	- 295	- 94	- 158
N_y	lb/in.	- 504	434	- 497	422	- 289	223
N_{xy}	lb/in.	- 35	- 14	- 315	249	- 189	228
ϵ_x	in./in.	$-806(10)^{-6}$	$-746(10)^{-6}$	$1154(10)^{-6}$	$19(10)^{-6}$	$861(10)^{-6}$	$-539(10)^{-6}$
ϵ_{xy}	in./in.	$48(10)^{-6}$	$-51(10)^{-6}$	$750(10)^{-6}$	$-13(10)^{-6}$	$331(10)^{-6}$	$-488(10)^{-6}$
p	lb/in.^{2}	±0.975	-1.423	±0.975	-1.89	±0.975	-1.43
$T_{(av)}$	^oF	1345	1343	1093	1236	1183	1307

[a] All loads and strains are ultimate

TABLE 8-24

LOADS FOR SEMIMONOCOQUE CHORDWISE TUBULAR PANELS BOTH SURFACES; EXPOSED SURFACES SHIELDED, PARTIAL INSULATION LOWER OUTBOARD; -0.5-g CONDITION[a]

Item	Units	A		B		C	
		Upper surface	Lower surface	Upper surface	Lower surface	Upper surface	Lower surface
N_x	lb/in.	- 32	- 166	- 44	- 166	- 58	- 112
N_y	lb/in.	149	- 127	42	- 17	7	15
N_{xy}	lb/in.	- 8	8	- 16	- 52	- 26	11
ϵ_x	in./in.	$1008(10)^{-6}$	$442(10)^{-6}$	$406(10)^{-6}$	$45(10)^{-6}$	$-244(10)^{-6}$	$143(10)^{-6}$
ϵ_{xy}	in./in.	$137(10)^{-6}$	$135(10)^{-6}$	$399(10)^{-6}$	$31(10)^{-6}$	$-221(10)^{-6}$	$-81(10)^{-6}$
p	$lb/in.^2$	±0.975	-0.975	±0.975	-0.975	±0.975	-0.975
$T_{(av)}$	^oF	1210	1259	1254	1302	1353	1288

[a] All loads and strains are ultimate

TABLE 8-25

LOADS FOR SEMIMONOCOQUE CHORDWISE TUBULAR PANELS BOTH SURFACES; EXPOSED SURFACES SHIELDED; PARTIAL INSULATION LOWER OUTBOARD; +2.0-g CONDITION[a]

Item	Units[a]	A		B		C	
		Upper Surface	Lower Surface	Upper Surface	Lower Surface	Upper Surface	Lower Surface
N_x	lb/in.	- 243	- 624	- 362	- 625	- 187	- 200
N_y	lb/in.	-1143	966	-1122	971	- 537	524
N_{xy}	lb/in.	- 80	0	- 758	580	- 457	557
ϵ_x	in./in.	$1173(10)^{-6}$	$- 142(10)^{-6}$	$827(10)^{-6}$	$- 341(10)^{-6}$	$- 57(10)^{-6}$	$- 129(10)^{-6}$
ϵ_{xy}	in./in.	$213(10)^{-6}$	$- 121(10)^{-6}$	$663(10)^{-6}$	$-.191(10)^{-6}$	$15(10)^{-6}$	$64(10)^{-6}$
p	$lb/in.^2$	±0.975	-1.89	±0.975	-2.85	±0.975	-1.91
$T_{(av)}$	^oF	1233	1350	1254	1398	1341	1353

[a] All loads and strains are ultimate.

TABLE 8-26

LOADS FOR SEMIMONOCOQUE CHORDWISE TUBULAR PANELS BOTH SURFACES; EXPOSED SURFACES SHIELDED. PARTIAL INSULATION LOWER OUTBOARD; CRUISE CONDITION[a]

Item	Units[a]	A		B		C	
		Upper Surface	Lower Surface	Upper Surface	Lower Surface	Upper Surface	Lower Surface
N_x	lb/in.	- 113	- 301	- 155	- 295	- 94	- 158
N_y	lb/in.	- 504	434	- 497	422	- 289	223
N_{xy}	lb/in.	- 35	- 14	- 315	249	- 189	228
ϵ_x	in./in.	$-1824(10)^{-6}$	$-2020(10)^{-6}$	$468(10)^{-6}$	$-744(10)^{-6}$	$1923(10)^{-6}$	$1206(10)^{-6}$
ϵ_{xy}	in./in.	$109(10)^{-6}$	$-138(10)^{-6}$	$304(10)^{-6}$	$-493(10)^{-6}$	$740(10)^{06}$	$760(10)^{-6}$
p	lb/in.^{2}	±0.975	-1.423	±0.975	-1.89	±0.975	-1.43
$T_{(av)}$	^oF	1345	1343	1093	1236	984	1065

[a]All loads and strains are ultimate.

TABLE 8-27

LOADS FOR SEMIMONOCOQUE CHORDWISE CONVEX BEADED UPPER, TUBULAR LOWER; LOWER EXPOSED SURFACE SHIELDED; -0.5-g CONDITION[a]

Item	Units	A		B		C	
		Upper surface	Lower surface	Upper surface	Lower surface	Upper surface	Lower surface
N_x	lb/in.	- 32	- 166	- 44	- 166	- 58	- 112
N_y	lb/in.	149	- 127	42	- 17	7	15
N_{xy}	lb/in.	- 8	8	- 16	- 52	- 26	11
ϵ_x	in./in.	$1387(10)^{-6}$	$1185(10)^{-6}$	$309(10)^{-6}$	$712(10)^{-6}$	$-846(10)^{-6}$	$-967(10)^{-6}$
ϵ_{xy}	in./in.	$188(10)^{-6}$	$1114(10)^{-6}$	$282(10)^{-6}$	$490(10)^{-6}$	$-752(10)^{-6}$	$549(10)^{-6}$
p	lb/in.^{2}	±0.975	-0.975	±0.975	-0.975	±0.975	-0.975
$T_{(av)}$	$^\circ$F	1210	1258	1303	1294	1539	1431

[a] All loads and strains are ultimate

TABLE 8-28

LOADS FOR SEMIMONOCOQUE CHORDWISE – CONVEX BEADED UPPER, TUBULAR LOWER; LOWER EXPOSED SURFACE SHIELDED; +2.0-g CONDITION[a]

Item	Units	A		B		C	
		Upper surface	Lower surface	Upper surface	Lower surface	Upper surface	Lower surface
N_x	lb/in.	- 243	- 624	- 362	- 625	- 187	- 200
N_y	lb/in.	-1143	966	-1122	971	- 537	524
N_{xy}	lb/in.	- 80	0	- 758	580	- 457	557
ϵ_x	in./in.	$1490(10)^{-6}$	$528(10)^{-6}$	$1257(10)^{-6}$	$- 29(10)^{-6}$	$- 275(10)^{-6}$	$-1929(10)^{-6}$
ϵ_{xy}	in./in.	$55(10)^{-6}$	$- 460(10)^{-6}$	$1008(10)^{-6}$	$- 16(10)^{-6}$	$- 242(10)^{-6}$	$- 953(10)^{-6}$
p	$lb/in.^2$	±0.975	-1.89	±0.975	-2.85	±0.975	-1.91
$T_{(av)}$	^oF	1232	1358	1277	1392	1406	1539

[a] All loads and strains are ultimate

TABLE 8-29

LOADS FOR SEMIMONOCOQUE CHORDWISE – CONVEX BEADED UPPER, TUBULAR LOWER; LOWER EXPOSED SURFACE SHIELDED; CRUISE CONDITION[a]

Item	Units	A		B		C	
		Upper surface	Lower surface	Upper surface	Lower surface	Upper surface	Lower surface
N_x	lb/in.	- 113	- 301	- 155	- 295	- 94	- 158
N_y	lb/in.	- 504	434	- 497	422	- 289	223
N_{xy}	lb/in.	- 35	- 14	- 315	249	- 189	228
ϵ_x	in./in.	$-1266(10)^{-6}$	$-120(10)^{-6}$	$1457(10)^{-6}$	$-104(10)^{-6}$	$1790(10)^{-6}$	$-428(10)^{-6}$
ϵ_{xy}	in./in.	$75(10)^{-6}$	$-83(10)^{-6}$	$947(10)^{-6}$	$-69(10)^{-6}$	$688(10)^{-6}$	$-270(10)^{-6}$
p	$lb/in.^2$	±0.975	-1.423	±0.975	-1.89	±0.975	-1.43
$T_{(av)}$	^oF	1345	1343	994	1196	1062	1255

[a] All loads and strains are ultimate

TABLE 8-30

LOADS FOR SEMIMONOCOQUE CHORDWISE — CONVEX BEADED UPPER, TUBULAR LOWER; LOWER EXPOSED SURFACE SHIELDED, PARTIAL INSULATION LOWER OUTBOARD, -0.5-g CONDITION[a]

Item	Units	A		B		C	
		Upper surface	Lower surface	Upper surface	Lower surface	Upper surface	Lower surface
N_x	lb/in.	- 32	- 166	- 44	- 166	- 58	- 112
N_y	lb/in.	149	- 127	42	- 17	7	15
N_{xy}	lb/in.	- 8	8	- 16	- 52	- 26	11
ϵ_x	in./in.	$1110(10)^{-6}$	$740(10)^{-6}$	$342(10)^{-6}$	$480(10)^{-6}$	$-719(10)^{-6}$	$-560(10)^{-6}$
ϵ_{xy}	in./in.	$151(10)^{-6}$	$227(10)^{-6}$	$302(10)^{-6}$	$331(10)^{-6}$	$-690(10)^{-6}$	$-318(10)^{-6}$
p	$lb/in.^2$	±0.975	-0.975	±0.975	-0.975	±0.975	-0.975
$T_{(av)}$	^oF	1210	1258	1303	1294	1505	1383

[a] All loads and strains are ultimate

TABLE 8-31

LOADS FOR SEMIMONOCOQUE CHORDWISE FOR CONVEX BEADED UPPER, TUBULAR LOWER; LOWER EXPOSED SURFACE SHIELDED, PARTIAL INSULATION LOWER OUTBOARD; +2.0-g CONDITION[a]

Item	Units[a]	A		B		C	
		Upper surface	Lower surface	Upper surface	Lower surface	Upper surface	Lower surface
N_x	lb/in.	- 243	- 624	- 362	- 625	- 187	- 200
N_y	lb/in.	-1143	966	-1122	971	- 537	524
N_{xy}	lb/in.	- 80	0	- 758	580	- 457	557
ϵ_x	in./in.	$952(10)^{-6}$	$- 98(10)^{-6}$	$1161(10)^{-6}$	$- 390(10)^{-6}$	$- 201(10)^{-6}$	$- 520(10)^{-6}$
ϵ_{xy}	in./in.	$353(10)^{-6}$	$- 78(10)^{-6}$	$931(10)^{-6}$	$- 218(10)^{-6}$	$- 189(10)^{-6}$	$257(10)^{-6}$
p	$lb/in.^2$	±0.975	-1.89	±0.975	-2.85	±0.975	-1.91
$T_{(av)}$	$^{\circ}F$	1232	1358	1277	1392	1273	1382

[a] All loads and strains are ultimate.

TABLE 8-32

LOADS FOR SEMIMONOCOQUE CHORDWISE CONVEX BEADED UPPER, TUBULAR LOWER; LOWER EXPOSED SURFACE SHIELDED, PARTIAL INSULATION LOWER OUTBOARD; CRUISE CONDITION[a]

Item	Units	A		B		C	
		Upper surface	Lower surface	Upper surface	Lower surface	Upper surface	Lower surface
N_x	lb/in.	- 113	- 301	- 155	- 295	- 94	- 158
N_y	lb/in.	- 504	434	- 497	422	- 289	223
N_{xy}	lb/in.	- 35	- 14	- 315	249	- 189	228
ϵ_x	in./in.	$-1947(10)^{-6}$	$-1958(10)^{-6}$	$1146(10)^{-6}$	$-562(10)^{-6}$	$2451(10)^{-6}$	$641(10)^{-6}$
ϵ_{xy}	in./in.	$116(10)^{-6}$	$-134(10)^{-6}$	$745(10)^{-6}$	$-372(10)^{-6}$	$943(10)^{-6}$	$404(10)^{-6}$
p	$lb/in.^2$	±0.975	-1.423	±0.975	-1.89	±0.975	-1.43
$T_{(av)}$	^oF	1345	1343	994	1196	945	1113

[a] All loads and strains are ultimate.

TABLE 8-33

LOADS FOR SEMIMONOCOQUE CHORDWISE CONVEX BEADED BOTH SURFACES; NO THERMAL PROTECTION; -0.5-g CONDITION[a]

Item	Units	A		B		C	
		Upper surface	Lower surface	Upper surface	Lower surface	Upper surface	Lower surface
N_x	lb/in.	- 32	- 166	- 44	- 166	- 58	- 112
N_y	lb/in.	149	- 127	42	- 17	7	15
N_{xy}	lb/in.	- 8	8	- 16	- 52	- 26	11
ϵ_x	in./in.	$366(10)^{-6}$	$971(10)^{-6}$	$86(10)^{-6}$	$836(10)^{-6}$	$-777(10)^{-6}$	$-462(10)^{-6}$
ϵ_{xy}	in./in.	$50(10)^{-6}$	$298(10)^{-6}$	$72(10)^{-6}$	$576(10)^{-6}$	$-694(10)^{-6}$	$-262(10)^{-6}$
p	$lb/in.^2$	±0.975	-0.975	±0.975	-0.975	±0.975	-0.975
$T_{(av)}$	^oF	1342	1317	1336	1314	1552	1425

[a]All loads and strains are ultimate.

TABLE 8-34

LOADS FOR SEMIMONOCOQUE CHORDWISE CONVEX BEADED BOTH SURFACES; NO THERMAL PROTECTION; +2.0-g CONDITION[a]

Item	Units	A		B		C	
		Upper surface	Lower surface	Upper surface	Lower surface	Upper surface	Lower surface
N_x	lb/in.	- 243	- 624	- 362	- 625	- 187	- 200
N_y	lb/in.	-1143	966	-1122	971	- 537	524
N_{xy}	lb/in.	- 80	0	- 758	580	- 457	557
ϵ_x	in./in.	$1480(10)^{-6}$	$- 426(10)^{-6}$	$2019(10)^{-6}$	$- 752(10)^{-6}$	$437(10)^{-6}$	$-2389(10)^{-6}$
ϵ_{xy}	in./in.	$547(10)^{-6}$	$- 396(10)^{-6}$	$1619(10)^{-6}$	$- 420(10)^{-6}$	$414(10)^{-6}$	$1156(10)^{-6}$
p	$lb/in.^2$	±0.975	-1.89	±0.975	-2.85	±0.975	-1.91
$T_{(av)}$	^oF	1373	1530	1307	1548	1448	1668

[a]All loads and strains are ultimate.

TABLE 8-35

LOADS FOR SEMIMONOCOQUE CHORDWISE CONVEX BEADED BOTH SURFACES; NO THERMAL PROTECTION; CRUISE CONDITION

Item	Units	A		B		C	
		Upper surface	Lower surface	Upper surface	Lower surface	Upper surface	Lower surface
N_x	lb/in.	- 113	- 301	- 155	- 295	- 94	- 158
N_y	lb/in.	- 504	434	- 497	422	- 289	223
N_{xy}	lb/in.	- 35	- 14	- 315	249	- 189	228
ϵ_x	in./in.	$-702(10)^{-6}$	$-731(10)^{-6}$	$1519(10)^{-6}$	$-386(10)^{-6}$	$1594(10)^{-6}$	$-1069(10)^{-6}$
ϵ_{xy}	in./in.	$42(10)^{-6}$	$-50(10)^{-6}$	$988(10)^{-6}$	$-255(10)^{-6}$	$1412(10)^{-6}$	$1009(10)^{-6}$
p	$lb/in.^2$	±0.975	-1.423	±0.975	-1.89	±0.975	-1.43
$T_{(av)}$	^oF	1342	1340	1061	1287	1115	1356

[a]All loads and strains are ultimate.

TABLE 8-36

LOADS FOR SEMIMONOCOQUE CHORDWISE CONVEX BEADED UPPER AND CENTER LOWER SURFACES, TUBULAR INBOARD AND OUTBOARD LOWER; PARTIAL HEAT SHIELD LOWER OUTBOARD; -0.5-g CONDITION[a]

Item	Units	A		B		C	
		Upper surface	Lower surface	Upper surface	Lower surface	Upper surface	Lower surface
N_x	lb/in.	- 32	- 166	- 44	- 166	- 58	- 112
N_y	lb/in.	149	- 127	42	- 17	7	15
N_{xy}	lb/in.	- 8	8	- 16	- 52	- 26	11
ϵ_x	in./in.	$347(10)^{-6}$	$950(10)^{-6}$	$190(10)^{-6}$	$870(10)^{-6}$	$-723(10)^{-6}$	$-567(10)^{-6}$
ϵ_{xy}	in./in.	$47(10)^{-6}$	$291(10)^{-6}$	$170(10)^{-6}$	$600(10)^{-6}$	$-685(10)^{-6}$	$-322(10)^{-6}$
p	lb/in.^{2}	±0.975	-0.975	±0.975	-0.975	±0.975	-0.975
$T_{(av)}$	^oF	1342	1317	1303	1294	1539	1431

[a]All loads and strains are ultimate.

TABLE 8-37

LOADS FOR SEMIMONOCOQUE CHORDWISE CONVEX BEADED UPPER AND CENTER LOWER SURFACES, TUBULAR INBOARD AND OUTBOARD LOWER; PARTIAL HEAT SHIELD LOWER OUTBOARD; +2.0-g CONDITION[a]

Item	Units	A		B		C	
		Upper surface	Lower surface	Upper surface	Lower surface	Upper surface	Lower surface
N_x	lb/in.	- 243	- 624	- 362	- 625	- 187	- 200
N_y	lb/in.	-1143	966	-1122	971	- 537	524
N_{xy}	lb/in.	- 80	0	- 758	580	- 457	557
ϵ_x	in./in.	$875(10)^{-6}$	$-899(10)^{-6}$	$1686(10)^{-6}$	$-440(10)^{-6}$	$520(10)^{-6}$	$-934(10)^{-6}$
ϵ_{xy}	in./in.	$299(10)^{-6}$	$-798(10)^{-6}$	$-1352(10)^{-6}$	$-246(10)^{-6}$	$480(10)^{-6}$	$462(10)^{-6}$
p	$lb/in.^2$	±0.975	-1.89	±0.975	-2.85	±0.975	-1.91
$T_{(av)}$	^oF	1373	1530	1256	1470	1498	1533

[a] All loads and strains are ultimate.

TABLE 8-38

LOADS FOR SEMIMONOCOQUE CHORDWISE CONVEX BEADED UPPER AND CENTER LOWER SURFACES, TUBULAR INBOARD AND OUTBOARD LOWER; PARTIAL HEAT SHIELD LOWER OUTBOARD; CRUISE CONDITION [a]

Item	Units	A		B		C	
		Upper surface	Lower surface	Upper surface	Lower surface	Upper surface	Lower surface
N_x	lb/in.	- 113	- 301	- 155	- 295	- 94	-158
N_y	lb/in.	- 504	434	- 497	422	- 289	223
N_{xy}	lb/in.	- 35	- 14	- 315	249	- 189	228
ϵ_x	in./in.	$-1144(10)^{-6}$	$-1280(10)^{-6}$	$1340(10)^{-6}$	$- 482(10)^{-6}$	$1888(10)^{-6}$	$-307(10)^{-6}$
ϵ_{xy}	in./in.	$68(10)^{-6}$	$- 88(10)^{-6}$	$- 319(10)^{-6}$	$- 319(10)^{-6}$	$726(10)^{-6}$	$-129(10)^{-6}$
p	$lb/in.^2$	±0.975	-1.423	±0.975	-1.89	±0.975	-1.43
$T_{(av)}$	^oF	1342	1340	994	1242	1049	1255

[a] All loads and strains are ultimate.

TABLE 8-39

LOADS FOR SEMIMONOCOQUE CHORDWISE CONVEX BEADED UPPER AND CENTER LOWER SURFACES, TUBULAR INBOARD AND OUTBOARD LOWER; PARTIAL HEAT SHIELD AND INSULATION; -0.5-g CONDITION[a]

Item	Units	A		B		C	
		Upper surface	Lower surface	Upper surface	Lower surface	Upper surface	Lower surface
N_x	lb/in.	- 32	- 166	- 44	- 166	- 58	- 112
N_y	lb/in.	149	- 127	42	- 17	7	15
N_{xy}	lb/in.	- 8	8	- 16	- 52	- 26	11
ϵ_x	in./in.	$366(10)^{-6}$	$970(10)^{-6}$	$40(10)^{-6}$	$855(10)^{-6}$	$665(10)^{-6}$	$-206(10)^{-6}$
ϵ_{xy}	in./in.	$50(10)^{-6}$	$297(10)^{-6}$	$32(10)^{-6}$	$589(10)^{-6}$	$-622(10)^{-6}$	$-37(10)^{-6}$
p	lb/in.^{2}	±0.975	-0.975	±0.975	-0.975	±0.975	-0.975
$T_{(av)}$	$^\circ$F	1342	1317	1303	1294	1527	1405

[a]All loads and strains are ultimate.

TABLE 8-40

LOADS FOR SEMIMONOCOQUE CHORDWISE CONVEX BEADED UPPER AND CENTER LOWER SURFACES, TUBULAR INBOARD AND OUTBOARD LOWER; PARTIAL HEAT SHIELD AND INSULATION; +2.0-g CONDITION[a]

Item	Units	A		B		C	
		Upper surface	Lower surface	Upper surface	Lower surface	Upper surface	Lower surface
N_x	lb/in.	- 243	- 624	- 362	- 625	- 187	- 200
N_y	lb/in.	-1143	966	-1122	971	- 537	524
N_{xy}	lb/in.	- 80	0	- 758	580	- 457	557
ϵ_x	in./in.	$736(10)^{-6}$	$-1078(10)^{-6}$	$1545(10)^{-6}$	$- 620(10)^{-6}$	$- 620(10)^{-6}$	$- 416(10)^{-6}$
ϵ_{xy}	in./in.	$273(10)^{-6}$	$-1022(10)^{-6}$	$1239(10)^{-6}$	$- 347(10)^{-6}$	$152(10)^{-6}$	$206(10)^{-6}$
p	lb/in.^{2}	±0.975	-1.89	±0.975	-2.85	±0.975	-1.91
$T_{(av)}$	$^\circ$F	1373	1530	1277	1470	1389	1483

[a] All loads and strains are ultimate.

TABLE 8-41

LOADS FOR SEMIMONOCOQUE CHORDWISE CONVEX BEADED UPPER AND CENTER LOWER SURFACES, TUBULAR INBOARD AND OUTBOARD LOWER; PARTIAL HEAT SHIELD AND INSULATION; CRUISE CONDITION[a]

Item	Units	A		B		C	
		Upper surface	Lower surface	Upper surface	Lower surface	Upper surface	Lower surface
N_x	lb/in.	- 113	- 301	- 155	- 295	- 94	- 158
N_y	lb/in.	- 504	434	- 497	422	- 289	223
N_{xy}	lb/in.	- 35	- 14	- 315	249	- 189	228
ϵ_x	in./in.	$-1523(10)^{-6}$	$-1762(10)^{-6}$	$953(10)^{-6}$	$-963(10)^{-6}$	$2250(10)^{-6}$	$551(10)^{-6}$
ϵ_{xy}	in.-in.	$91(10)^{-6}$	$-121(10)^{-6}$	$619(10)^{-6}$	$-638(10)^{-6}$	$866(10)^{-6}$	$347(10)^{-6}$
p	lb/in.^{2}	±0.975	-1.423	±0.975	-1.89	±0.975	-1.43
$T_{(av)}$	^oF	1342	1340	994	1242	983	1147

[a] All loads and strains are ultimate.

TABLE 8-42

FINAL CHORDWISE ULTIMATE LOADS[a]
(Average Loads Between Stations 2274 and 2366)

Wing panel location	Load vector	Ultimate loads, lb/in.[a]					
		-0.5-g condition		+2.0-g condition		Cruise condition	
		Upper	Lower	Upper	Lower	Upper	Lower
$\mathcal{L}_L$ - BL 120 Area A	N_x	-50(470)	-157(138)	-300(320)	-547(-280)	-142(-1205)	-253(-950)
	N_y	182(143)	-153(156)	-992(78)	885(60)	-443(-217)	405(-145)
	N_{xy}	-12(17)	14(22)	-54(38)	19(-17)	-24(44)	4(19)
BL 120 to BL 212 Area B	N_x	-55(25)	-168(190)	-353(658)	-680(-327)	-155(1153)	-315(-283)
	N_y	64(94)	-31(140)	-965(27)	865(99)	-420(-151)	380(-70)
	N_{xy}	-24(115)	-37(46)	-461(206)	359(-38)	-191(190)	155(-39)
BL 212 to BL 350 Area C	N_x	-62(-600)	-72(-40)	-146(120)	-138(-160)	-134(1077)	-50(159)
	N_y	20(-169)	-4(61)	-418(-144)	433(95)	-181(-20)	186(34)
	N_{xy}	-16(-339)	9)-59)	-290(-220)	425(64)	-122(269)	175(79)

[a]Load code: Air load (thermal load). Flexibilities for semimonocoque chordwise tubular lower/convex-beaded upper concept.

TABLE 8-43

FINAL LOADS FOR SEMIMONOCOQUE CHORDWISE CONCEPT; CONVEX BEADED UPPER, TUBULAR LOWER; HEAT SHIELD AND INSULATION; -0.5-g CONDITION[a]

Item	Units	A		B		C	
		Upper surface	Lower surface	Upper surface	Lower surface	Upper surface	Lower surface
N_x	lb/in.	-50	-157	-55	-168	-62	-72
N_y	lb/in.	182	-153	64	-31	20	-4
N_{xy}	lb/in.	-12	14	-24	-37	-16	9
ϵ_x	in./in.	777×10^{-6}	229×10^{-6}	34×10^{-6}	258×10^{-6}	-853×10^{-6}	-63×10^{-6}
ϵ_y	in./in.	295×10^{-6}	448×10^{-6}	162×10^{-6}	468×10^{-6}	-392×10^{-6}	223×10^{-6}
ϵ_{xy}	in./in.	114×10^{-6}	164×10^{-6}	490×10^{-6}	260×10^{-6}	-168×10^{-6}	-393×10^{-6}
p	$lb/in.^2$	±0.975	-0.975	±0.975	-0.975	±0.975	-0.975
$T_{(av)}$	^oF	1210	1258	1303	1294	1505	1383

[a]All loads and strains are ultimate.

TABLE 8-44

FINAL LOADS FOR SEMIMONOCOQUE CHORDWISE CONCEPT; CONVEX BEADED UPPER, TUBULAR LOWER; HEAT SHIELD AND INSULATION; +2.0-g CONDITION[a]

Item	Units	A		B		C	
		Upper surface	Lower surface	Upper surface	Lower surface	Upper surface	Lower surface
N_x	lb/in.	-300	-547	-353	-680	-146	-138
N_y	lb/in.	-992	885	-965	865	-418	433
N_{xy}	lb/in.	-54	19	-461	359	-290	425
ϵ_x	in./in.	529×10^{-6}	-464×10^{-6}	906×10^{-6}	-444×10^{-6}	-171×10^{-6}	-251×10^{-6}
ϵ_y	in./in.	161×10^{-6}	172×10^{-6}	47×10^{-6}	331×10^{-6}	-334×10^{-6}	347×10^{-6}
ϵ_{xy}	in./in.	256×10^{-6}	-127×10^{-6}	883×10^{-6}	-214×10^{-6}	-109×10^{-6}	426×10^{-6}
p	$lb/in.^2$	±0.975	-1.89	±0.975	-2.85	±0.975	-1.91
$T_{(av)}$	^oF	1232	1358	1277	1392		1382

[a]All loads and strains are ultimate.

TABLE 8-45

FINAL LOADS FOR SEMIMONOCOQUE CHORDWISE CONCEPT; CONVEX BEADED UPPER, TUBULAR LOWER; HEAT SHIELD AND INSULATION; CRUISE CONDITION

Item	Units	A		B		C	
		Upper surface	Lower surface	Upper surface	Lower surface	Upper surface	Lower surface
N_x	lb/in.	-142	-253	-155	-315	-134	-50
N_y	lb/in.	-443	405	-420	380	-181	186
N_{xy}	lb/in.	-24	4	-191	155	-122	175
ϵ_x	in./in.	-1992×10^{-6}	-1575×10^{-6}	1588×10^{-6}	-385×10^{-6}	1531×10^{-6}	249×10^{-6}
ϵ_y	in./in.	-448×10^{-6}	-391×10^{-6}	-260×10^{-6}	-234×10^{-6}	-46×10^{-6}	124×10^{-6}
ϵ_{xy}	in./in.	297×10^{-6}	142×10^{-6}	815×10^{-6}	-220×10^{-6}	1334×10^{-6}	526×10^{-6}
p	$lb/in.^2$	±0.975	-1.423	±0.975	-1.89	±0.975	-1.43
$T_{(av)}$	^oF	1345	1343	994	1196	945	1113

[a]All loads and strains are ultimate.

Table 8-46

FINAL REDUNDANT MODEL COMPARISON, SEMIMONOCOQUE (CHORDWISE)

		Center		Inboard		Outboard		Spacing [c]	
		Upper	Lower	Upper	Lower	Upper	Lower	Rib	Spar
Final redundant model (input)	(a) t_s x	0.025	0.026	0.031	0.033	0.031	0.028	60 75 75	24 24 24
	y	0.014	0.010	0.017	0.009	0.013	0.009		
	(b) t_s	0.016	0.015	0.025	0.020	0.023	0.017		
Minimum-weight structural arrangement	(a) t_e x	0.029	0.026	0.029	0.034	0.038	0.025	60 75 75	24 24 24
	y	0.011	0.011	0.011	0.012	0.009	0.008		
	(b) t_s	0.017	0.015	0.023	0.020	0.030	0.016		

[a] t_e = Equivalent extension thickness; x denotes spanwise direction and y denotes chordwise direction.

[b] t_s = Equivalent surface panel shear thickness.

[c] Rib and spar spacing from center to outboard area, respectively.

Table 8-47

FINAL STATICALLY DETERMINATE DESIGN ULTIMATE LOADS[a]

Location	Load vector	Ultimate loads, lb/in.[a]					
		-0.5-g condition		+2.0-g condition		Cruise condition	
		Upper	Lower	Upper	Lower	Upper	Lower
℄ - BL 120	N_x	0(0)	0(0)	0(0)	0(0)	0(0)	0(0)
	N_y	181(-35)	-180(35)	-616(-119)	611(118)	-293(-14)	291(15)
	N_{xy}	0(0)	0(0)	0(0)	0(0)	0(0)	0(0)
BL 120-212	N_x	0(0)	0(0)	0(0)	0(0)	0(0)	0(0)
	N_y	76(-45)	-77(37)	-535(-65)	538(65)	-245(40)	246(-25)
	N_{xy}	13(-10)	013(9)	-147(-16)	147(16)	-43(-7.6)	64.7(12)
BL 212 – outboard	N_x	0(0)	0(0)	0(0)	0(0)	0(0)	0(0)
	N_y	29(-85)	-28(81)	-201(-35)	195(27)	-92(10)	89(-10)
	N_{xy}	11(-107)	8(107)	-119(-40)	119(40)	51.8(5)	51.8(-5)

[a]Average loads between stations 2274-2366.

TABLE 8-48

FINAL REDUNDANT-MODEL COMPARISON, STATICALLY DETERMINATE PRIMARY-STRUCTURE CONCEPT

		Center		Inboard		Outboard		Spacing	
		Upper	Lower	Upper	Lower	Upper	Lower	Rib	Spar
Final redundant model(input)	t_e x [a]	0	0	0	0	0	0	46	92
	t_e y	0.028	0.026	0.028	0.030	0.028	0.028		
	t_s [b]	0.016	0.015	0.016	0.018	0.016	0.016		
Minimum-weight concept circular beaded	t_e x	0	0	0	0	0	0	60[c]	90[c]
	t_e y	0.031	0.021	0.029	0.025	0.021	0.020	50	90
	t_s	0.018	0.012	0.017	0.014	0.012	0.011	40	90

[a] t_e = Equivalent extensional thickness; x denotes spanwise direction, and y denotes chordwise direction.

[b] t_s = Equivalent surface panel shear thickness.

[c] = Rib and spar spacing from center to outboard areas, respectively.

TABLE 8-50

FINAL LOADS FOR STATICALLY DETERMINATE CONCEPT; HEAT SHIELDS, NO INSULATION; +2.0-g CONDITION[a]

Item	Units	A		B		C	
		Upper surface	Lower surface	Upper surface	Lower surface	Upper surface	Lower surface
N_x	lb/in.	0	0	0	0	0	0
N_y	lb/in.	-616	611	-535	538	-201	195
N_{xy}	lb/in.	0	0	-147	147	-119	119
ϵ_x	in./in.	0	0	0	0	0	0
ϵ_y	in./in.	$-174(10)^{-6}$	$194(10)^{-6}$	$-96(10)^{-6}$	$-96(10)^{-6}$	$-56(10)^{-6}$	$49(10)^{-6}$
ϵ_{xy}	in./in.	0	0	$-108(10)^{-6}$	$101(10)^{-6}$	$-291(10)^{-6}$	$305(10)^{-6}$
p	$lb/in.^2$	±0.975	1.89	±0.975	2.85	±0.975	1.91
T(av)	°F	1220	1350	1300	1420	1430	1550

[a]All loads and strains are ultimate.

TABLE 8-49

FINAL LOADS FOR STATICALLY DETERMINATE CONCEPT; HEAT SHIELDS, NO INSULATION; -0.5-g CONDITION[a]

Item	Units	A		B		C	
		Upper surface	Lower surface	Upper surface	Lower surface	Upper surface	Lower surface
N_x	lb/in.	0	0	0	0	0	0
N_y	lb/in.	181	-180	76	-77	29	-28
N_{xy}	lb/in.	0	0	13	-13.1	11.1	-7.3
ϵ_x	in./in.	0	0	0	0	0	0
ϵ_y	in./in.	$-51(10)^{-6}$	$57(10)^{-6}$	$-67(10)^{-6}$	$55(10)^{-6}$	$-137(10)^{-6}$	$147(10)^{-6}$
ϵ_{xy}	in./in.	0	0	$-68\ (10)^{-6}$	$60\ (10)^{-6}$	$-762(10)^{-6}$	$815(10)^{-6}$
p	lb/in.^{2}	±0.975	-0.975	±0.975	-0.975	±0.975	-0.975
T(av)	°F	1220	1260	1300	1330	1430	1430

[a] All loads and strains are ultimate.

TABLE 8-51

LOADS FOR STATICALLY DETERMINATE CONCEPT; HEAT SHIELDS, NO INSULATION; CRUISE CONDITION[a]

Item	Units	A		B		C	
		Upper surface	Lower surface	Upper surface	Lower surface	Upper surface	Lower surface
N_x	lb/in.	0	0	0	0	0	0
N_y	lb/in.	-293	291	-245	246	-92	89
N_{xy}	lb/in.	0	0	-43	64.7	-51.8	51.8
ϵ_x	in./in.	0	0	0	0	0	0
ϵ_y	in./in.	$-20(10)^{-6}$	$25(10)^{-6}$	$59(10)^{-6}$	$-37(10)^{-6}$	$16(10)^{-6}$	$-18(10)^{-6}$
ϵ_{xy}	in./in.	0	0	$-51(10)^{-6}$	$78(10)^{-6}$	$36(10)^{-6}$	$38(10)^{-6}$
p	$lb/in.^2$	±0.975	-1.423	±0.975	-1.89	±0.975	-1.43
T(av)	°F	1320	1330	1130	1260	1170	1310

[a] All loads and strains are ultimate.

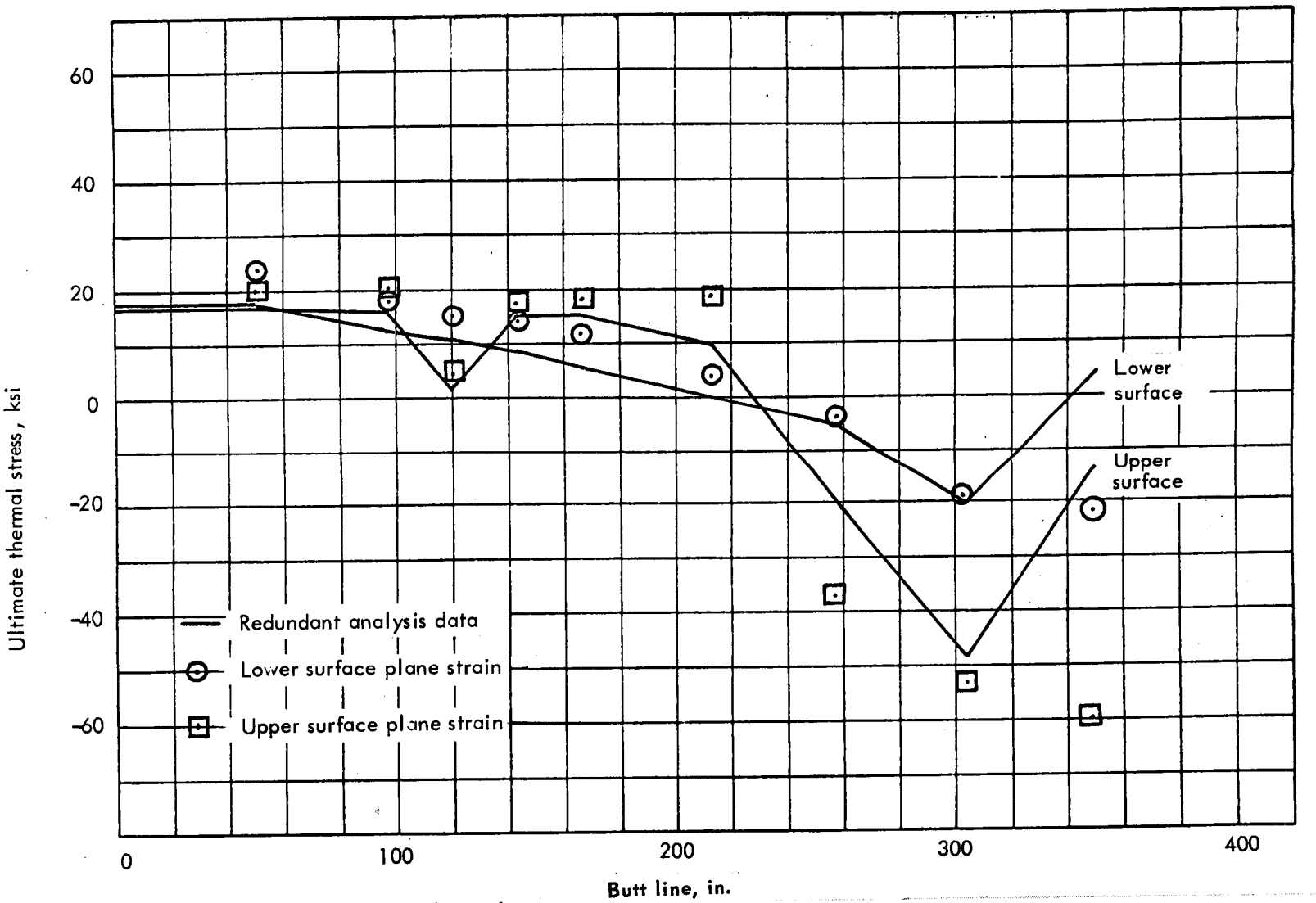

Figure 8-1. Ultimate chordwise thermal stress distribution at Sta. 2320, -0.5-g condition for monocoque waffle concept with partial heat shield at outboard area lower surface

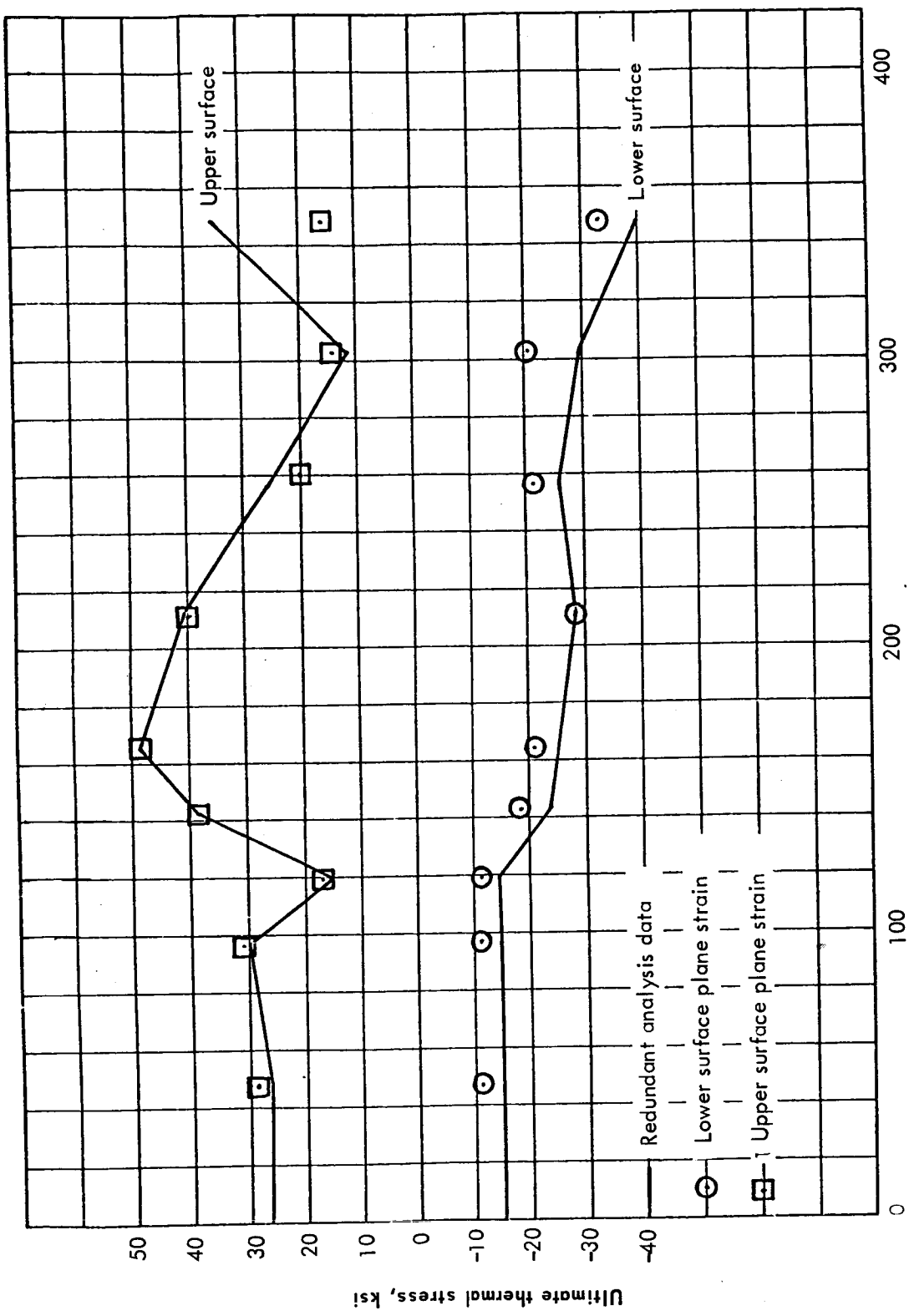

Figure 8-2. Ultimate chordwise thermal stress distribution at Sta. 2320, +2.0-g condition for monocoque waffle concept with partial heat shield at outboard area lower surface

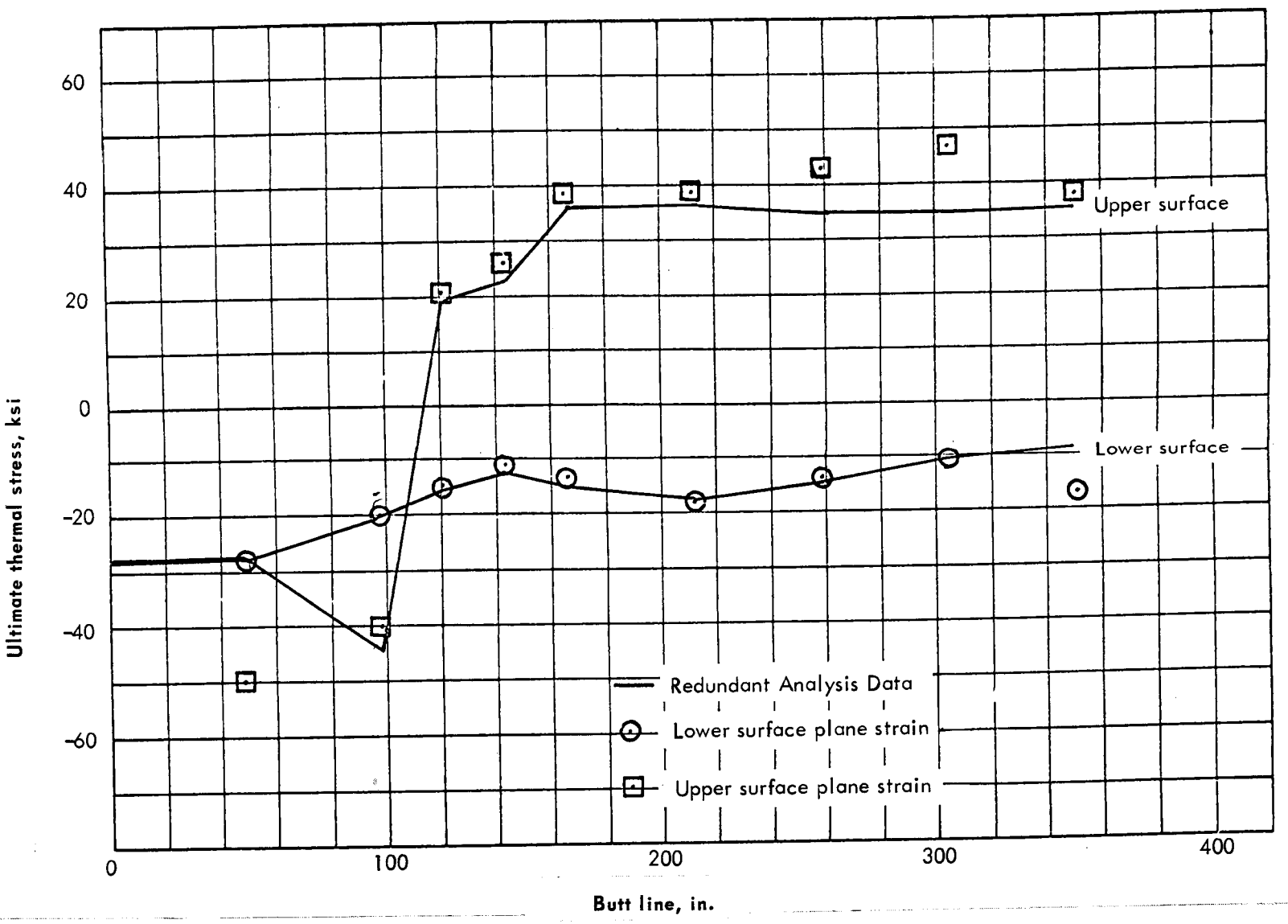

Figure 8-3. Ultimate chordwise thermal stress distribution at Sta. 2320, cruise condition for monocoque waffle concept with partial heat shield at outboard area lower surface

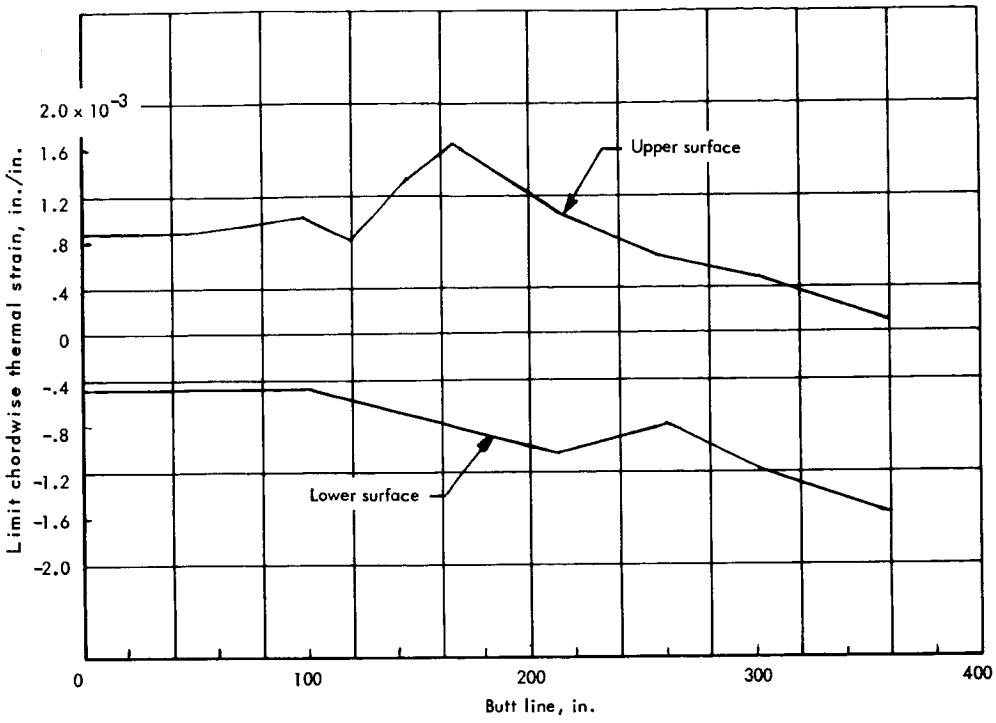

Figure 8-4. Spanwise thermal strain distribution for monocoque waffle concept with partial heat shield at outboard area lower surface

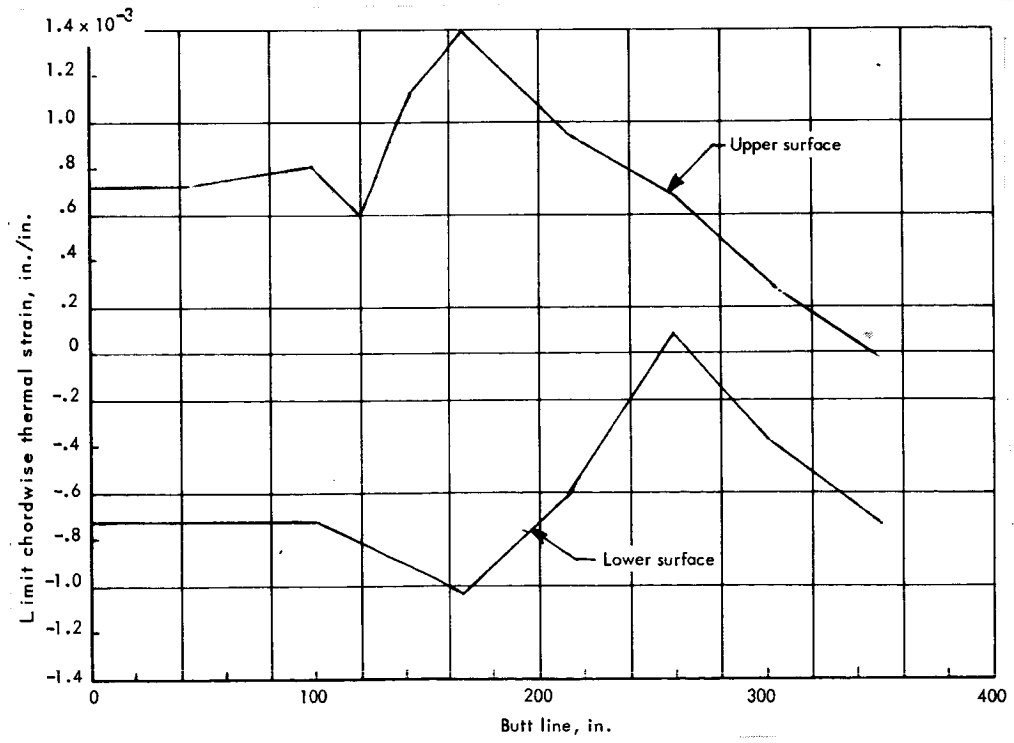

Figure 8-5. Spanwise thermal strain distribution for monocoque waffle concept with partial heat shield at outboard area lower surface with insulation

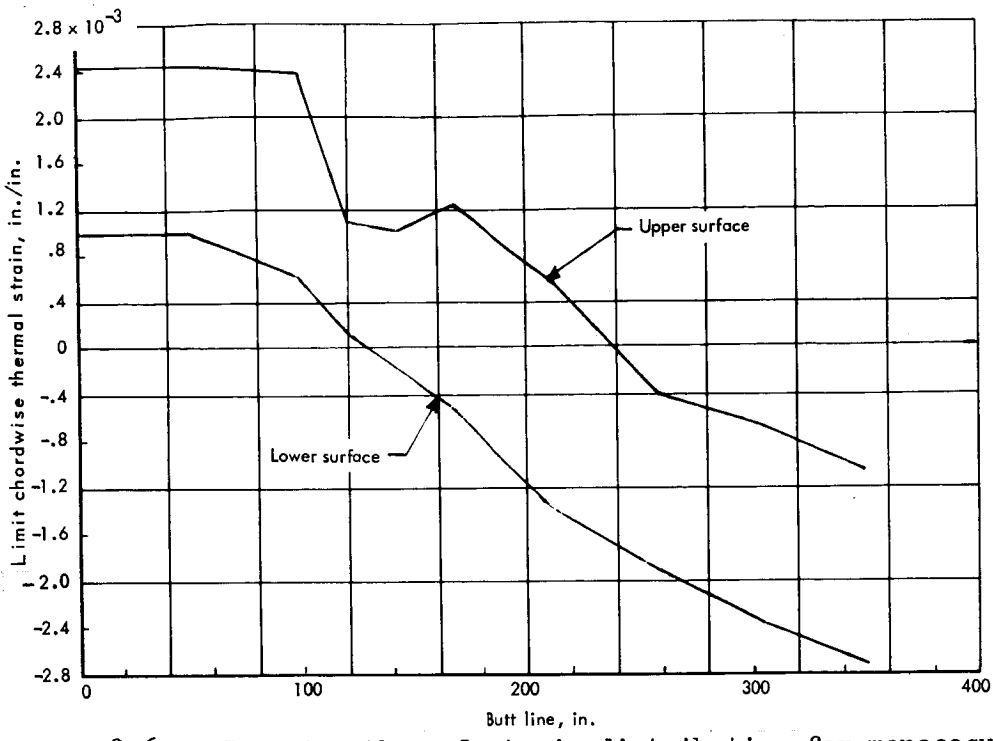

Figure 8-6. Spanwise thermal strain distribution for monocoque waffle concept with heat shield on entire lower surface

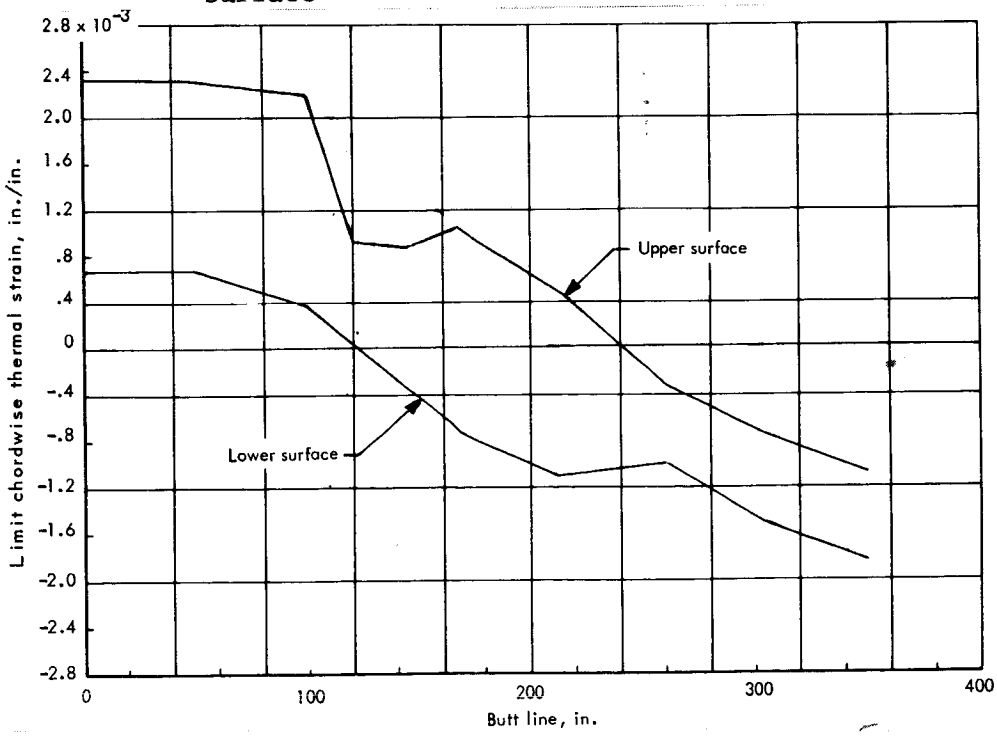

Figure 8-7. Spanwise thermal strain distribution for monocoque waffle concept with heat shield on entire lower surface with insulation at outboard area

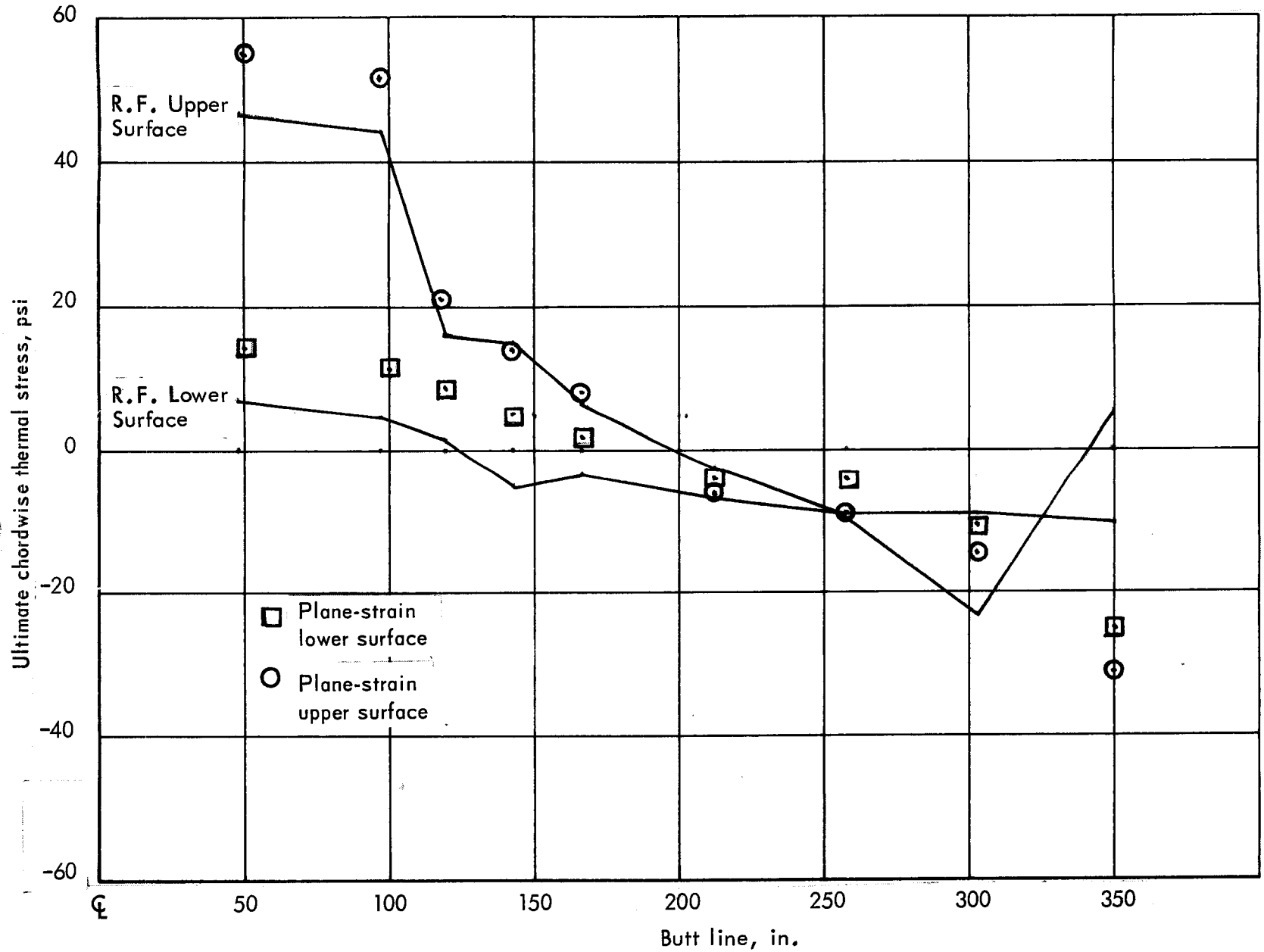

Figure 8-9. Plane-strain vs redundant force for semimonocoque spanwise concept at -0.5-g condition

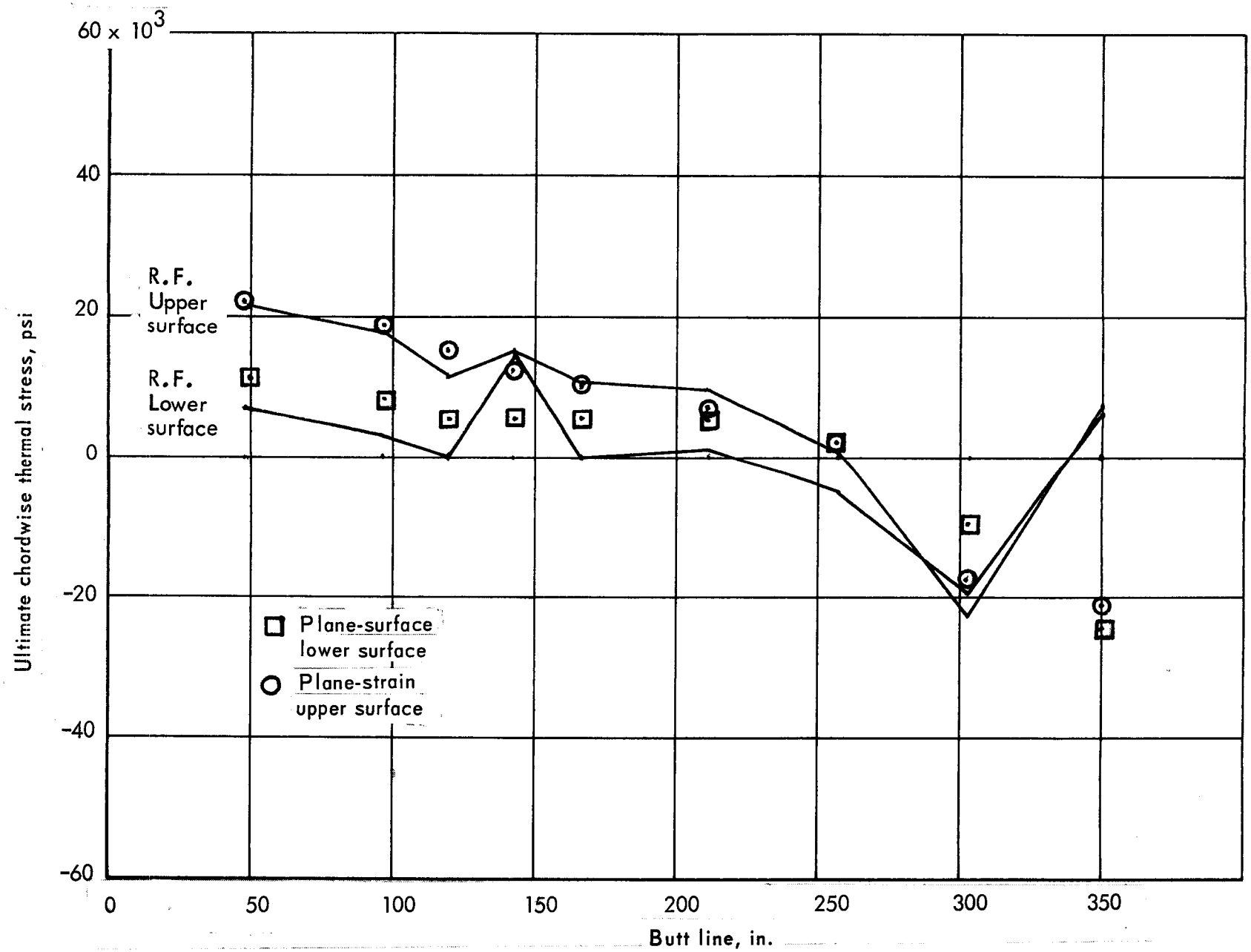

Figure 8-10. Plane-strain vs redundant force for semimonocoque spanwise concept at +2.0-g condition

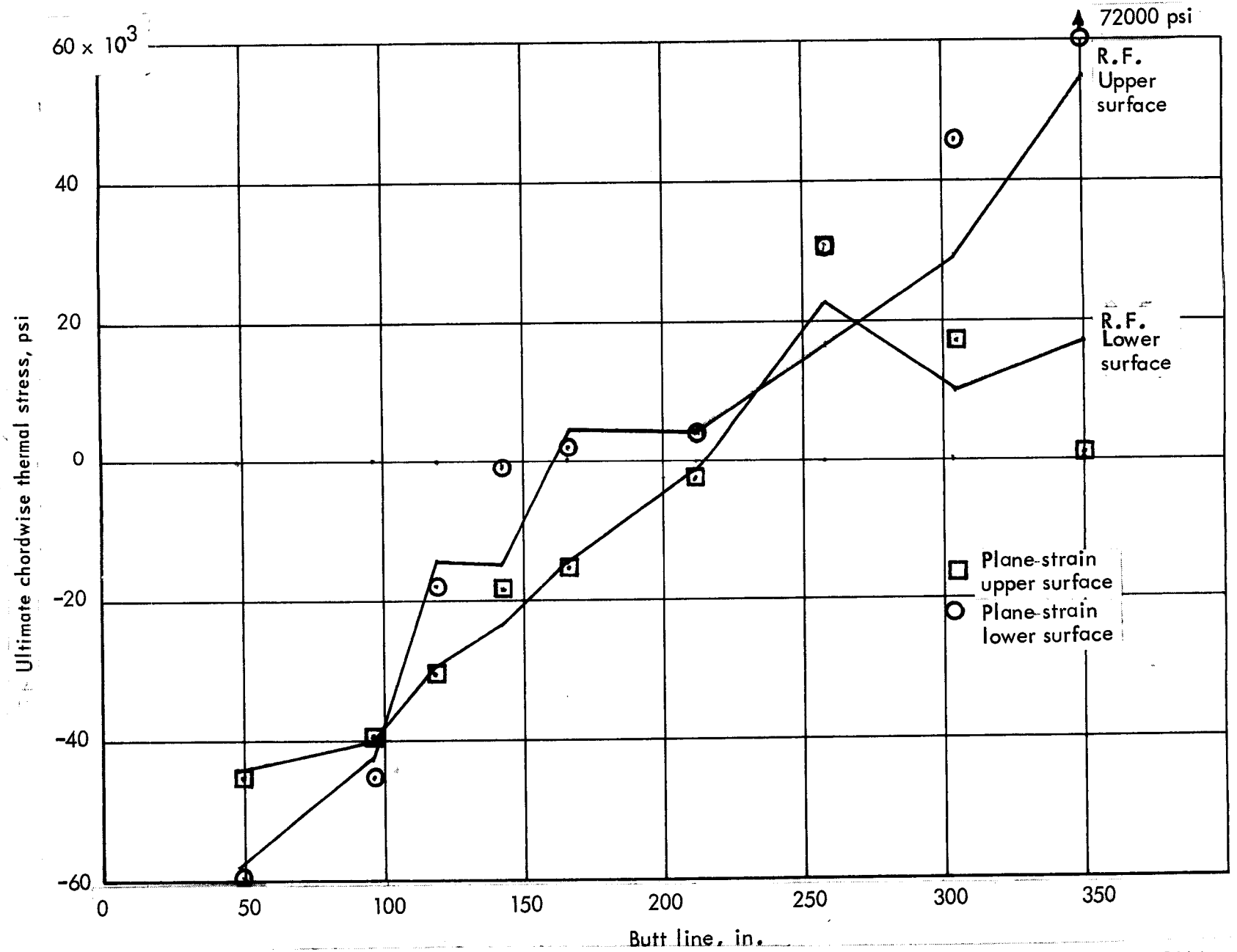

Figure 8-11. Plane-strain vs redundant force for semimonocoque spanwise concept cruise condition

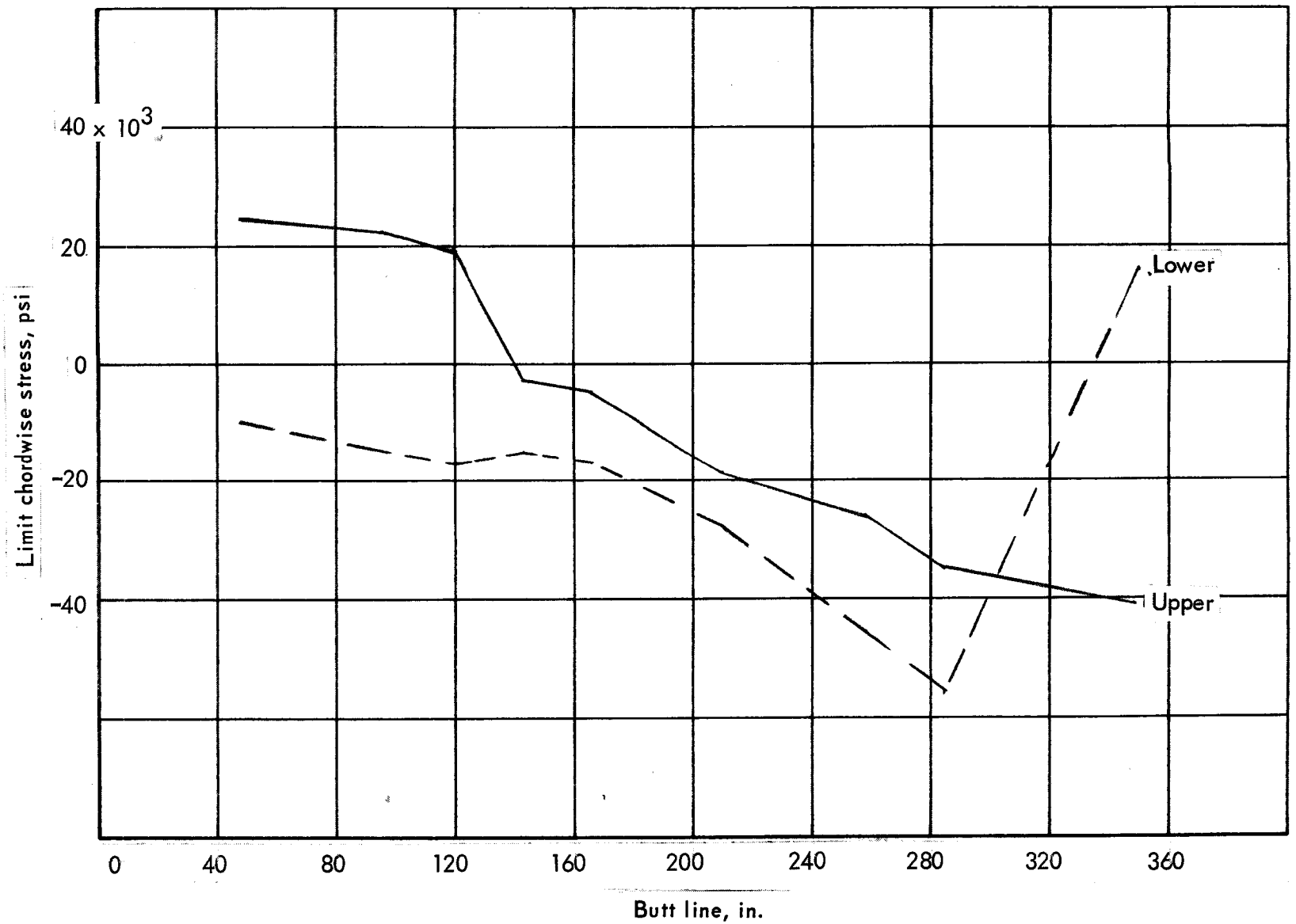

Figure 8-12. Limit thermal stress distribution for semimonocoque spanwise concept without insulation at-0.5-g condition

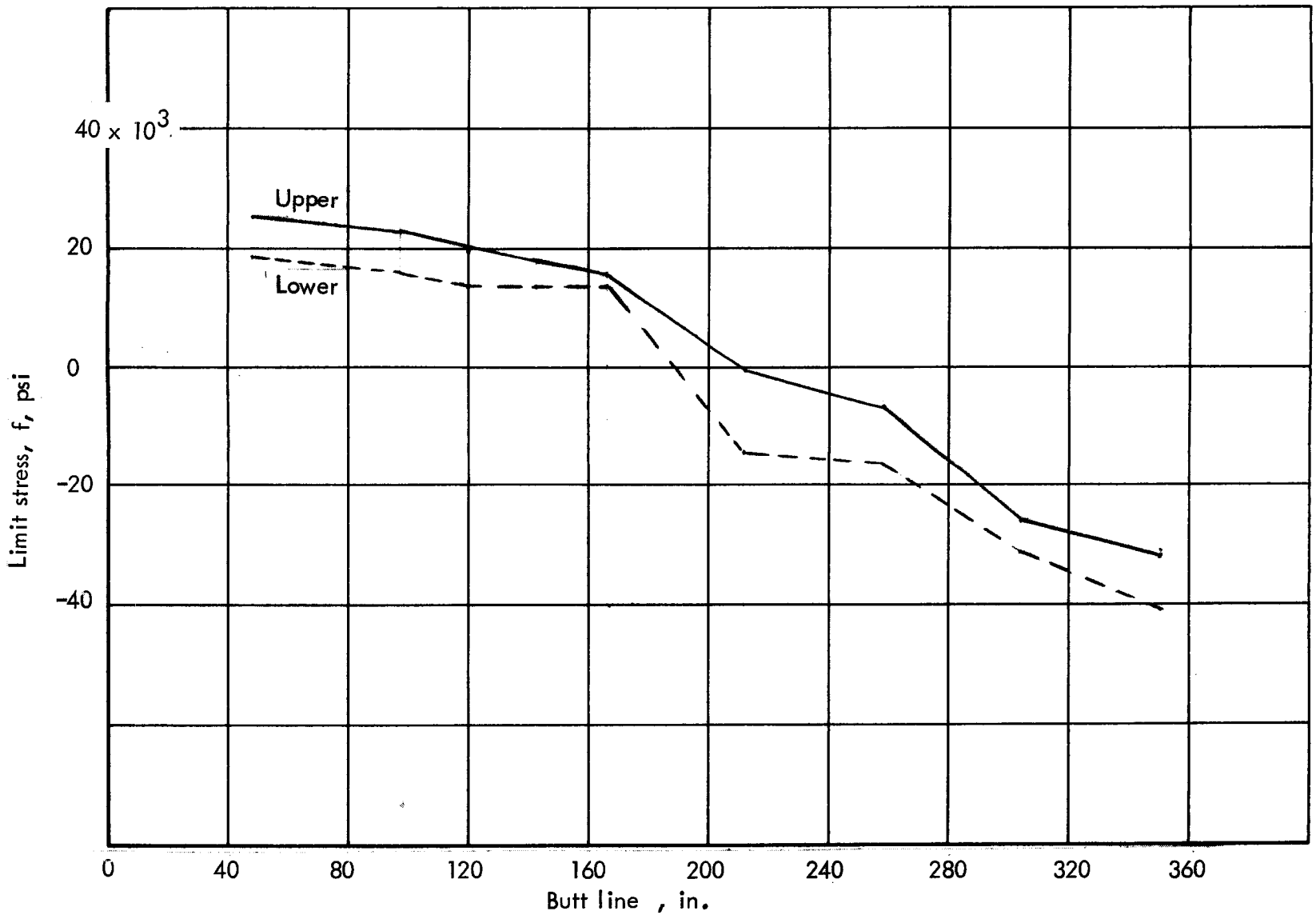

Figure 8-13. Limit thermal stress distribution for semimonocoque spanwise concept without insulation at +2.0-g condition

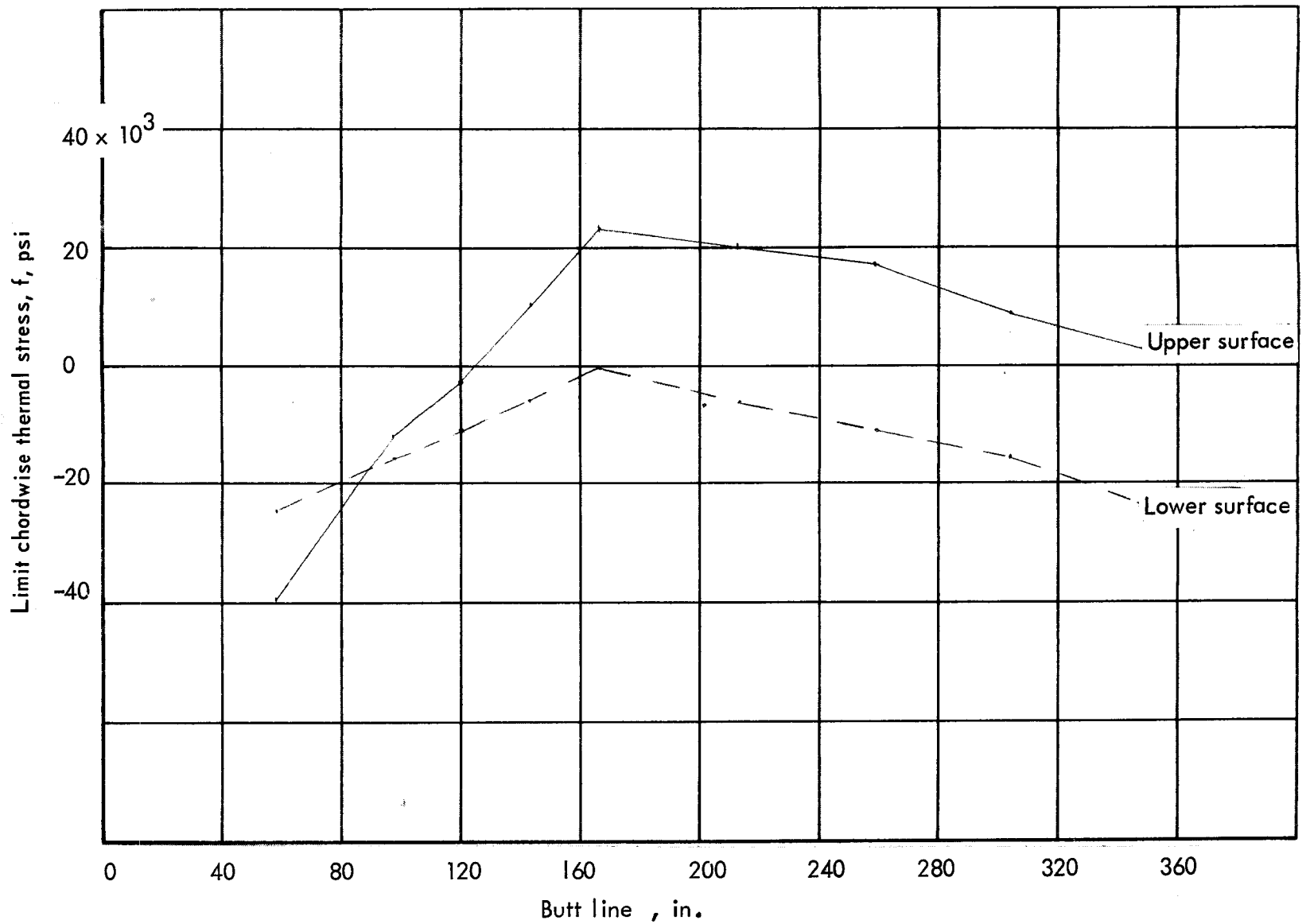

Figure 8-14. Limit thermal stress distribution for semimonocoque spanwise concept without insulation at cruise condition

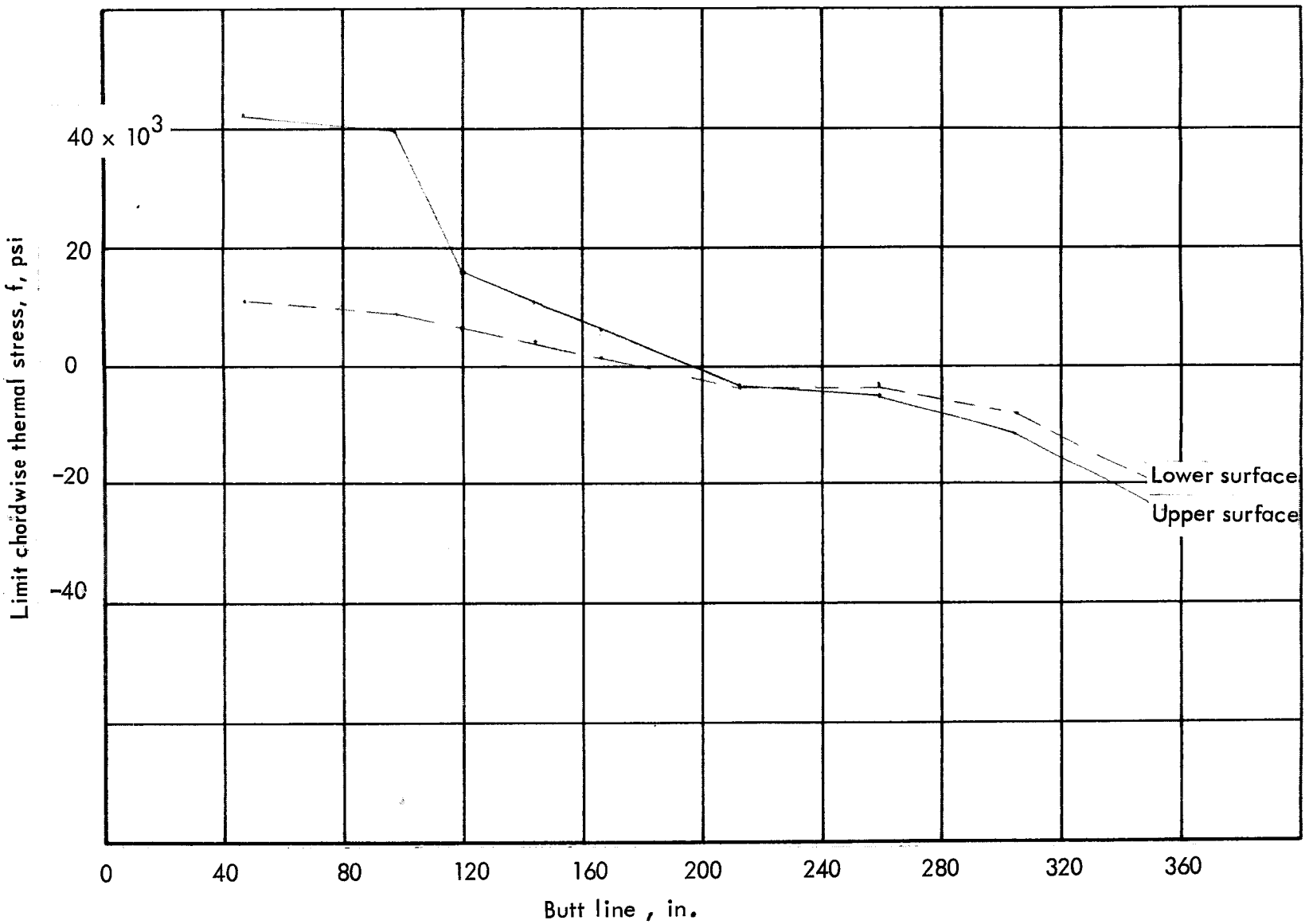

Figure 8-15. Limit thermal stress distribution for semimonocoque spanwise concept with insulation at -0.5-g condition

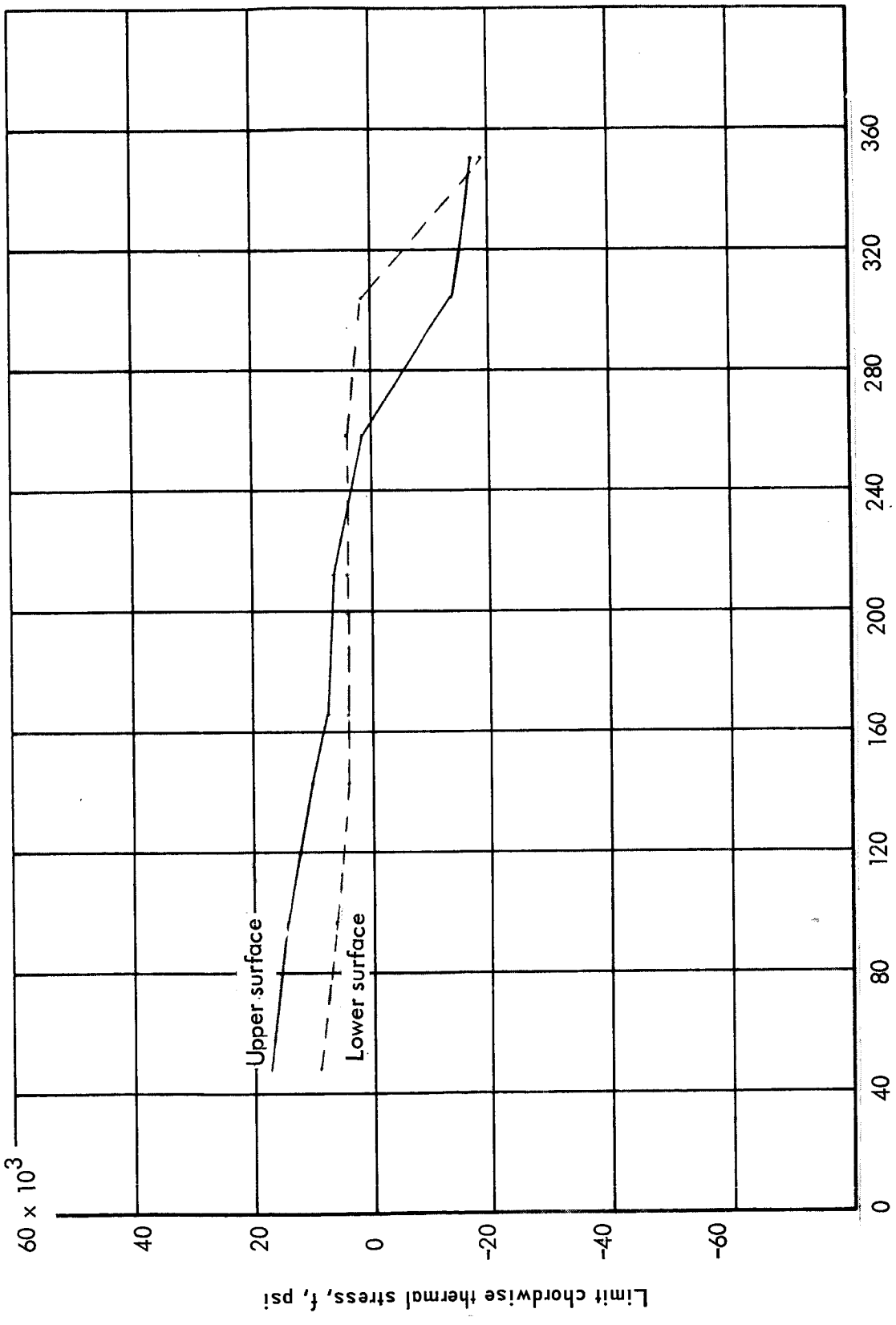

Figure 8-16. Limit thermal stress distribution for semimonocoque spanwise concept with insulation at +2.0-g condition

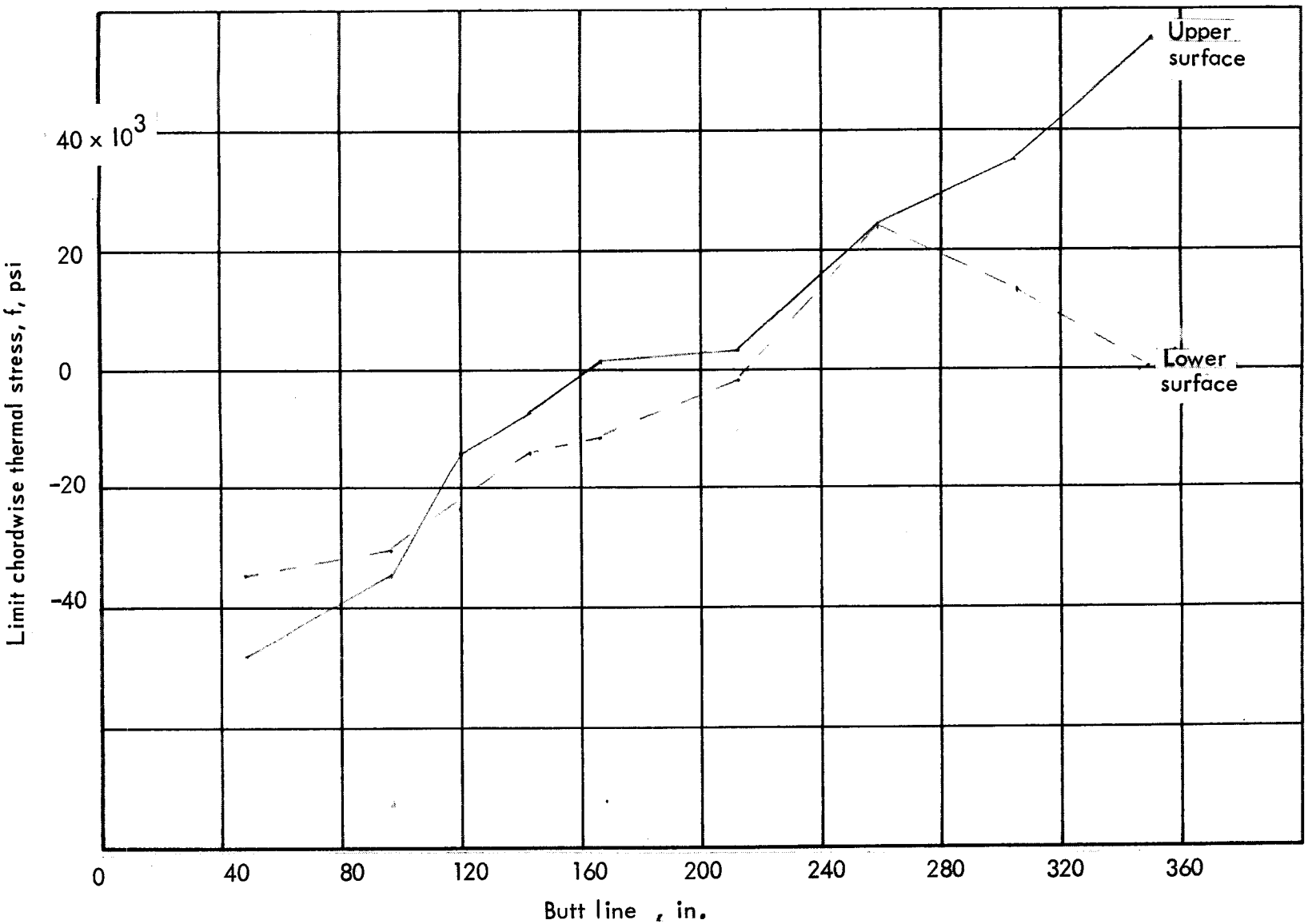

Figure 8-17. Limit thermal stress distribution for semimonocoque spanwise concept with insulation at cruise condition

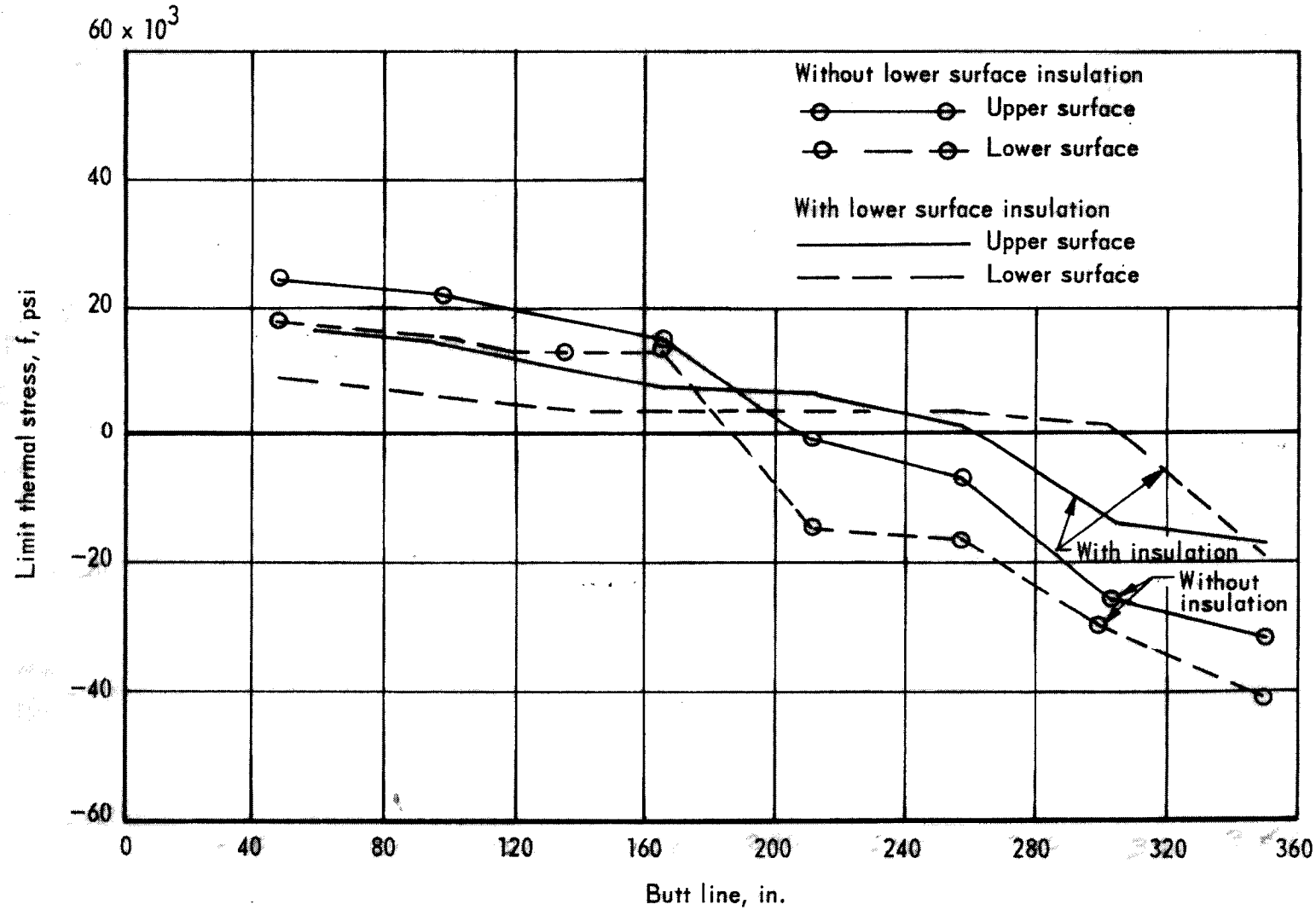

Figure 8-18. Limit thermal stresses in the chordwise direction at +2.0-g condition for semimonocoque spanwise-stiffened panels with and without insulation

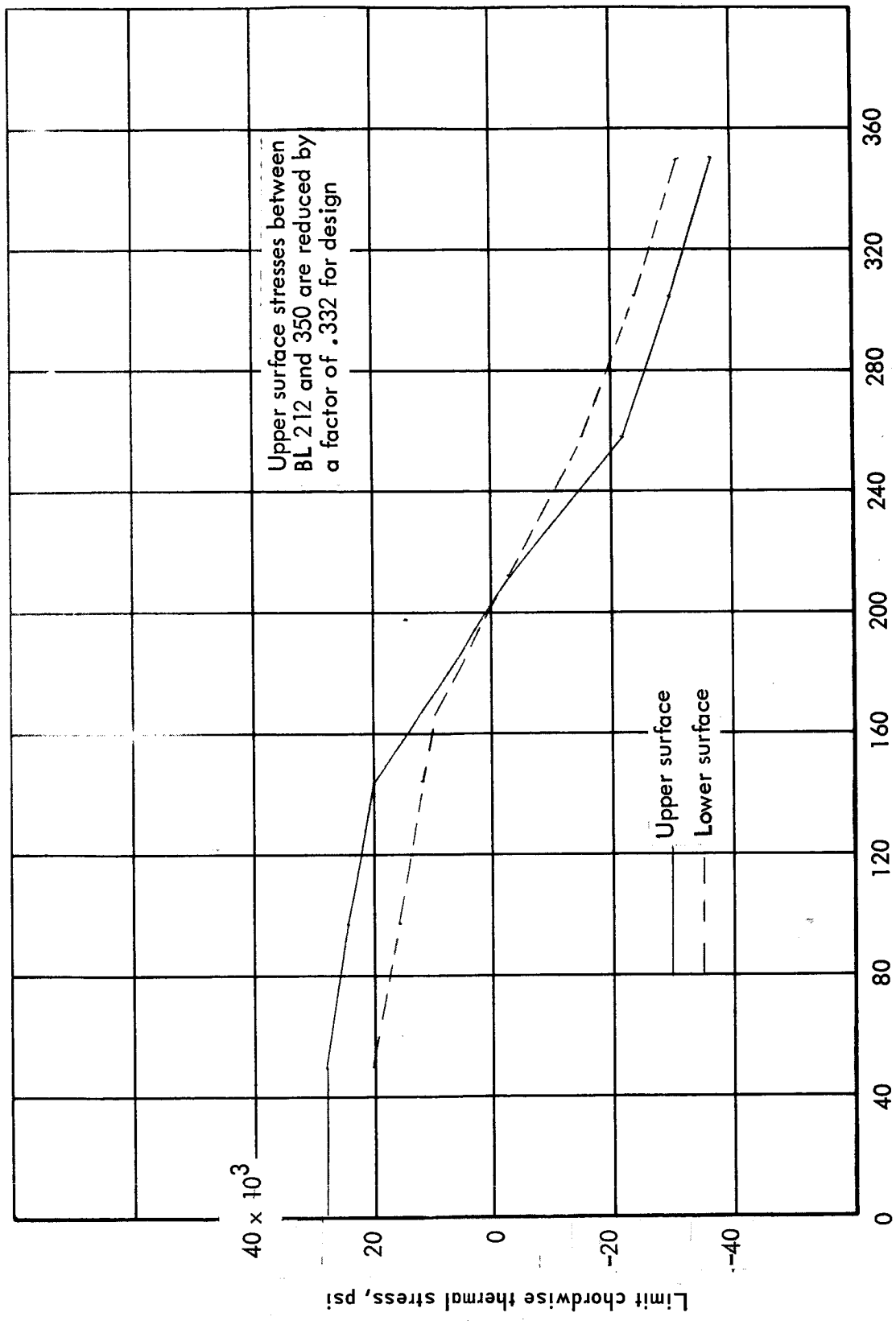

Figure 8-19. Limit thermal stress distribution at Sta. 2320 for semimonocoque chordwise concept: -0.5-g condition, tubular panel, both surfaces heat shielded, no insulation

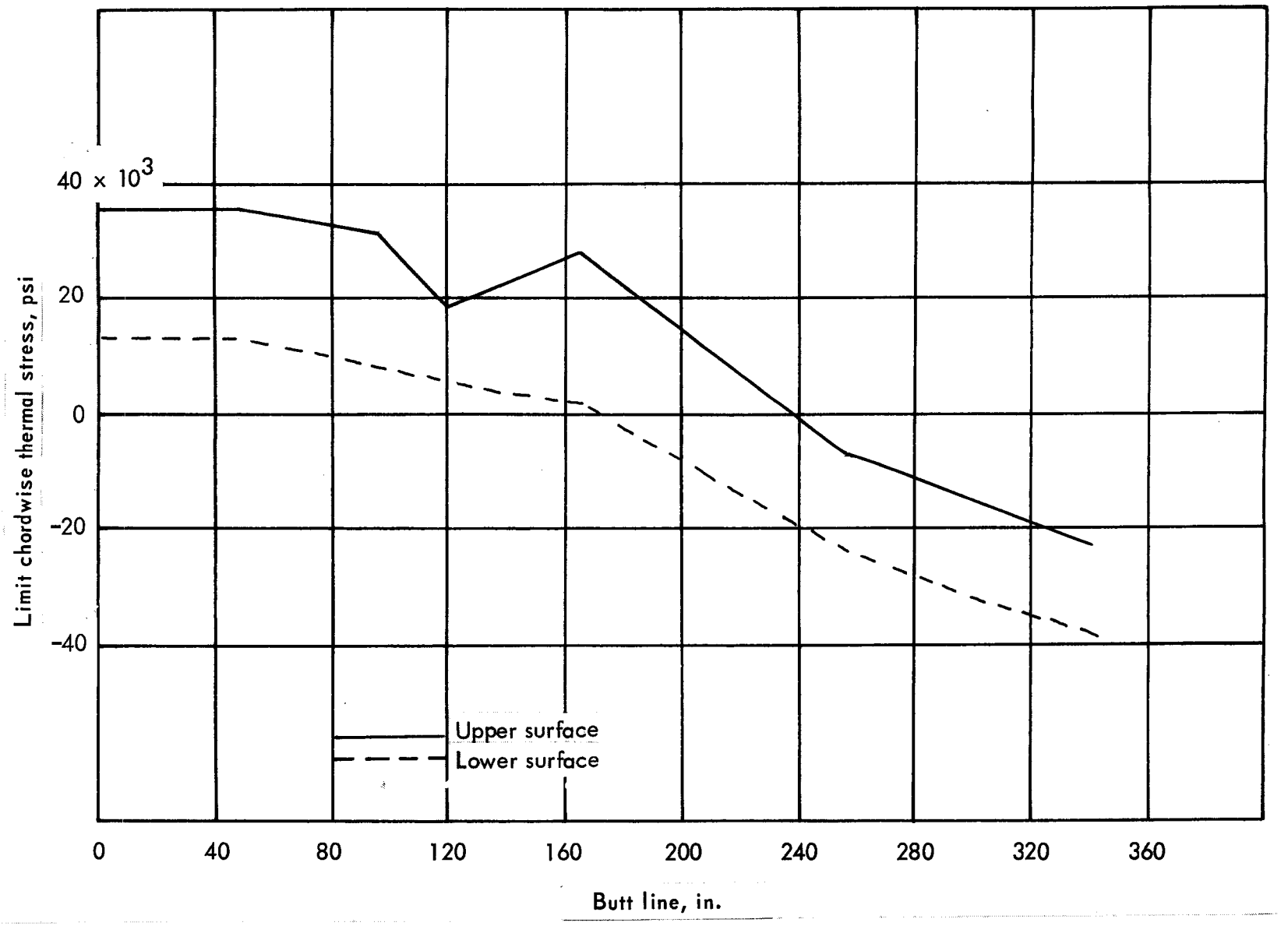

Figure 8-20. Limit thermal stress distribution at Sta. 2320 for semimonocoque chordwise concept: +2.0-g condition, tubular panel, both surfaces heat shielded, no insulation

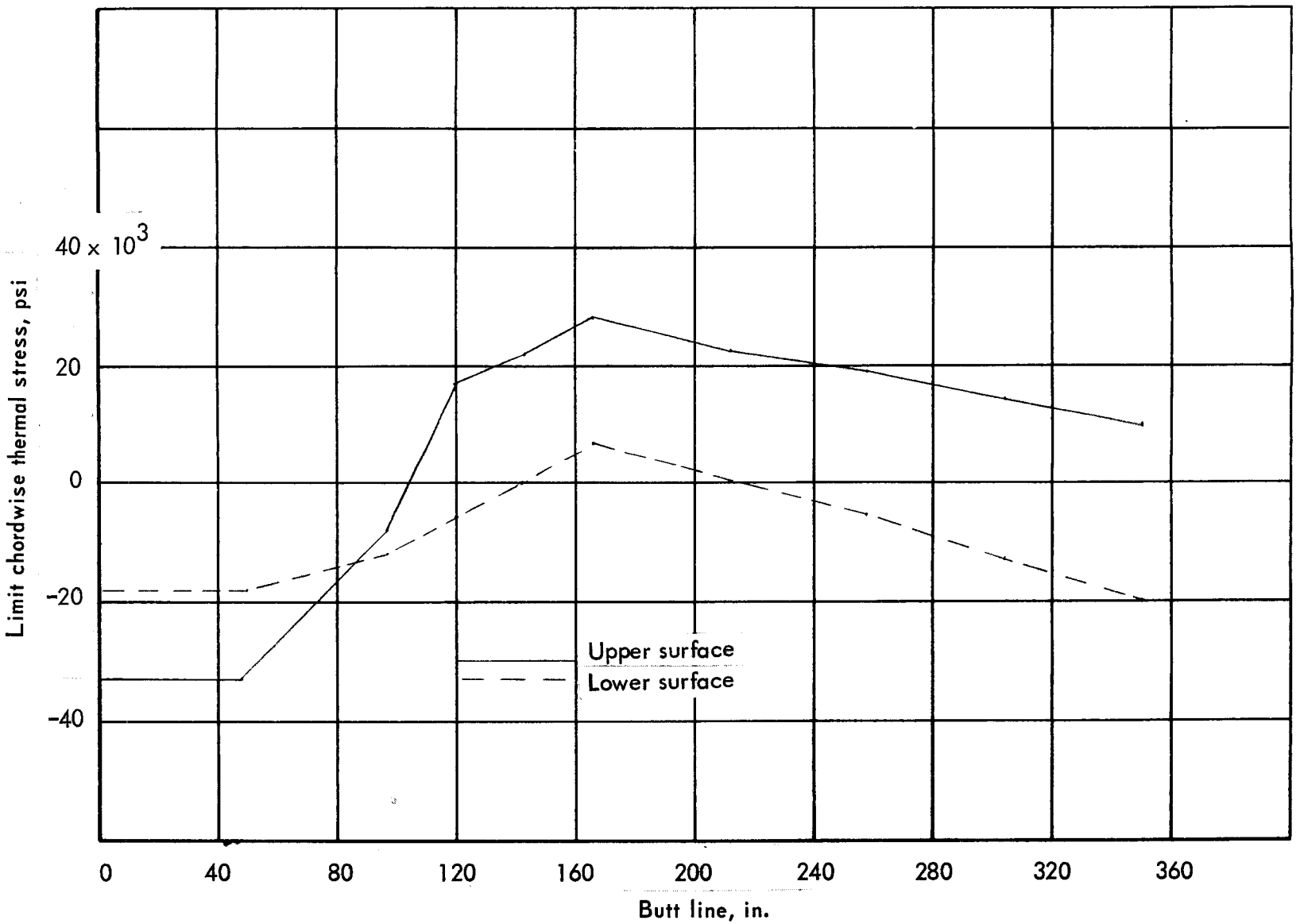

Figure 8-21. Limit thermal stress distribution at Sta. 2320 for semimonocoque chordwise concept: cruise condition, tubular panel, both surfaces heat shielded, no insulation

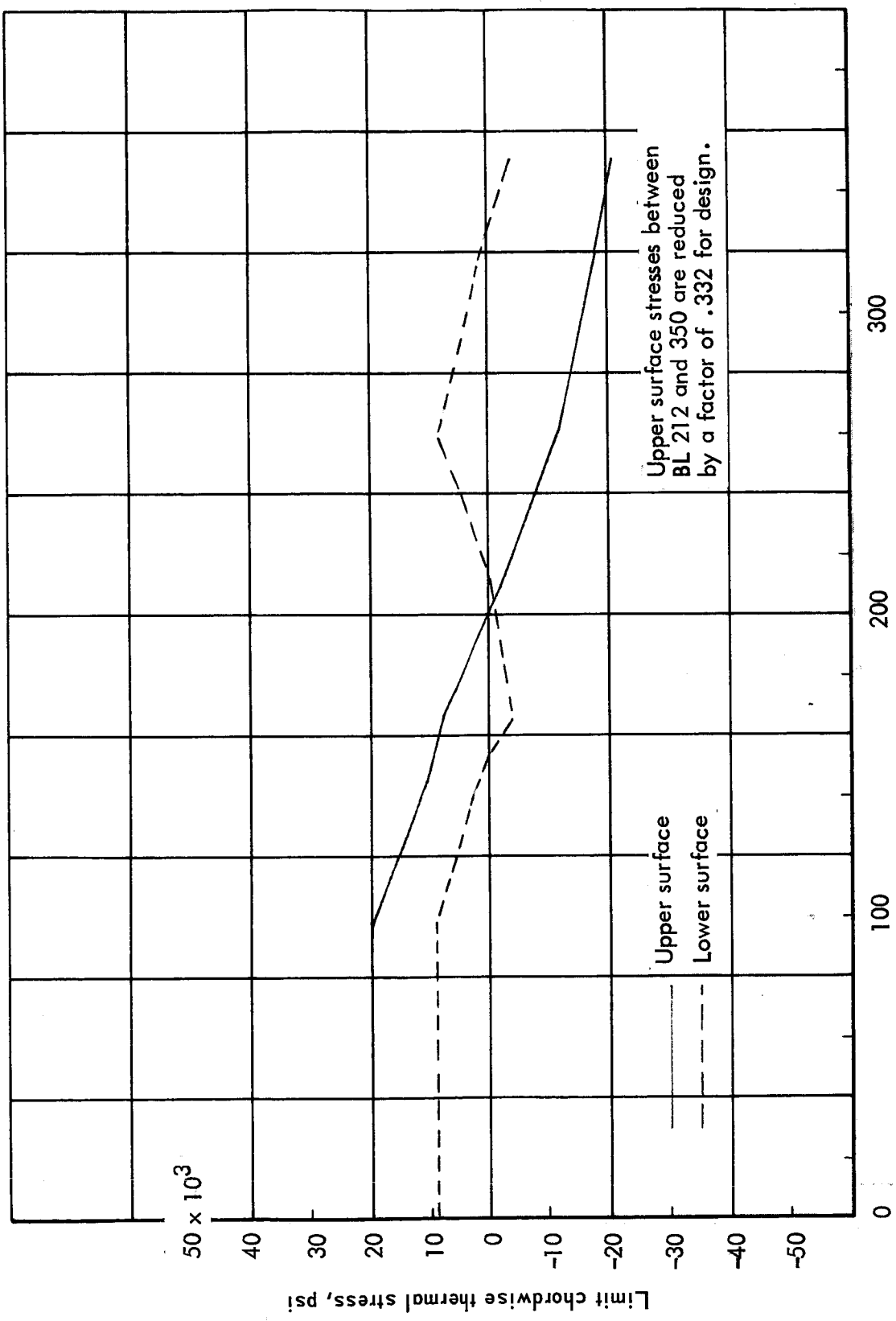

Figure 8-22. Limit thermal stress distribution at Sta. 2320 for semimonocoque chordwise concept: -0.5-g condition, tubular panel, both surfaces heat shielded, partial insulation lower outboard

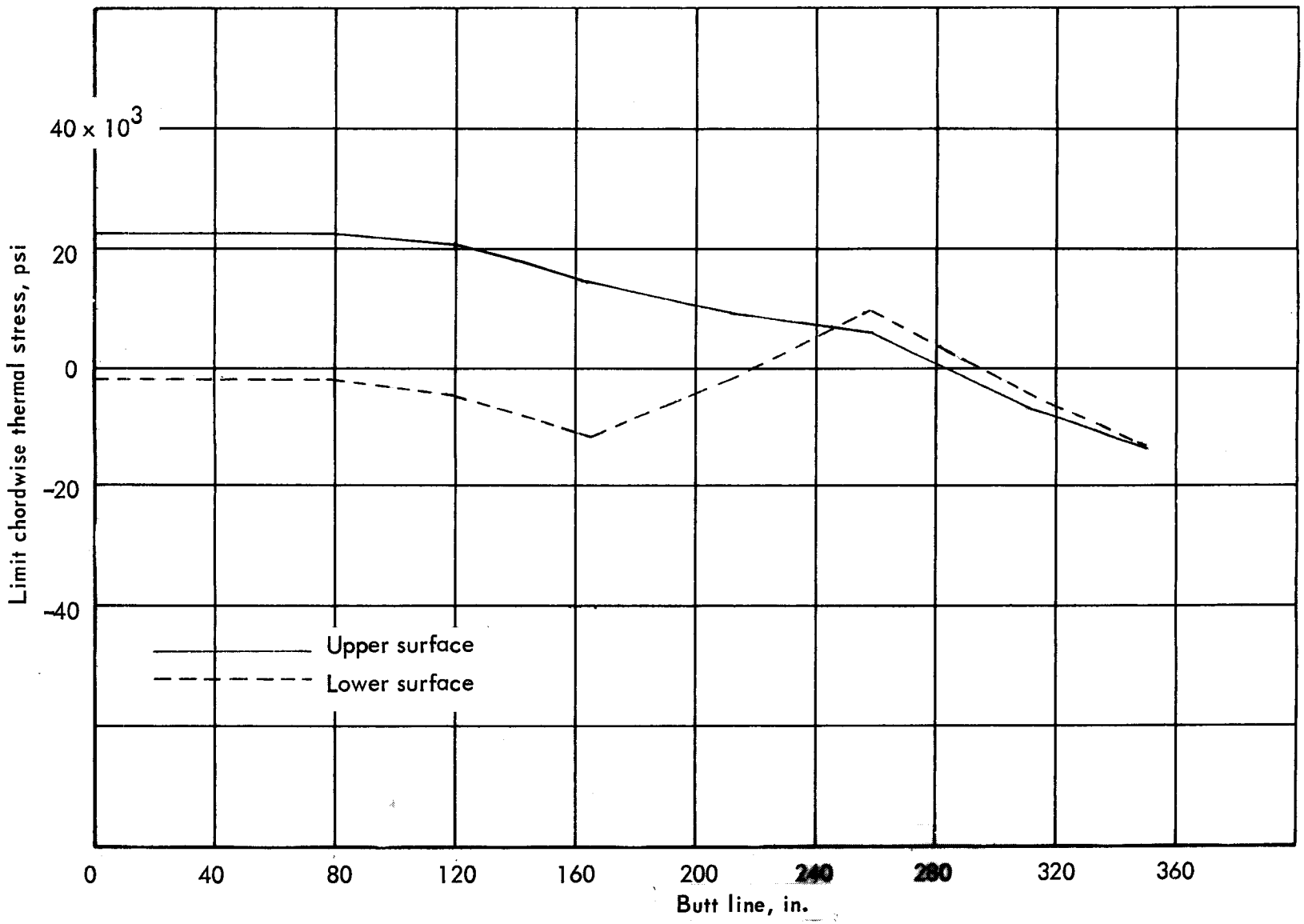

Figure 8-23. Limit thermal stress distribution at Sta. 2320 for semimonocoque chordwise concept: 2.0-g condition, tubular panel, both surfaces heat shielded, partial insulation lower outboard

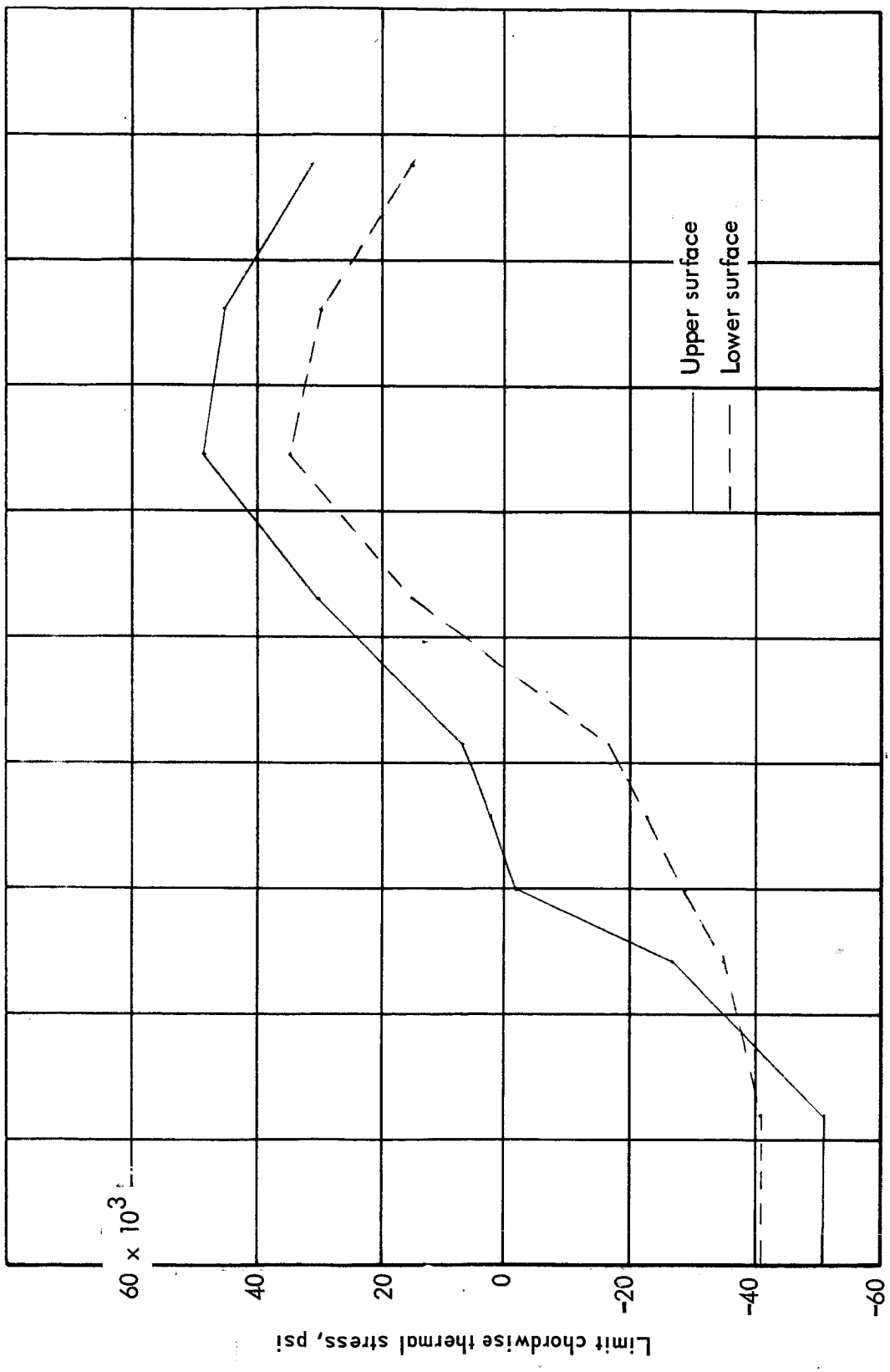

Figure 8-24. Limit thermal stress distribution at Sta. 2320 for semimonocoque chordwise concept: cruise condition, tubular panel, both surfaces heat shielded, partial insulation lower outboard

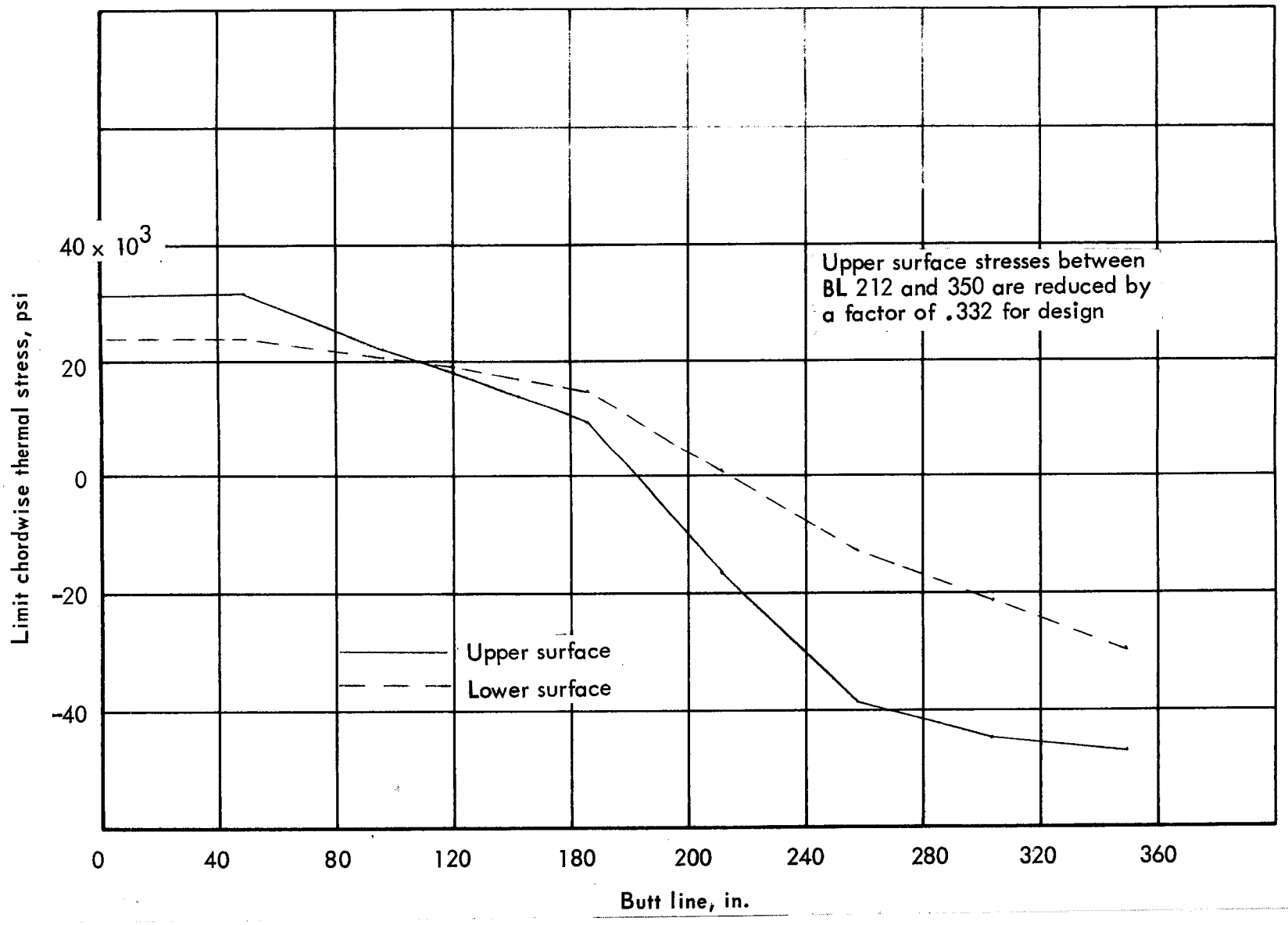

Figure 8-25. Limit thermal stress distribution at Sta. 2320 for semimonocoque chordwise concept: -0.5-g condition, convex beaded (upper) and tubular (lower) panel, lower surface heat shielded, no insulation

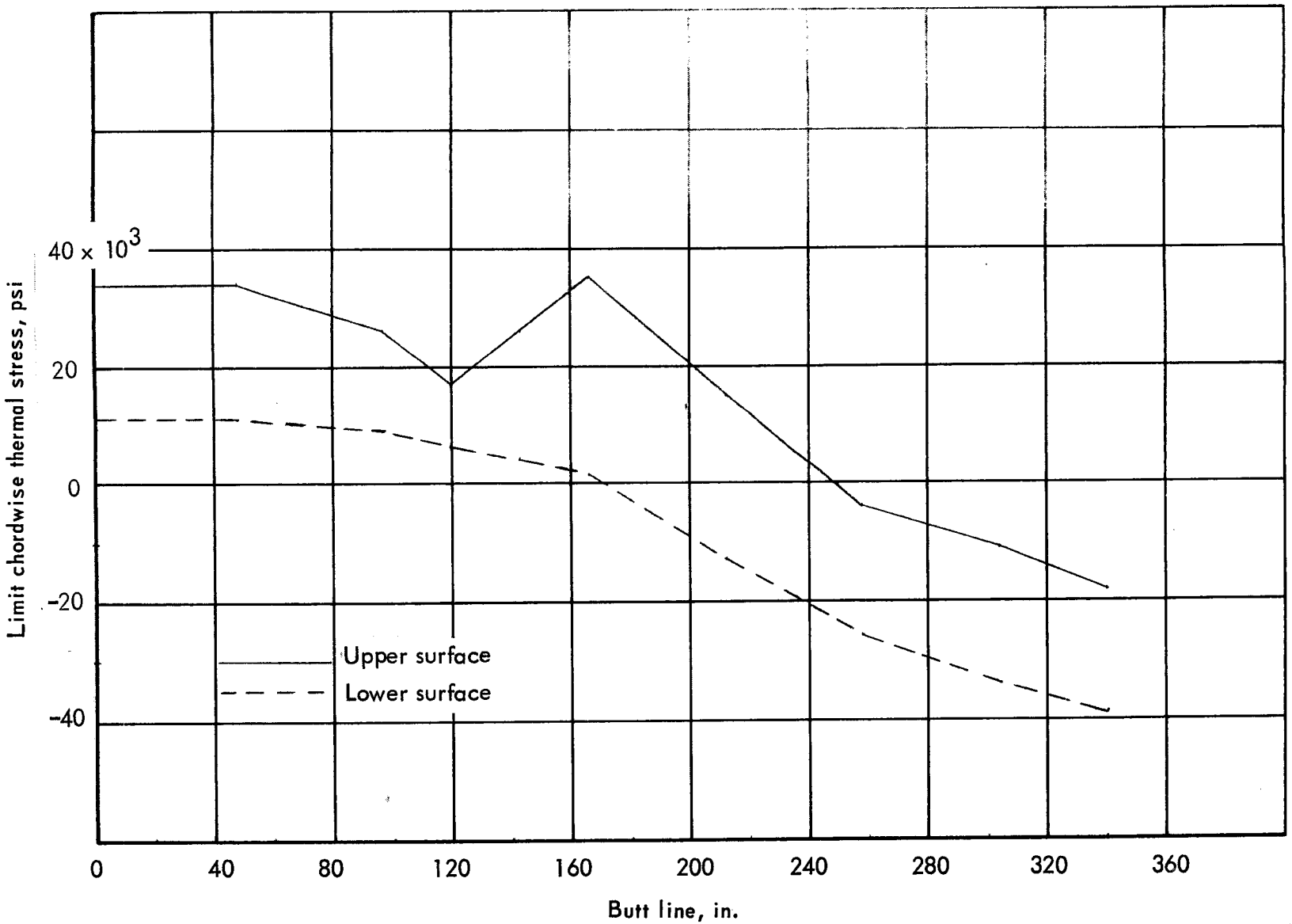

Figure 8-26. Limit thermal stress distribution at Sta. 2320 for semimonocoque chordwise concept: +2.0-g condition, convex beaded (upper) and tubular (lower) panel, lower surface heat shielded, no insulation

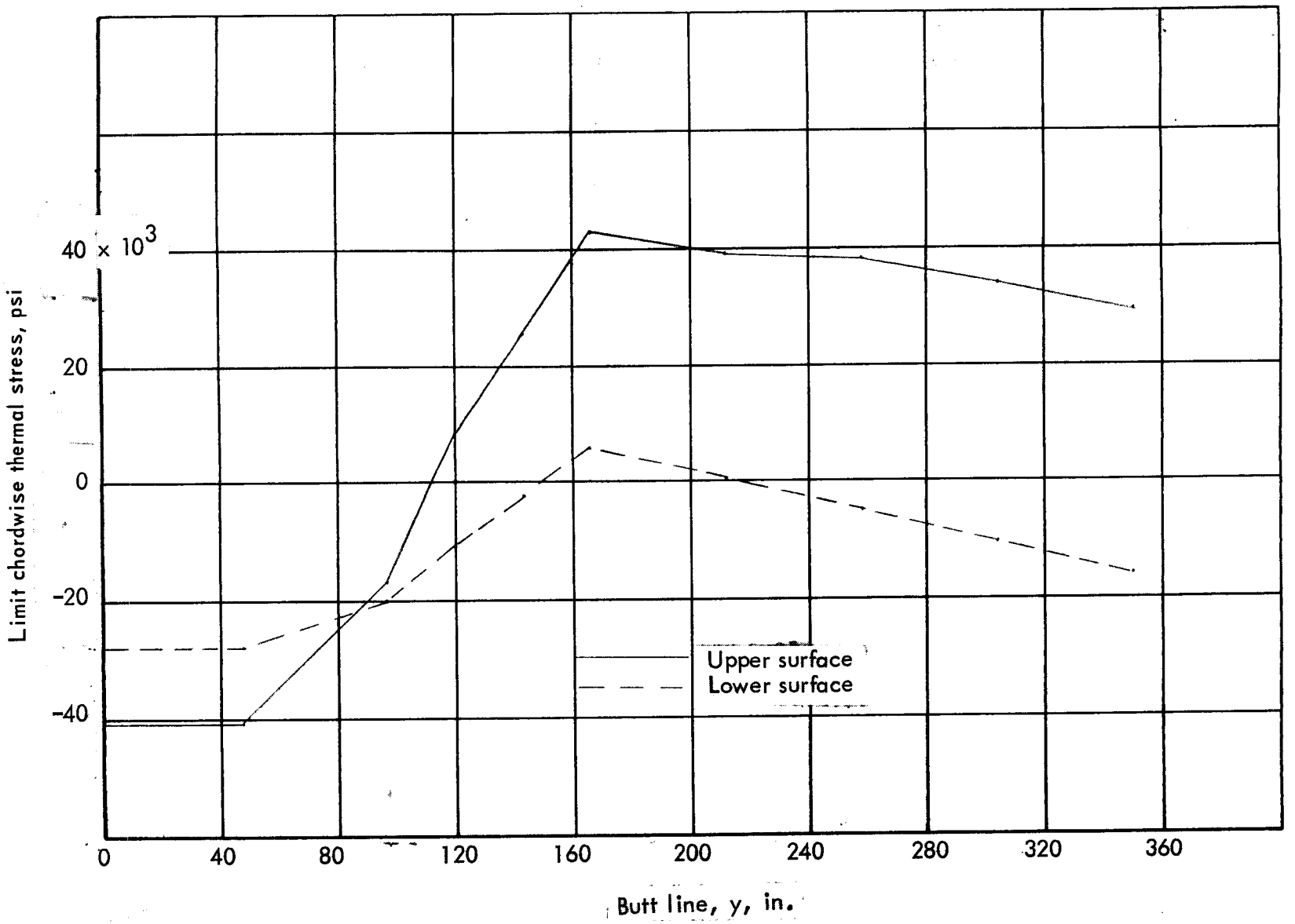

Figure 8-27. Limit thermal stress distribution at Sta. 2320 for cruise condition, convex beaded upper) and tubular (lower) panel, lower surface heat shielded, no insulation

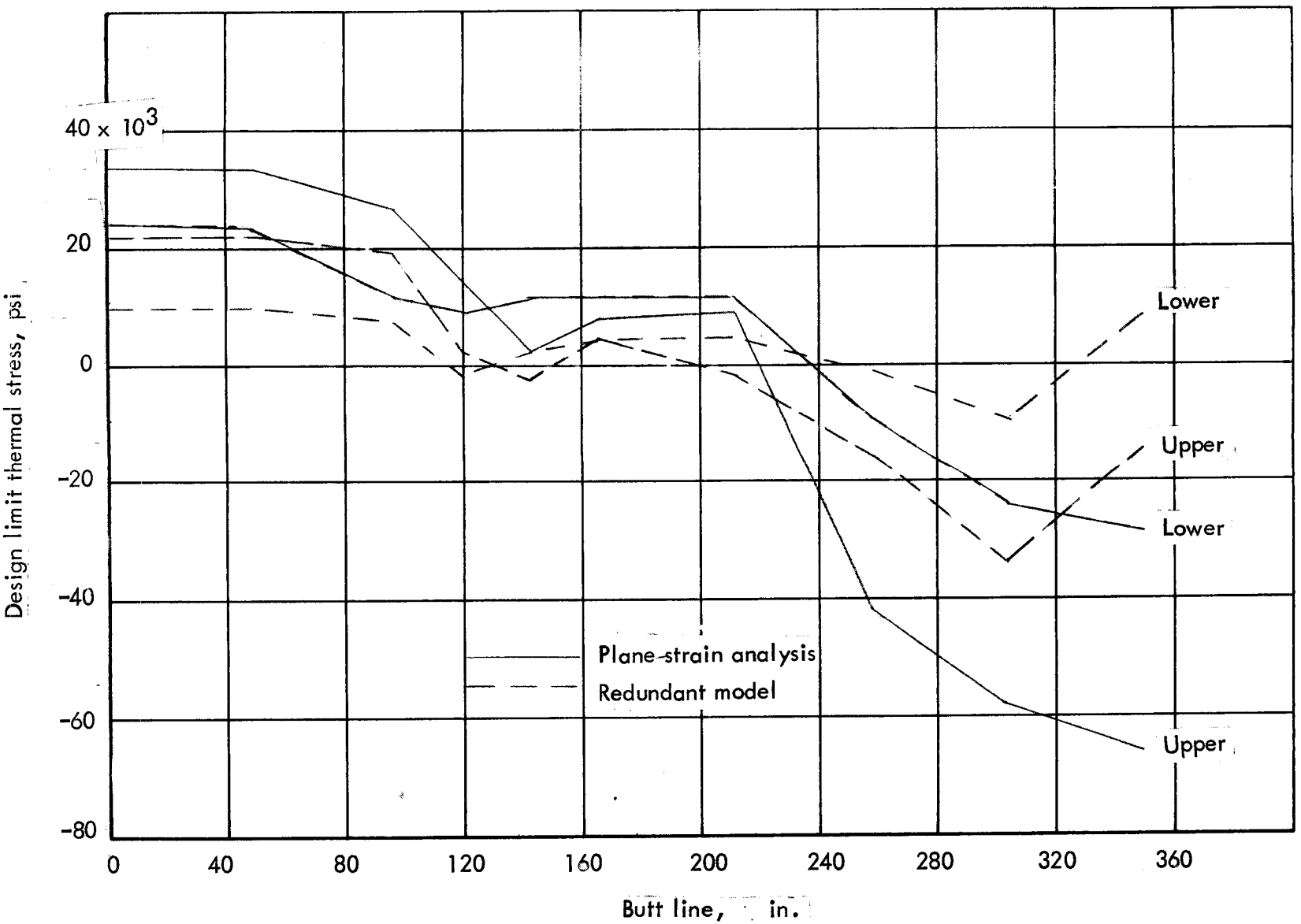

Figure 8-28. Limit thermal stress distribution at Sta. 2320 for -0.5-g condition, convex beaded upper and tubular lower panel; lower surface heat shielded, partial insulation lower outboard

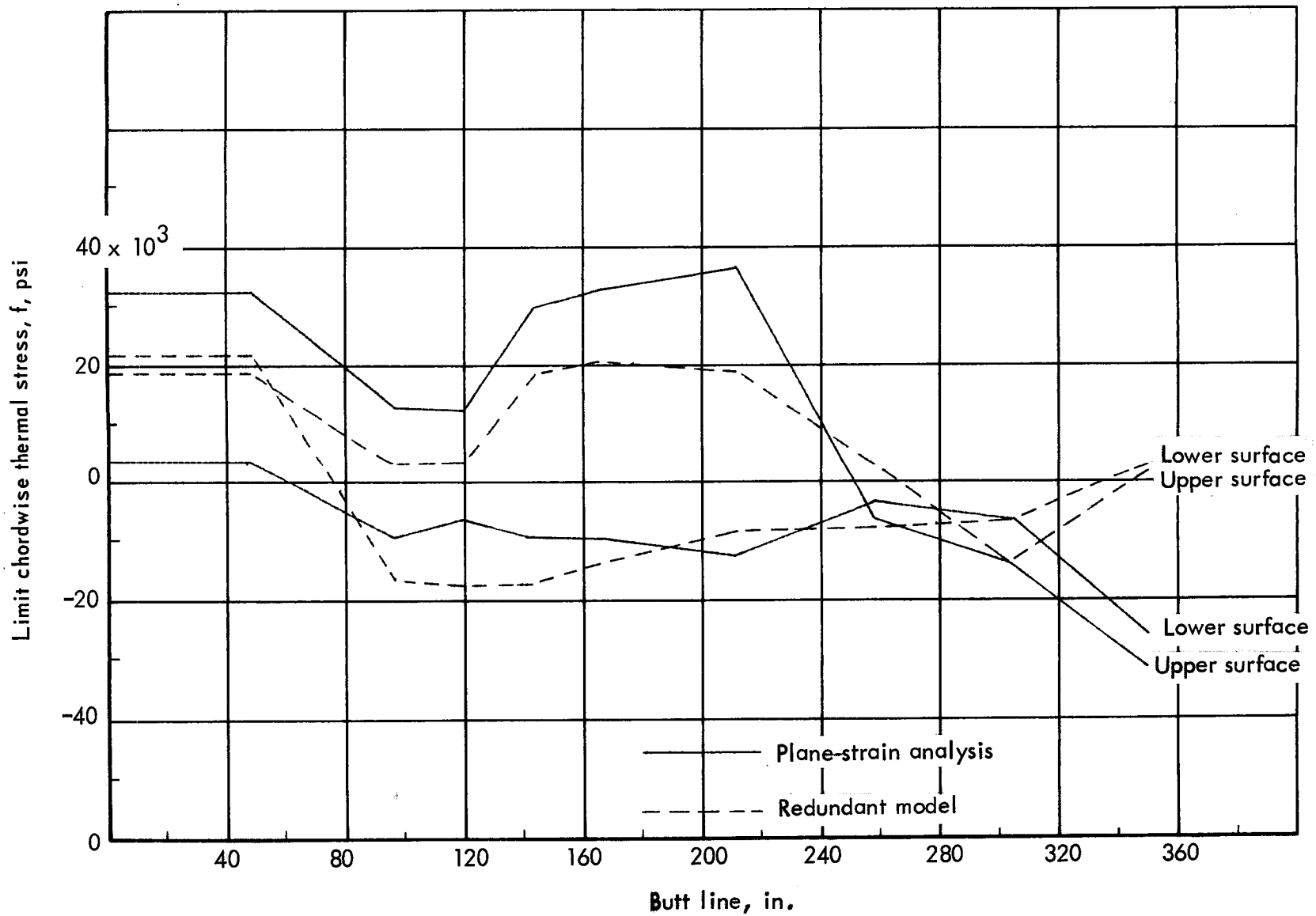

Figure 8-29. Limit thermal stress distribution at Sta. 2320 for +2.0-g condition, convex beaded upper and tubular lower panel, lower surface heat shielded, partial insulation lower outboard

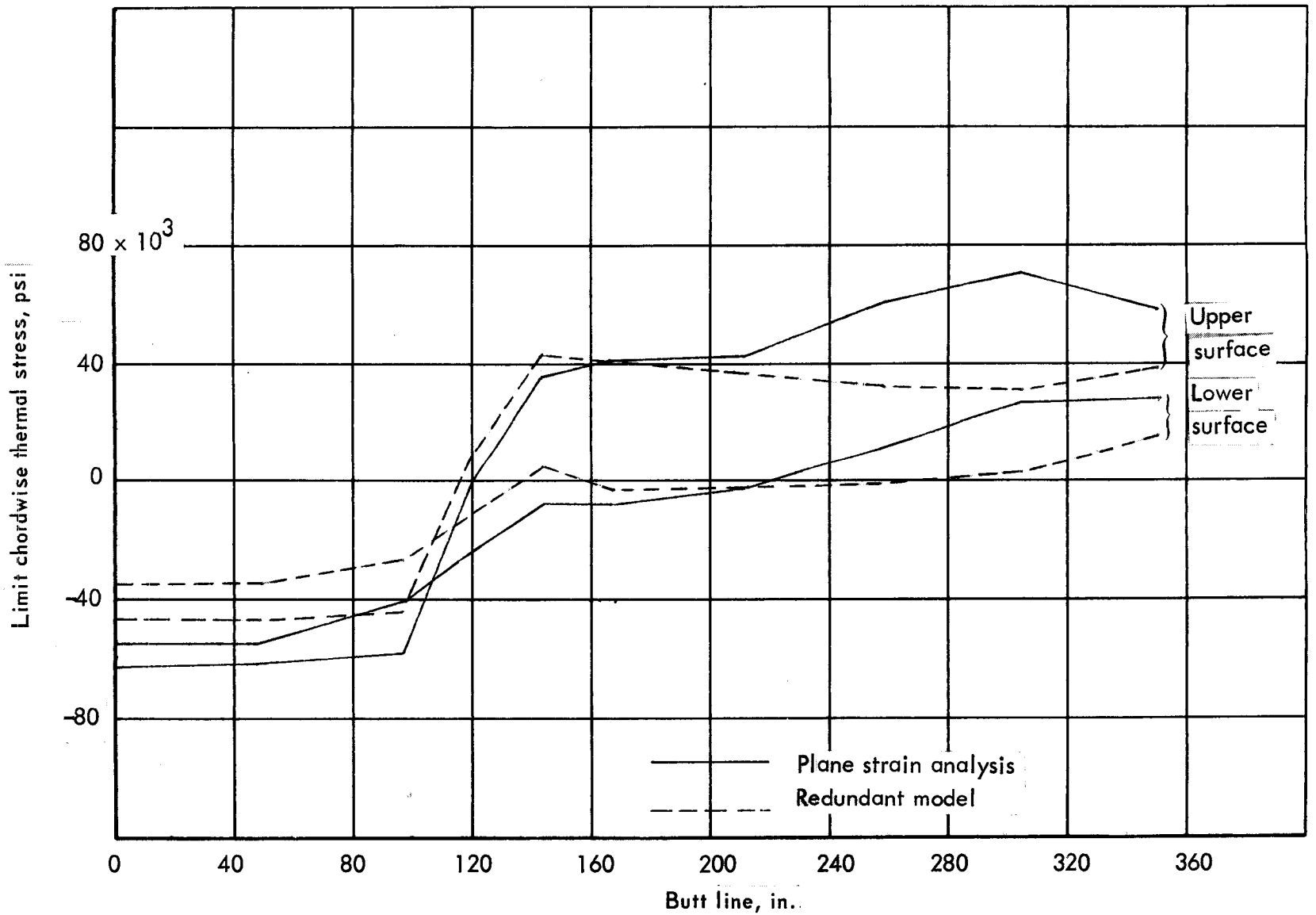

Figure 8-30. Limit thermal stress distribution at Sta. 2320 for cruise condition, convex beaded upper and tubular lower panel; lower surface heat shielded, partial insulation lower outboard

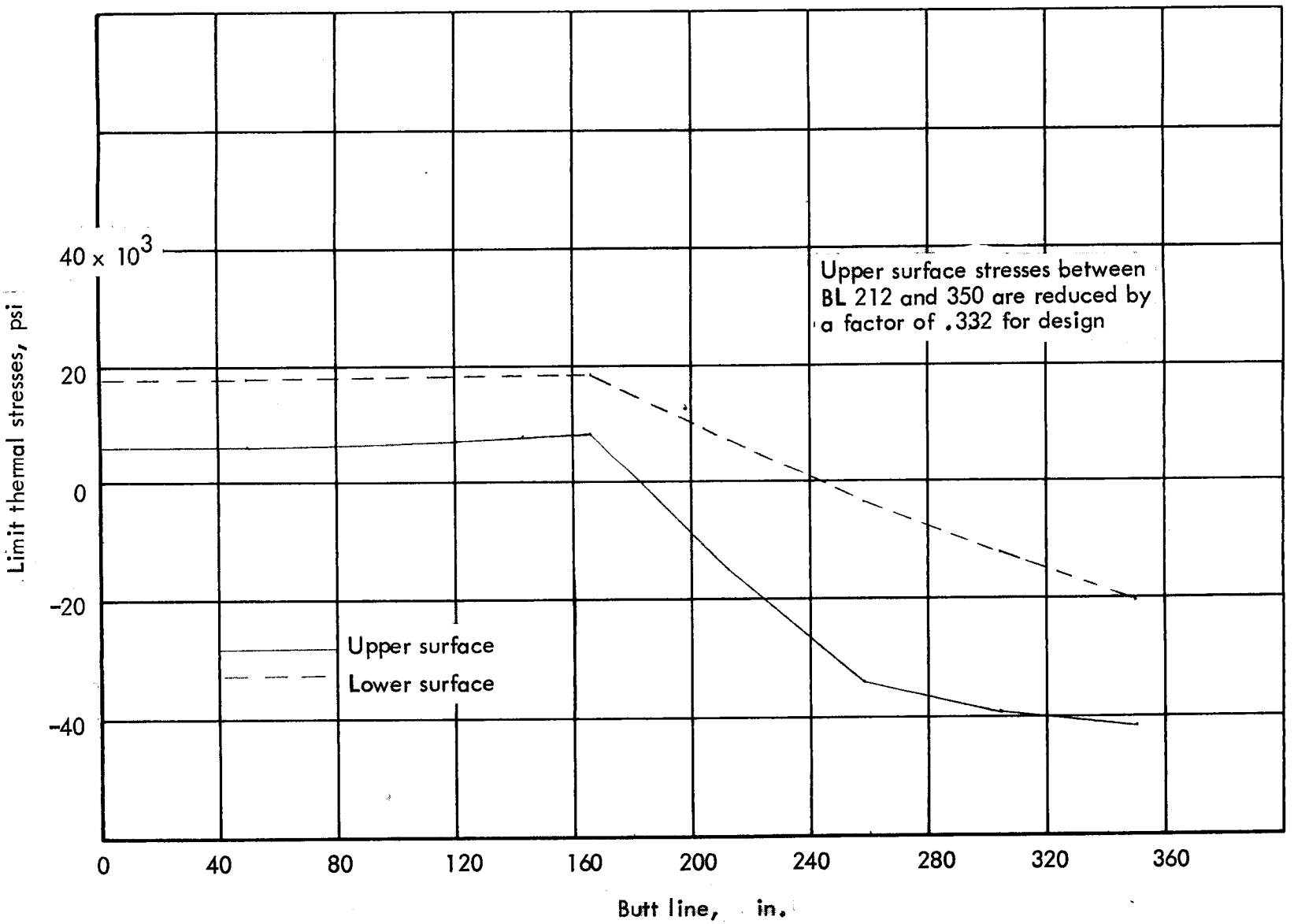

Figure 8-31. Limit thermal stress distribution at Sta. 2320 for -0.5-g condition, convex beaded panel, no heat shields or insulation

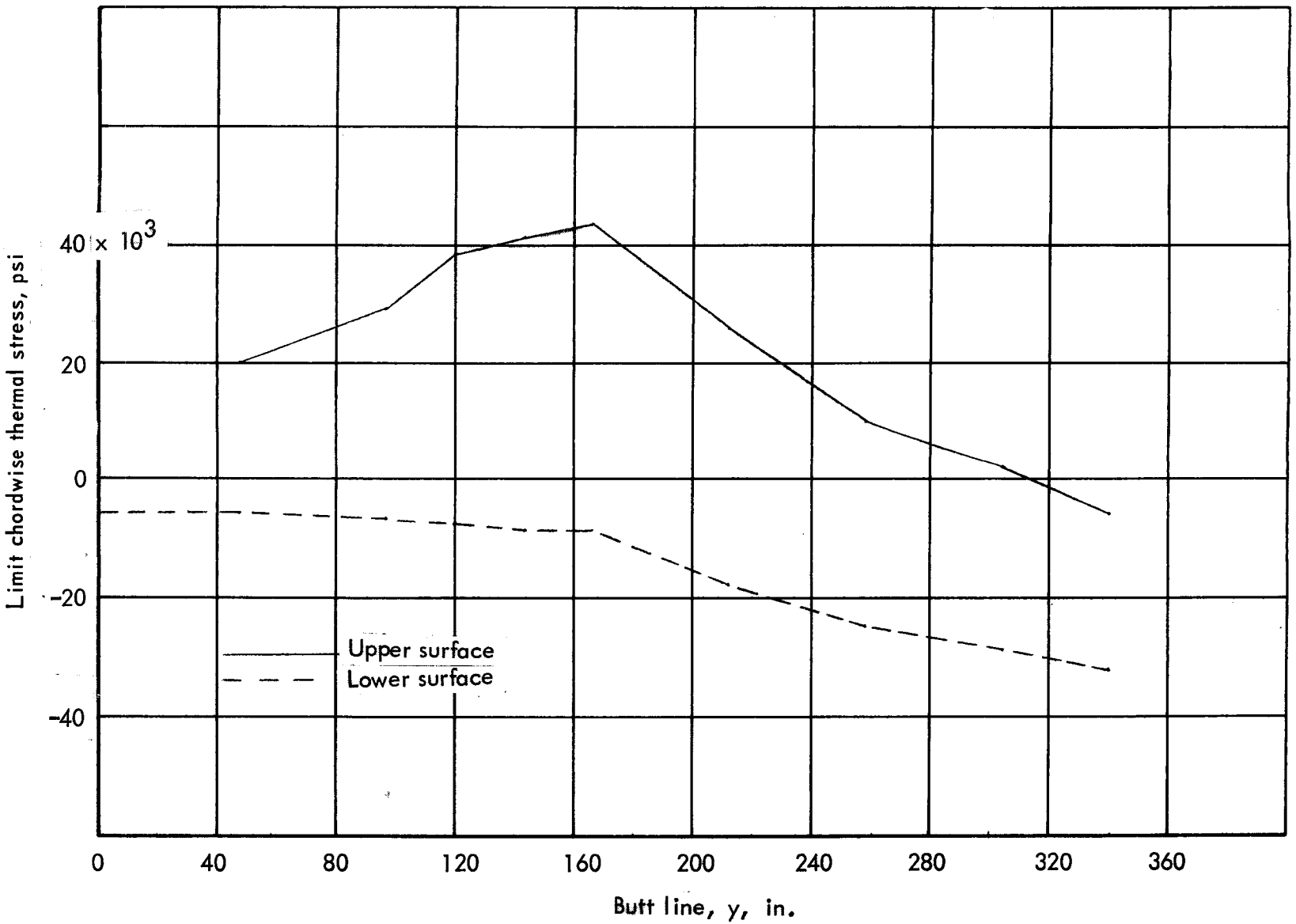

Figure 8-32. Limit thermal stress distribution at Sta. 2320 for +2.0-g condition, convex beaded panel, no heat shields or insulation

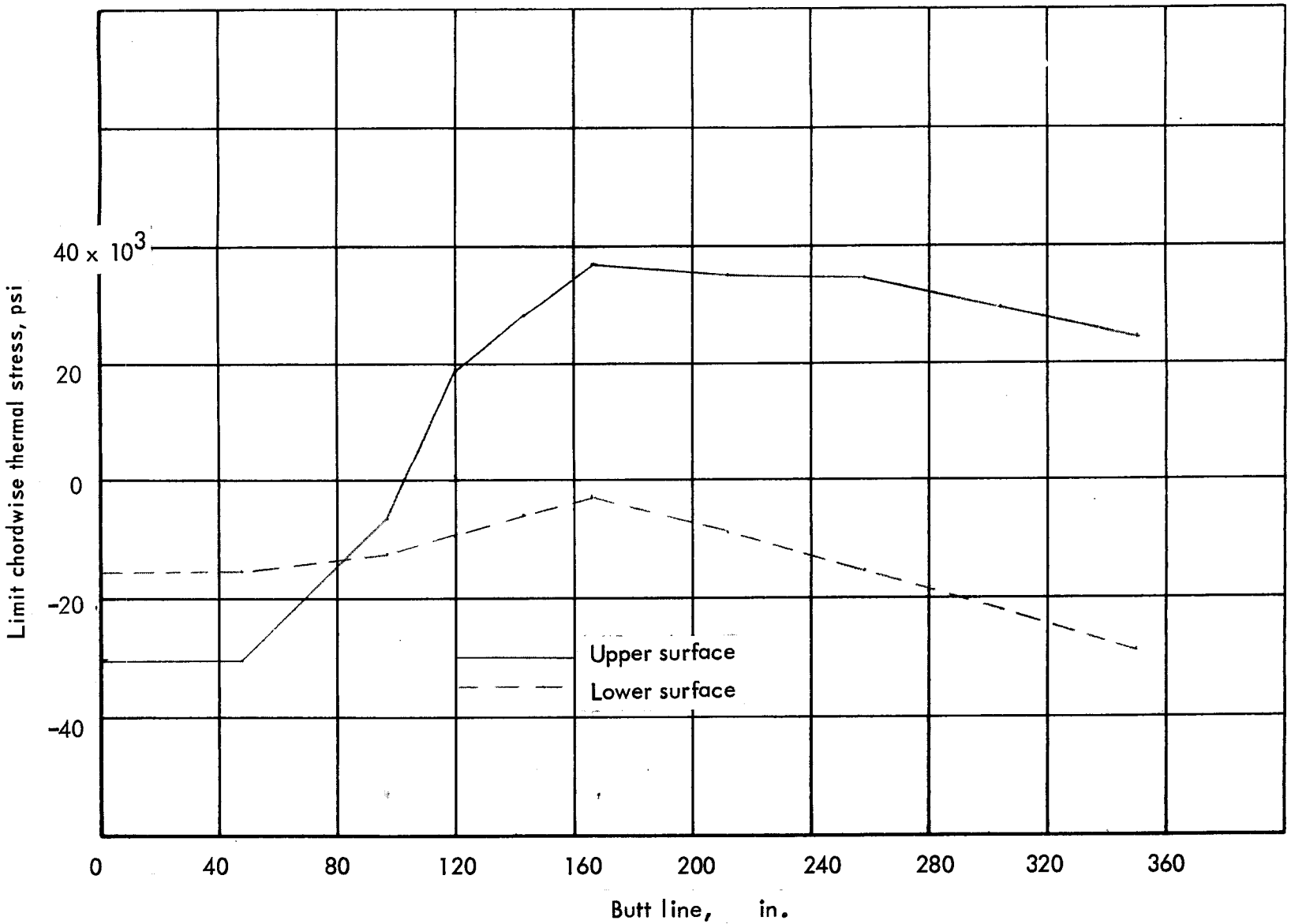

Figure 8-33. Limit thermal stress distribution at Sta. 2320 for cruise condition, convex beaded panel, no heat shields or insulation

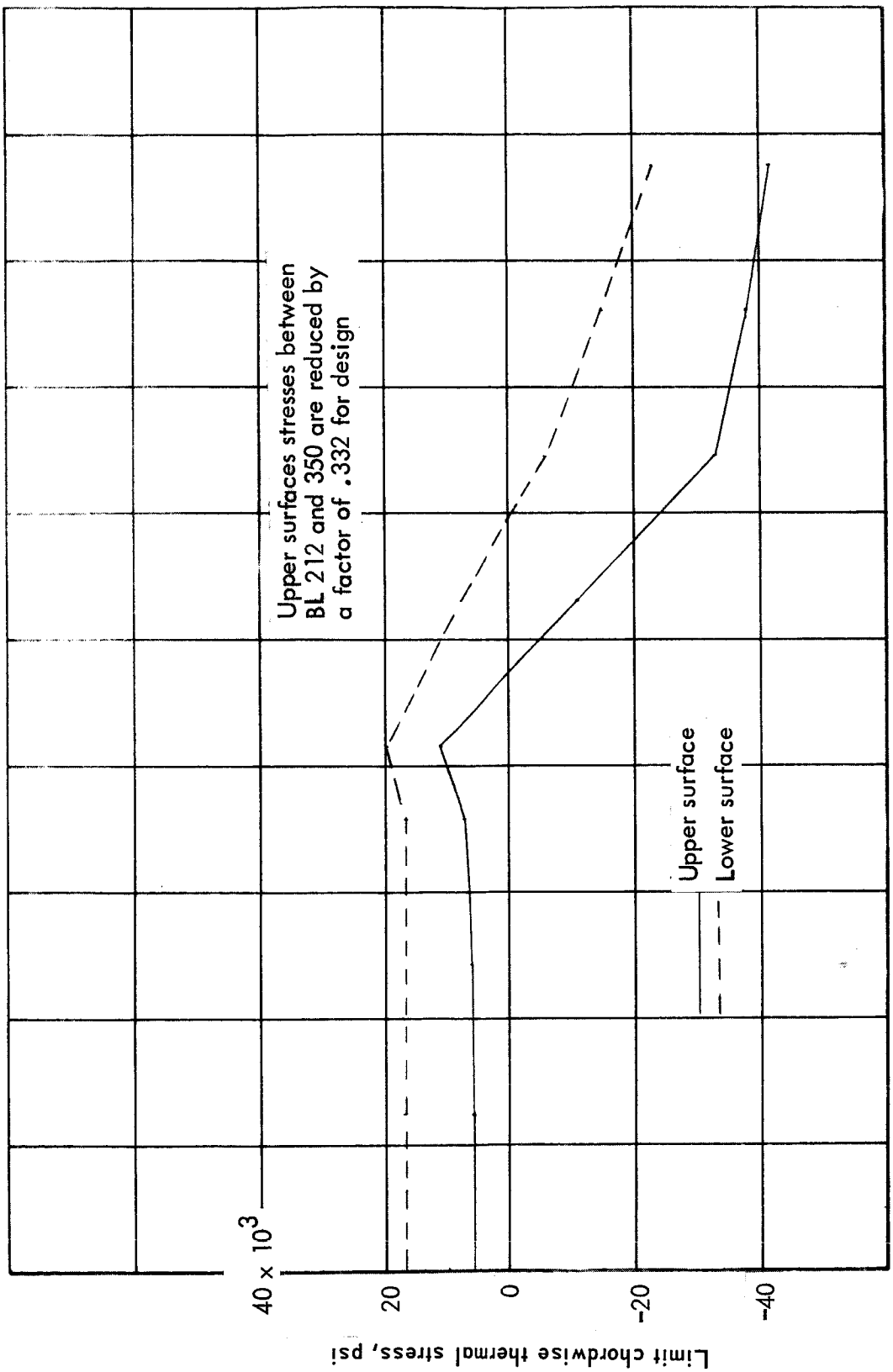

Figure 8-34. Limit thermal stress distribution at Sta 2320 for semimonocoque chordwise concept: -0.5-g condition, convex beaded panels, upper and center lower surfaces, tubular lower inboard and outboard, partial heat shield lower outboard, no insulation

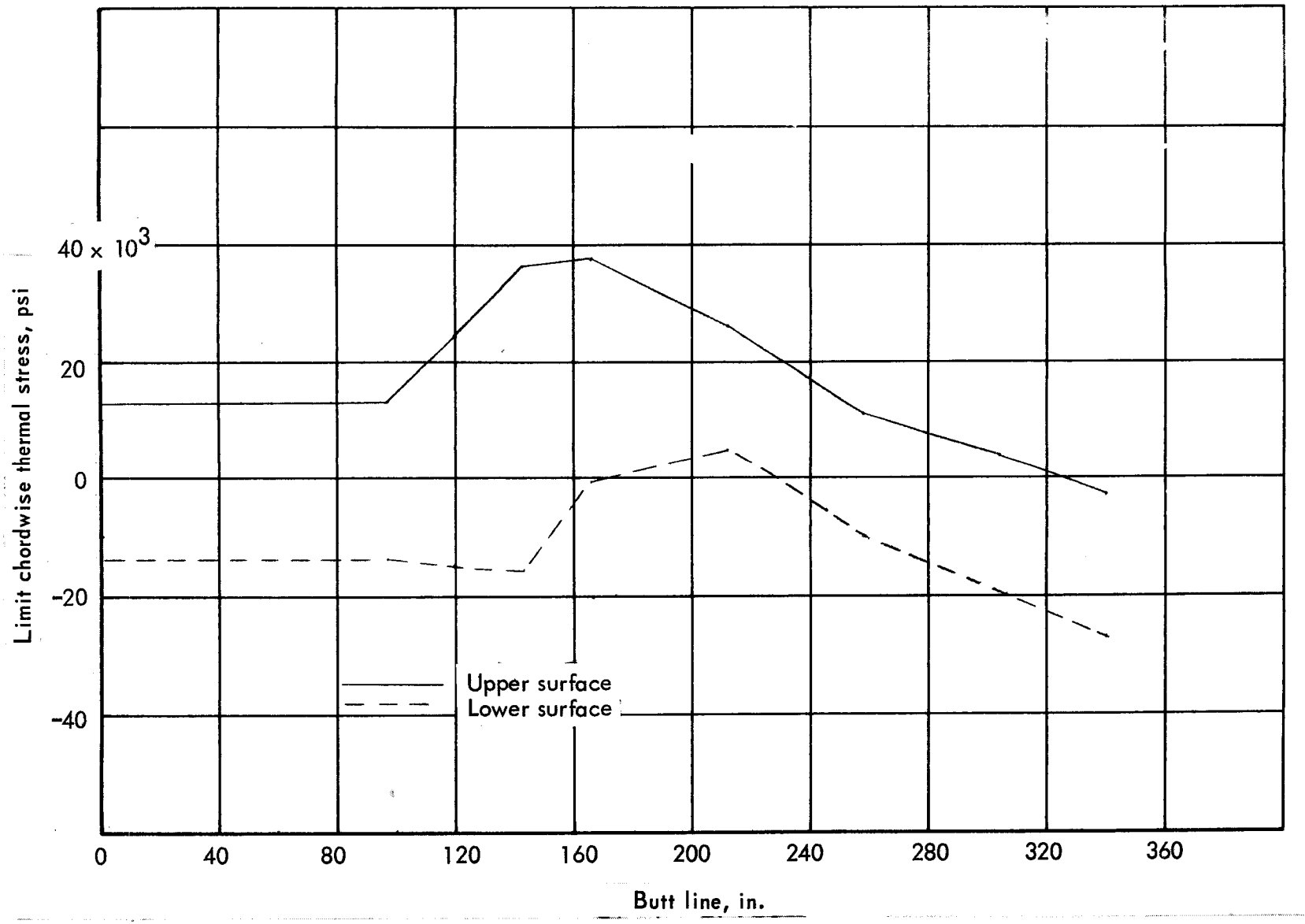

Figure 8-35. Limit thermal stress distribution at Sta. 2320 for semimonocoque chordwise concept: +2.0-g condition, convex beaded panels upper and center lower surfaces, tubular lower inboard and outboard, partial heat shield outboard, no insulation

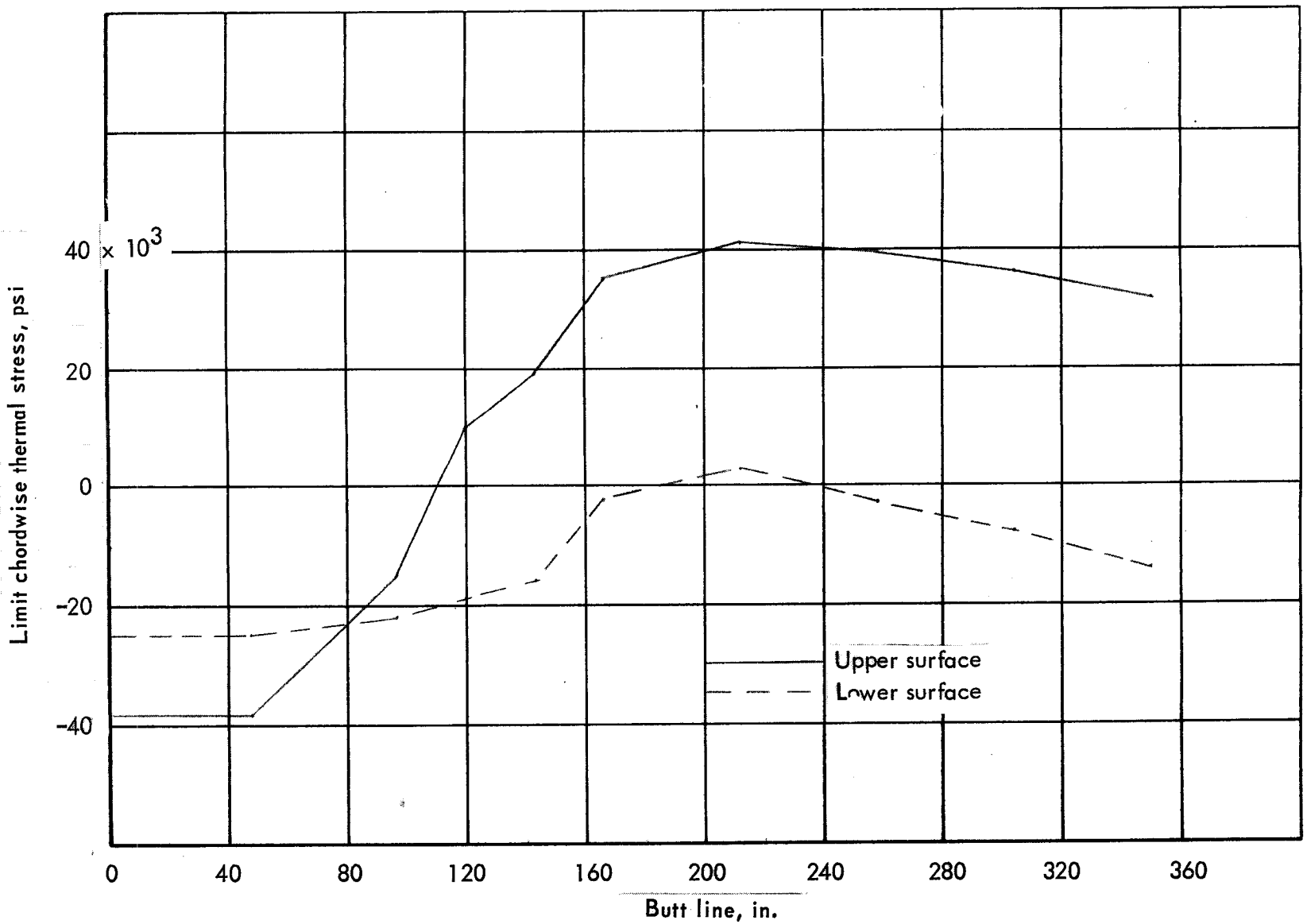

Figure 8-36. Limit thermal stress distribution at Sta. 2320 for semimonocoque chordwise concept: cruise condition, convex beaded panels upper and center lower surfaces, tubular lower inboard and outboard; partial heat shield outboard, no insulation

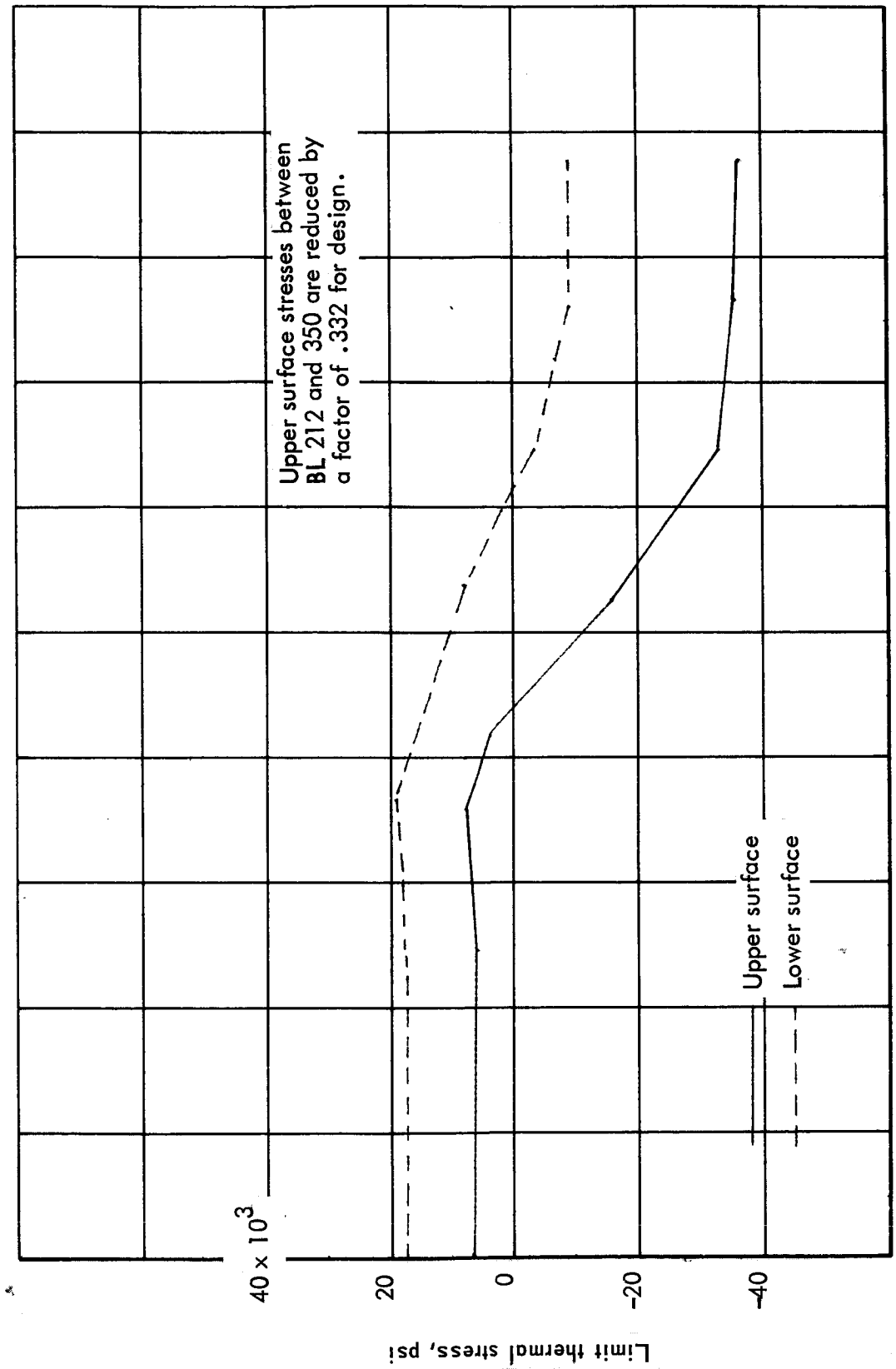

Figure 8-37. Limit thermal stress distribution at Sta 2320 for semimonocoque chordwise concept: -0.5-g condition, convex beaded panels, upper and center lower surfaces, tubular inboard and outboard lower, partial heat shield and insulation, lower outboard

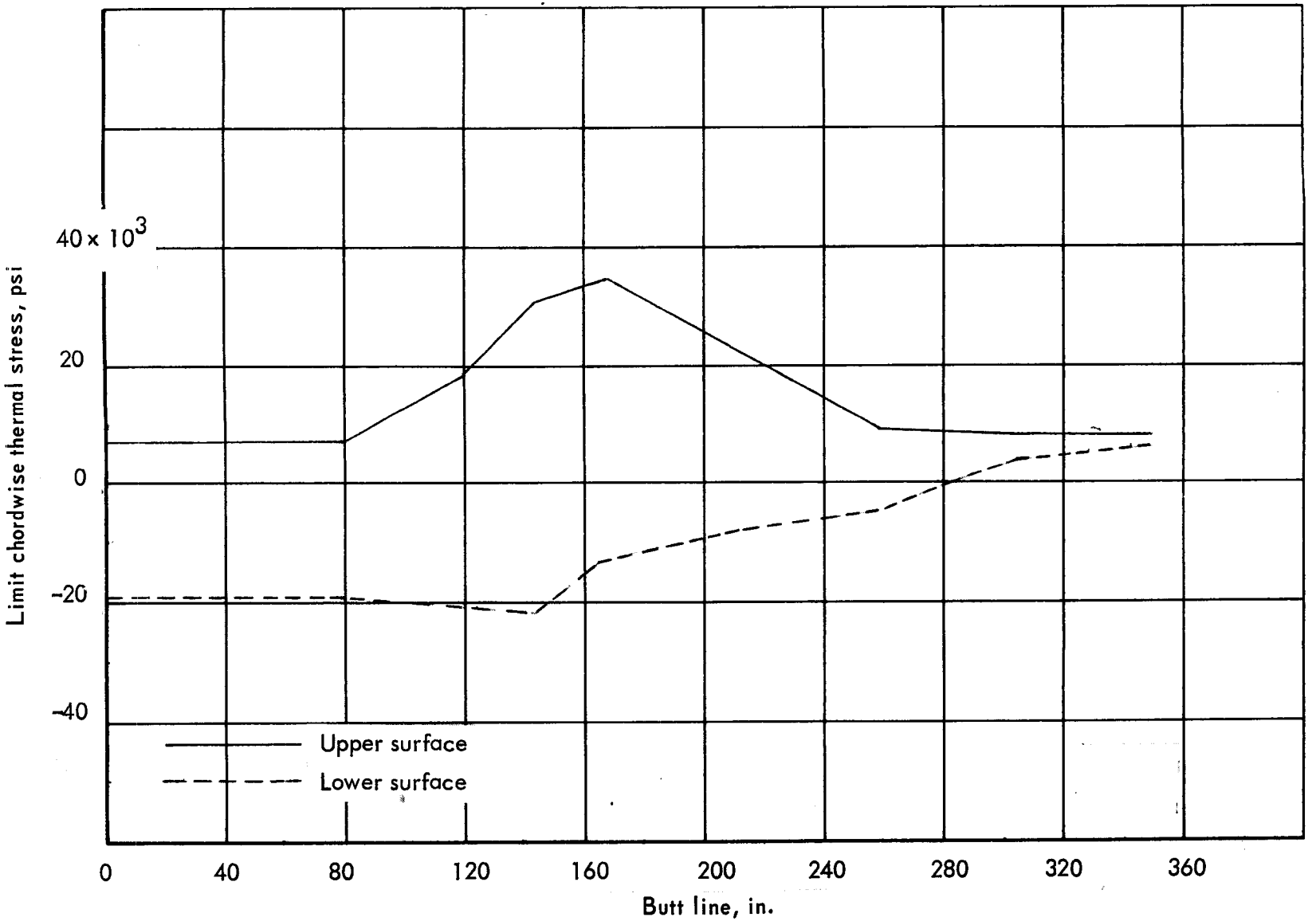

Figure 8-38. Limit thermal stress distribution at Sta. 2320 for semimonocoque chordwise concept: +2.0-g condition, convex beaded panels upper and center lower surfaces, tubular inboard and outboard lower, partial heat shield and insulation, lower outboard

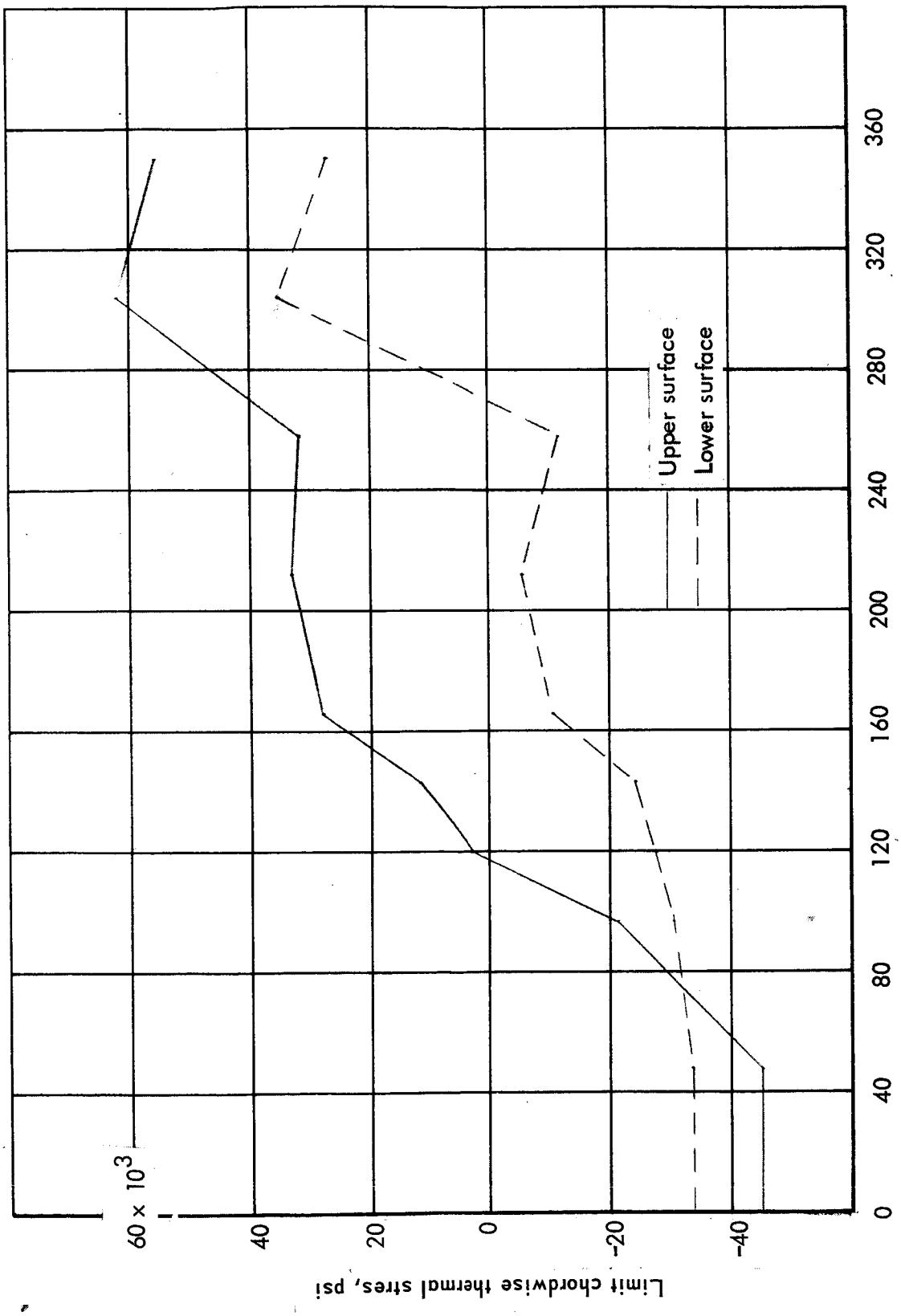

Figure 8-39. Limit thermal stress distribution at Sta. 2320 for semimonocoque chordwise concept: cruise condition, convex beaded panels upper and center lower surfaces, tubular inboard and outboard lower, partial heat shield and insulation, lower outboard

Section 9

INTERNAL THERMAL ANALYSIS

by

D. A. Brogan, F. R. Mastroly, and F. L. Guard

CONTENTS

ILLUSTRATIONS

TABLES

Section 9

SYMBOLS

Area A	Area between ℄ and BL 120 of wing study area
Area B	Area between BL 120 and BL 212 of wing study area
Area C	Area between BL 212 and BL 350 of wing study area
BL	Butt Line
FS	Fuselage Station
g	Gravitational acceleration
T	Temperature
T_1	Honeycomb-core sandwich panel external skin temperature
T_2	Honeycomb-core sandwich panel internal skin temperature
T(1)	Exterior face temperature of upper surface panel of semimonocoque concepts; waffle skin temperature
T(2)	Interior face temperature of upper surface panel of semimonocoque concepts; waffle temperature at base of stiffener
T(3)	Interior face temperature of lower surface panel of semimonocoque concepts; temperature at tip of stiffener on waffle panel
T(4)	Exterior face temperature of lower surface panel of semimonocoque concepts
T_{HS}	Heat shield temperature
$\bar{t}$	Equivalent thickness
ΔT	Temperature difference between external and internal face sheets of honeycomb-core sandwich panel
ΔT_a	Waffle-panel skin to stiffener-tip temperature differential
ΔT_b	Waffle-panel stiffener base to tip temperature differential
ΔT_{lower}	Semimonocoque lower surface panel temperature differential
ΔT_{upper}	Semimonocoque upper surface panel temperature differential

Section 9

INTERNAL THERMAL ANALYSIS

Detail internal thermal analyses were conducted. The thermal analyses required for the heat shield and leading edge comparison evaluations are presented in sections 20 and 21.

MONOCOQUE WAFFLE CONCEPTS

The thermal-protection arrangements were determined on the basis of material capability, practicality of design for the given wing cross-section, and detailed thermal analysis data. The thermal analysis data include transient effects on structural temperatures and isotherms generated for each candidate thermal-protection arrangement. The transient effects are based on a general thermal-model which includes effects of heat-shield placement, lower surface insulation, and spar/rib size. Typical temperature distributions for the candidate thermal-protection arrangements at FS 2320 are shown in figure 9-1.

Figure 9-1 presents wing-fuselage temperatures (+2.0-g condition) for the candidate thermal-protection system arrangements and indicates the temperature and gradient compatability of the fuselage and wing. The most vertical temperature profiles of figure 9-1 indicates the lowest thermal gradient through the wing and fuselage cross-section. When these profiles are close together horizontally, the spanwise wing surface thermal gradients are lowest. Using these criteria, the arrangement with lower surface heat shields and insulation outboard of the one-third wing chord provides the lowest spanwise wing thermal gradients, and the closest match between the fuselage gradient and the gradient through the wing.

Thermal analysis of the monocoque (waffle panel) structural concept was accomplished with three different approaches. All were transient analyses using the computer program of reference 9-1 for the solution of thermal networks representing the actual structure with varying degrees of complexity. The first method, or "gross model" approach, analyzed the section of wing between FS 2320 and FS 2412 and from vehicle centerline to the wing leading edge, as shown in the sketch below:

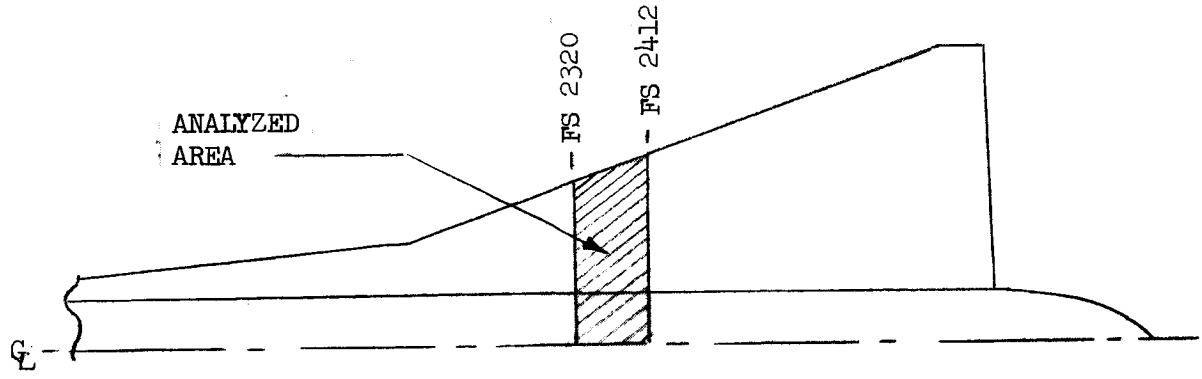

Primary structures (upper and lower panels and vertical webs) were represented by flat plates of uniform thickness and temperature. Internal heat transfer was by radiation only, with configuration factors determined for diffusely emitting and reflecting gray surfaces by the Hottel matrix method. The gross model approach was used to determine mean temperature histories for panels, webs, and heat shields, beam cap temperature histories, and the effects on all temperatures of varying insulation thickness in thermally protected areas. The second approach was used to develop isotherms for the entire wing structure and employed the same degree of thermal network complexity as the gross model approach. Thirty locations on the wing were examined. This provided an adequate base from which to draw temperature pattern lines for the entire upper and lower wing surfaces at specific trajectory times. The third approach was a detailed analysis of the waffle panel structure, using a thermal network of five nodes (one for the waffle skin and four along the stiffener) to account for conduction and radiation through the panel. Upper and lower surface panels were examined at locations along FS 2366 (under fuselage, inboard wing, and outboard wing), accounting for radiation heat transfer within the panel-web wing box structure by the Hottel matrix method. The detailed temperatures derived were used to determine local stresses and deflections due to temperature gradients through the panel structure.

Preliminary temperatures determined from the radiation equilibrium analyses indicated that thermal protection is required at the outboard wing areas to limit primary structure temperatures to under 1600°F and to control thermal gradients. To determine the extent of thermal protection required for the monocoque concept, the variation in structure temperatures with insulation thickness was examined at one fuselage station (FS 2366) from BL 240 to BL 360. These temperatures, derived from the gross model analysis, were examined at the

-0.5g condition (20.3 minutes in the trajectory) to observe upper surface peaks, at the +2.0g condition (20.6 minutes) to observe lower surface peaks, and during cruise (40 minutes) to observe near steady-state effects. The gross model assumed flat structural panels with an equivalent thickness $\bar{t}$ of 0.05 inch and 0.06 inch for the upper and lower surfaces, respectively. A 0.011 inch flat sheet of Rene' 41 was assumed for the heat shield on the lower surface. The upper surface was unshielded. Insulation material was 6.0 pcf Dyna-Flex. Figures 9-2, 9-3, and 9-4 show waffle panel and lower heat shield temperatures along FS 2366 for the three flight conditions, respectively. Each figure shows the temperatures derived for no insulation and for insulation thicknesses of 0.25 and 0.50 inch attached to the inner surface of the shield. The general effect of insulation in this area is to lower panel temperatures and to increase heat shield temperatures. Insulation thickness for the monocoque waffle concept was selected to maintain the 1600°F material limit and to minimize temperature level differences in the spanwise direction to lower thermal stresses. Accordingly, based on the temperatures at FS 2366 shown in these figures, an insulation thickness of 0.25 inch is used from the leading edge to BL 341, a thickness of 0.12 inch is used between BL 341 and BL 268, and no insulation is used with the heat shield from BL 268 to BL 232. The remaining inboard lower surface is unshielded. Application of these results to the entire wing is shown in figure 9-5. The 0.25 inch insulation is used from the leading edge inboard to a line 34 inches from the edge and running parallel to it. The 0.12 inch insulation covers from this line to three-fourths of the distance to the inboard edge of the heat shield. This distance varies because the inboard heat shield edge follows roughly a line under the forward upper surface slope break, which does not parallel the leading edge. The entire lower surface is shielded outboard of BL 442 to protect against higher surface temperatures due to shorter leading edge distances in this area.

Isotherms for the monocoque waffle primary structure and heat shield are shown in figures 9-6, 9-7, and 9-8 for the -0.5g, +2.0g, and cruise flight conditions, respectively. Since the analysis method for the 30 wing locations used to derive the isotherm temperatures did not account for insulation effects, temperatures in the shielded area were adjusted for insulation by using the curves in figures 9-2 through 9-4. Dashed lines shown on the lower surface are located under the upper surface slope breaks, shown with solid lines on the upper surface diagram. Some lower surface isotherms are located along these dashed lines, reflecting the influence of sharp temperature differences between differently sloped sections of the upper surface. The heat shield is shown displaced from its position covering part of the lower surface for illustration clarity. The effect of the heat shield on the temperatures of both surfaces is illustrated particularly at BL 442. Comparison of the temperatures of unshielded areas of the monocoque waffle wing with the radiation equilibrium isotherms shown in the aerodynamic heating section, section 3, substantiates the trend to overpredict temperatures when transient effects are neglected during peak heating. The transient analysis of the monocoque waffle concept predicts temperature for the upper surface at the -0.5g condition and for the lower surface at the +2.0g condition that are 100°F to 200°F below the steady-state predictions of the radiation equilibrium analysis. At cruise, however, both methods predict similar temperatures because of the

near steady-state heating conditions. The results of the isotherm analysis were used on the redundant model stress program to determine stress levels over the wing.

To aid in the selection of spar and rib cap configurations, an analysis was performed to determine temperature gradients in the fuselage-wing intersection area of the monocoque waffle structural concept. The thermal model was similar to the gross model approach at this location with the following additional details (see figure 9-9): (1) a small section (15 inches) of the fuselage skin was included in the analysis to determine fuselage temperatures at the intersection corner and their effect on wing temperatures; (2) upper panels and the fuselage section were divided into several nodes to determine panel temperature variations; the effect of the fuel tank inside the fuselage was estimated with an approximate thermal model of an insulated cryogenic tank. The single shear joint beam caps and the double shear joint upper cap at BL 120 were heated by radiation heat transfer from the internal structure and by aerodynamic heating when applicable. Conduction from panels to caps is of a small order compared to radiation at high temperatures, and was therefore neglected to yield conservative results for panel to cap temperature gradients. Figure 9-9 shows temperatures for panels, beam caps, and webs at FS 2345 between BL 90 and BL 143 for three flight conditions. The temperatures at the right of the figure are arranged schematically to refer to the circled node locations on the sketch at the left of the figure. Temperature variations on the upper surface panel are 10°F over a distance of approximately 15 inches at the panel center. Panel to beam cap temperature differences at BL 120 are under 70°F for the two transient conditions and at cruise. These temperature variations occur over a distance of about 5 inches across the panel. Peak temperature differential between the fuselage skin and the upper cap at BL 120 occurs at the +2.0g condition and is 96°F over a distance of about 3 inches. The panel to cap temperature differences derived at BL 90 and BL 143 are typical for the wing structure under the fuselage and on the "flat" (parallel surface) portion of the wing, respectively.

Panel and rib cap temperatures at the insulated outboard location between BL 321 and BL 365 at FS 2366 are shown in figure 9-10. Insulation thickness is 0.12 inch between BL 321 BL 341 and 0.25 inch outboard. Temperatures derived from the gross model approach are shown for the -0.5g, +2.0g, and cruise flight conditions. Mid-panel to cap temperature differentials are below 50°F for all conditions except for the upper caps at BL 321 and BL 343 during -0.5g (BL 321 cap is 60°F cooler than adjacent panel at BL 332 and BL 343 caps is 75°F cooler than adjacent panel at BL 354) and the upper cap at BL 365 during +2.0g and cruise (60°F hotter than adjacent panel at BL 354). Peak differentials at -0.5g are caused by peak heating on the upper surface and the temperature response lag of the cap due to its greater mass per exposed area. The differential between the upper panel at BL 354 and the upper cap at BL 365 during +2.0g maneuver is also caused by the response lag of the cap as the upper structure cools from its peak temperature condition at -0.5g. This differential is maintained through cruise.

A detailed thermal analysis was performed to determine local stresses and deflections due to temperature gradients through the panel structure. Typical results of the transient analysis of detailed waffle panel structure are shown in figure 9-11 for an inboard location (BL 166) and in figure 9-12 for an outboard surface waffle skin and stiffener tip are shown from take-off (time equal zero) to mid-cruise (time equal 40 minutes). The outboard location temperatures are based on using a heat shield with 0.25 inch insulation for thermal protection. During the climb portion of the trajectory (first 20 minutes), temperature increases for both the waffle skin and tip are regular for both surfaces at the inboard and at the outboard locations. Thermal gradients across any of the panels are under 70°F. During the trajectory perturbations at the end of climb, large gradients (over 150°F) are experienced by some panels, and these are detailed below. After the perturbations, panel gradients stabilize rapidly to values under 65°F. Thus, from take-off to mid-cruise the peak thermal gradients as well as peak temperatures occur at the -0.5g or +2.0g condition, and these have correctly been defined as the thermally critical conditions.

Peak panel gradients at the critical conditions and the stabilized values at cruise are shown in figure 9-13 for four wing locations at FS 2366. Panels under the fuselage (BL 60), at the inboard location (BL 166), at an outboard location without insulation (BL 258), and at the insulated outboard location (BL 350), were analyzed. Panel gradients at BL 350 are shown also for the case of no insulation. Temperature differences from waffle skin to stiffener tip and from stiffener base to tip are shown. Because of relatively small mass and large exposure area, the skin portion of the waffle is more sensitive to peak transient heating than the stiffener. Thus gradients from skin to stiffener tip are generally higher than those from stiffener base to tip during the trajectory perturbations. The largest gradients for the upper surface occur at the outboard (forward wedge) locations during the -0.5g condition, and for the lower surface at the inboard (unshielded) locations during the +2.0g condition. The major effects of removing insulation at BL 350 are to diminish peak upper surface gradients slightly for the -0.5g condition and to increase all panel gradients at +2.0g and cruise substantially.

HONEYCOMB-CORE SANDWICH CONCEPT

A detailed transient thermal analysis was conducted to determine local stresses and deflections caused by temperature gradients through the panel structure. Figures 9-14 to 9-17 show structure and heat-shield temperatures for the lower surface insulation outboard arrangement. Additional temperature and thermal gradient data are shown in table 9-1 for the three flight conditions. During the structural sizing, various combinations of face thicknesses, core densities, and sandwich heights were considered to minimize the panel thermal gradients. As indicated in table 9-1, the largest thermal gradient (323°F) occurs at the +2.0-g maneuver condition on the wing lower surface panel under the fuselage.

SEMIMONOCOQUE SPANWISE CONCEPTS

Analysis of the semimonocoque primary structure concepts were conducted with the same procedures outlined for the monocoque waffle structural concept. A gross model analysis, assuming flat uniform panels, was used to determine mean temperature histories for the primary structure and the effects of varying insulation thickness in thermally protected areas. Isotherms based on analysis at 30 wing locations were developed for both surfaces of the wing for various combinations of heat shields and insulation. Analyses were performed for detailed thermal models of the various semimonocoque panel concepts to determine local stresses and deflections due to temperature gradients through the panel structure. The gross model and isotherm analyses for the semimonocoque structure are applicable to both the spanwise stiffened and chordwise stiffened concepts, but are presented only in the spanwise concepts discussion and referenced in the chordwise concepts section.

Preliminary temperatures determined from the radiation equilibrium analysis indicated that thermal protection is required at the outboard and forward wing areas to limit primary structure temperatures to 1600°F and to control thermal gradients. To determine the extent of thermal protection required for the semimonocoque concepts, the variation in structure temperatures with insulation thickness and heat shield placement was examined at one fuselage station (FS 2366) from BL 240 to BL 360. These temperatures, derived from the gross model analysis, were examined at the -0.5g condition to observe upper surface maximums, at the 2.0g condition to observe lower surface maximums, and at mid-cruise to observe near steady-state effects. The gross model assumed flat structural panels with an equivalent weight thickness of 0.029 inch for all semimonocoque concepts. Heat shields were assumed to be 0.011-inch flat sheets of Rene' 41, and insulation material was 6.0 lb/ft^3 Dyna-Flex. Figures 9-18, 9-19, and 9-20, show temperatures along FS 2366 for semimonocoque panels and upper and lower heat shields at the three flight conditions. Figures 9-21, 9-22, and 9-23, show temperatures for the same conditions but with a lower surface heat shield only. Each of the figures shows temperatures derived for no insulation and for insulation thicknesses of 0.25 and 0.50 inch attached to the inner surface of the shield.

The general effect of insulation in this area is to reduce structural panel temperatures and to increase lower surface heat shield temperatures. The most noticeable effect occurs as insulation is increased from none to a thickness of 0.25 inch. The resulting temperature change is more than twice the additional change caused by increasing the thickness from 0.25 to 0.50 inch. At the transient conditions (-0.5g and 2.0g), insulation reduces lower panel temperatures more severly than upper panel temperatures, and affects upper heat shield temperatures less than either panel. This non-uniform change in temperatures through the structure may cause temperature lines to cross, as seen in figures 9-18, 9-19, 9-21, and 9-22 for the insulation cases. The uninsulated transient cases and all cases during the steady-state conditions of cruise show a normal temperature progression from one external surface of the structure to the other. The effect of deleting the upper heat shield is most noticeable on the upper panel. Upper panel temperatures are hotter by 100° to 150°F at the -0.5g condition for the cases without an upper surface shield. At cruise, upper and lower panel temperatures are cooler by 50° to 100°F with no upper heat shield, due to direct radiation relief to space for the upper panel.

Placement of insulation for the semimonocoque concepts was selected to maintain the 1600°F material limit and to minimize temperature differences in the spanwise direction and to control the gradient through the wing to match the fuselage gradient. Temperatures derived from the insulated semimonocoque structures, either with or without an upper surface heat shield, were based on the insulation placement shown in figure 9-24. The cross section at FS 2320 in this illustration shows 0.25-inch insulation used from BL 212 to BL 258, and 0.50-inch insulation from BL 258 to the leading edge.

Isotherms for the semimonocoque primary structure concepts were derived for three arrangements of heat shields and insulation. Figures 9-25 through 9-30 show primary structure and heat shield temperatures at the -0.5g, 2.0g, and cruise flight conditions for the case with upper and lower heat shields and no insulation. Figures 9-31 through 9-36 show structure and heat shield temperatures for the same structure configuration and flight conditions but with insulation per figure 9-24. Figures 9-37 through 9-42 show temperatures for the arrangement with lower heat shield only and insulation per figure 9-24.

For each flight condition, structural panel temperatures are shown first and then heat shield temperatures in the figure immediately following. Dashed lines shown on the lower surface in each figure are located under the upper surface slope breaks, shown with solid lines on the upper surface diagram. Some lower surface isotherms are located along these dashed lines, reflecting the influence of sharp temperature differences between differently sloped sections of the upper surface. The effect of the fuselage on the wing is an increase in upper surface temperatures near the fuselage-wing intersection as radiation relief to space is reduced. General conclusions made upon examination of the isotherms for the different thermal protection arrangements are the following: (a) upper surface (panel and heat shield) temperatures are maximum at the -0.5g flight condition; (b) lower surface temperatures are maximum at the 2.0g flight condition; (c) the effect of insulation at the forward wing area is generally to reduce peak structural temperatures by 100° to 250°F and to increase lower heat shield temperatures by 50° to 100°F; and (d) omitting the upper surface heat shield increases upper panel temperatures at the forward section of the wing by 150°F during the -0.5g maneuver and generally reduces all structure temperatures by 50° to 100°F at the other conditions. The results of the semi-monocoque isotherm analysis were used in the redundant model stress program to determine stress levels over the wing.

To aid in the selection of spar and rib cap configurations, a parametric analysis was conducted to determine the variation in panel-to-cap temperature different with cap mass. Typical geometries for caps examined with the semimonocoque structure are shown in figure 9-43. Cap mass is represented by the cross section area of the channel cap plus the area of the end closeout immediately above the cap. Total cross section area ranged from 0.2 to 0.8 square inch for a range of channel cap thickness from 0.030 to 0.125 inch. Temperature differences from mid-panel to an adjacent cap were examined along FS 2366 from under the fuselage to the leading edge. Except for surfaces experiencing peak heating conditions (upper surface at -0.5g and lower surface at 2.0g), temperature differentials are under 50°F at all flight conditions for the range of cap areas examined and a variety of heat shield/insulation arrangements. Temperature differences are smaller with the thinner caps, except that, at the steady-state heating conditions of cruise, beam cap temperatures are independent of mass and depend more on location (i.e., distance from the leading edge). For the transient peak heating conditions on either surface, the differential from panel to cap is generally above 50°F because of the temperature response lag of the cap due to its greater mass per exposed area. Figure 9-24 presents an attempt to correlate temperature differentials during peak heating computed at a number of locations with varying cap areas. Data are shown separately for surfaces with a heat shield and for surfaces without a heat shield. Within a 30°F band (shaded in the figures), temperature differentials seem to be fairly independent of panel location (upper or lower surface, inboard or outboard) and of cap location (outboard, inboard, forward or rearward) relative to the middile of the panel. Surfaces without a heat shield exhibit a greater differential compared to those with a heat shield due to direct exposure to aerodynamic heating.

A detailed thermal analysis was performed to determine local stresses and deflection due to temperature gradients through the spanwise stiffened semi-monocoque panel structure concepts. Typical results of the transient analysis for the tubular panel are shown in figure 9-45 for an inboard location (BL166) and in figures 9-46 and 9-47 for an outboard location (BL 300) with and without insulation, respectively. Temperature-time histories are shown from takeoff (time zero) to mid-cruise (time = 40 minutes). Both locations assume use of upper and lower heat shields. During cruise, in addition to lowering structure temperatures, insulation reduces the overall temperature gradient from the top of the upper panel to the bottom of the lower panel (point a to point d). This temperature difference is 150°F for the insulated concept (figure 9-46) compared to 260°F for the uninsulated concept (Figure 9-47). The lower panel with insulation also shows a lower peak temperature (1370°F) at the 2.0g maneuver compared to the sharp peak temperature (1630°F) for the uninsulated panel. During climb, insulation delays heating of the lower panel and causes a large temperature difference (350°F at time = 10 minutes) from the top of the upper panel to the bottom of the lower panel. For the uninsulated cases (inboard and outboard), this difference is under 100°F until about 15 minutes into climb. Peak temperature gradients across the individual panels during climb are about 200°F for all cases except for lower panel of the insulated arrangement, which shows practically no temperature difference until the end of climb.

The temperature-time histories shown for the tubular panels are representative of temperature histories for the other spanwise stiffened panel concepts with both heat shields. The other concepts (beaded and trapezoidal corrugation), however, have a single layer construction and exhibit less of a temperature differential between the outermost and intermost points on the panel. Thus, curves for temperatures on these panel concepts would lie between the curves shown for the outermost and innermost points of the tubular panel. A comparison between detailed panel temperatures for all three spanwise concepts with temperatures derived in the isotherm analysis (using the flat, uniform panel assumption) has shown that mean panel temperatures serived from both analysis methods are within 25°F for all flight conditions.

Panel gradients at the critical flight conditions (-0.5g and 2.0g) and at cruise are shown in figures 9-48, 9-49, and 9-50 for the tubular trapezoidal corrugated, and beaded panels, respectively. Temperature differences are shown in each case for three locations at FS 2366: under the fuselage (BL 60), inboard wing (BL 166), and outboard wing (BL 300). All cases assume upper and lower heat shields, and the outboard location is shown for no insulation and for insulation thicknesses of 0.25 and 0.50 inch. Panel graidents at the cited flight conditions are 40°F or less for the trapezoidal corrugation and under 20°F for the beaded. These low gradients are the result of the single-layer construction of these panel concepts. The tubular panel is of double layer construction and exhibits gradients up to 155°F at the 2.0g condition. The effect of insulation at the outboard location for all the spanwise stiffened concepts is generally to reduce the temperature differential across the outboard panel, except during the -0.5g condition on the upper surface where the differential

almost doubles for 0.50-inch insulation compared to no insulation. These gradients were used to evaluate local thermal stresses and deflections in the panels and their effect on the overall stress levels of the wing.

SEMIMONOCOQUE CHORDWISE CONCEPT

The parametric insulation analysis, panel-to-spar and-rib cap gradient analysis, and the isotherms developed for the semimonocoque primary structure are generally applicable to both the spanwise and chordwise stiffened concepts, and have been shown in the spanwise concepts section. Of particular interest for the chordwise concept are the previous curves which show the effect of insulation on structure temperatures with a lower heat shield only (figures 9-21 to 9-23), and the curves which present isotherms (figures 9-37 to 9-42) for the semimonocoque structure with a lower heat shield only. These curves are applicable to the chordwise stiffened concept which utilized an unshielded upper surface convex-beaded panel and shielded lower surface, and were used in the redundant model stress program to determine stress levels over the wing for this concept.

A detailed thermal analysis was conducted for the chordwise stiffened concept to determine local stresses and deflections due to temperature gradients through the panel structure. Figures 9-51 and 9-52 show temperature-time histories for the concept using convex-beaded upper surface panels and tubular lower surface panels with a lower heat shield. Temperatures are shown from takeoff to mid-cruise for an uninsulated inboard location (FS 2366, BL 166) and an insulated outboard location (FS 2366, BL 300). For both locations, temperatures increase rapidly through the climb portion of the trajectory, peak sharply during the maneuvers at the end of climb, then settle gradually to cruise values. At the outboard location, lower panel temperature peaks are attenuated at the 2.0g condition by the insulation, but the convex bead on the upper surface undergoes direct peak heating at the -0.5g condition and its temperature peaks sharply. The start of the bead near the leading edge experiences additional high local heating due to the ramp effect of the bead closeout. An estimate of 25 percent increase in the local heat transfer coefficient due to a 3-degree maximum chordwise slope at the closeout yields a local temperature increase of 90°F at the -0.5g condition.

Panel gradients at the critical flight conditions (-0.5g and 2.0g) and at cruise are shown in figure 9-53 for chordwise stiffened panels with a convex beaded upper surface. Temperature differences across the panels are shown for three locations at FS 2366: under the fuselage (BL 60), inboard wing (BL 166), and outboard wing (BL 300). A lower surface heat shield is assumed, and the temperature for the outboard location is shown for no insulation and for insulation thicknesses of 0.25 and 0.50 inch. Temperature differentials through the lower panel for this concept are almost identical to those for the spanwise tubular concept because of configuration similarity of the lower surface. The convex beaded upper surface, however, is directly exposed to the airstream and panel gradients for the outboard area are double at -0.5g and 50 percent higher at cruise compared to the shielded tubular

upper panel. The effect of insulation at the outboard location is generally to reduce temperature differentials across the panels, except for the upper surface at the -0.5g condition where the differential increases from 115°F for no insulation to 162°F for 0.50-inch insulation.

STATICALLY DETERMINATE CONCEPT

Heat shields covered all exposed surfaces and three thermal-protection arrangements were considered: (1) no insulation, (2) insulation on the lower surface from ℄ to BL 212 (Areas A and B), and (3) insulation at the lower surface outboard of the one-third wing chordline.

The second thermal-protection arrangement (inboard) was included to investigate structural temperatures even lower than 1600°F to provide minimum-gage panel designs, since the spanwise loads were low. Because of noncontinuous ribs and the allowable wing rotation at the fuselage, wing-to-fuselage temperature compatibility is less important in this concept.

Detailed transient thermal analyses were conducted for the thermal-protection arrangements to determine local stresses and deflections from temperature gradients through the panel structure. Average panel temperatures for the candidate thermal protection arrangements are presented in tables 9-2 through 9-5.

Isotherms used for the redundant model input were for the heat shielded and no insulation arrangement. These isotherms are identical to those shown for the semimonocoque spanwise in figures 9-25 through 9-30.

REFERENCES

9-1 Schultz, H. D.: Thermal Analyzer Computer Program for the Solution of General Heat Transfer Problems, Lockheed-California Company, LR 18902 July 1965. Published under NASA Contract NAS9-3349.

TABLE 9-1

HONEYCOMB SANDWICH TEMPERATURES AND THERMAL GRADIENTS [a,b]

TABLE 18. – TEMPERATURES[a] AND THERMAL GRADIENTS FOR MONOCOQUE HONEYCOMB-CORE SANDWICH PANELS WITH OUTBOARD LOWER SURFACE HEAT SHIELD AND INSULATION

Loading condition	Wing panel location	Item	Face sheet temperature, °F			
			BL 60	BL 166	BL 258	BL 350
-0.5-g	Upper	T_1	980	1312	<u>1588</u>	<u>1661</u>
		T_2	1055	1225	1386	1416
		ΔT	-74	86	201	244
	Lower	ΔT	95	41	21	17
		T_2	1166	1286	1396	1403
		T_1	1260	1327	1416	1420
		T_{HS}	–	–	1366	1425
+2.0-g	Upper	T_1	1007	1172	1362	1409
		T_2	1077	1252	1409	1443
		ΔT	-70	-79	-47	-33
	Lower	ΔT	<u>323</u>	257	122	18
		T_2	1211	<u>1323</u>	1434	1437
		T_1	1534	1579	1557	1456
		T_{HS}	–	–	<u>1693</u>	<u>1828</u>
Cruise	Upper	T_1	1240	888	946	945
		T_2	1276	1107	1137	1085
		ΔT	-35	-219	-191	-139
	Lower	ΔT	28	120	104	84
		T_2	1298	1215	1241	1149
		T_1	<u>1326</u>	1335	1344	1233
		T_{HS}	–	–	1402	1494

a. Insulation and heat shield at outboard lower surface.
b. Symbols: T_1 = external face sheet temperature
T_2 = internal face sheet temperature
ΔT = $T_1 - T_2$
T_{HS} = heat-shield temperature
Maximum temperatures are underlined.

TABLE 9-3

PANEL TEMPERATURES FOR STATICALLY DETERMINATE BEADED CONCEPT,
HEAT SHIELDS ON EXPOSED SURFACES, 1/8-IN. INSULATION ON LOWER SURFACE FROM ℄ TO BL 212

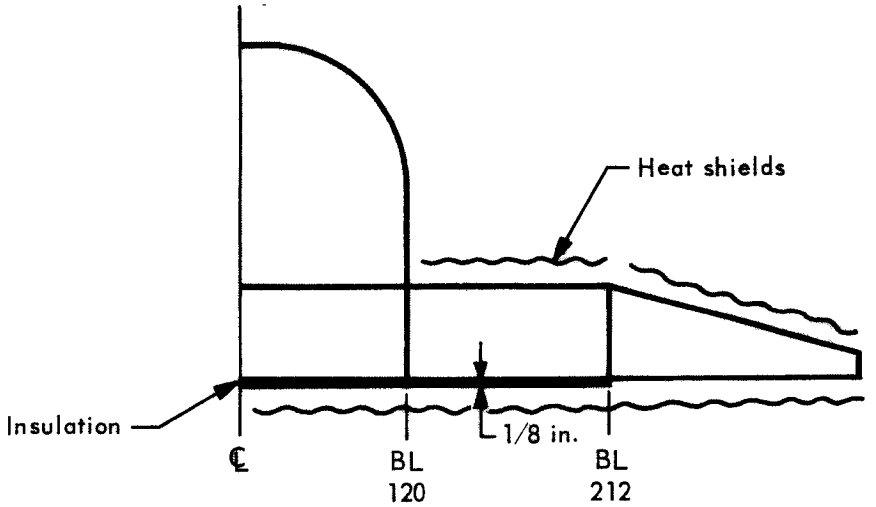

Area	℄ to BL 120 (A)			BL 120 to BL 212 (B)			BL 212 to OUTB'D (C)		
Surface	-0.5-g	+2.0-g	CRUISE	-0.5-g	+2.0-g	CRUISE	-0.5-g	+2.0-g	CRUISE
Upper	945		1250	1135		1050	1450	1440	1160
Lower	1050	1150	1280	1165	1200	1190	1430	1540	1300

TABLE 9-4

PANEL TEMPERATURES FOR STATICALLY DETERMINATE BEADED CONCEPT,
HEAT SHIELDS ON EXPOSED SURFACES, 1/4-IN. INSULATION ON LOWER SURFACES FROM ℄ TO BL 212

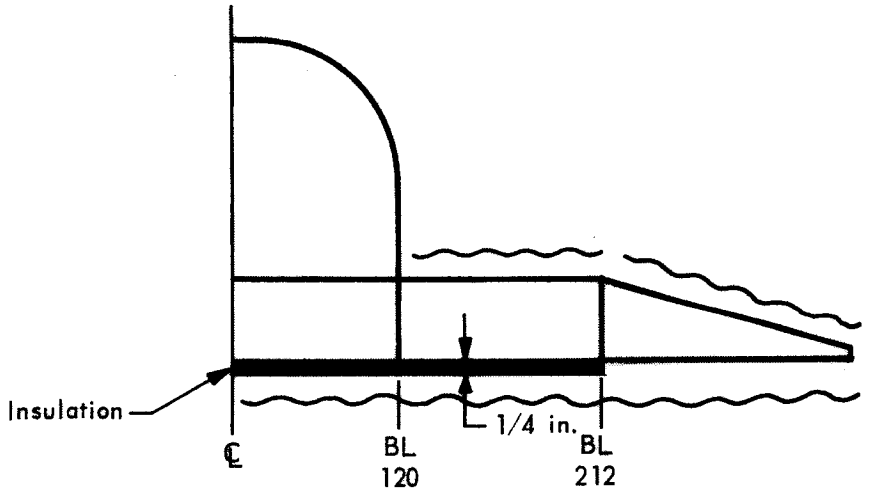

Area	℄ to BL 120 (A)			BL 120 to BL 212 (B)			BL 212 to OUTB'D (C)		
Surface	-0.5-g	+2.0-g	CRUISE	-0.5-g	+2.0-g	CRUISE	-0.5-g	+2.0-g	CRUISE
Upper	800	940	1200	1070	1095	1000	1450	1440	1160
Lower	915	950	1240	1075	1090	1130	1430	1540	1300

TABLE 9-5

PANEL TEMPERATURES FOR STATICALLY DETERMINATE BEADED CONCEPT,
HEAT SHIELDS ON EXPOSED SURFACES, 1/8-IN. INSULATION ON LOWER SURFACE FROM BL 304 TO OUTBOARD

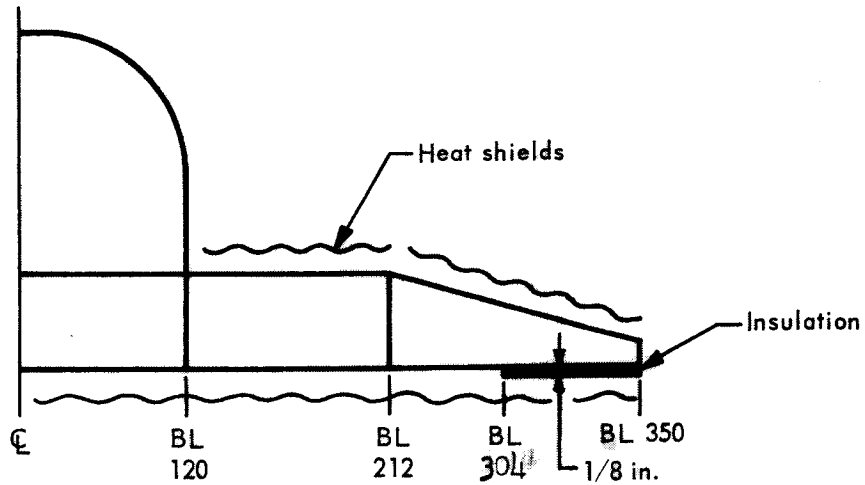

Area	℄ to BL 120 (A)			BL 120 to BL 212 (B)			BL 212 to OUTB'D (C)		
Surface	-0.5-g	+2.0-g	CRUISE	-0.5-g	+2.0-g	CRUISE	-0.5-g	+2.0-g	CRUISE
Upper	1210	1240	1300	1270	1280	1100	1430	1420	1130
Lower	1270	1350	1330	1320	1400	1250	1400	1490	1250

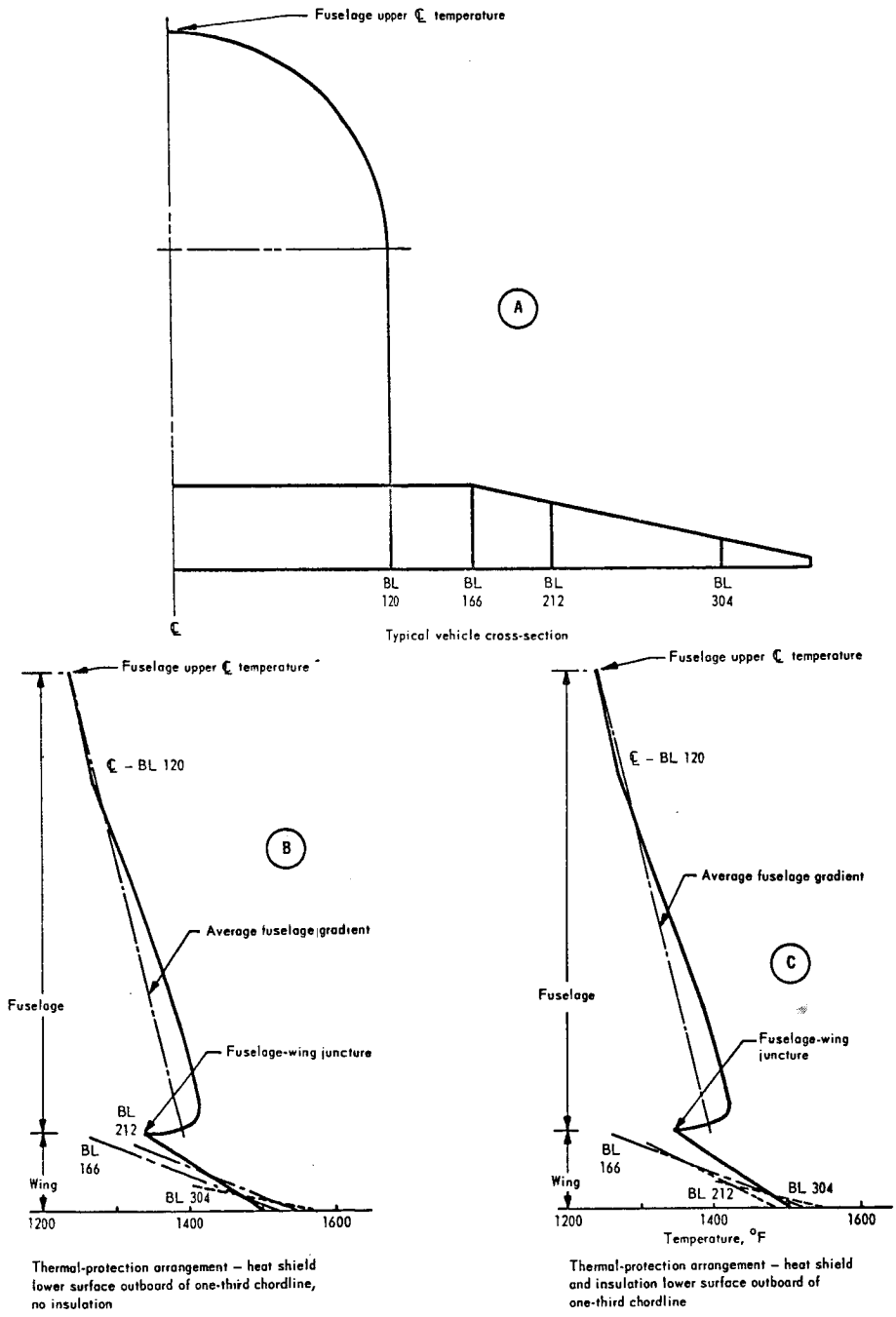

Figure 9-1. Wing-fuselage cross-section temperatures for candidate thermal protection arrangements at +2.0-g condition

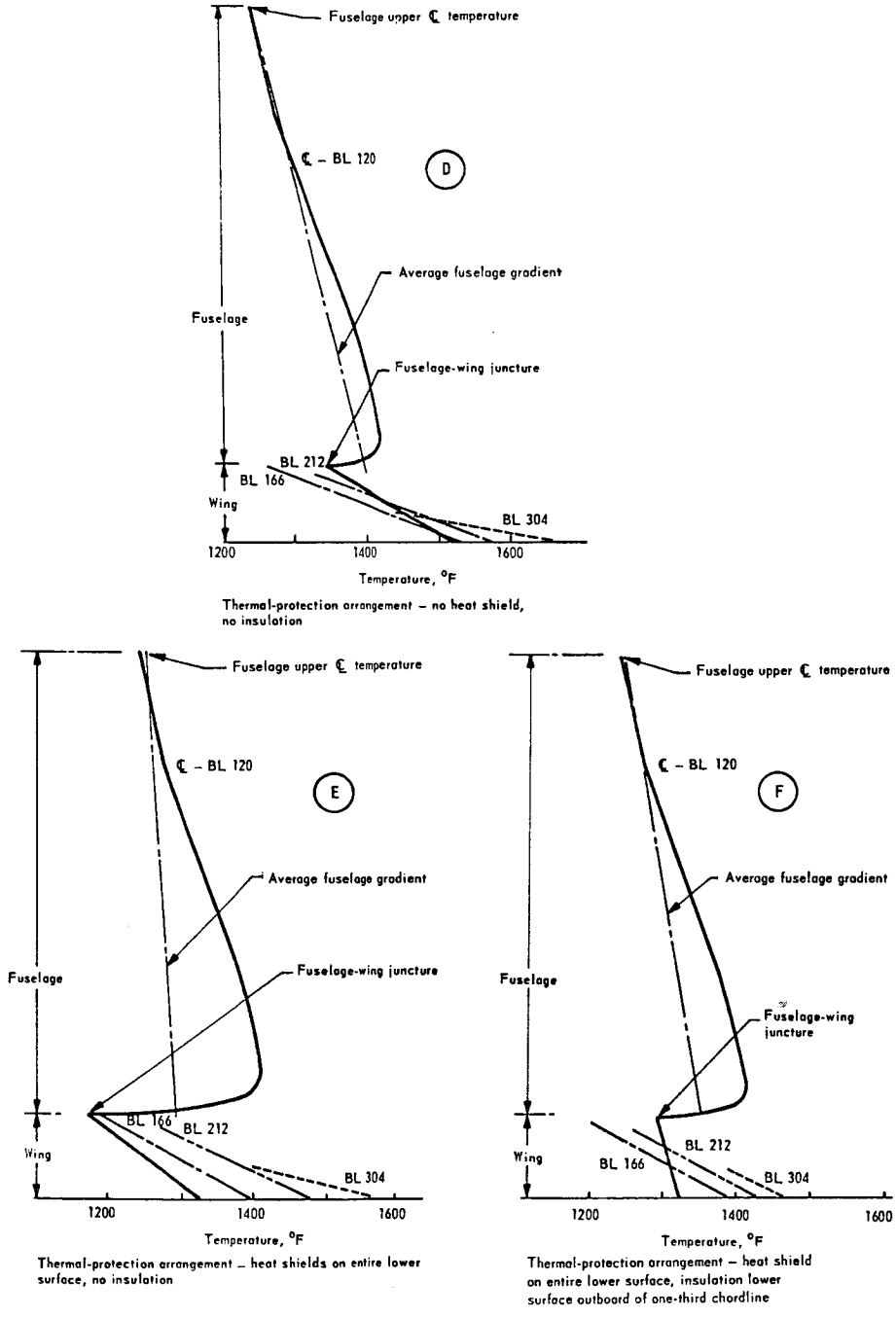

Figure 9-1. Wing fuselage cross-section temperatures for candidate thermal protection arrangements at +2.0-g condition (Continued)

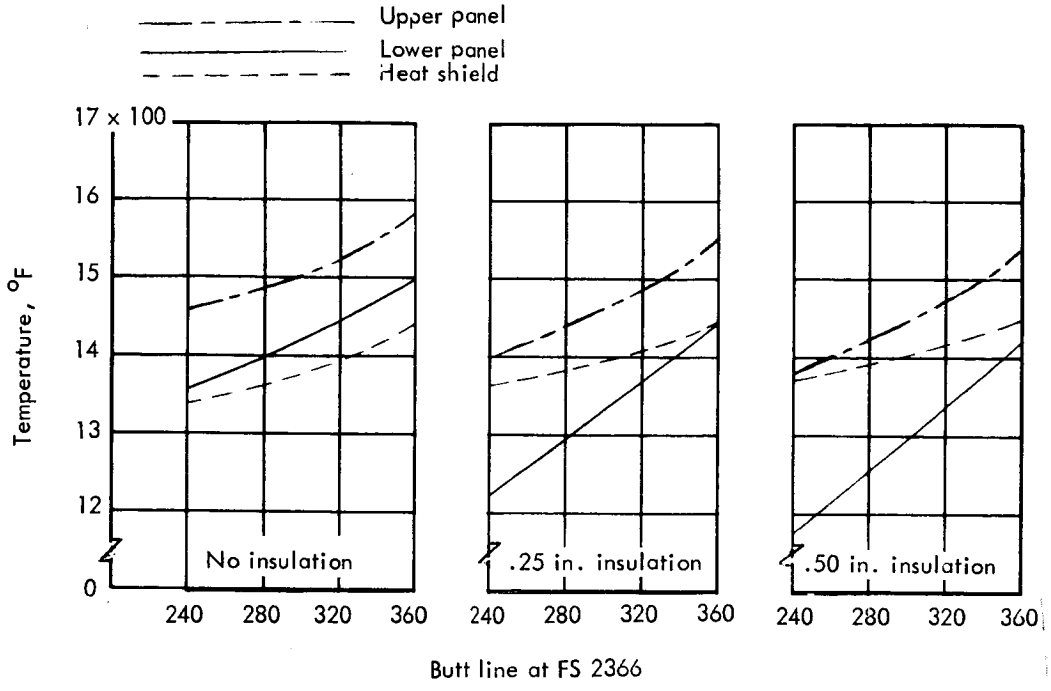

Figure 9-2. Temperatures at -0.5-g condition for outboard monocoque waffle panels and heat shield vs insulation thickness

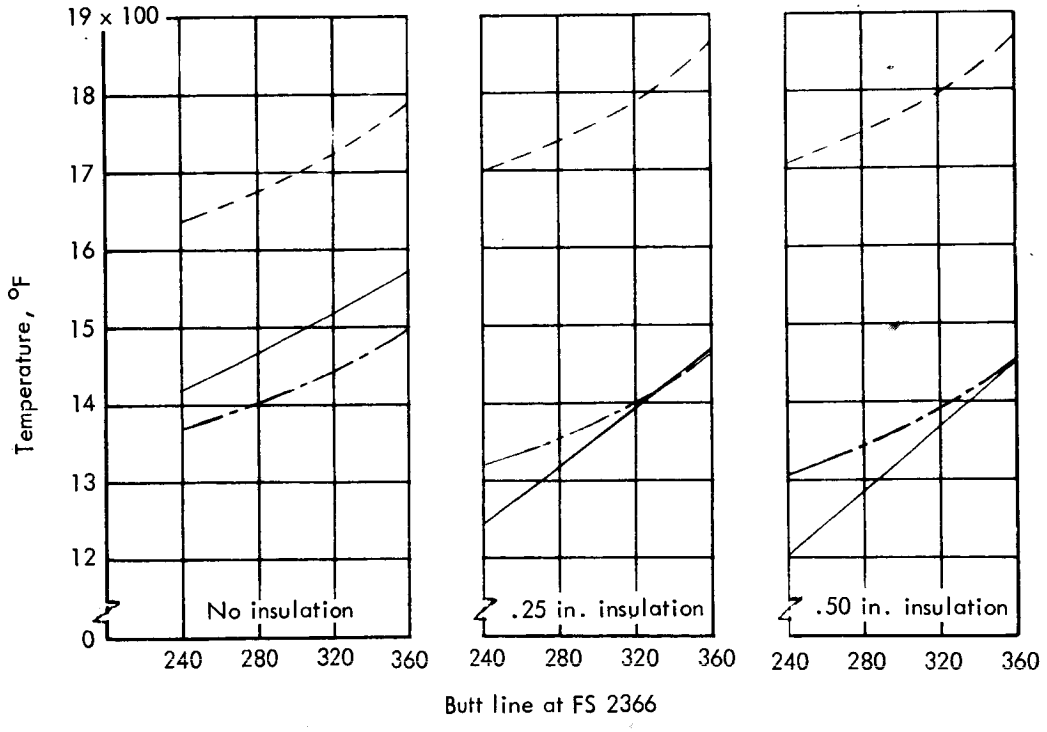

Figure 9-3. Temperatures at +2.0-g condition for outboard monocoque waffle panels and heat shield vs insulation thickness

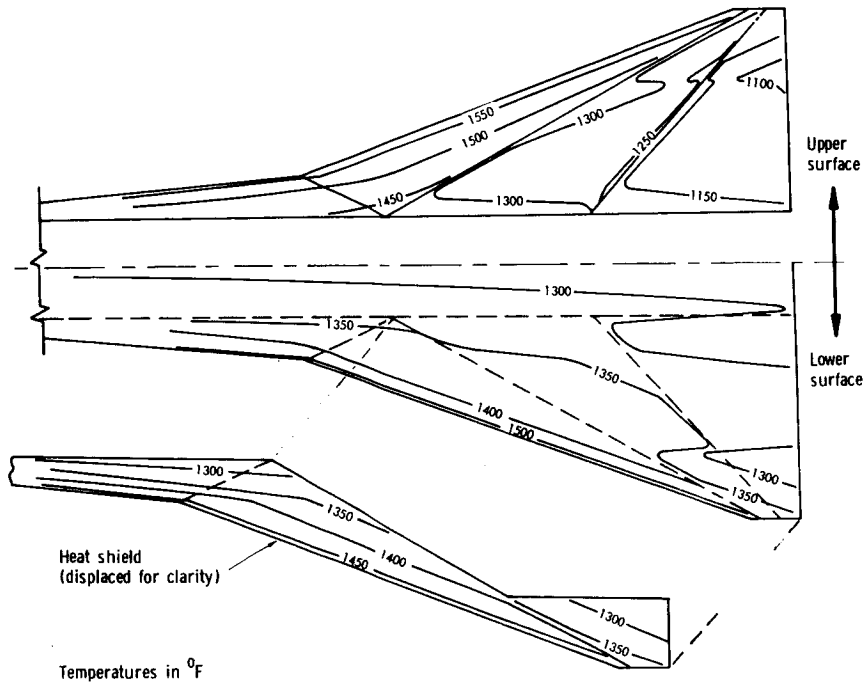

Figure 9-6. Wing isotherms at -0.5-g condition for monocoque waffle panels with partial lower heat shield and insulation

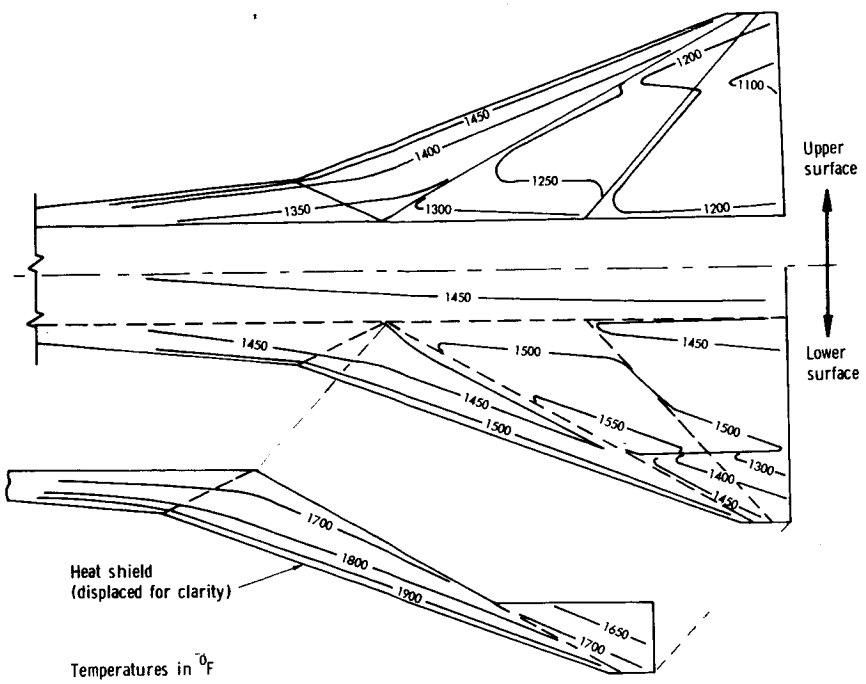

Figure 9-7. Wing isotherms at +2.0-g condition for monocoque waffle panels with partial lower heat shield and insulation

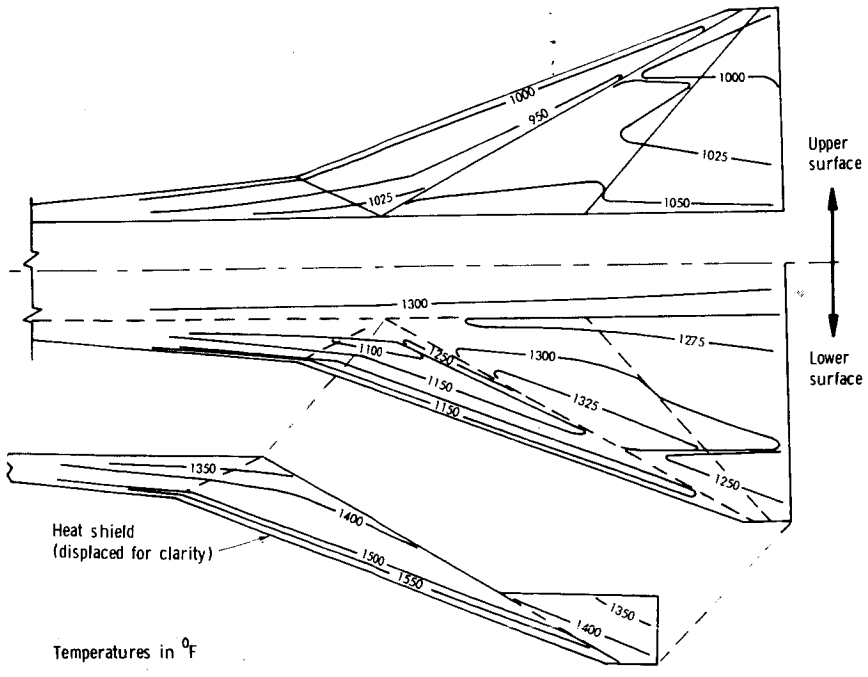

Figure 9-8. Wing isotherms at cruise condition for monocoque waffle panels with partial lower heat shield and insulation

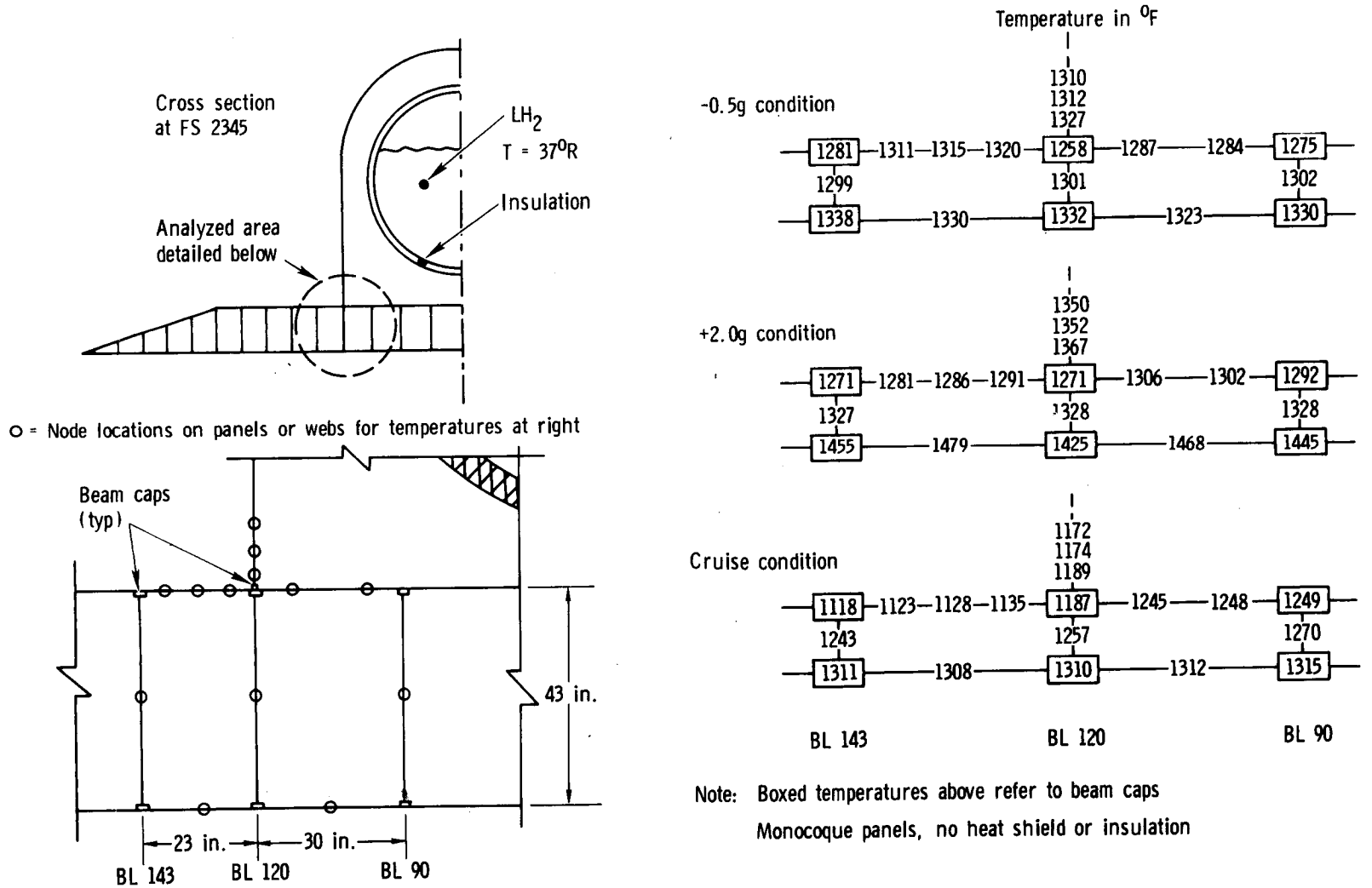

Figure 9-9. Panel and beam cap temperatures in °F at fuselage-wing intersection area for monocoque waffle concept

- Cross section at FS 2366
- Monocoque panels with single shear joint beam caps

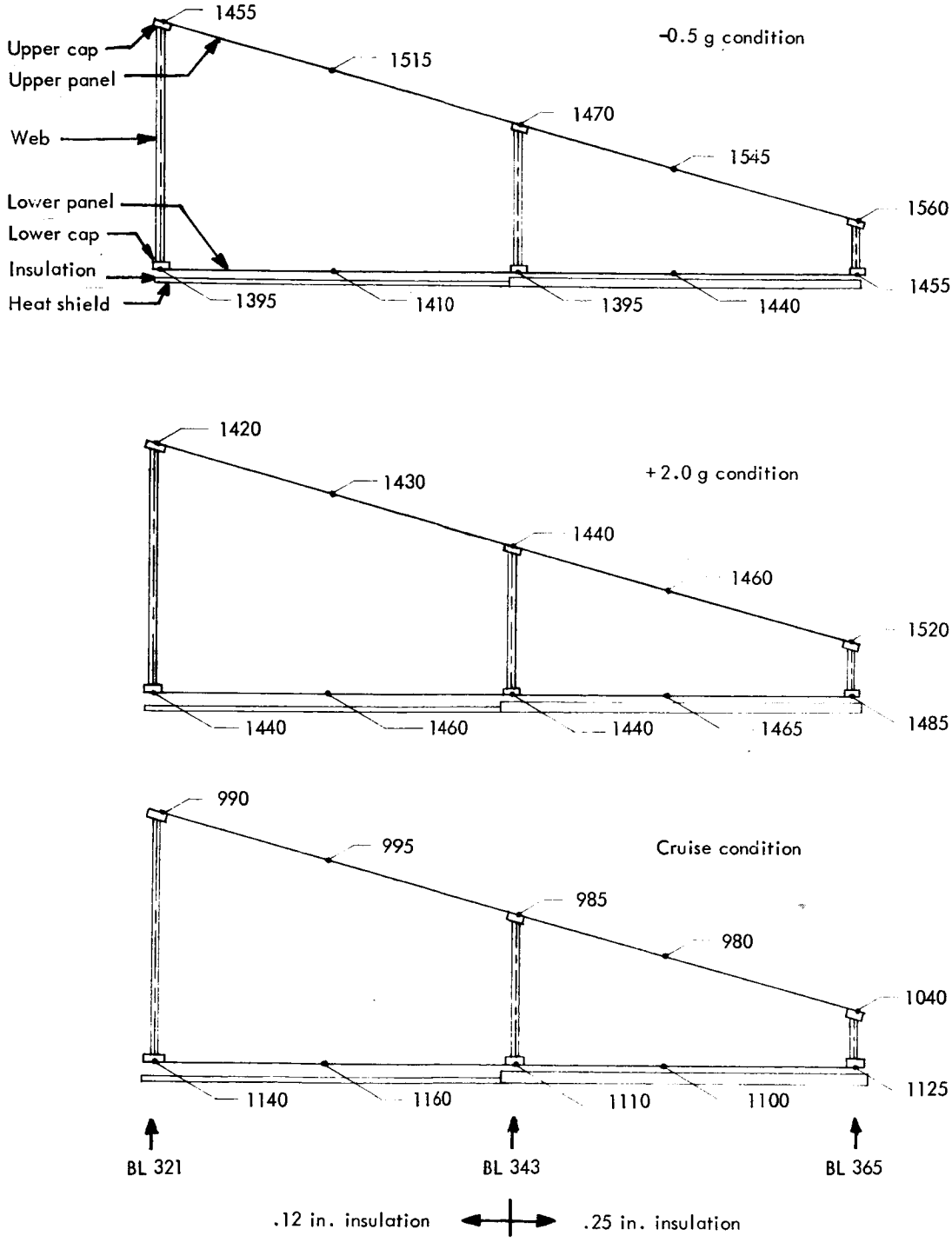

Figure 9-10. Panel and beam cap temperatures in ^{o}F at outboard area for monocoque waffle concept

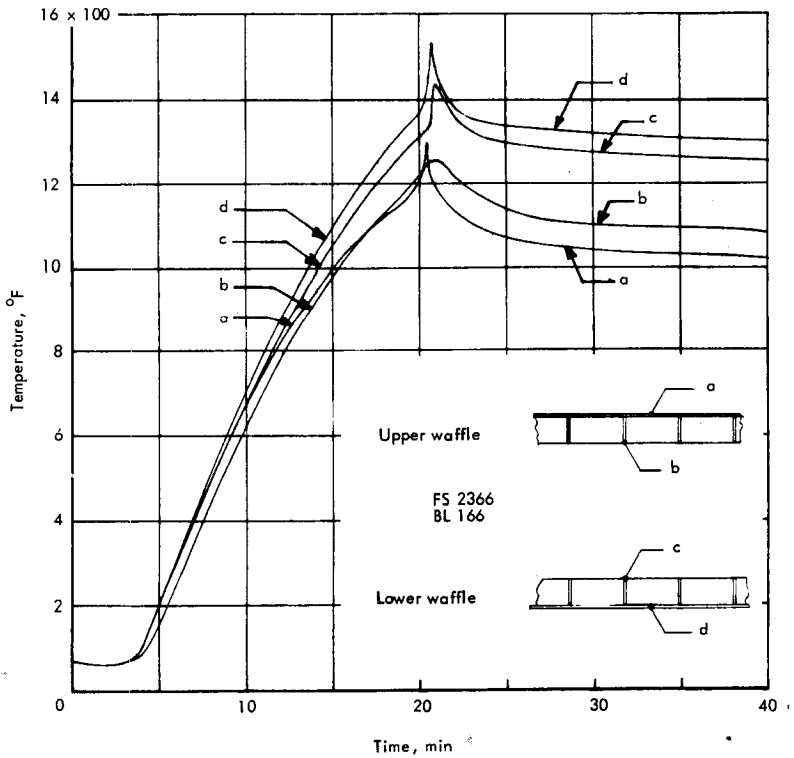

Figure 9-11. Waffle panels temperatures (skin and stiffener tip) vs time, inboard location

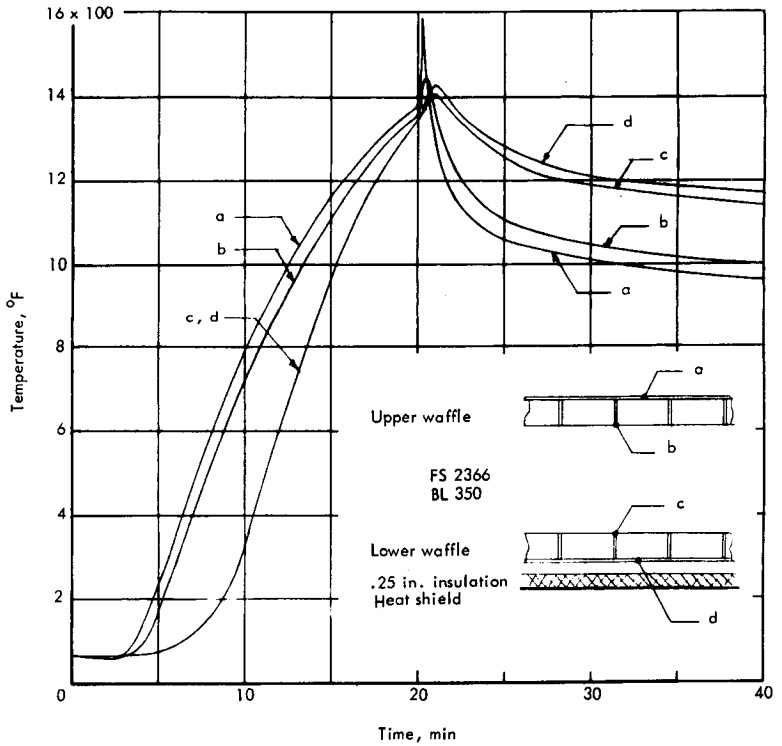

Figure 9-12 Waffle panel temperatures (skin and stiffener tip) vs time, outboard location

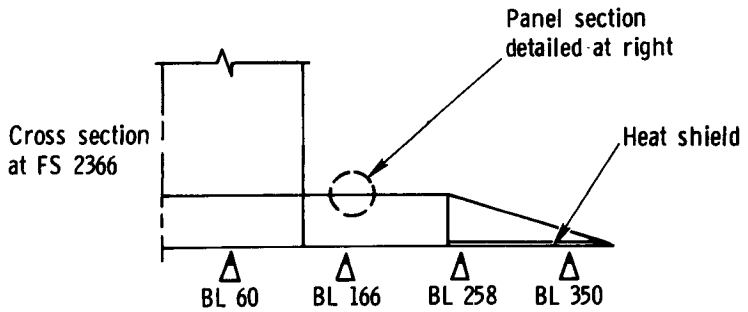

Locations for waffle gradient analysis

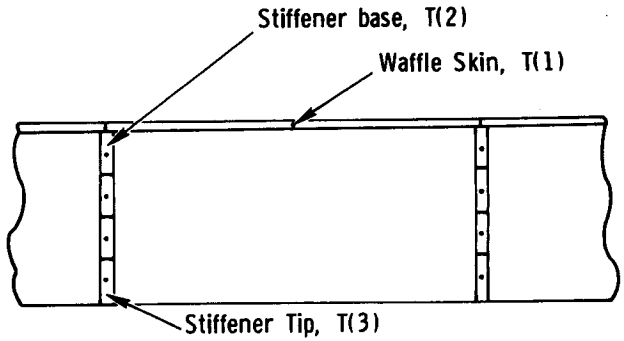

Detail of typical node system for waffle

Condition	Location	Temperatures °F									
		Inboard				Outboard					
		BL 60		BL 166		BL 258 (a)		BL 350 (b)		BL 350 (c)	
		ΔT_a	ΔT_b	ΔT_a	ΔT_b	ΔT_a	ΔT_b	ΔT_a	ΔT_b	ΔT_a	ΔT_b
-0.5g	Upper panel	-3	-4	71	37	148	87	183	110	155	90
	Lower Panel	4	9	-5	3	9	9	6	3	4	6
2.0g	Upper Panel	-3	-4	-40	-27	-28	-18	-24	-14	-43	-28
	Lower Panel	151	100	148	97	71	44	14	7	73	45
Cruise	Upper Panel	0	0	-61	-44	-59	-42	-34	-25	-63	-45
	Lower Panel	-2	-1	47	33	45	32	27	19	47	34

ΔT_a = T(1) - T(3), waffle skin to stiffener tip

ΔT_b = T(2) - T(3), stiffener base to tip

NOTE

Inboard locations and upper surface outboard - no shield

Outboard lower surface:
(a) Heat shield only, no insulation
(b) Heat shield with 0.25 inch insulation
(c) Heat shield only, no insulation

Figure 9-13. Temperature differentials through monocoque waffle cross sections

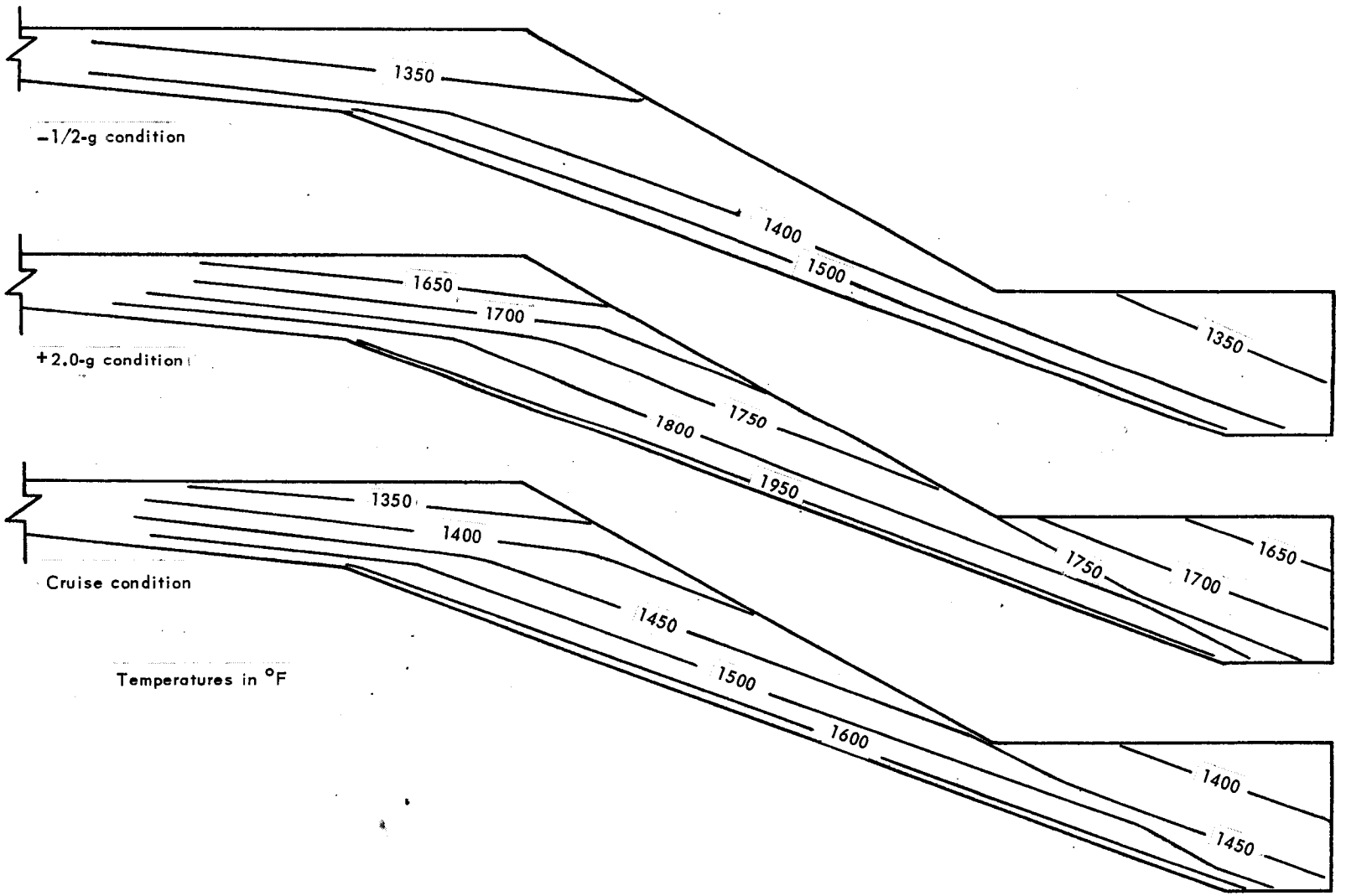

Figure 9-14. Heat-shield isotherms for honeycomb sandwich with heat shield and insulation on lower surface outboard

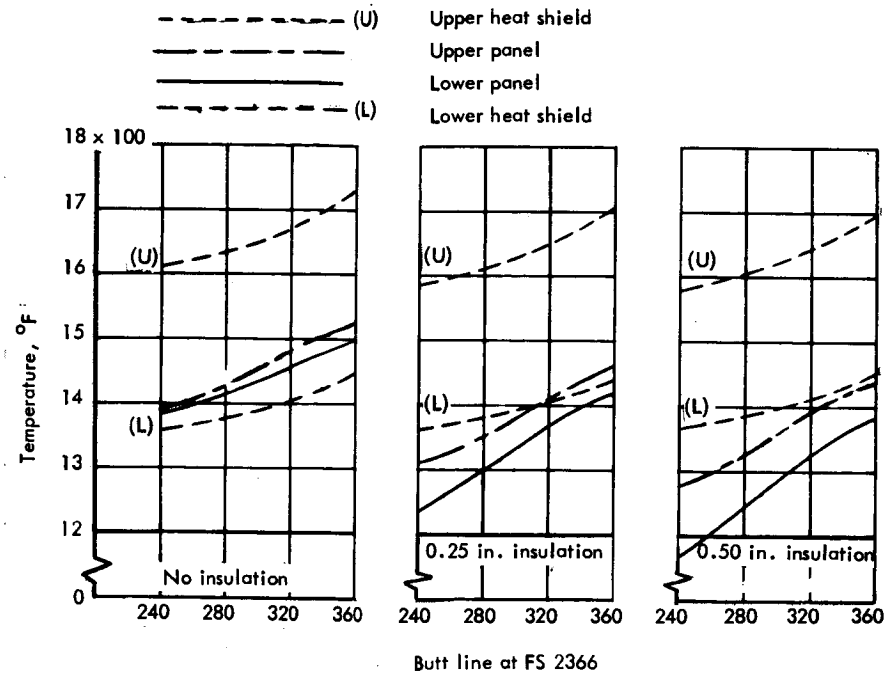

Figure 9-18. Temperatures at -0.5-g condition for outboard semimonocoque panels with upper and lower heat shields vs insulation thickness

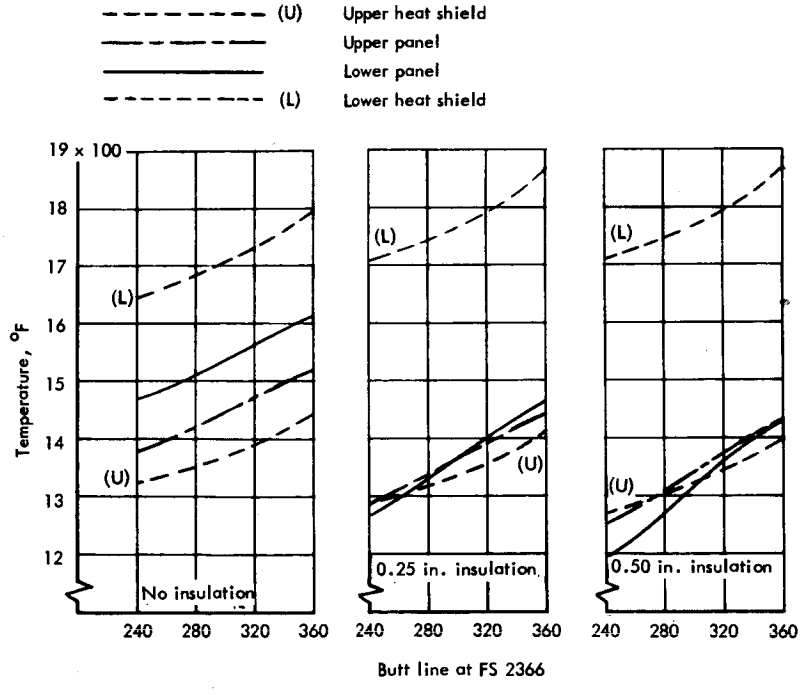

Figure 9-19. Temperatures at +2.0-g condition for outboard semimonocoque panels with upper and lower heat shields vs insulation thickness

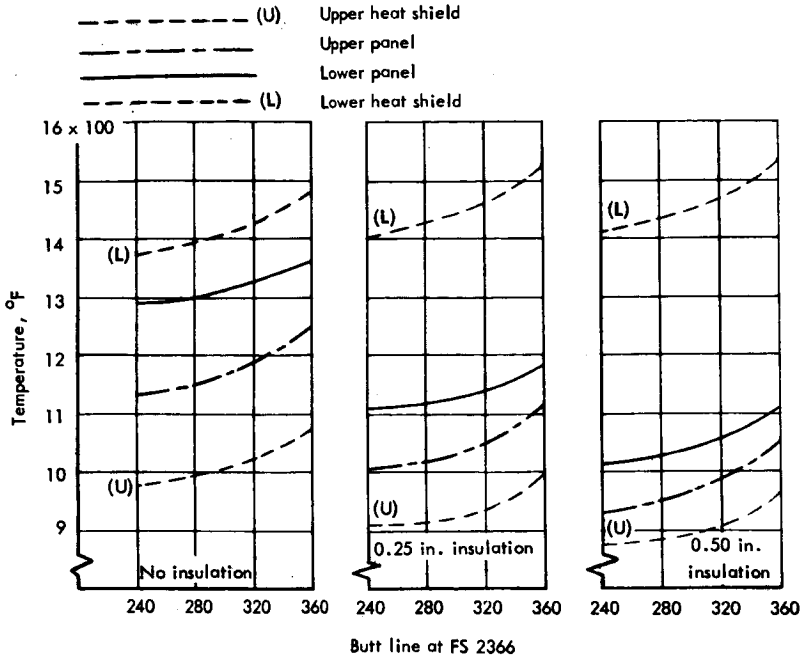

Figure 9-20. Temperatures at cruise condition for outboard semimonocoque panels with upper and lower heat shields vs insulation thickness

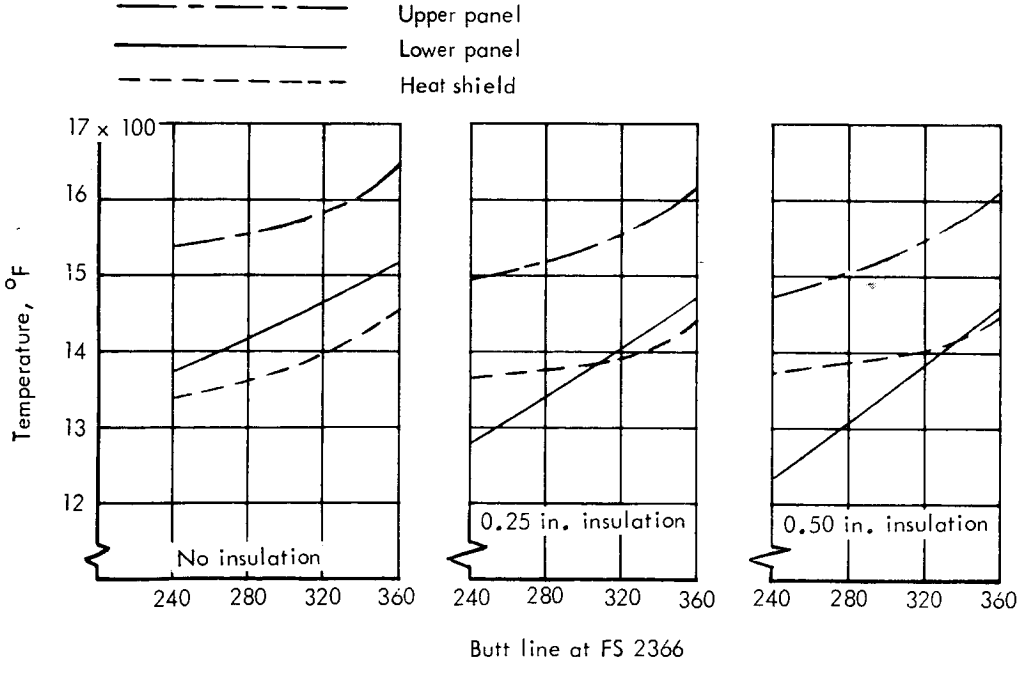

Figure 9-21. Temperatures at -0.5-g condition for outboard semimonocoque panels with lower heat shield only vs insulation thickness

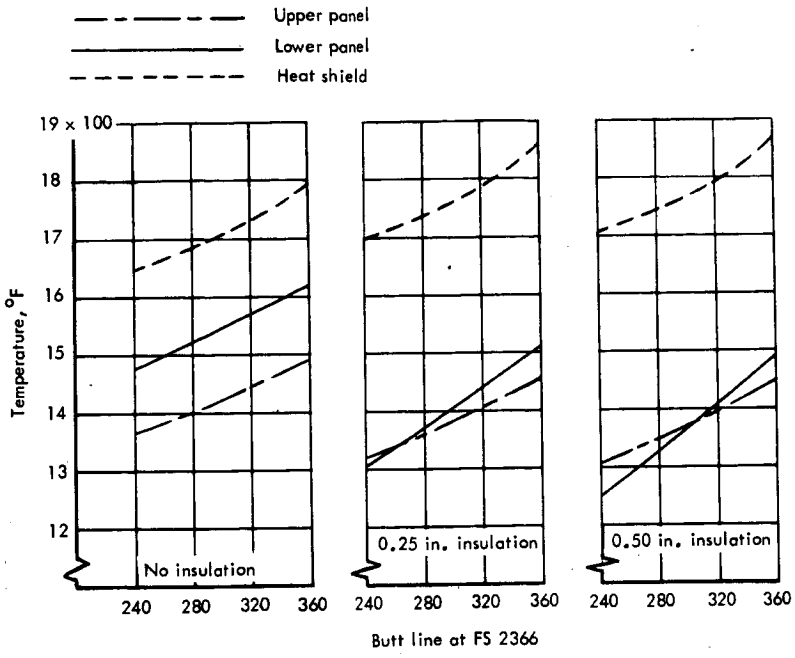

Fig. 9-22. Temperatures at +2.0-g condition for outboard semimonocoque panels with lower heat shield only vs insulation thickness

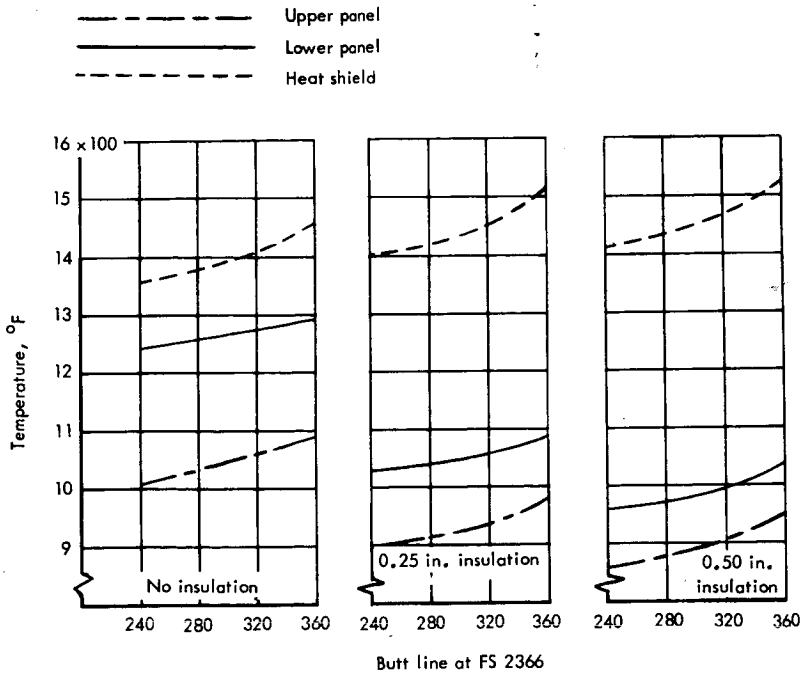

Fig. 9-23. Temperatures at cruise for outboard semimonocoque panels with lower heat shield only vs insulation thickness

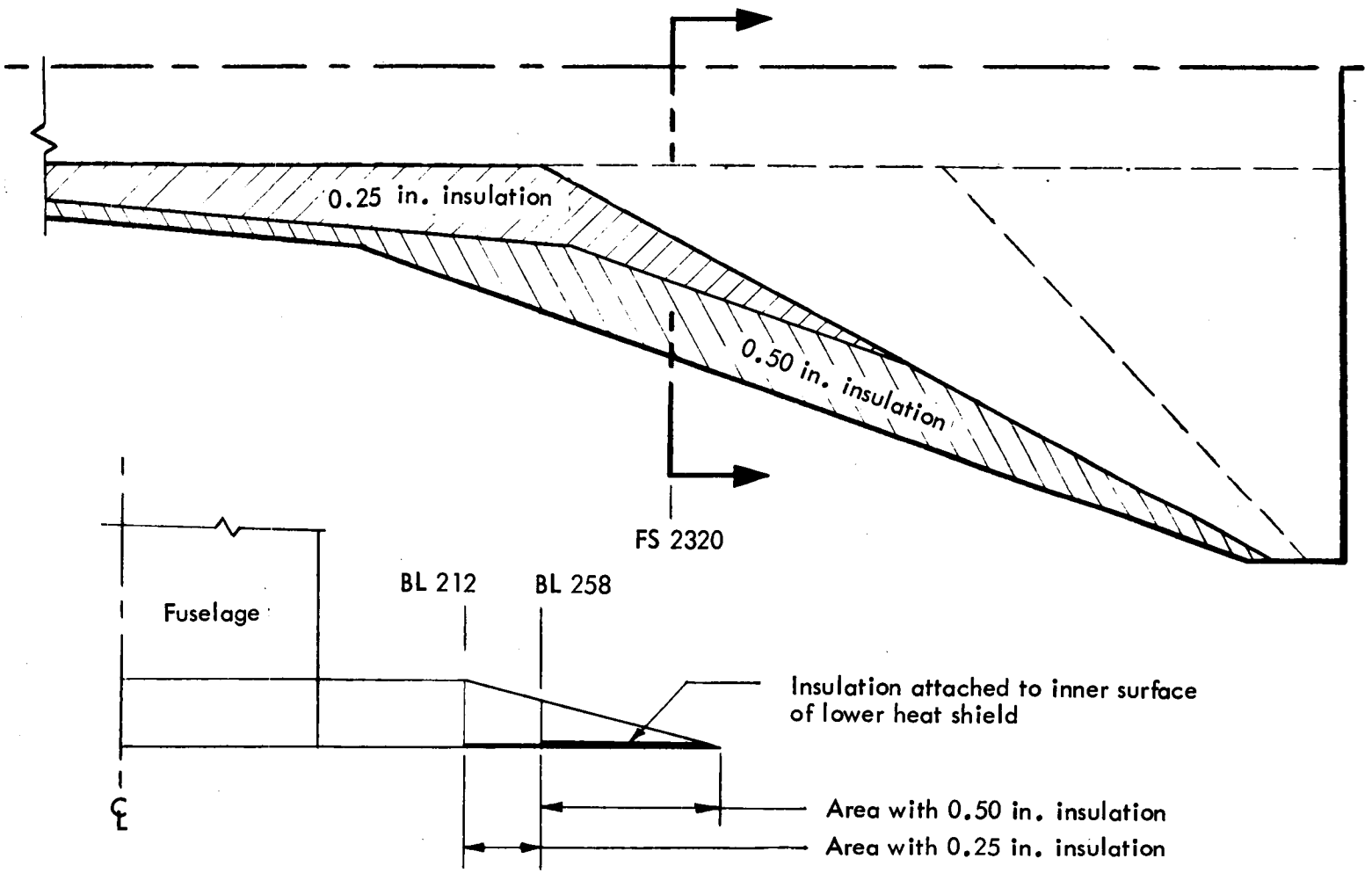

Figure 9-24. Insulation placement for semimonocoque primary-structure-concepts thermal analysis

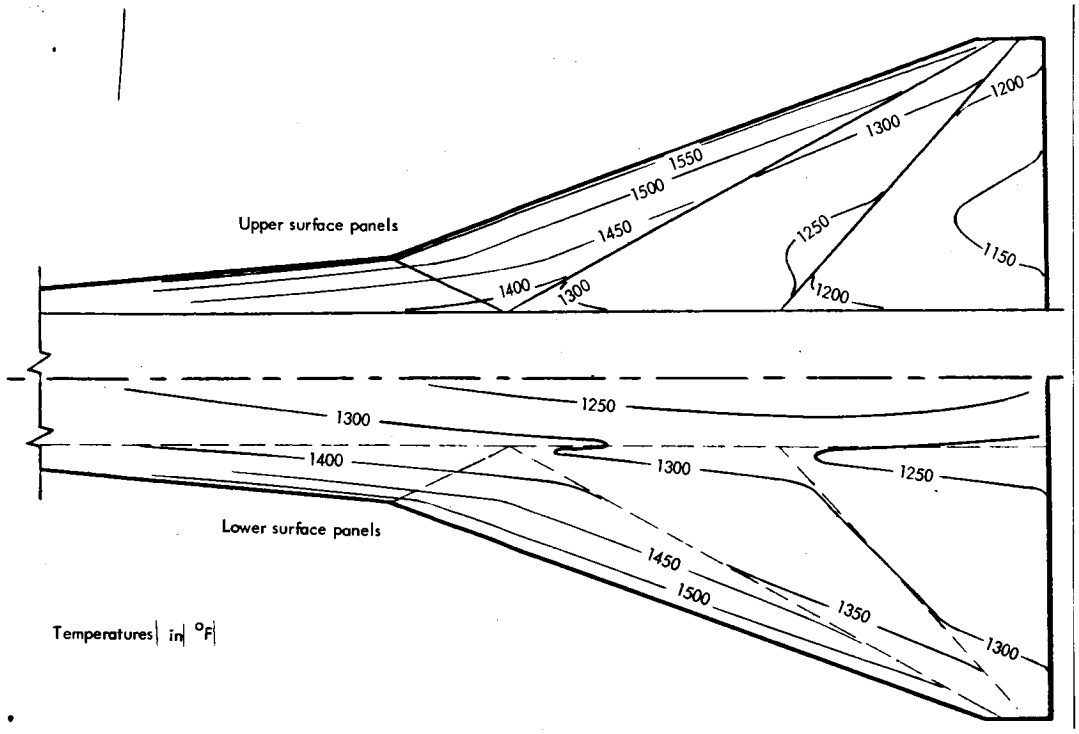

Figure 9-25. Panel isotherms at -0.5-g condition for semimonocoque panels with upper and lower heat shields and no insulation

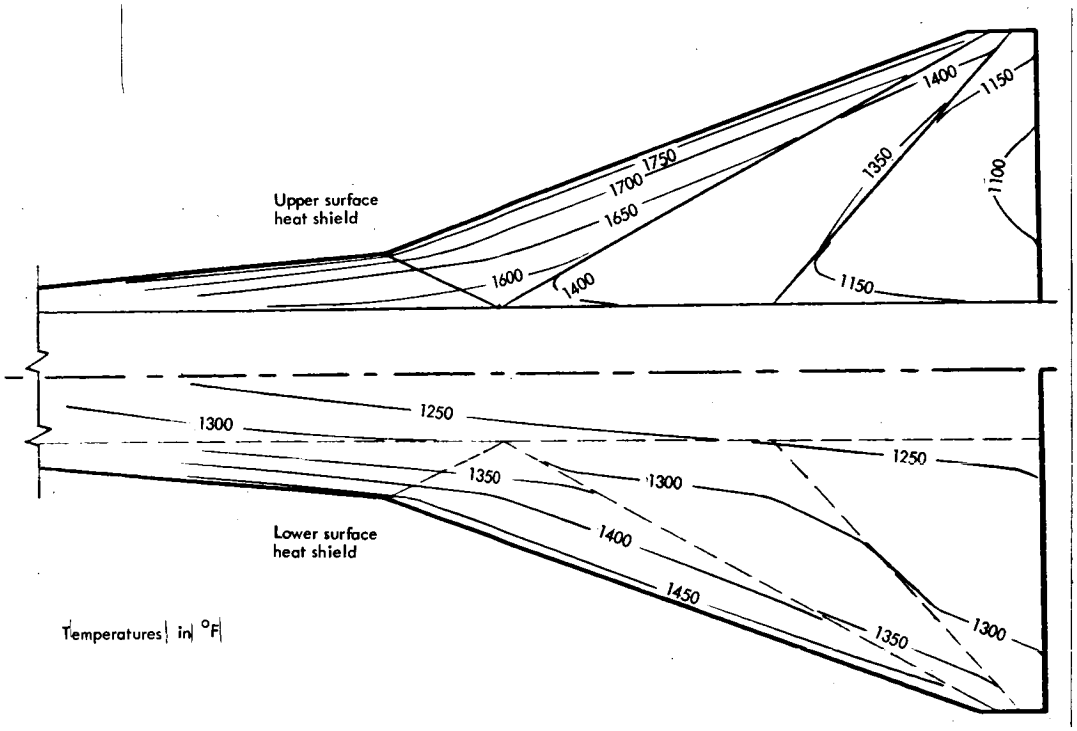

Figure 9-26. Heat-shield isotherms at -0.5-g condition for semimonocoque panels with upper and lower heat shields and no insulation

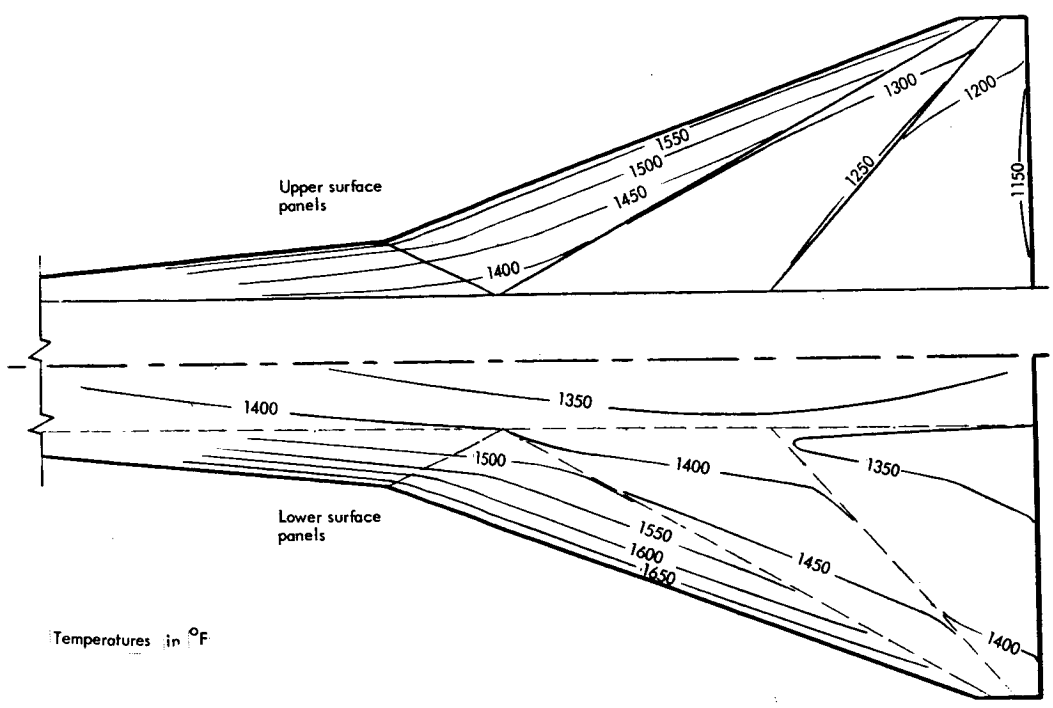

Figure 9-27. Panel isotherms at +2.0-g condition for semimonocoque panels with upper and lower heat shields and no insulation

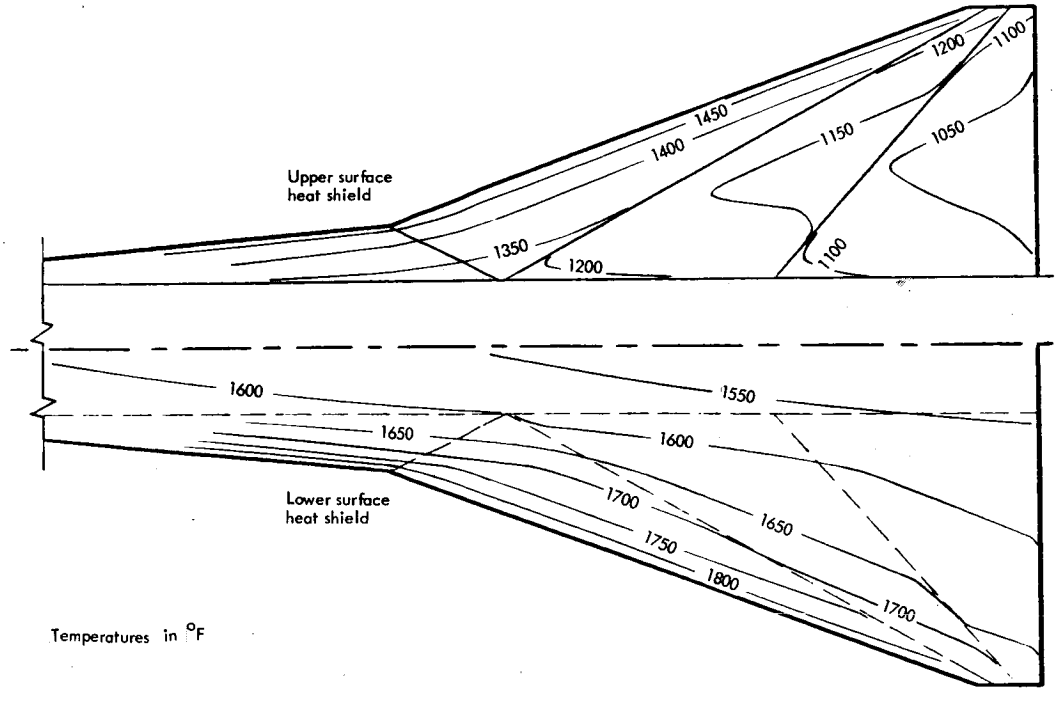

Figure 9-28. Heat-shield isotherms at +2.0-g condition for semimonocoque panels with upper and lower heat shields and no insulation

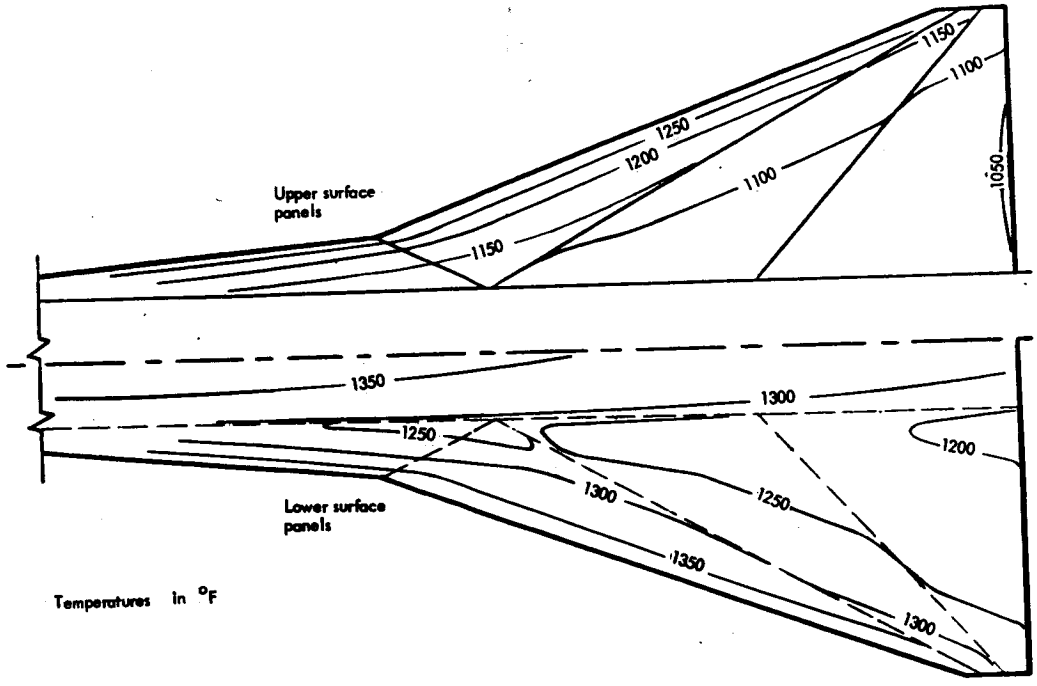

Figure 9-29. Panel isotherms at cruise condition for semimonocoque panels with upper and lower heat shields and no insulation

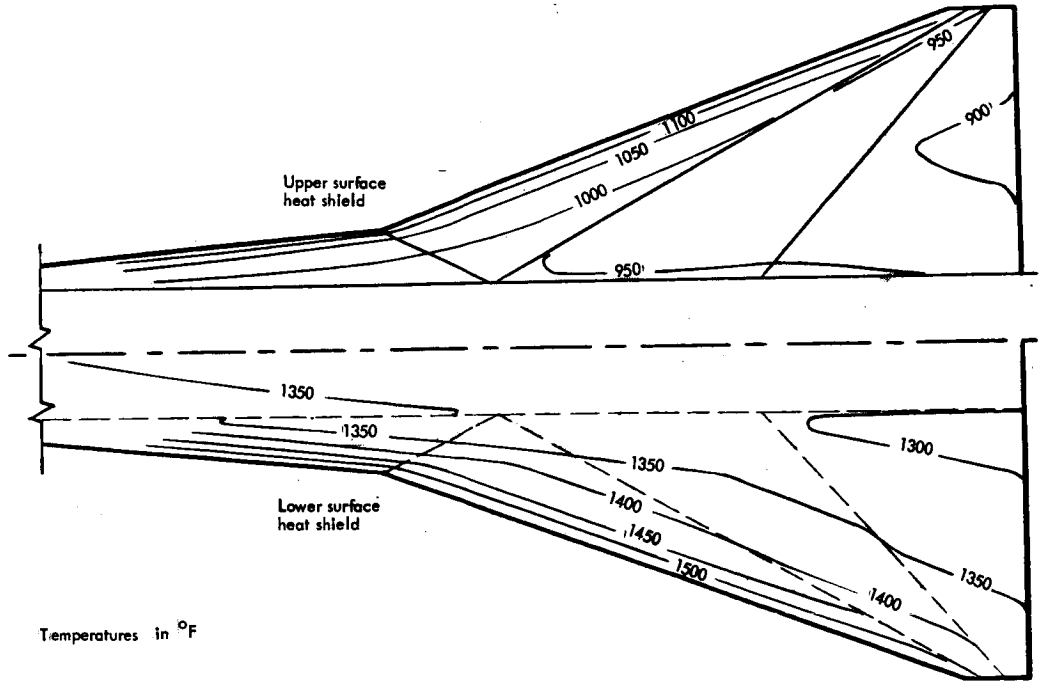

Figure 9-30. Panel isotherms at cruise condition for semimonocoque panels with upper and lower heat shields and no insulation

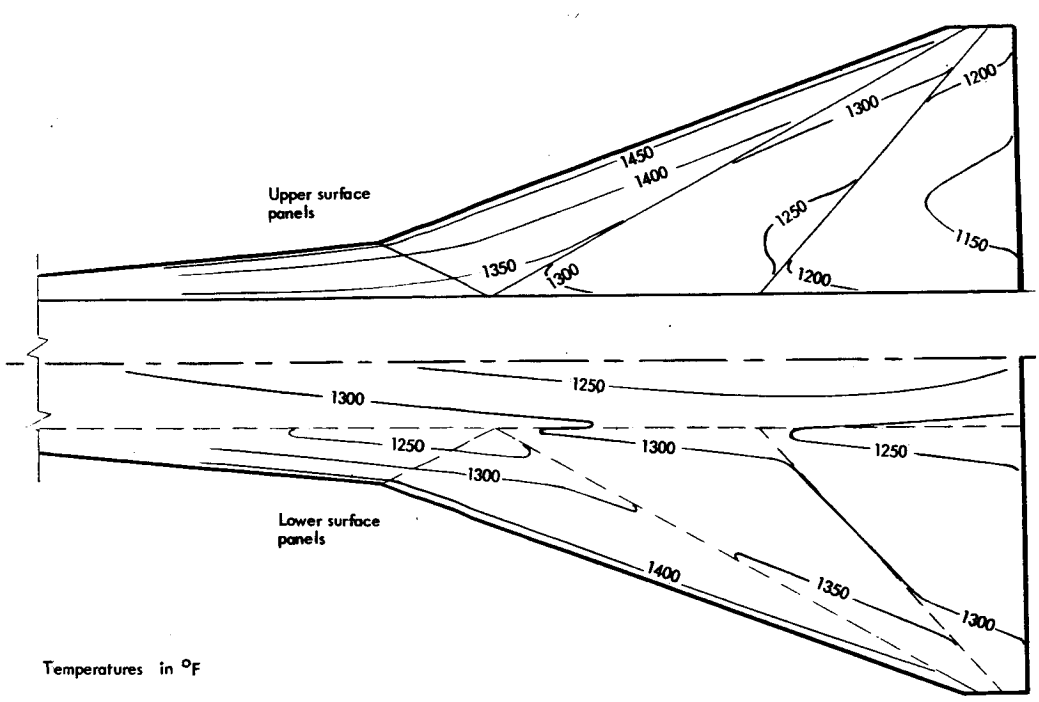

Figure 9-31. Panel isotherms at -0.5-g condition for semimonocoque panels with upper and lower heat shields and partial insulation

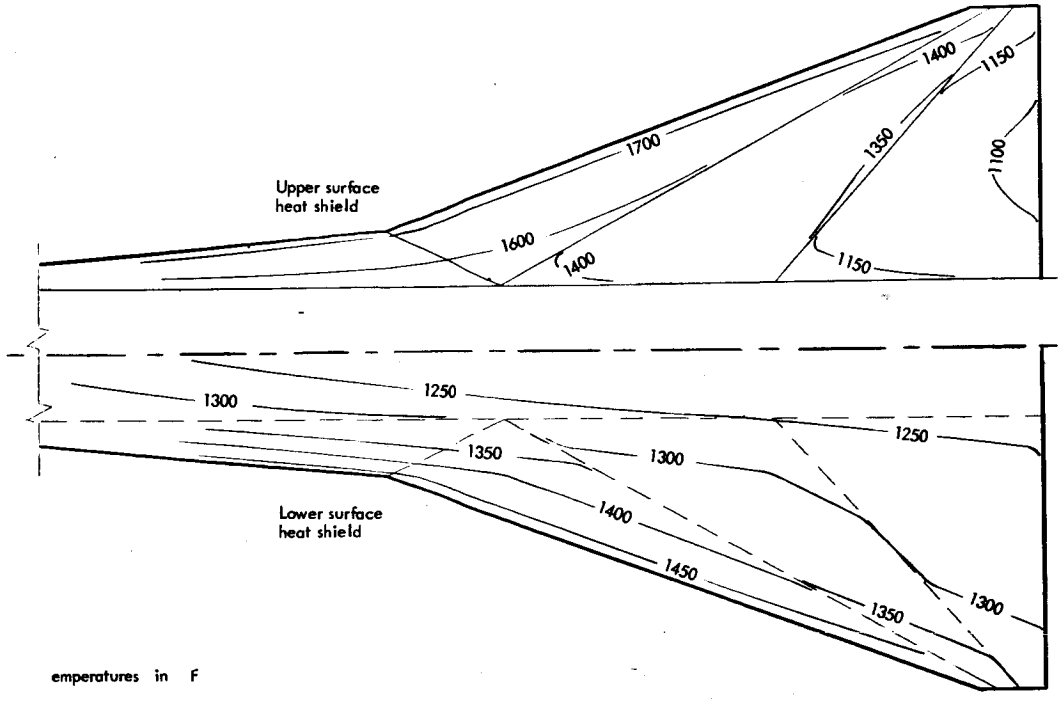

Figure 9-32. Heat-shield isotherms at -0.5-g condition for semimonocoque panels with upper and lower heat shields and partial insulation

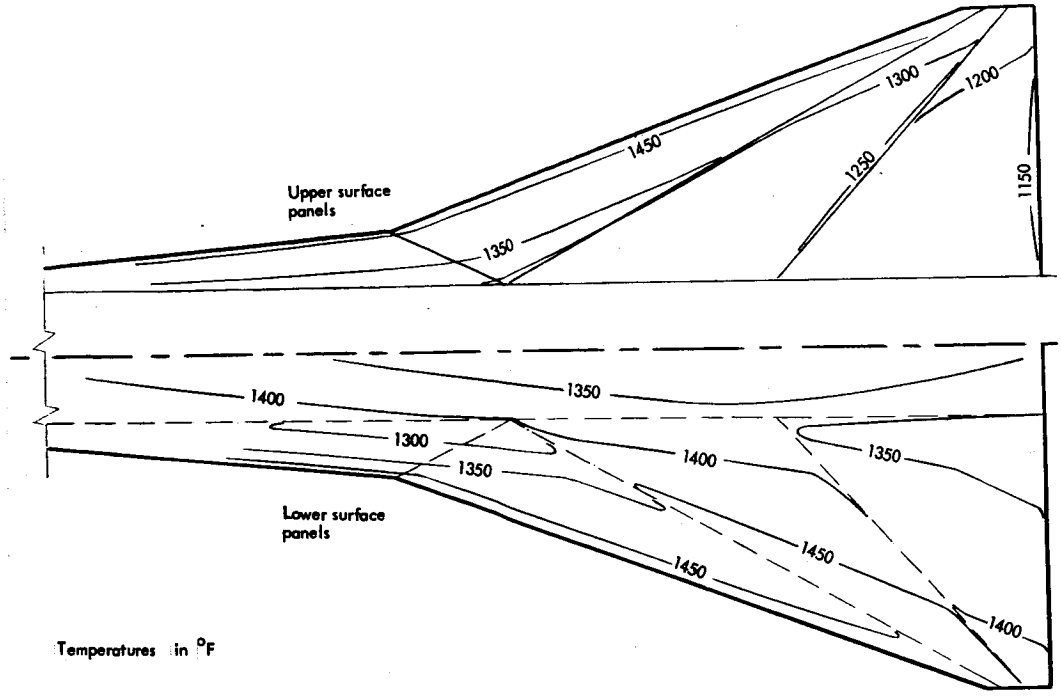

Figure 9-33. Panel isotherms at +2.0-g condition for semimonocoque panels with upper and lower heat shields and partial insulation

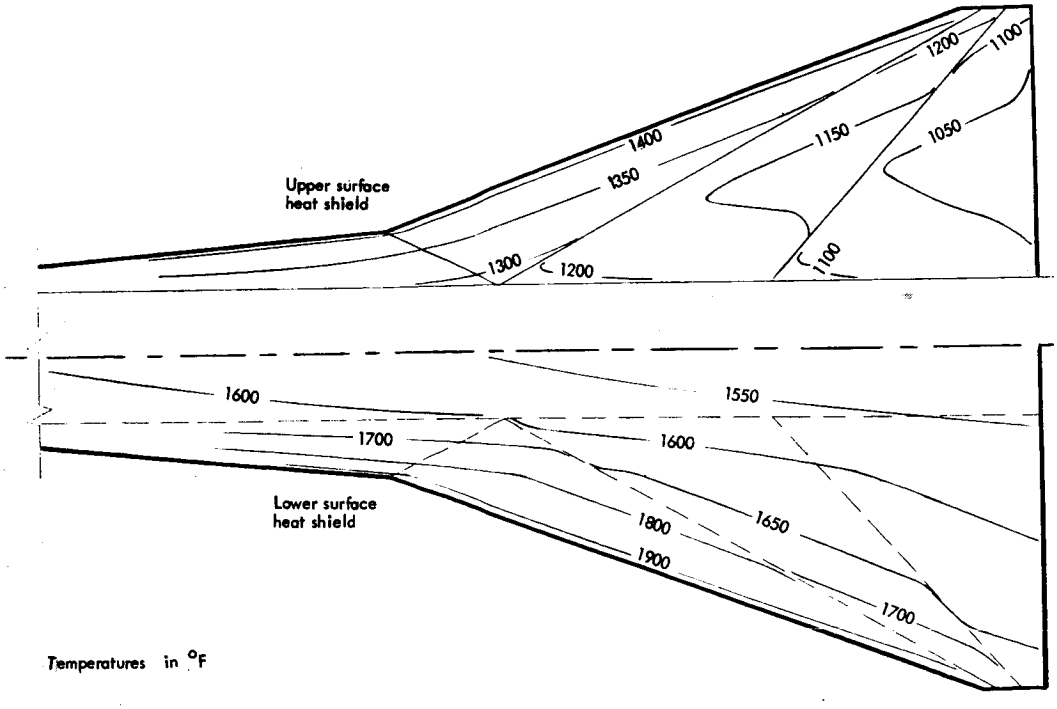

Figure 9-34. Heat-shield isotherms at +2.0-g condition for upper and lower heat shields with semimonocoque panels and partial insulation

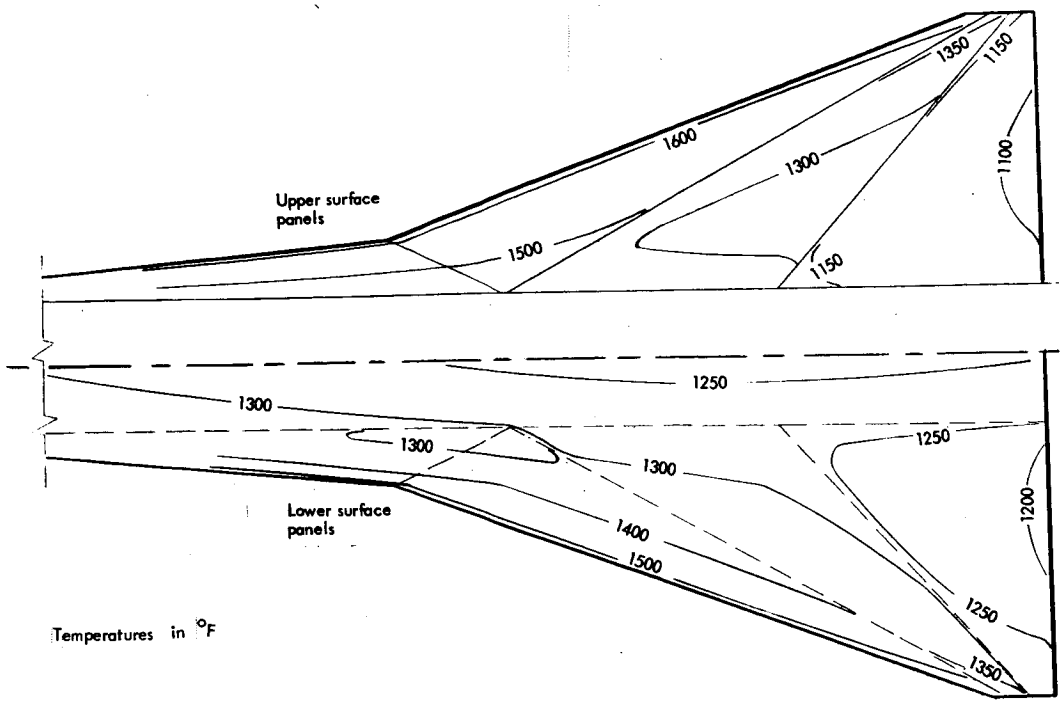

Figure 9-37. Panel isotherms at -0.5-g condition for semimonocoque panels with lower heat shield only and partial insulation

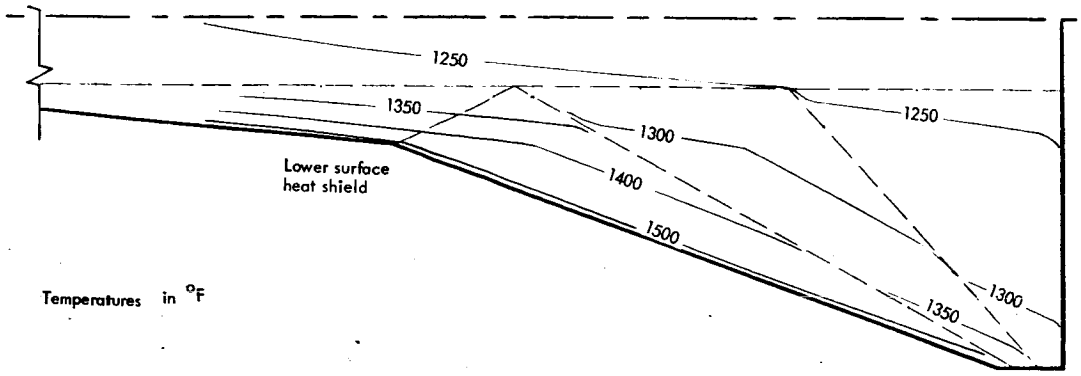

Figure 9-38. Heat-shield isotherms at -0.5-g condition for semimonocoque panels with lower heat shield and partial insulation

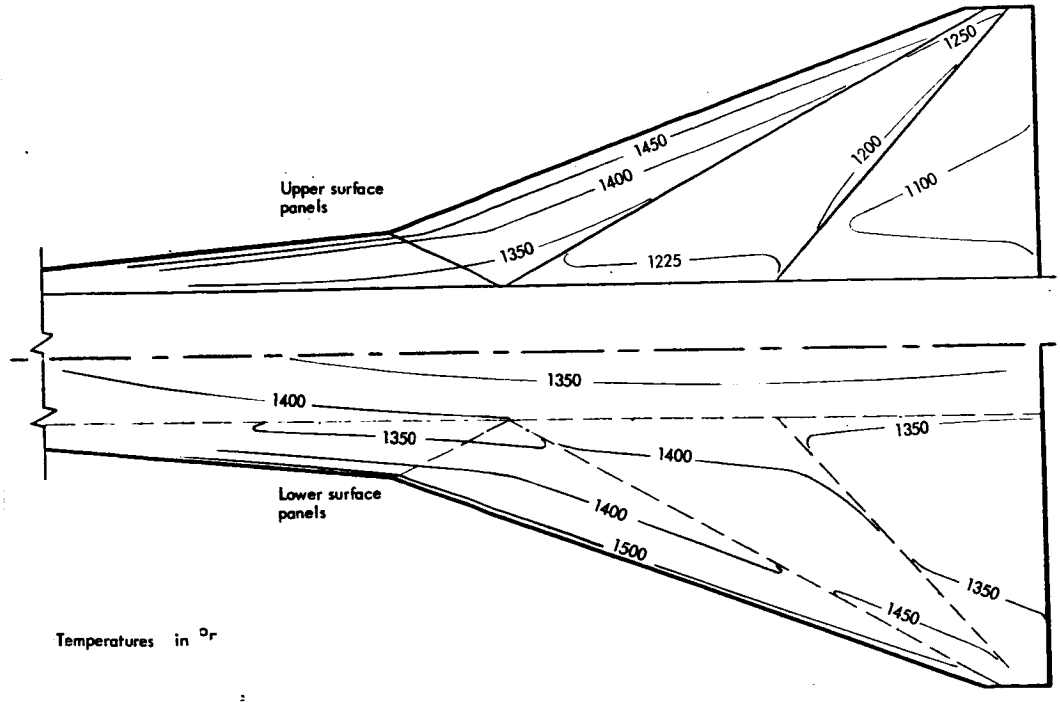

Figure 9-39. Panel isotherms at +2.0-g condition for semimonocoque panels with lower heat shield only and partial insulation

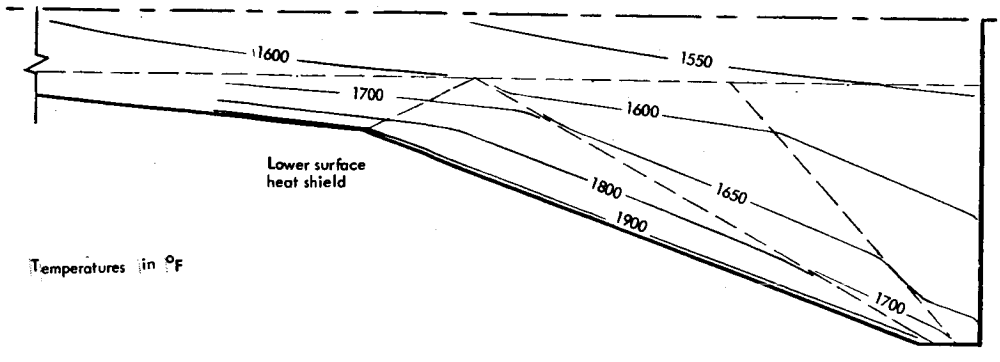

Figure 9-40. Heat-shield isotherms at +2.0-g condition for semimonocoque panels with lower heat shield and partial insulation

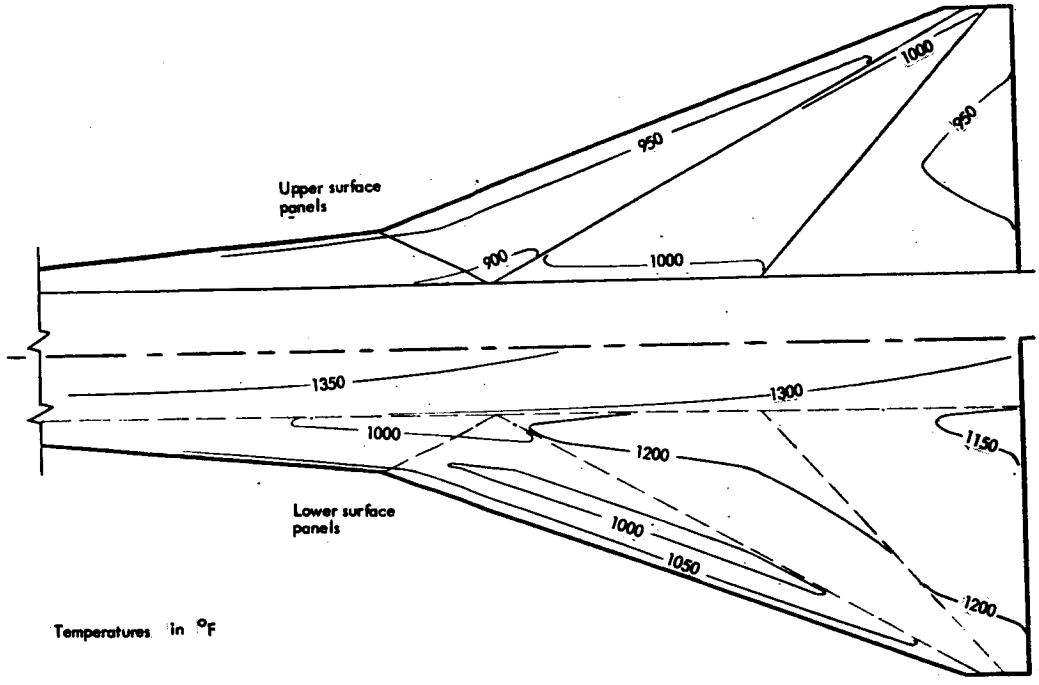

Figure 9-41. Wing isotherms at cruise condition for semimonocoque panels with lower heat shield only and partial insulation

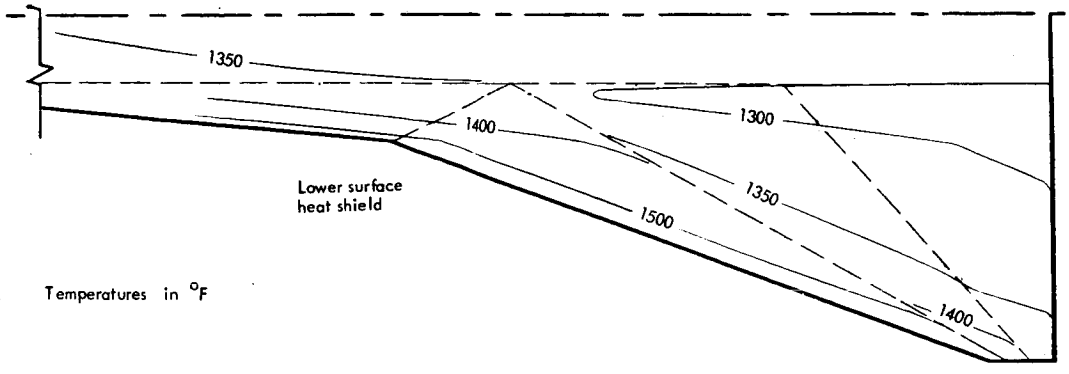

Figure 9-42. Wing isotherms at cruise condition for semimonocoque panels with partial insulation and lower heat shield

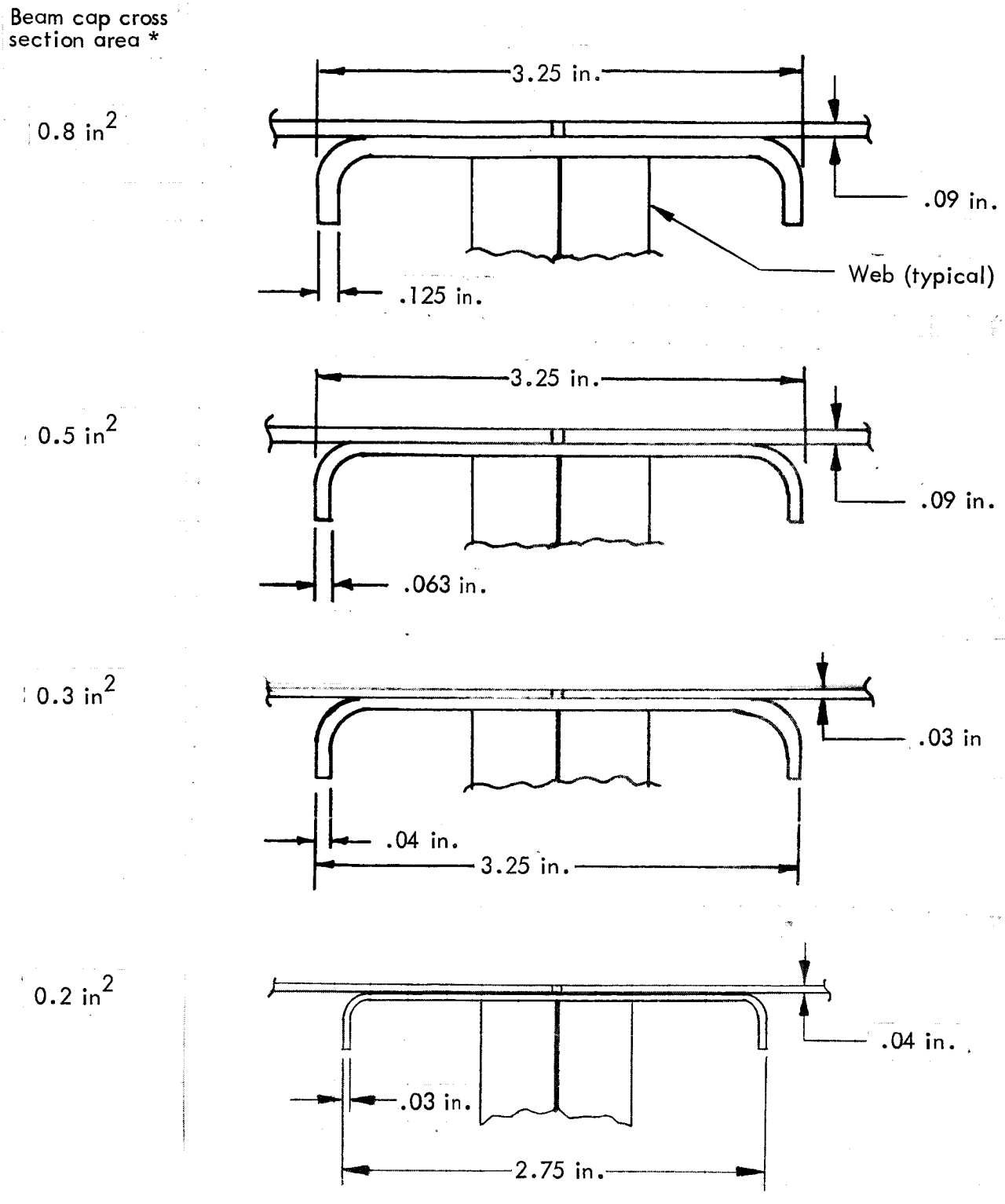

* Includes area of end close-out above cap

Figure 9-43. Typical geometries of beam cap studies for semimonocoque primary structure thermal analysis

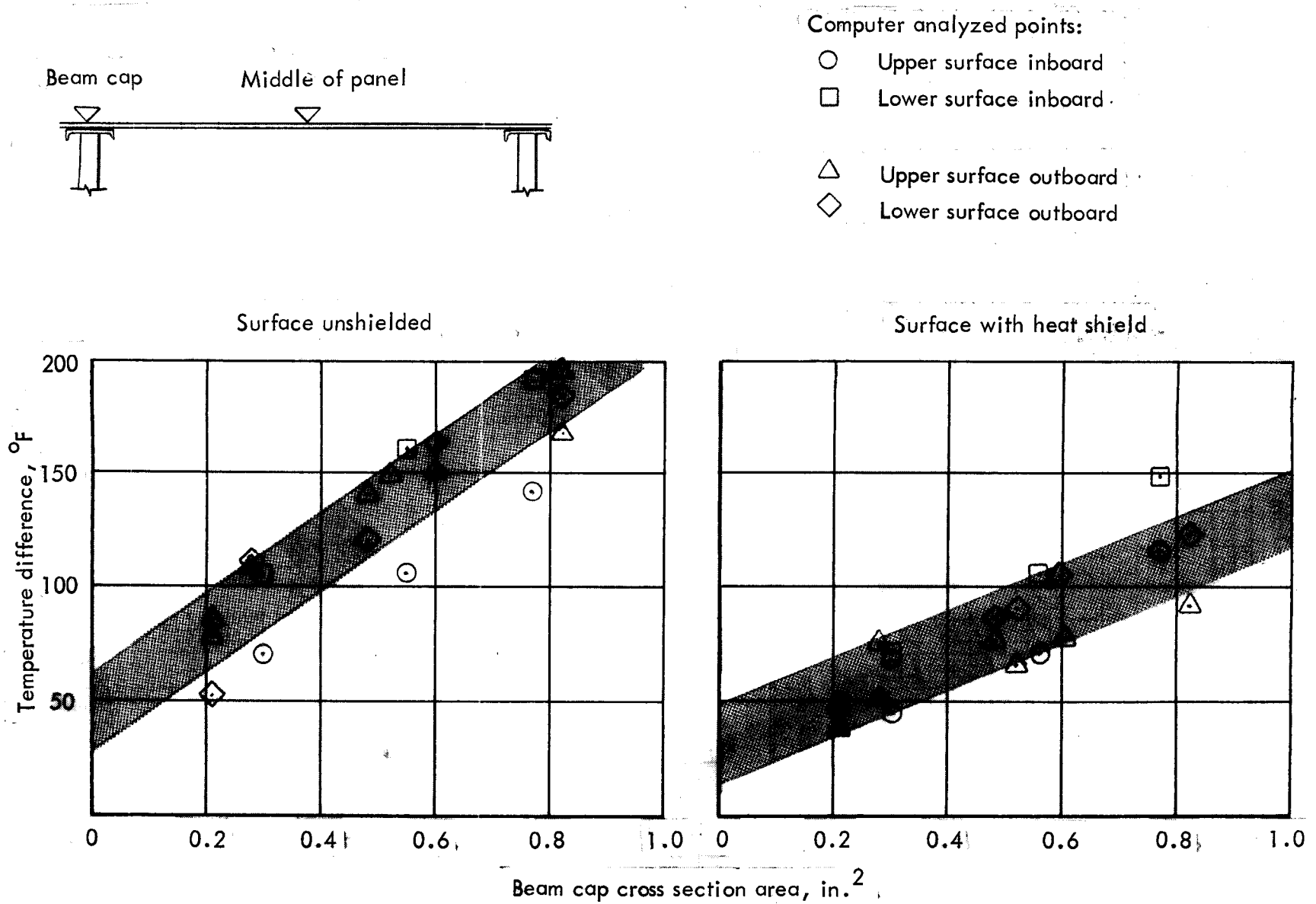

Figure 9-44. Temperature difference from middle of panel to adjacent beam cap for upper surface at -0.5-g and for lower surface at +2.0-g for semimonocoque panels.

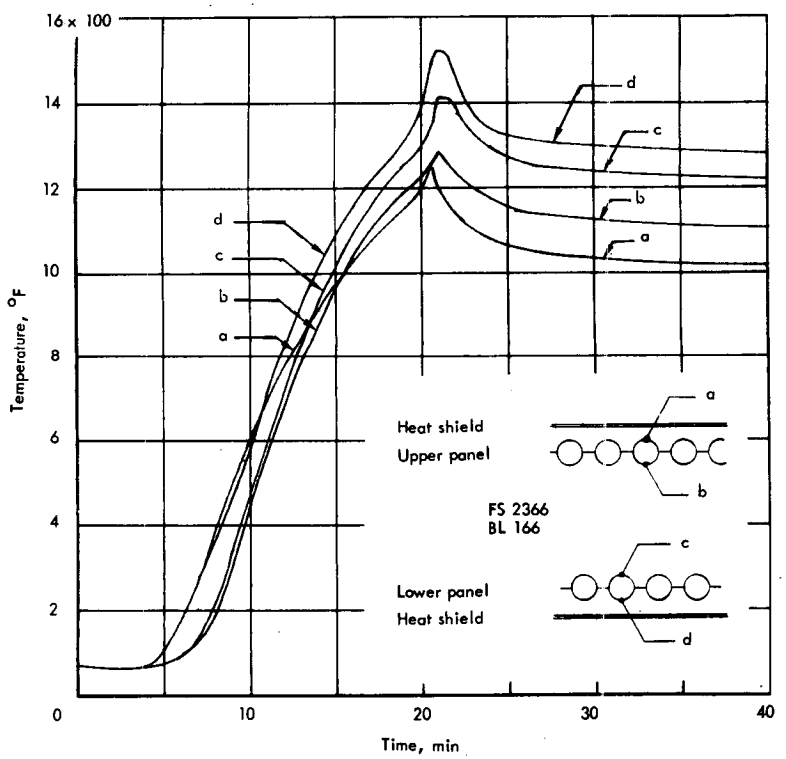

Figure 9-45. Tubular panel vs time at inboard location

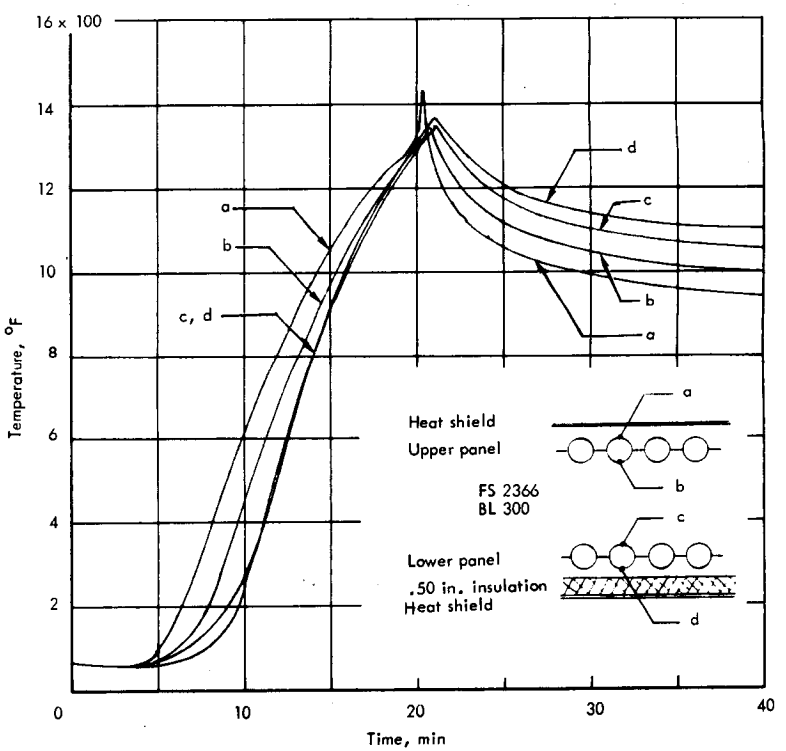

Figure 9-46. Tubular panel temperatures vs time at outboard location with insulation

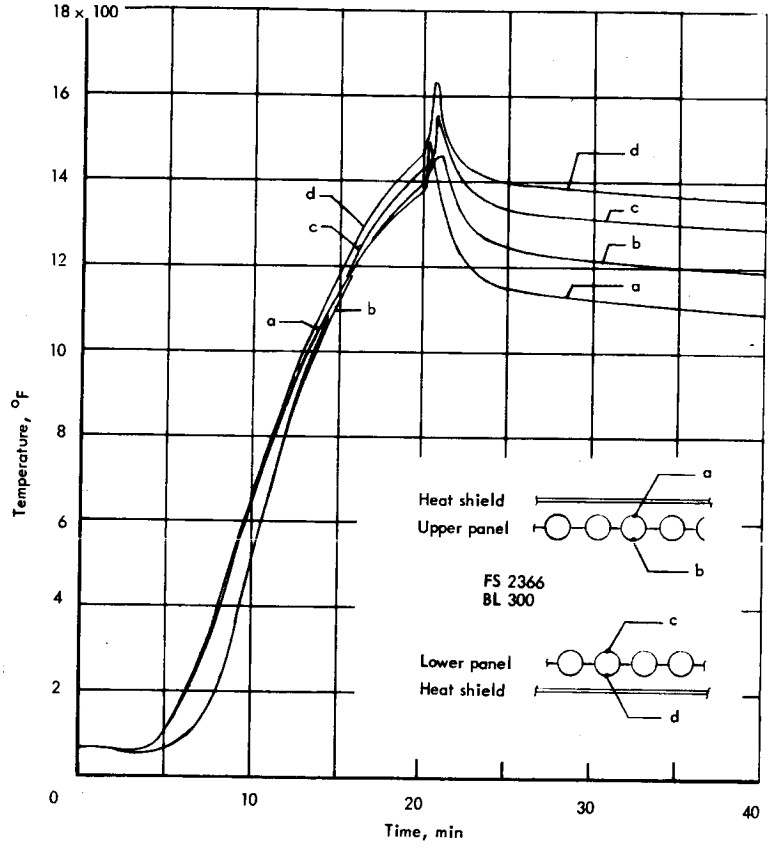

Figure 9-47. Tubular panel temperatures vs time at outboard location without insulation

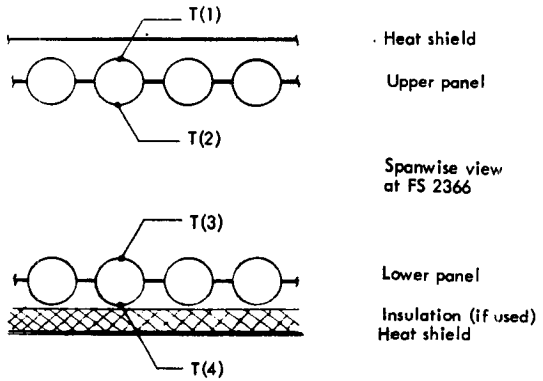

$\Delta T_{Upper} = T(1) - T(2)$

$\Delta T_{Lower} = T(4) - T(3)$

Condition	Location	Inboard		Outboard		
		BL 60	BL 166	BL 300		
	Insulation	None	None	None	0.25 in.	0.50 in.
-0.5g	ΔT_{Upper}	-52	0	48	72	85
	ΔT_{Lower}	64	25	0	11	6
2.0g	ΔT_{Upper}	-49	-35	-29	-3	8
	ΔT_{Lower}	155	114	88	20	1
Cruise	ΔT_{Upper}	0	-91	-95	-66	-52
	ΔT_{Lower}	-2	62	68	50	40

Figure 9-48. Temperature differentials in ^{o}F through semimonocoque spanwise tubular-stiffened panels

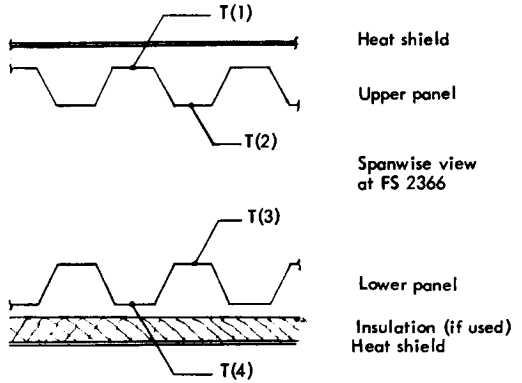

$\Delta T_{Upper} = T(1) - T(2)$

$\Delta T_{Lower} = T(4) - T(3)$

Condition	Location	Inboard		Outboard		
		BL 60	BL 166	BL 300		
	Insulation	None	None	None	0.25 in.	0.50 in.
-0.5g	ΔT_{Upper}	-10	-4	9	16	19
	ΔT_{Lower}	16	10	1	3	1
2.0g	ΔT_{Upper}	-10	-10	-9	1	4
	ΔT_{Lower}	41	36	28	6	0
Cruise	ΔT_{Upper}	0	-29	-31	-20	-15
	ΔT_{Lower}	0	21	23	16	12

Figure 9-49. Temperature differentials in ^{o}F through semimonocoque spanwise trapezoidal-corrugation panels

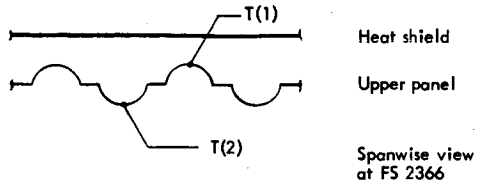

Condition	Location	Inboard		Outboard		
		BL 60	BL 166	BL 300		
	Insulation	None	None	None	0.25 in.	0.50 in.
-0.5g	ΔT_{Upper}	-3	-2	6	9	11
	ΔT_{Lower}	4	4	0	1	0
2.0g	ΔT_{Upper}	-3	-7	-7	-2	0
	ΔT_{Lower}	17	17	14	3	0
Cruise	ΔT_{Upper}	0	-15	-16	-11	-8
	ΔT_{Lower}	0	11	12	8	7

Figure 9-50. Temperature differentials in ^{o}F through semimonocoque spanwise-beaded panels

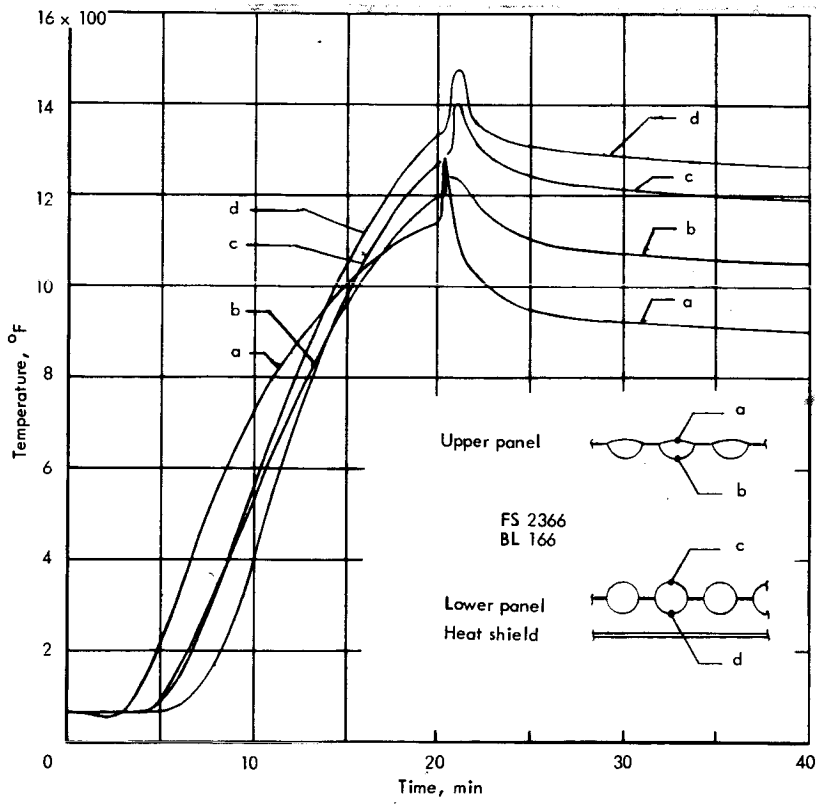

Figure 9-51. Semimonocoque chordwise-stiffened panel temperatures vs time at inboard location

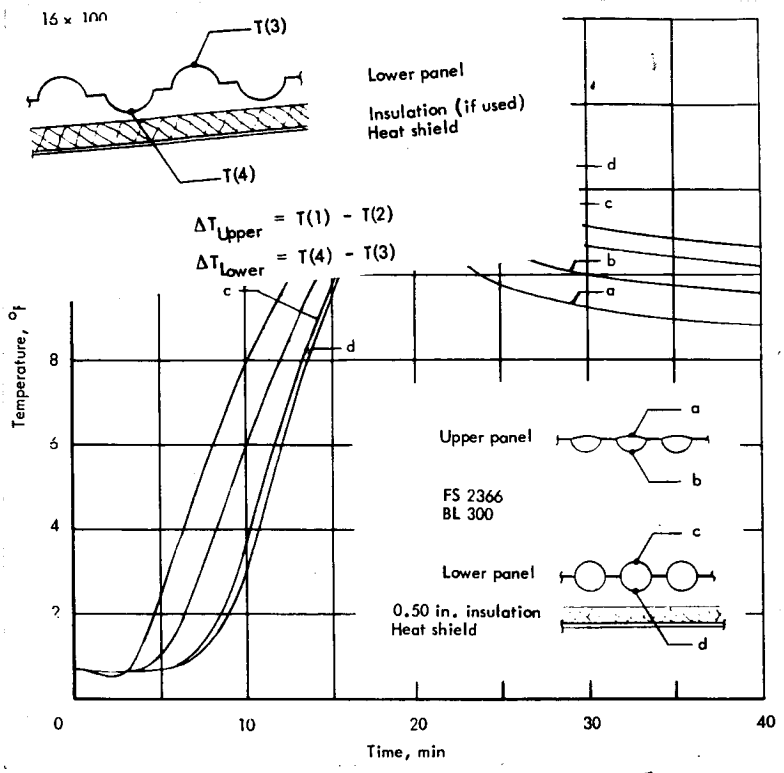

Figure 9-52 Semimonocoque chordwise-stiffened panel temperatures vs time at outboard location with insulation

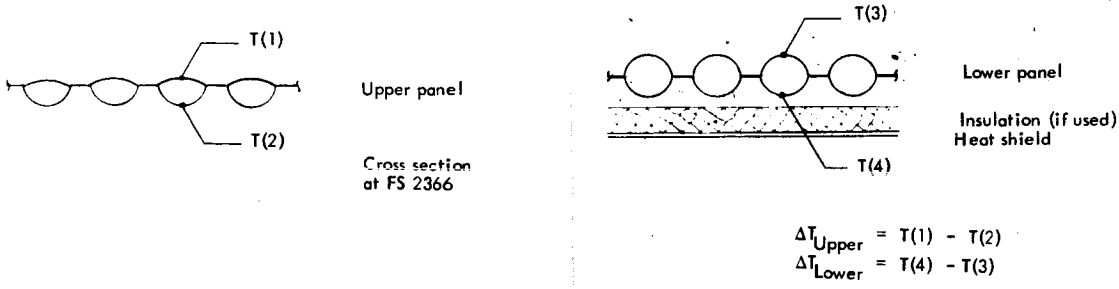

Condition	Location	Inboard		Outboard		
		BL 60	BL 166	BL 300		
	Insulation	None	None	None	0.25 in.	0.50 in.
-0.5g	ΔT_{Upper}	-54	45	115	148	162
	ΔT_{Lower}	74	39	3	7	0
2.0g	ΔT_{Upper}	-50	-50	-46	-14	-2
	ΔT_{Lower}	159	112	86	14	-4
Cruise	ΔT_{Upper}	0	-151	-157	-99	-75
	ΔT_{Lower}	-1	74	82	57	45

Figure 9-53. Temperature differentials in °F through semimonocoque chordwise-stiffened panel with convex beaded upper surface

Section 10

OPTIMIZATION PROCEDURE FOR PANELS OF MONOCOQUE STRUCTURE

by

R. E. Hubka

CONTENTS

ILLUSTRATIONS

SYMBOLS

A_{cap}	Cap area
a,b	X and y distances between simply supported edges of plate
b_c, b_s	Widths of core and skin elements of truss-core sandwich
b_f	Width of flange of flanged waffle
b_s	Pitch
C_{ij}	Stiffness coefficients
D_1, D_2, D_3	Stiffness coefficients of governing differential equation of plate
d	Width of interface of core ribbons of honeycomb-core sandwich
E	Modulus of elasticity
E_c	Compressive Modulus of elasticity
E_{el}	Elastic Modulus of elasticity
E_{tan}, E_{sec}	Extensional tangent and secant moduli
e_x, e_y	Eccentricity of x and y compressive loading
F_{ij}	Flexibility coefficients
$F_{0.7}$	Stress corresponding to modulus of 0.7 E_{el}
f_b, f_c, f_s	Bending, compressive and shear stresses
f_{cap}	Cap stress
f_{IB}, f_{WR}	Intercell (dimpling) and wrinkling stresses of honeycomb-core sandwich
f_w	Extensional stress of stiffeners of waffle
f_x, f_y, f_{xy}	Extensional stresses and shear stress in xy coordinate system
$f_{y,c}, f_{sy,c}$	Extensional stresses and shear stress of core of truss-core sandwich

G_{el}	$\cong E_{el}/2(1+\upsilon_{el})$: elastic shear modulus
$\bar{I}_x, \bar{I}_y$	Moments of inertial per unit length of section associated with x-wise and y-wise bending of orthotropic plate
k, k_c	Buckling coefficients in analyses of local compressive buckling
k_{xy}, k_s	Buckling coefficients in analyses of local shear buckling
L	Length
M_x, M_y, M_{xy}	Bending moments and twisting moment in xy coordinate system per unit length of section.
m	Number of half waves in plate buckling equations
N_x, N_y, N_{xy}	Extensional forces and shear force in xy coordinate system per unit length of section
$\bar{N}_x, \bar{N}_y$	Extensional forces in xy coordinate system per unit length of section of plate.
n	Exponent of interaction equation
q	Pressure
R_c	Compressive stress ratio in general instability analyses
R_{xy}, R_s	Shear stress ratios in general instability analyses
r_c, r_x, r_y	Compressive stress ratios in local buckling analyses
r_s, r_{xy}	Shear stress ratios in local buckling analyses
T	Temperature
[T]	Transformation matrix defined by equation 10-6
t	Thickness
$\bar{t}$	Equivalent panel thickness
$\bar{t}_s$	Effective thickness in expression of shear stiffness
U	Strain energy; utilization factor
w	Deflection measured in z direction

x,y,z	Rectangular Cartesian coordinates of panel
$\bar{z}$	Location of neutral "surface" of plate
α	Mean coefficient of thermal expansion
χ_x,χ_y,χ_{xy}	Curvatures and twist in xy coordinate system
ΔT	Temperature difference between inner and outer extremities of panel
ϵ_{xy}	$\equiv 0.5\gamma_{xy}$: shear strain
$\epsilon_x,\epsilon_y,\epsilon_{xy}$	Extensional strains and shear strain in xy coordinate system
$\bar{\epsilon}_x,\bar{\epsilon}_y,\gamma_{xy}$	Extensional strains and shear strain of reference "surface" of waffle plates in xy coordinate system
ν	Poisson's ratio
ν_{el}	Elastic Poisson's ratio
$\bar{\nu}_{xb},\bar{\nu}_{yb}$	$\equiv D_{12}/D_{22}$, D_{12}/D_{11}: Poisson's ratios associated with x and y bending deformations of orthotropic plate
θ	Angular dimension of panel cross section
ζ,η,z	Rectangular Cartesian coordinates coinciding with stiffeners of -45 x 45 deg waffle plates
$\{\ \}$	Column matrix
$[\ ]$	Square matrix

Subscripts

c	Indicates quantity pertains to core of truss-core or honeycomb-core sandwich; quantities due to compression or coupling
cap	Indicates quantity pertains to cap
cr	Denotes buckling stress or load
f	Indicates quantity pertains to flange of flanged waffle
GI	Denotes quantity associated with general instability

i	Number of loading condition
	General subscript
s	Indicates quantity pertains to skin of waffle plates, faces of honeycomb-core sandwich plate or faces of truss-core sandwich plate
T	Indicates quantity is due to thermal effects
w	Indicates quantity pertains to stiffeners of waffle plates or to stiffener web of flanged waffle plate when used with dimensional notation
x,y	Denotes quantities with respect to x and y directions
$\xi\eta$	Denote quantities with respect to ξ and η
1,2	Denotes lower and upper faces of honeycomb- and truss-core sandwich plate

SECTION 10

OPTIMIZATION PROCEDURE FOR PANELS OF MONOCOQUE STRUCTURE

Equations of the two computer programs which were used to design the panels of the monocoque structure are presented in this section. The analyses are formulated for the synthesis concept of structural optimization. A general optimization subroutine is used in the programs to direct a constrained minimization of the weight of the structure. The mathematical procedure of the subroutine, which is not presented, is based on the maximum gradient method.

STRESS ANALYSIS PROCEDURE OF COMPUTER PROGRAM NO. 1

A typical panel is shown in figure 10-1. Neglecting coupling between inplane and out-of-plane deformations, the extensional and shearing strains of the plate are:

$$\begin{Bmatrix} \varepsilon_x \\ \varepsilon_y \\ \varepsilon_{xy} \end{Bmatrix}_i = \begin{bmatrix} F_{11} & F_{12} & F_{13} \\ F_{12} & F_{22} & F_{23} \\ F_{13}/2 & F_{23}/2 & F_{33}/2 \end{bmatrix}_i \begin{Bmatrix} \overline{N}_x \\ \overline{N}_y \\ N_{xy} \end{Bmatrix}_i \qquad (10\text{-}1)$$

in which $\varepsilon_{xy} = \gamma_{xy}/2$ and

$$[F] = \begin{bmatrix} C_{11} & C_{12} & 2C_{13} \\ C_{12} & C_{22} & 2C_{23} \\ C_{13} & C_{23} & 2C_{33} \end{bmatrix}^{-1}$$

The stiffness coefficients with plasticity effects included are evaluated with equations of reference 10-1. The subscript i denotes number of loading condition. It is to be noted that the coefficients C_{13} and C_{23} are zero for all plates except the 45° x 45° waffle (fig. 10-2) when an unequal amount of plastic deformation occurs in the ξ-wise and η-wise stiffeners.

Assuming plane sections before loading remain plane after loading, the cap stresses are

$$f_{cap,\ell,i} = E_{sec,\ cap,\ell,i}\varepsilon_{\ell,i} \qquad (\ell = x,y) \tag{10-2}$$

The extensional stress resultants of the plate are

$$\begin{Bmatrix} \bar{N}_x \\ \bar{N}_y \end{Bmatrix}_i = \begin{bmatrix} A_{11} & A_{12} \\ A_{21} & A_{22} \end{bmatrix}_i^{-1} \begin{Bmatrix} B_1 \\ B_2 \end{Bmatrix}_i \tag{10-3a}$$

where

$$\begin{aligned} A_{11,i} &= L_{p,y} + A_{cap,x}E_{sec,cap,x,i}F_{11,i} \\ A_{12,i} &= A_{cap,x}E_{sec,cap,x,i}F_{12,i} \\ A_{21,i} &= A_{cap,y}E_{sec,cap,y,i}F_{12,i} \\ A_{22,i} &= L_{p,x} + A_{cap,y}E_{sec,cap,y,i}F_{22,i} \\ B_{1,i} &= L_y N_{x,i} - A_{cap,x}E_{sec,cap,x,i}F_{13,i}N_{xy,i} \\ B_{2,i} &= L_x N_{y,i} - A_{cap,y}E_{sec,cap,y,i}F_{23,i}N_{xy,i} \end{aligned} \tag{10-3b}$$

Expressions of the stiffener and skin stresses of the 0 x 90° waffle (fig. 10-3) are

$$f_{w,\ell,i} = E_{sec,w,\ell,i}\varepsilon_{\ell,i} \qquad (\ell = x,y) \tag{10-4a}$$

and

$$\begin{Bmatrix} f_{x,s} \\ f_{y,s} \\ f_{xy,s} \end{Bmatrix}_i = \frac{E_{sec,s,i}}{1 - \nu_{s,i}^2} \begin{bmatrix} 1 & \nu_s & 0 \\ \nu_s & 1 & 0 \\ 0 & 0 & 1 - \nu_s \end{bmatrix}_i \begin{Bmatrix} \varepsilon_x \\ \varepsilon_y \\ \varepsilon_{xy} \end{Bmatrix}_i \qquad (10\text{-}4b)$$

or

$$\{f\}_i = \left[C_s\right]_i \{\varepsilon\}_i \qquad (10\text{-}4c)$$

where the subscripts s and w denote skin and stiffener. The effective Poisson's ratio of the above equations is expressed as follows (ref. 10-2):

$$\nu = 0.5 - \eta_{sec} \left(0.5 - \nu_{el}\right) \qquad (10\text{-}5)$$

Strains of the 45° x 45° waffle of figure 10-2 are (ref. 10-3)

$$\begin{Bmatrix} \varepsilon_\xi \\ \varepsilon_\eta \\ \varepsilon_{\xi\eta} \end{Bmatrix}_i = \begin{bmatrix} 0.5 & 0.5 & 1 \\ 0.5 & 0.5 & -1 \\ -0.5 & 0.5 & 0 \end{bmatrix} \begin{Bmatrix} \varepsilon_x \\ \varepsilon_y \\ \varepsilon_{xy} \end{Bmatrix}_i \qquad (10\text{-}6a)$$

or

$$\{\varepsilon'\}_i = [T]\{\varepsilon\}_i \qquad (10\text{-}6b)$$

Expressions of the stiffener and skin stresses are

$$f_{w,\ell,i} = E_{sec,\ell,i}\varepsilon_{\ell,i} \qquad (\ell = \xi,\eta) \qquad (10\text{-}7a)$$

and

$$\begin{Bmatrix} f_{\xi,s} \\ f_{\eta,s} \\ f_{\xi\eta,s} \end{Bmatrix}_i = \{f'\}_i = \left[C_{s\ i} \right] \{\varepsilon'\}_i \qquad (10\text{-}7b)$$

The skin stresses in the xy coordinate system are

$$\{f\}_i = [T]^{-1} \{f'\}_i \qquad (10\text{-}8)$$

The material properties of the faces of the honeycomb core sandwich (fig. 10-4) are assumed to be equal. Hence, the expression of the skin stresses is the same as that of the 0 x 90° waffle, equation (10-4c).

Expressions of the core stresses of the truss-core sandwich (fig. 10-5) are

$$f_{y,c,i} = E_{sec,c,i} \varepsilon_{y,i}$$

$$f_{sy,c,i} = \frac{E_{sec,c,i}}{1 + \nu_{c,i}} \varepsilon_{xy,i} \cos\theta \qquad (10\text{-}9)$$

The face stresses are given by equation (10-4c).

It is to be noted that Computer Program No. 1 automatically iterates the stress analysis when a significant amount of plastic deformation occurs.

LOCAL INSTABILITY ANALYSIS PROCEDURE OF COMPUTER PROGRAM NO. 1

0 x 90° Flanged Waffle

The buckling stress of the 0 x 90° biaxially-compressed waffle skin element, which is assumed to be simply supported, is expressed as follows (ref. 10-4):

$$f_{\ell,s,cr,i} = 0.82 \frac{E_{s,i}}{1 - \nu_{s,i}^2} \frac{t_s^2}{(a_s b_s)_i} \frac{\left(m^2 \frac{b_s}{a_s} + \frac{a_s}{b_s}\right)_i^2}{\left(m^2 \frac{b_s}{a_s} + \beta \frac{a_s}{b_s}\right)_i} \tag{10-10}$$

where

$$a_{s,i} = p_y - t_{w,y},\ b_{s,i} = p_x - t_{w,x},\ \beta_i = f_{y,s,i}/f_{x,s,i},\ \ell = x$$

if

$$f_{x,s,i} \geq f_{y,s,i}$$

and

$$a_{s,i} = p_x - t_{w,x},\ b_{s,i} = p_y - t_{w,y},\ \beta_i = f_{x,s,i}/f_{y,s,i},\ \ell = y$$

if

$$f_{y,s,i} > f_{x,s,i}$$

The effective modulus is approximated with the expression

$$E = \left[C_1 \eta_{ST} + (1 - C_1)\, \eta_r\right] E_{el} \tag{10-11}$$

in which (ref. 10-5)

$$\eta_{ST} = \frac{E_{ST}}{E_{el}} = 0.5\, \eta_{sec} \left[1 + 0.5 \left(1 + 3 \frac{\eta_{tan}}{\eta_{sec}}\right)^{1/2}\right] \tag{10-12a}$$

$$\eta_r = \frac{E_r}{E_{el}} = 0.25\, \eta_{sec} \left(1 + 3 \frac{\eta_{tan}}{\eta_{sec}}\right) \tag{10-12b}$$

and C_1 $(0 \leq C_1 \leq 1)$ is an empirical coefficient, dependent on the loading and aspect ratio of the plate. Some guidance for evaluating the empirical coefficient is given in reference 10-1. The effective Poisson's ratio is defined by equation (10-5). The buckling stress of the skin is the minimum of $f_{\ell,s,cr}$ with respect to positive integers of m. Negative or zero values of the denominator of the buckling equation are not applicable. Note that $f_{\ell,s,cr}$ is the correct buckling stress only when

$$\max\left(f_{x,s,i},\ f_{y,s,i}\right) \equiv f_{\ell,s,cr}$$

The shear buckling stress of the skin is (ref. 10-4)

$$f_{xy,s,cr,i} = 0.82\ \frac{E_{s,i}}{1-\nu_{s,i}^2}\left[5.34 + 4\left(\frac{b_s}{a_s}\right)^2\right]\left(\frac{t_s}{b_s}\right)^2 \qquad (10\text{-}13a)$$

in which the dimensions of skin are now denoted as follows:

$$\begin{aligned} a_s &= \max\left(p_x - t_{w,x},\ p_y - t_{w,y}\right) \\ b_s &= \min\left(p_x - t_{w,x},\ p_y - t_{w,y}\right) \end{aligned} \qquad (10\text{-}13b)$$

E and ν are defined by equations (10-11) and (10-5), respectively.

Using the interaction equation

$$r_{c,s} + r_{xy,s}^2 = 1$$

where

$$r_{c,s} = f_{\ell,s}/f_{\ell,s,cr}$$

$$r_{xy,s} = f_{xy,s}/f_{xy,s,cr}$$

the utilization factor for combined shear and biaxial "compressive" loading of the skin is expressed as

$$U_{s,i} = \frac{r_{c,s,i} + \left(r_{c,s,i}^2 + 4r_{xy,s,i}^2\right)^{1/2}}{2} \qquad (10\text{-}14)$$

Treating the stiffener web as a plate which is elastically supported along the flange side and simply supported along the other three sides, stable equilibrium of the stiffener web and that of the stiffener as a whole can be expressed by a single transcendental equation (ref. 10-6). An alternate to using the transcendental equation is to design the stiffener so that (1) the stiffener web can be treated as a simply supported plate, and (2) general instability of the stiffener does not occur. The latter procedure, which is somewhat simpler, is considered to be adequate for the present minimum weight analysis. The two conditions are satisfied if (ref. 10-6):

$$\bar{I}_{f,z,\ell} \geq \max\left(\bar{I}_{\ell,1}, \bar{I}_{\ell,2}\right) \quad (\ell = x,y) \qquad (10\text{-}15a)$$

in which

$$\bar{I}_{f,z,\ell} = \frac{1}{12}\frac{t_f}{\bar{z}_f}\left(\frac{b_{f,\ell}}{t_{w,\ell}}\right)^3 \quad (\ell = x,y) \qquad (10\text{-}15b)$$

$$\bar{I}_{\ell,1} = 1.85 + 2.73\frac{A_{f,\ell}p_\ell}{\bar{z}_f t_{w,\ell}} \quad (\ell = x,y) \qquad (10\text{-}15c)$$

$$\bar{I}_{\ell,2} = 1.18\left(\frac{p_m - t_{w,m}}{\bar{z}_f} - 0.41\right)^2 + 0.47 + 0.43\frac{A_{f,\ell}p_\ell}{\bar{z}_f t_{w,\ell}}\left(\frac{p_m - t_{w,m}}{\bar{z}_f}\right)^2$$

$$(\ell,m = x,y;\ y,x)$$

where

$$A_{f,\ell} = b_{f,\ell}\, t_f / p_\ell \quad (\ell = x,y)$$

$$\bar{z}_f = 0.5\,(t_s + t_f) + h_w \qquad (10\text{-}16)$$

Note that the subscripting of the expression of $\bar{I}_{\ell,2}$ denotes one equation in which $\ell = x$ and $m = y$ and another equation in which $\ell = y$ and $m = x$. The buckling stresses of the stiffener webs are then expressed as

$$f_{w,\ell,cr,i} = 0.82k_{w,\ell} \frac{E_{ST,w,\ell,i}}{1 - \nu^2_{w,\ell,i}} \left(\frac{t_{w,\ell}}{h_w}\right)^2 \quad (\ell = x,y) \qquad (10\text{-}17)$$

where

$$k_{w,\ell} = \begin{cases} 4; \ \left(p_m - t_{w,m}\right)/h_w \geq 1 \\ \left[h_w/\left(p_m - t_{w,m}\right) + \left(p_m - t_{w,m}\right)/h_w\right]^2; \ \left(p_m - t_{w,m}\right)/h_w < 1 \end{cases}$$

$$(\ell,m = x,y; \ y,x)$$

Considering one half of the flange element as a plate with three simply supported edges and one free edge, the local buckling stresses of the flanges are expressed as follows:

$$f_{f,\ell,cr,i} = 0.82 \frac{E_{ST,w,\ell,i}}{1 - \nu^2_{w,\ell,i}} \left[0.61\left(1 - \nu_{w,\ell,i}\right) + \left(\frac{1}{2}\frac{b_{f,\ell} - t_{w,\ell}}{p_m - t_{w,m}}\right)^2\right]\left(\frac{2t_f}{b_{f,\ell} - t_{w,\ell}}\right)^2 \qquad (10\text{-}18)$$

$$(\ell,m = x,y; \ y,x)$$

This equation corresponds to that of reference 10-4, the formulation of which is based on $\nu = 0.25$.

In addition to the flexural modes of failure already considered, a torsional mode of instability of the flanged stiffener is possible. Assuming simply supported boundary conditions at the ends and unrestrained rotation about the toe of the stiffener web, the buckling stress is expressed as (ref. 10-6)

$$f_{st,\ell,cr,i} = 9.87 \frac{E_{tan,w,\ell,i}}{(L/r)_\ell^2} \quad (\ell = x,y) \tag{10-19a}$$

where

$$(L/r)_\ell = \left(p_m - t_{w,m}\right) \left[\frac{I_{pc,\ell}}{I_{st,z,\ell}\bar{z}_f^2 + \Gamma_\ell + 0.0390 J_{st,\ell} \left(p_m - t_{w,m}\right)^2} \right]^{1/2}$$

$$(\ell,m = x,y;\ y,x) \tag{10-19b}$$

in which the stiffener properties are defined as follows:

$$\Gamma_\ell = \frac{1}{144 p_\ell} \left(t_f^3 b_{f,\ell}^3 + 4 t_{w,\ell}^3 \bar{z}_f^3 \right)$$

$$I_{pc,\ell} = I_{st,\ell} + I_{st,z,\ell} + A_{st,\ell}\bar{z}_{st,\ell}^2$$

$$I_{st,\ell} = I_{f,\ell} + A_{f,\ell}\bar{z}_f^2 + I_{w,\ell} + A_{w,\ell}\bar{z}_{w,\ell}^2 - A_{st,\ell}\bar{z}_{st,\ell}^2 \tag{10-19c}$$

$$I_{st,z,\ell} = \frac{1}{12} \left(A_{f,\ell} b_{f,\ell}^2 + A_{w,\ell} t_{w,\ell}^2 \right)$$

$$\bar{z}_{st,\ell} = \left(A_{f,\ell}\bar{z}_f + A_{w,\ell}\bar{z}_{w,\ell} \right) / A_{st,\ell}$$

$$A_{st,\ell} = A_{f,\ell} + A_{w,\ell}$$

The properties $A_{f,\ell}$ and $\bar{z}_f$ are defined by equation 10-16, and

$$A_{w,\ell} = h_w \, t_{w,\ell} / p_\ell \quad (\ell = x,y)$$

$$I_{w,\ell} = A_{w,\ell} \, h_w^2 / 12 \quad (\ell = x,y) \tag{10-20}$$

$$\bar{z}_{w,\ell} \equiv \bar{z}_w = 0.5 \left(t_s + h_w \right)$$

$$J_{st,\ell} = \frac{A_{w,\ell} \, t_{w,\ell}^2 + A_{f,\ell} \, t_f^2}{6 \left(1 + \nu_{w,\ell} \right)} \quad (\ell = x,y)$$

0 x 90° Unflanged Waffle

The equations for the buckling analysis of the skin element of the unflanged 0 x 90° waffle are the same as those for the flanged waffle, equations (10-10), (10-13) and (10-14). Considering the stiffener as a plate with three simply supported edges and one free edge, the buckling stress of the stiffeners is expressed with an equation corresponding to equation (10-18) as follows:

$$f_{w,\ell,cr,i} = 0.82 \frac{E_{ST,w,\ell,i}}{1 - \nu_{w,\ell,i}^2} \left[0.61 \left(1 - \nu_{w,\ell,i} \right) + \left(\frac{h_{w,\ell}}{p_m - t_{w,m}} \right)^2 \right] \left(\frac{t_{w,\ell}}{h_{w,\ell}} \right)^2 \quad (\ell,m = x,y;\ y,x) \tag{10-21}$$

Note that the above equation is written with the provision for $h_{w,x} \neq h_{w,y}$ which is permissible for some designs in which the stiffener stresses in one direction are small or tensile. The height of the stiffeners in this direction can be larger than that of the stiffeners in the other direction.

45° x 45° Waffle

A specialized form of equations (10-10) through (10-21) is used for the local instability analysis of the flanged and unflanged 45° x 45° waffles.

Honeycomb-Core Sandwich

Procedures for the analysis of local instability of honeycomb-core sandwich plates subjected to uniaxial compressive loading are presented in reference 10-7. Some of these analytical methods are adapted herein for the local instability analysis of the honeycomb-core sandwich subjected to combined loading.

The basis of the intercell buckling (dimpling) expression of reference 10-7 is the classical buckling equation of a square plate. Using the notation of figure 10-4, the intercell buckling stress of the faces due to biaxial inplane loading is expressed as

$$f_{IB,i} = 0.82C_1 \frac{E_{s,i}}{1 - \nu_{s,i}^2} \left[\frac{\min\left(t_1, t_2\right)}{s}\right]^2 \frac{\left(m_i^2 + 1\right)^2}{m_i^2 + \beta_i} \qquad (10\text{-}22)$$

where

$$\beta_i = f_{II,i}/f_{I,i}$$

in which

$$f_I = \frac{f_{x,s} + f_{y,s}}{2} + \left[\left(\frac{f_{x,s} - f_{y,s}}{2}\right)^2 + f_{xy,s}^2\right]^{1/2}$$

$$f_{II} = \frac{f_{x,s} + f_{y,s}}{2} - \left[\left(\frac{f_{x,s} - f_{y,s}}{2}\right)^2 + f_{xy,s}^2\right]^{1/2}$$

The critical stress is the maximum value of f_{IB} with respect to positive integers of m. Negative or zero values of $m^2 + \beta$ are not applicable. Unequal face thicknesses are considered to provide for different minimum thickness requirements of the faces. Comparing equation (10-22) to that of reference 10-7 for uniaxial loading, it is noted that $C_1 \approx 0.61$.

The wrinkling stress of the faces due to uniaxial compressive loading is expressed as (ref. 10-7)

$$f_{WR,i} = \frac{0.82C_2 \left[\frac{\bar{E}_{c,i} \min(t_1, t_2)}{E_{r,s,i} h_c} \right]^{1/2} E_{r,s,i}}{1 + 0.64K_i} \qquad (10\text{-}23a)$$

where C_2 is a correction factor, $E_{r,s}$ is the effective skin modulus expressed by equation (10-12b), and

$$K_i = \frac{\delta_o \bar{E}_{c,i}}{h_c \bar{F}_{c,i}} \qquad (10\text{-}23b)$$

δ_o of equation (10-23b) denotes the amplitude of initial imperfection of the thinnest face.

The core modulus $\bar{E}_c$ and allowable strength $\bar{F}_c$, which appear in equations (10-23), are properties which are measured perpendicularly to the sandwich plate. These properties are usually evaluated experimentally. However, when new materials are initially considered, test data, especially for high temperature applications, is not available. Therefore, it is necessary to approximate the properties analytically. Assuming the compressive strength to be critical, the crushing load carried by the core is considered in two parts, prebuckling load and postbuckling load. The buckling stress of the foil (side of a cell) is conservatively expressed by simply supported plate theory as

$$f'_{c,i} = 0.82k \frac{E_{ST,c,i}}{1 - \nu_{c,i}^2} \left(\frac{t_c}{s} \right)^2 \qquad (10\text{-}24a)$$

where

$$k = \begin{cases} \left(\frac{s}{h_c} + \frac{h_c}{s} \right)^2 & ; \frac{h_c}{s} < 1 \\ 4 & ; \frac{h_c}{s} \geq 1 \end{cases}$$

in which $h_c = h - t_1 - t_2$. $E_{ST,c}$ and ν_c are effective properties of the core material given by equations (10-12a) and (10-5).

After the foil buckles, additional loading is carried by the material at the core nodes. The average stress produced by the post-buckling loading of the effective material is

$$f''_{c,i} = f_{c,max,i} - f'_{c,i} \tag{10-24b}$$

in which $f_{c,max}$ is the stress corresponding to $\eta_{tan,c} = 0.1$. The compressive strength of the core is then expressed as

$$\bar{F}_{c,i} = \frac{2t_c}{s}\left(f'_c + \frac{2b_{ef}}{s} f''_c\right) \tag{10-25}$$

where

$$b_{ef} = \min\left(C_3 t_c + 0.5d,\ C_4 s\right)$$

in which C_3 and C_4 are empirical coefficients.

The secant modulus of the core corresponding to the compressive strength $\bar{F}_c$ is approximated as

$$\bar{E}_{c,i} = 2t_c \frac{sf'_{c,i} + 2b_{ef} f''_{c,i}}{f_{c,max,i}} \frac{E^*_{sec,c,i}}{s^2} \tag{10-26}$$

where $E^*_{sec,c}$ is the secant modulus of the core material which corresponds to the stress $f_{c,max}$.

The following values of the C coefficients, d and δ_o were used in the design of the honeycomb-core sandwich plates: $C_1 = 0.61$, $C_2 = 1$, $C_3 = 15$, $C_4 = 0.25$, $d = 0.025$ and $\delta_o = 0$. In reference 10-1, a comparison of analytical data, which were obtained with the above values, with test data of reference 10-8 indicates that the reported analyses of dimpling and wrinkling stresses are adequate for the present investigation.

Truss-Core Sandwich

Treating the face and core elements as long, simply supported plates, the truss-core sandwich is analyzed for local instability with the theory of reference 10-9, an analysis of long, simply supported, orthotropic plates. The face buckling stresses, when the loading components act individually, are

$$f_{x,s,cr,i} = 0.82 \frac{E_{s,i}}{1 - \nu_{s,i}^2} \left[\frac{\min \left(t_1, t_2 \right)}{b_s} \right]^2$$

$$f_{y,s,cr,i} = 3.29 \frac{E_{s,i}}{1 - \nu_{s,i}^2} \left[\frac{\min \left(t_1, t_2 \right)}{b_s} \right]^2 \qquad (10\text{-}27)$$

$$f_{xy,cr,i} = 4.40 \frac{E_{s,i}}{1 - \nu_{s,i}^2} \left[\frac{\min \left(t_1, t_2 \right)}{b_s} \right]^2$$

Defining stress ratios as

$$r_{x,c,i} = f_{x,s,i} / f_{x,s,cr,i}$$

$$r_{y,s,i} = f_{y,s,i} / f_{y,s,cr,i} \qquad (10\text{-}28)$$

$$r_{xy,s,i} = f_{xy,s,i} / f_{xy,s,cr,i}$$

and specializing the interaction equation of reference 10-9 to an isotropic plate as

$$\phi \left(\bar{r}_1, \bar{r}_2, \bar{r}_3, \bar{r}_4 \right) = \left(\frac{1 + \bar{r}_4}{2} - \bar{r}_1 \right) \left(\frac{6 - \bar{r}_2 + 2\bar{r}_4}{8} \right) - \bar{r}_3^2 \qquad (10\text{-}29)$$

the utilization factor U_s of the thinnest face for combined loading then is determined with the procedure of figure 10-6. Note that stable equilibrium of the face exists if $\phi \geq 0$.

The core is subjected to a compressive loading in the y-direction and a shear loading. Expressions of the corresponding buckling stresses are

$$f_{y,c,cr,i} = 3.29 \frac{E_{ST,c,i}}{1 - \nu_{c,i}^2}\left(\frac{t_c}{b_c}\right)^2$$

$$f_{sy,c,cr,i} = 4.40 \frac{E_{ST,c,i}}{1 - \nu_{c,i}^2}\left(\frac{t_c}{b_c}\right)^2 \qquad (10\text{-}30)$$

where $E_{ST,c}$ and ν_c are effective material properties of the core element which are expressed by equations (10-12a) and (10-5), respectively. The interaction equation for combined loading is

$$r_{c,c} + r_{sy,c}^2 = 1 \qquad (10\text{-}31)$$

in which

$$r_{c,c} = f_{y,c}/f_{y,c,cr}$$

$$r_{sy,c} = f_{sy,c}/f_{sy,c,cr} \qquad (10\text{-}32)$$

It is to be noted that equation (10-31), for the combined loading of the core, is equivalent to equation (10-29). The expression for the factor of utilization or strength ratio for the interaction equation (10-31) is

$$U_{c,i} = \frac{r_{c,c,i} + \left(r_{c,c,i}^2 + 4r_{sy,c,i}^2\right)^{1/2}}{2} \qquad (10\text{-}33)$$

The true margin of safety, then, can be computed from the following equation

$$M.S. = \frac{1}{u} - 1$$

GENERAL INSTABILITY PROCEDURE OF COMPUTER PROGRAM NO. 1

Assuming simply supported boundary conditions, the compression buckling theory of reference 10-10 and the shear buckling theory of reference 10-11, together with an appropriate interaction equation, are used to analyze the waffle, honeycomb-core sandwich and truss-core sandwich plates for general instability.

The compressive buckling load for a biaxially-compressed, simply supported orthotropic plate (ref. 10-10) is

$$N_{I,cr,i} = k_{c,i}\pi^2 D_{I,i}/x_{II,i}^2 \tag{10-34a}$$

where

$$k_{c,i} = \frac{\left(2\frac{x_{I,i}^2}{x_{II,i}^2}\frac{D_{3,i}}{D_{I,i}} + m_i^2\right)m_i^2 + \beta_{c,i}^4}{m_i^2 + \frac{x_{I,i}^2}{x_{II,i}^2}\frac{N_{II,i}}{N_{I,i}}}\frac{x_{II,i}^2}{x_{I,i}^2} \tag{10-34b}$$

in which

$$\beta_{c,i} = \frac{x_{I,i}}{x_{II,i}}\left(\frac{D_{II,i}}{D_{I,i}}\right)^{1/4} \tag{10-34c}$$

The dimensional, loading, and stiffness quantities of equation (10-34) are defined as follows:

$$x_{I,i} = a,\ x_{II,i} = b;\ N_{I,i} = \bar{N}_{x,i},\ N_{II,i} = \bar{N}_{y,i};\ D_{I,i} = D_{1,i},\ D_{II,i} = D_{2,i}$$

if

$$2\pi^2\left(\frac{D_{2,i}}{b^2}+\frac{D_{3,i}}{a^2}\right)-\bar{N}_{y,i}>0 \text{ and } \bar{N}_x>\bar{N}_y$$

Otherwise,

$$x_{I,i}=b,\ x_{II,i}=a;\ N_{I,i}=\bar{N}_{y,i},\ N_{II,i}=\bar{N}_{x,i};\ D_{I,i}=D_{2,i},\ D_{II,i}=D_{1,i}$$

The plate stiffnesses D_1,D_2,and D_3 are evaluated with equations of reference 10-1. E_{tan} is used for the modulus of the stiffeners of the waffle and the core elements of the truss-core sandwich. The moduli of the faces of the honeycomb-core and truss-core sandwiches are approximated with equation (10-11). The expression

$$E=\left[C_2\,\eta_{ST}+\left(1-C_2\right)\eta_{tan}\right]E_{el}$$

is used to evaluate the moduli of the skins of the 0 x 90° and 45° x 45° waffles. The coefficient $C_2\left(0\le C_2\le 1\right)$ is an empirical coefficient dependent on loading and aspect ratio of the plate. Some guidance for evaluating the coefficient is given in reference 10-1.

The buckling load of the plate is the minimum value of $N_{I,cr}$ with respect to positive integers of m. Negative or zero values of the denominator of equation (10-34b) are not applicable. Not that $N_{I,cr}$ is the correct buckling load only when $N_I \equiv N_{I,cr}$.

The shear buckling stress of the plate is (ref. 10-11)

$$N_{xy,cr,i}=k_{s,i}\pi^2\left(D_{I,i}D_{II,i}^3\right)^{1/4}\Big/x_{II,i}^2 \qquad (10\text{-}36)$$

where

$$x_{I,i} = a,\ x_{II,i} = b;\ D_{I,i} = D_{1,i},\ D_{II,i} = D_{2,i}$$

if

$$\frac{b}{a}\left(\frac{D_{1,i}}{D_{2,i}}\right)^{1/4} \leq \frac{a}{b}\left(\frac{D_{2,i}}{D_{1,i}}\right)^{1/4}$$

Otherwise,

$$x_{I,i} = b,\ x_{II,i} = a;\ D_{I,i} = D_{2,i},\ D_{II,i} = D_{1,i}$$

Values of the shear buckling coefficient which correspond to those given by the theory of reference 10-11 are presented in reference 10-12. Curves of the coefficient are given in figure 10-8 of this section. The stiffness parameter, κ, of the figure is defined as

$$\kappa_i = D_{3,i} \Big/ \left(D_{1,i} D_{2,i}\right)^{1/2} \qquad (10\text{-}37a)$$

and the effective aspect ratio as

$$\beta_{s,i} = \frac{x_{II,i}}{x_{I,i}}\left(\frac{D_{I,i}}{D_{II,i}}\right)^{1/4} \qquad (10\text{-}37b)$$

The procedure for evaluating the stiffnesses D_1, D_2, and D_3 is the same as that for compressive loading.

Using the interaction equation

$$R_{c,i} + R_{xy,i}^2 = 1$$

in which

$$R_{c,i} = N_{I,i}/N_{I,cr,i}$$

$$R_{xy,i} = N_{xy,i}/N_{xy,cr,i}$$

the utilization factor for combined shear and biaxial compressive loading of the plate is

$$U_{GI,i} = \frac{R_{c,i} + \left(R_{c,i}^2 + 4R_{xy,i}^2\right)^{1/2}}{2} \qquad (10\text{-}38)$$

In evaluating the loading ratios of equation (10-38), one set of stiffnesses in which the effective moduli are based on the stress state due to the combined compressive and shear loads is used.

Using a general instability theory, which neglects shear deformation, significantly limits the extent to which Computer Program No. 1 can be applied to honeycomb-core plate problems. However, in the present investigation, the simplified analysis did not have a significant effect on the plate weight because the compressive loading along the long edges of the panel was considerable with respect to that along the short edges.

OPTIMIZATION PROCEDURE

Equations which were used for the stress and stability analysis of the waffle, honeycomb-core sandwich and truss-core sandwich plates have been presented. For each of the structural concepts, these equations, together with constraint functions which remain to be given, define a "region" of permissible design within an nth order "design space" in terms of the design variables. The coordinates which make the merit (weight) function assume a minimum value and which fall within the permissible design region are the dimensions of the optimum configuration for a given single or multiple loading condition. As already stated, the modification of the structure in searching for the optimum design is directed by a constrained minimization procedure, which is based on the "maximum gradient" method.

The variables which are used in Computer Program No. 1 are the dimensions of the plates as follows:

0 x 90° Flanged Waffle

$$b_{f,x},\ b_{f,y},\ h\left(\equiv h_w + t_s + t_f\right),\ p_x,\ p_y,\ t_f,\ t_s,\ t_{w,x} \text{ and } t_{w,y}$$

0 x 90° Unflanged Waffle

$$h_x\left(\equiv h_{w,x} + t_s\right),\ h_y\left(\equiv h_{w,y} + t_s\right),\ p_x,\ p_y,\ t_s,\ t_{w,x} \text{ and } t_{w,y}$$

-45° x 45° Flanged Waffle

$$b_f,\ h\left(\equiv h_w + t_s + t_f\right),\ p,\ t_f,\ t_s \text{ and } t_w$$

-45° x 45° Unflanged Waffle

$$h\left(\equiv h_w + t_s\right),\ p,\ t_s \text{ and } t_w$$

Honeycomb-Core Sandwich

$$h,\ s,\ t_c,\ t_1 \text{ and } t_2$$

Truss-Core Sandwich

$$h,\ t_c,\ t_1,\ t_2 \text{ and } \theta$$

The constraints of the design space which have been incorporated into Computer Program No. 1 can be grouped into two types: (1) behavioral constraints and (2) side constraints. The first type limits the design to those configurations which satisfy the failure criteria of the structure. The second type constrains the design, for example, within real space limitations and manufacturing capabilities. As an example of the system of constraints of Computer Program No. 1, constraint functions of the unflanged $45^\circ \times 45^\circ$ waffle program are:

$$G_{1,i} = 1 - U_{GI,i} \geq 0$$

$$G_{2,i} = 1 - U_{s,i} \geq 0$$

$$G_{3,i} = 1 - f_{w,\ell,i}/f_{w,\ell,cr,i} \geq 0 \qquad (\ell = \xi \text{ or } \eta)$$

$$G_{4,i} = \eta_{tan,s,i} - \eta_{tan,min,i} \geq 0$$

$$G_{5,i} = \eta_{tan,w,\ell,i} - \eta_{tan,min,i} \geq 0 \qquad (\ell = \xi \text{ or } \eta)$$

$$G_6 = t_s - t_{s,min} \geq 0$$

$$G_7 = t_w - t_{w,min} \geq 0$$

$$G_8 = \left(h_w/t_w\right)_{max} - h_w/t_w \geq 0$$

It is to be noted that in the design of the $45^\circ \times 45^\circ$ waffle, only the stiffener with the maximum compressive stress is analyzed for buckling.

ANALYTICAL PROCEDURES OF COMPUTER PROGRAM NO. 2

As already indicated, only the unflanged $45^\circ \times 45^\circ$ and $0 \times 90^\circ$ waffle plates and the honeycomb-core sandwich plate are considered in Computer Program No. 2. The program system was developed from the programs of Computer Program No. 1. Hence, many of the procedures for designing the unflanged waffle and honeycomb-core sandwich plates are common in the two program systems, the basic

differences being in the analysis of the overall strength and the local failure of the waffle plates. The analytical procedures which are peculiar to Computer Program No. 2 are presented on the following pages.

Stress and Deflection Analyses of Waffle Plates

The total in-plane stress resultants acting on the 45° x 45° waffle panel are

$$N_{x,i} = N'_{x,i} + \left(AE_{sec,i}\bar{\varepsilon}_{T,i}\right)_{cap,x}/L_{c,y} + \left(C_{11}\bar{\varepsilon}_{x,T,plate} + C_{12}\bar{\varepsilon}_{y,T,plate}\right)_i \frac{L_{p,y}}{L_{c,y}}$$

$$N_{y,i} = N'_{y,i} + \left(AE_{sec,i}\bar{\varepsilon}_{T,i}\right)_{cap,y}/L_{c,x} + \left(C_{12}\bar{\varepsilon}_{x,T,plate} + C_{22}\bar{\varepsilon}_{y,T,plate}\right)_i \frac{L_{p,x}}{L_{c,x}} \qquad (10\text{-}39)$$

$$N_{xy} = N'_{xy,i} + C_{33,i}\bar{\gamma}_{xy,T,i}$$

where N'_x, N'_y and N'_{xy} are stress resultants in which the thermal loading is excluded and the subscript T denotes thermal strain. In the 0 x 90° waffle program, C_{12} in equations(10-39) is equated to zero, $C_{11} = F_{11}^{-1}$ and $C_{22} = F_{22}^{-1}$. The procedure for evaluating the thermal portion of the loading is consistent with the analyses of the internal loads of the aircraft. Using the loads given by Equations(10-39),the total stress resultants of the plate, $\bar{N}_x$ and $\bar{N}_y$, are determined with the use of equations (10-3).

Moments due to coupling between in-plane and out-of-plane deformations of the -45° x 45° and 0 x 90° waffles are

$$\{M\}_{c,i} = \begin{Bmatrix} M_x \\ M_y \end{Bmatrix}_{c,i} = \begin{bmatrix} 0 & e_{12} \\ e_{21} & 0 \end{bmatrix}_i \begin{Bmatrix} \bar{N}_x \\ \bar{N}_y \end{Bmatrix}_i \qquad (10\text{-}40a)$$

where e_{12} and e_{21} are eccentricities which are properties of the plates as defined in reference 10-1. The coupling moments occur as force couples (skin forces opposing stiffener forces) in the waffle plates. Edge moments of $-\{M\}_c$ are superimposed on the plates to remove the couples from the edges of the plates, which are assumed to have simply supported boundary conditions. The moment sign convention is shown in figure 10-9.

Moments due to eccentric loading at the edges of the plate are

$$\begin{Bmatrix} M_x \\ M_y \end{Bmatrix}_{e,i} = \begin{Bmatrix} \bar{N}_x\, e_x \\ \bar{N}_y\, e_y \end{Bmatrix}_i \qquad (10\text{-}40b)$$

were e_x and e_y are prescribed eccentricities.

Moments due to variation of temperature through the thickness of the plate are determined with the use of superposition of loading. The temperature gradient is assumed to be linear, which is considered to be an adequate approximation for the present investigation. Considering the plate first with free boundary conditions, curvatures due to the temperature gradient, which is assumed to be constant along the width and length of the plate, then are $\chi_{x,T} = \chi_{y,T} = \chi_T$. The curvatures, which have sign convention as shown in figure 10-9. are removed with the application of moments along the free edges of the plate. The moments are

$$\{M\}_{T,i} = \begin{Bmatrix} M_x \\ M_y \end{Bmatrix}_{T,i} = -\begin{bmatrix} D_{11} & D_{12} \\ D_{12} & D_{22} \end{bmatrix}_i \begin{Bmatrix} \chi_T \\ \chi_T \end{Bmatrix}_i \qquad (10\text{-}40c)$$

where $D_{11} \equiv D_1$, $D_{22} \equiv D_2$ and $D_{12} \equiv \bar{\nu}_{xb} D_2 \equiv \bar{\nu}_{yb} D_1$ are the bending stiffness coefficients of the waffle plates. The desired plate loading is finally obtained by imposing simply supported boundary conditions onto the plate and then superimposing the moments $-\{M\}_T$ along the edges.

As already staged, Computer Program No. 2 was implemented for problems in which the plate bows so that the moments at the center of the panel are adequate approximations of the maximum moments. Assuming that N_{xy} constitutes a negligible portion of the panel loading with respect to general failure, the deflection and bending moments at the center of the plate due to the coupling moments, the eccentric loading at the edges, the temperature gradient through the thickness and the "compressive" edge loads are expressed as follows (ref. 10-13 and 10-14):

$$w'_i = \frac{16}{\pi^2} \sum_{m=1}^{M_M} \sum_{n=1}^{N_M} \frac{1}{\lambda_{mn,i}} \left[M_{X,i} \left(\frac{m\pi}{a}\right)^2 + M_{Y,i} \left(\frac{n\pi}{b}\right)^2 \right] (-1)^{\frac{m+n}{2} - 1} \qquad (10\text{-}41a)$$

$$M'_{x,i} = \frac{16D_{1,i}}{\pi^2} \sum_{m=1}^{M_M} \sum_{n=1}^{N_M} \frac{1}{\lambda_{mn,i}} \left[M_{X,i} \left(\frac{m\pi}{a}\right)^2 + M_{Y,i} \left(\frac{n\pi}{b}\right)^2 \right]$$

$$\left[\left(\frac{m\pi}{a}\right)^2 + \bar{\nu}_{yb} \left(\frac{n\pi}{b}\right)^2 \right] (-1)^{\frac{m+n}{2}-1} + M_{x,T,i}$$

$$M'_{y,i} = \frac{16D_{2,i}}{\pi^2} \sum_{m=1}^{M_M} \sum_{n=1}^{N_M} \frac{1}{\lambda_{mn,i}} \left[M_{X,i} \left(\frac{m\pi}{a}\right)^2 + M_{Y,i} \left(\frac{n\pi}{b}\right)^2 \right] \qquad (10\text{-}41b)$$

$$\left[\bar{\nu}_{xb} \left(\frac{m\pi}{a}\right)^2 + \left(\frac{n\pi}{b}\right)^2 \right] (-1)^{\frac{m+n}{2}-1} + M_{y,T,i}$$

$$(m = 1, 3, \ldots, M_M;\ n = 1, 3, \ldots, N_M;\ M_M = N_M)$$

where

$$\lambda_{mn,i} = mn \left[D_{1,i} \left(\frac{m\pi}{a}\right)^4 + 2 D_{3,i} \left(\frac{m\pi}{a}\right)^2 \left(\frac{n\pi}{b}\right)^2 \right. \qquad (10\text{-}42)$$

$$\left. + D_{2,i} \left(\frac{n\pi}{b}\right)^4 - \bar{N}_{x,i} \left(\frac{m\pi}{a}\right)^2 - \bar{N}_{y,i} \left(\frac{n\pi}{b}\right)^2 \right]$$

and

$$\begin{Bmatrix} M_X \\ M_Y \end{Bmatrix}_i = - \begin{Bmatrix} M_x \\ M_y \end{Bmatrix}_{c,i} + \begin{Bmatrix} M_x \\ M_y \end{Bmatrix}_{e,i} - \begin{Bmatrix} M_x \\ M_y \end{Bmatrix}_{T,i} \qquad (10\text{-}43)$$

Deflection and moments at center of plate due to inplane edge loads and uniform pressure are

$$w''_i = \frac{16q_i}{\pi^2} \sum_{m=1}^{M_q} \sum_{n=1}^{N_q} \frac{1}{\lambda_{mn,i}} (-1)^{\frac{m+n}{2}-1} \qquad (10\text{-}44a)$$

$$M''_{x,i} = \frac{16q_i D_{1,i}}{\pi^2} \sum_{m=1}^{M_q} \sum_{n=1}^{N_q} \frac{1}{\lambda_{mn,i}} \left[\left(\frac{m\pi}{a}\right)^2 + \bar{\nu}_{yb} \left(\frac{n\pi}{b}\right)^2 \right] (-1)^{\frac{m+n}{2}-1}$$

$$M''_{y,i} = \frac{16q_i D_{2,i}}{\pi^2} \sum_{m=1}^{M_q} \sum_{n=1}^{N_q} \frac{1}{\lambda_{mn,i}} \left[\bar{\nu}_{xb} \left(\frac{m\pi}{a}\right)^2 + \left(\frac{n\pi}{b}\right)^2 \right] (-1)^{\frac{m+n}{2}-1} \quad (10\text{-}44b)$$

$$(m = 1, 3, \ldots, M_q;\ n = 1, 3, \ldots, N_q;\ M_q = N_q)$$

Deflection and moments at the center of plate due to inplane edge loads and an initial sinusoidal deflection are

$$w'''_i = a_{11,i} \left\{ 1 + \frac{1}{\lambda_{11,i}} \left[\bar{N}_{x,i} \left(\frac{\pi}{a}\right)^2 + \bar{N}_{y,i} \left(\frac{\pi}{b}\right)^2 \right] \right\}$$

$$M'''_{x,i} = a_{11,i} \frac{D_{1,i}}{\lambda_{11,i}} \left[\bar{N}_{x,i} \left(\frac{\pi}{a}\right)^2 + \bar{N}_{y,i} \left(\frac{\pi}{b}\right)^2 \right] \left[\left(\frac{\pi}{a}\right)^2 + \bar{\nu}_{yb,i} \left(\frac{\pi}{b}\right)^2 \right] \quad (10\text{-}45)$$

$$M'''_{y,i} = a_{11,i} \frac{D_{2,i}}{\lambda_{11,i}} \left[\bar{N}_{x,i} \left(\frac{\pi}{a}\right)^2 + \bar{N}_{y,i} \left(\frac{\pi}{b}\right)^2 \right] \left[\bar{\nu}_{xb,i} \left(\frac{\pi}{a}\right)^2 + \left(\frac{\pi}{b}\right)^2 \right]$$

in which a_{11} is the initial deflection and λ_{11} is expressed by equation (10-42) with m=n=1.

Using the secant modulus, the plate stiffnesses, which appear in the deflection and moment equations, are evaluated with equations of reference 10-1. Poisson's ratios ν_s and ν_w of the skin and stiffeners in the stiffness equations are approximated with equation (10-5). It is conservatively assumed that the elastic-plastic state at the center of the waffle exist over the entire area of the waffle plate.

The total deflection and the total moments at the center of the plate are

$$w_i = w'_i + w''_i + w'''_i \quad (10\text{-}46a)$$

$$M_{x,i} = M'_{x,i} + M''_{x,i} + M'''_{x,i}$$

$$M_{y,i} = M'_{y,i} + M''_{y,i} + M'''_{y,i}$$

$$M_{xy,i} = 0 \qquad (10\text{-}46b)$$

The effective curvatures and twist corresponding to the above moments are

$$\begin{Bmatrix} \chi_x \\ \chi_y \\ \chi_{xy} \end{Bmatrix}_i = \begin{bmatrix} D_{11} & D_{12} & 0 \\ D_{12} & D_{22} & 0 \\ 0 & 0 & 2D_{33} \end{bmatrix}_i^{-1} \begin{Bmatrix} Mx \\ M_y \\ M_{xy} \end{Bmatrix}_i \qquad (10\text{-}47a)$$

Strains of the reference surface are

$$\begin{Bmatrix} \bar{\varepsilon}_x \\ \bar{\varepsilon}_y \\ 0.5\bar{\gamma}_{xy} \end{Bmatrix}_i = \begin{bmatrix} C_{11} & C_{12} & 0 \\ C_{12} & C_{22} & 0 \\ 0 & 0 & 2C_{33} \end{bmatrix}_i^{-1} \begin{Bmatrix} \bar{N}_x \\ \bar{N}_y \\ N_{xy} \end{Bmatrix}_i - \begin{bmatrix} C_{11} & C_{12} & 0 \\ C_{12} & C_{22} & 0 \\ 0 & 0 & 2C_{33} \end{bmatrix}_i^{-1} \begin{bmatrix} C_{14} & C_{15} & 0 \\ C_{24} & C_{25} & 0 \\ 0 & 0 & 2C_{36} \end{bmatrix}_i \begin{Bmatrix} \chi_x \\ \chi_y \\ \chi_{xy} \end{Bmatrix}_i \qquad (10\text{-}47b)$$

where the stiffness coefficients are evaluated with equations of reference 10-1. Secant moduli corresponding to the stresses of equations (10-49) are used in computing the stiffnesses.

The C_{ij} stiffness coefficients are formulated with respect to the mid-plane of the waffle skins. Average strains of the waffle skin then are

$$\begin{Bmatrix} \varepsilon_x \\ \varepsilon_y \\ 0.5\gamma_{xy} \end{Bmatrix}_{s,i} = \begin{Bmatrix} \bar{\varepsilon}_x \\ \bar{\varepsilon}_y \\ 0.5\bar{\gamma}_{xy} \end{Bmatrix}_i \qquad (10\text{-}48a)$$

The stiffener cross section is subdivided into five equal increments for the stress analyses of the waffle plates. For the 0 x 90° waffle, the average strains of these increments are

$$\varepsilon_{w,\ell,k,i} = \left| \bar{\varepsilon}_{\ell} + \left[0.5\, t_s + (0.2k - 0.1)\, h_{w,\ell} \right] \chi_{\ell} \right|_i \qquad (\ell = x,y;\ k = 1, 2, 3, 4, 5) \qquad (10\text{-}48b)$$

Expressions of the skin and stiffener stresses are

$$\begin{Bmatrix} f_x \\ f_y \\ f_{xy} \end{Bmatrix}_{s,i} = \frac{E_{sec,s,i}}{1-\nu_{s,i}^2} \begin{bmatrix} 1 & \nu_s & 0 \\ \nu_s & 1 & 0 \\ 0 & 0 & 1-\nu_s \end{bmatrix}_i \begin{Bmatrix} \varepsilon_x \\ \varepsilon_y \\ 0.5\gamma_{xy} \end{Bmatrix}_{s,i} \qquad (10\text{-}49a)$$

$$f_{w,\ell,k,i} = E_{sec,w,\ell,k,i}\ \varepsilon_{\ell,w,k,i} \qquad (\ell = x,y;\ k = 1, 2, 3, 4, 5) \qquad (10\text{-}49b)$$

Stresses of the caps are computed with equations (10-1) and (10-2)

Using strain and curvature components in the $\xi\eta$-coordinate system, the skin and stiffener stresses of the 45° x 45° waffle are obtained in the same manner as those of the 0 x 90° waffle. The transformation equation for the deformations is

$$\begin{Bmatrix} \bar{\varepsilon}_{\xi} \\ \bar{\varepsilon}_{\eta} \\ 0.5\bar{\gamma}_{\xi\eta} \\ \hline \chi_{\xi} \\ \chi_{\eta} \\ \chi_{\xi\eta} \end{Bmatrix}_i = \left[\begin{array}{c|c} [T] & [0] \\ \hline [0] & [T] \end{array}\right]_i \begin{Bmatrix} \bar{\varepsilon}_x \\ \bar{\varepsilon}_y \\ 0.5\bar{\gamma}_{xy} \\ \hline \chi_x \\ \chi_y \\ \chi_{xy} \end{Bmatrix}_i \qquad (10\text{-}50)$$

where the submatrix $[T]$ is the same as that of equation (10-6b)

Local Instability Analyses of Waffle Plates

The skin buckling analyses of Computer Program No. 1 are used in Computer Program No. 2. As already stated, a conservative, simplified procedure is used for the stiffener buckling analyses in Computer Program No. 2. Consider first the 0 x 90° waffle. The stiffener buckling stress due to uniform loading is computed with the same equations as used in Computer Program No. 1. The stresses

$$\begin{Bmatrix} f_{w,x} \\ f_{w,y} \end{Bmatrix}_i = \begin{Bmatrix} \max\left(f_{w,x,k}\right) \\ \max\left(f_{w,y,k}\right) \end{Bmatrix}_i \quad (k = 3,5)$$

as obtained in equation(10-49b) are compared with the buckling stresses to determine if stable equilibrium of the stiffeners exists. Effective moduli corresponding to the above stresses are used in the computation of the stiffener buckling stresses.

The stiffener buckling analyses of the 45° x 45° waffle are the same as those for the 0 x 90° waffle.

Analytical Procedures for Honeycomb-Core Sandwich Plate

The equations for determining the deflection and moments of the honeycomb-core sandwich plate are the same as those for the waffle plate, except the coupling moments due to extensional and bending deformation are not involved. The faces of the sandwich are analyzed for local buckling with the procedure of Computer Program No. 1.

Constraints

The constraints of Computer Program No. 2 are the same as those of Computer Program No. 1, except that a deflection constraint, which was not used after initial development of the program system, replaces the general instability constraint. In addition, the constraints of the honeycomb-core sandwich program were expanded to provide separate load dependent constraints for each of the two faces.

REFERENCES

10-1 Hubka, R.E.: Structural Optimization of Six Different Types of Rectangular Plates Subjected to Combined Shear and Biaxial-Compressive Loading, Lockheed Report 21662, Lockheed-California Co. 1968.

10-2 Gerard, George; and Wildhorn, Sorrell: A Study of Poisson's Ratio in the Yield Range. NACA TN 2561, 1952.

10-3 Wang, Chi-Teh: Applied Elasticity. McGraw-Hill Book Co., Inc., 1955.

10-4 Timoshenko, Stephen P.; and Gere, James M.: Theory of Elastic Stability. Second ed., McGraw-Hill Book Co., Inc., 1961.

10-5 Stowell, Elbridge : A Unified Theory of Plastic Buckling of Columns and Plates. NACA TR 898, 1948.

10-6 Bleich, Friedrich: Buckling Strength of Metal Structures. McGraw-Hill Book Co., Inc., 1952.

10-7 U.S. Department of Defense: Structural Sandwich Composites, MIL-HDBK-23. Government Printing Office, Washington, D.C., 1967 (Preliminary issue).

10-8 Konishi, Donald Yukio: Optimum Design of a Flat Honeycomb Sandwich Panel Under In-plane Loading. Thesis, College of Engineering, University of California, Los Angeles, 1964.

10-9 Modlinski, J.; and Uyehara, I.: Buckling of Orthotropic Plates Under Biaxial Compression and Shear, Lockheed Report 18473, Rev. A, Lockheed-California Co., 1966.

10-10 Wittrick, W.H.: Correlation Between Some Stability Problems for Orthotropic and Isotropic Plates Under Biaxial and Uniaxial Direct Stress. Aeronautical Quarterly, Vol. 4, Part I, 1952.

10-11 Seydel, E.: Uher das Ausbeulen von rechteckigen, isotropen order orthogonal - anisotropen Platten bei Schubbeanspruchung, Igenieur-Archiv, Vol. IV, Band 1933.

10-12 Contini, R.: Shear Buckling Coefficients for Simply Supported Orthotropic Rectangular Plates. Lockheed Report 21579, Lockheed-California Co., 1968.

10-13 Timoshenko, S.; and Woinowsky-Krieger, S.: Theory of Plates and Shells, McGraw-Hill Book Co., Inc..

REFERENCES (Cont)

10-14 Boley, Bruno A.; and Weiner, Jerome H.: Theory of Thermal Stresses. John Wiley and Sons, Inc., 1960.

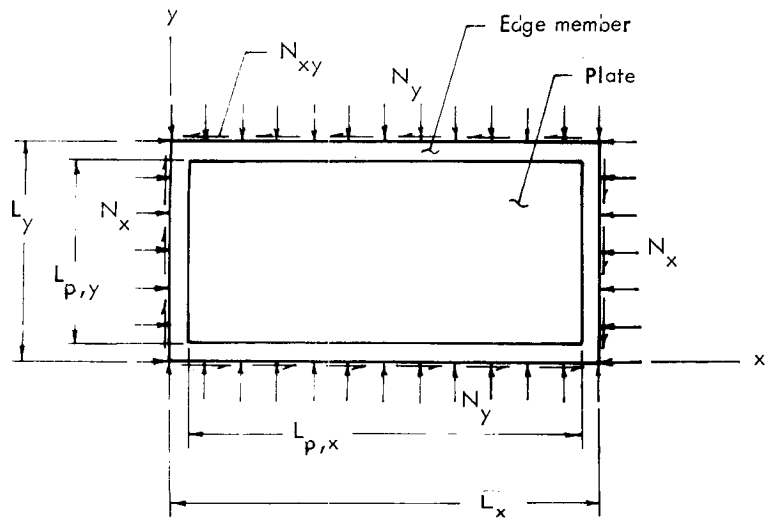

(a) Panel geometry and applied loads

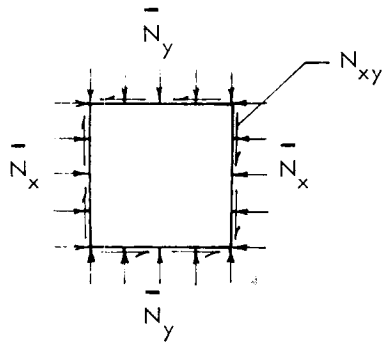

(b) Stress resultants of plate element

Figure 10-1. Geometry, applied loading and stress resultants of typical panel

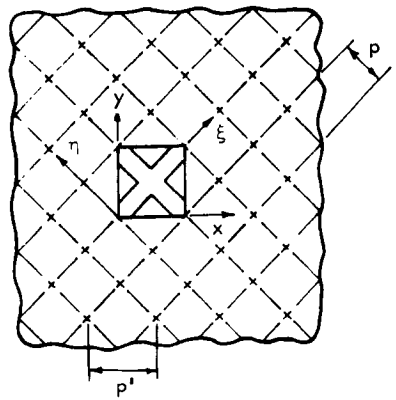

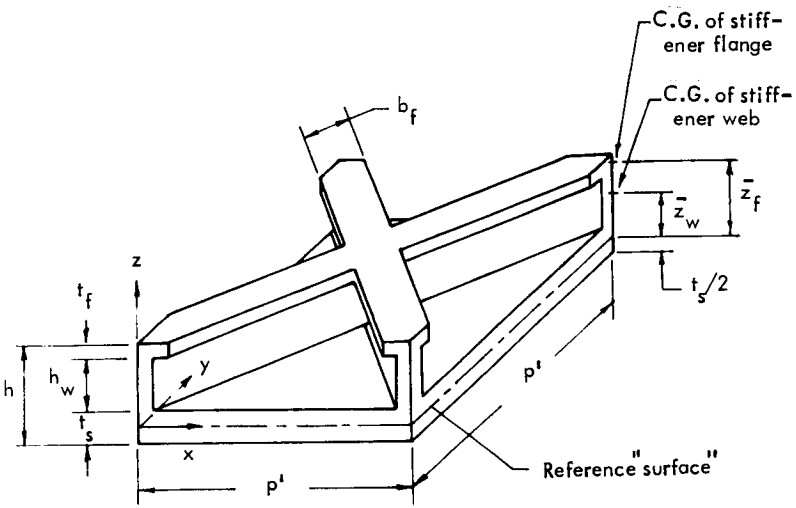

Figure 10-2. Typical element of 45° x 45° waffle plate

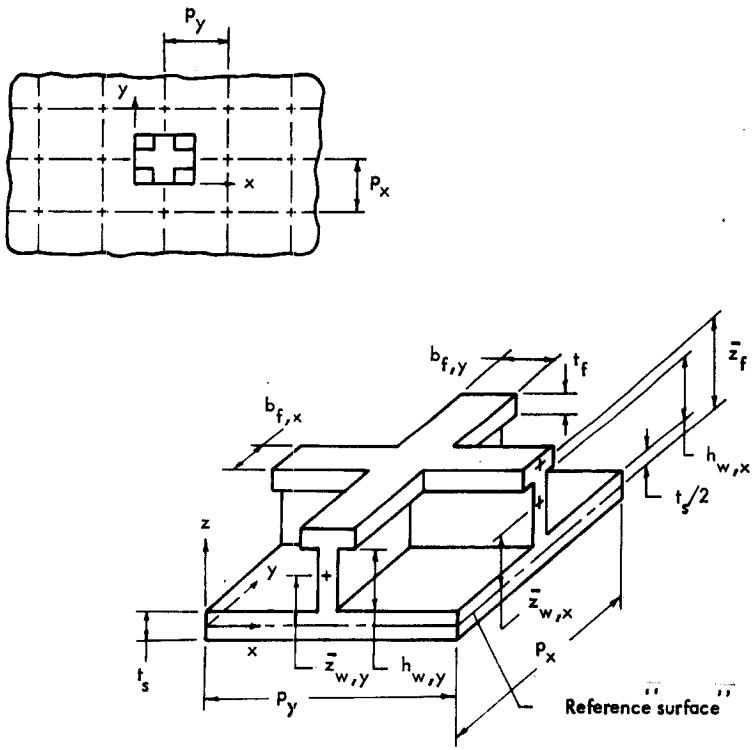

Notes: 1) + denotes centroid of stiffener elements.

2) Stiffener web thickness in x and y directions, which are not shown, are denoted as $t_{w,x}$ and $t_{w,y}$.

3) Notation provides for different stiffener heights of the unflanged configuration of stiffened plate. $h_{w,x} \equiv h_{w,y} = h_w$ for flanged configuration.

Figure 10-3. Typical element of 0 x 90° waffle plate

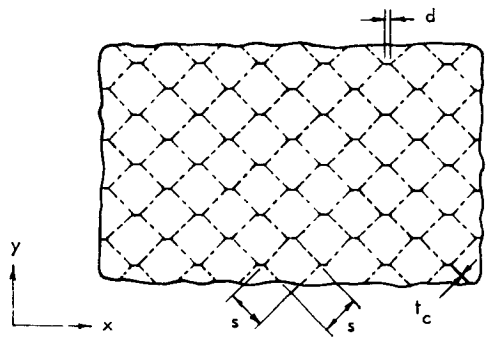

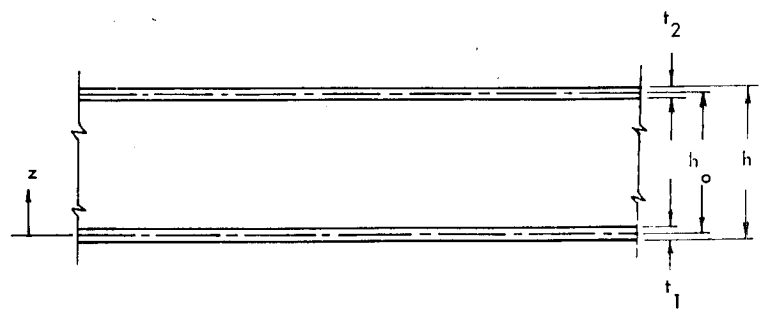

Figure 10-4. Geometry of honeycomb core sandwich plate

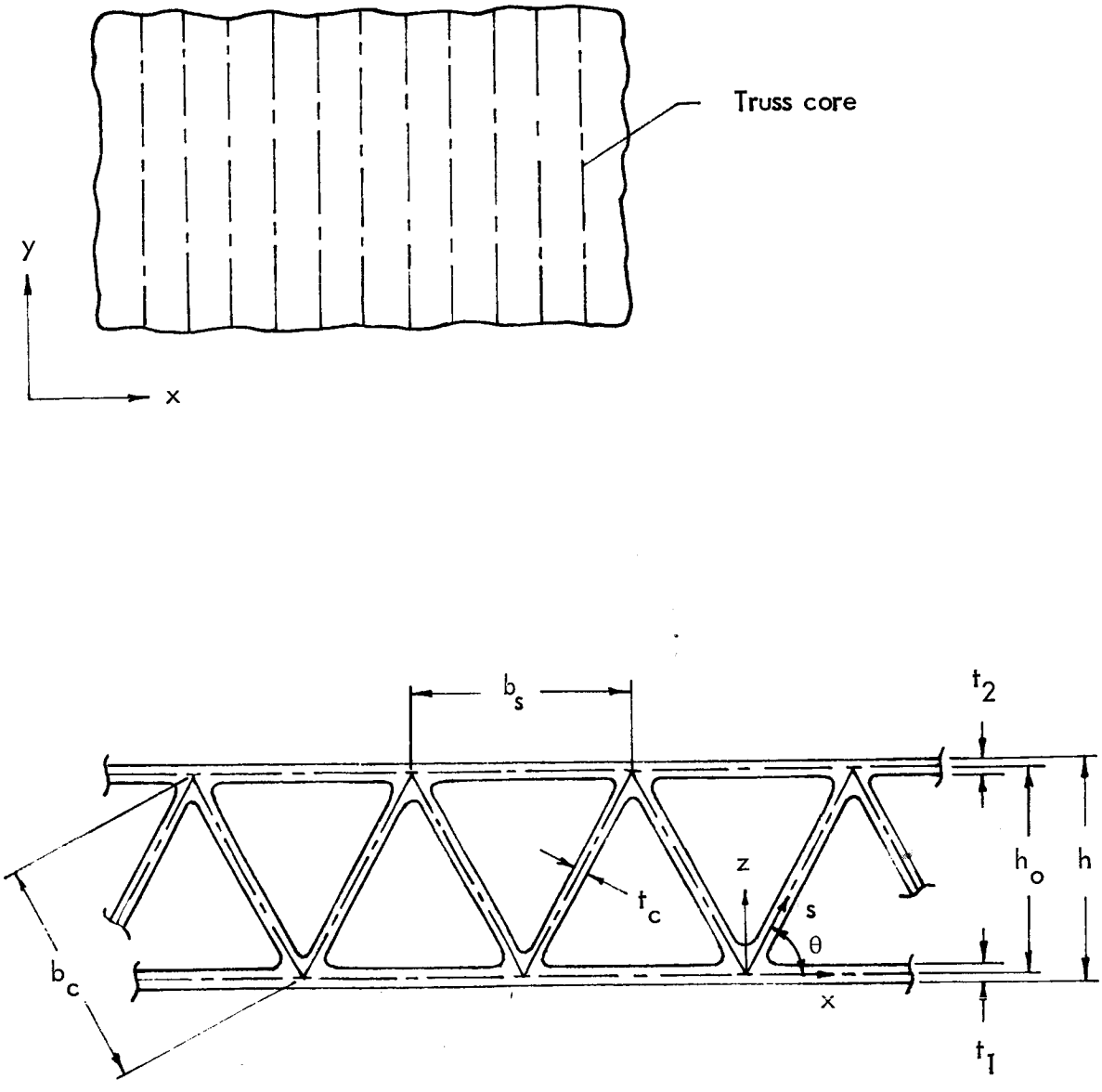

Figure 10-5. Geometry of truss-core sandwich plate

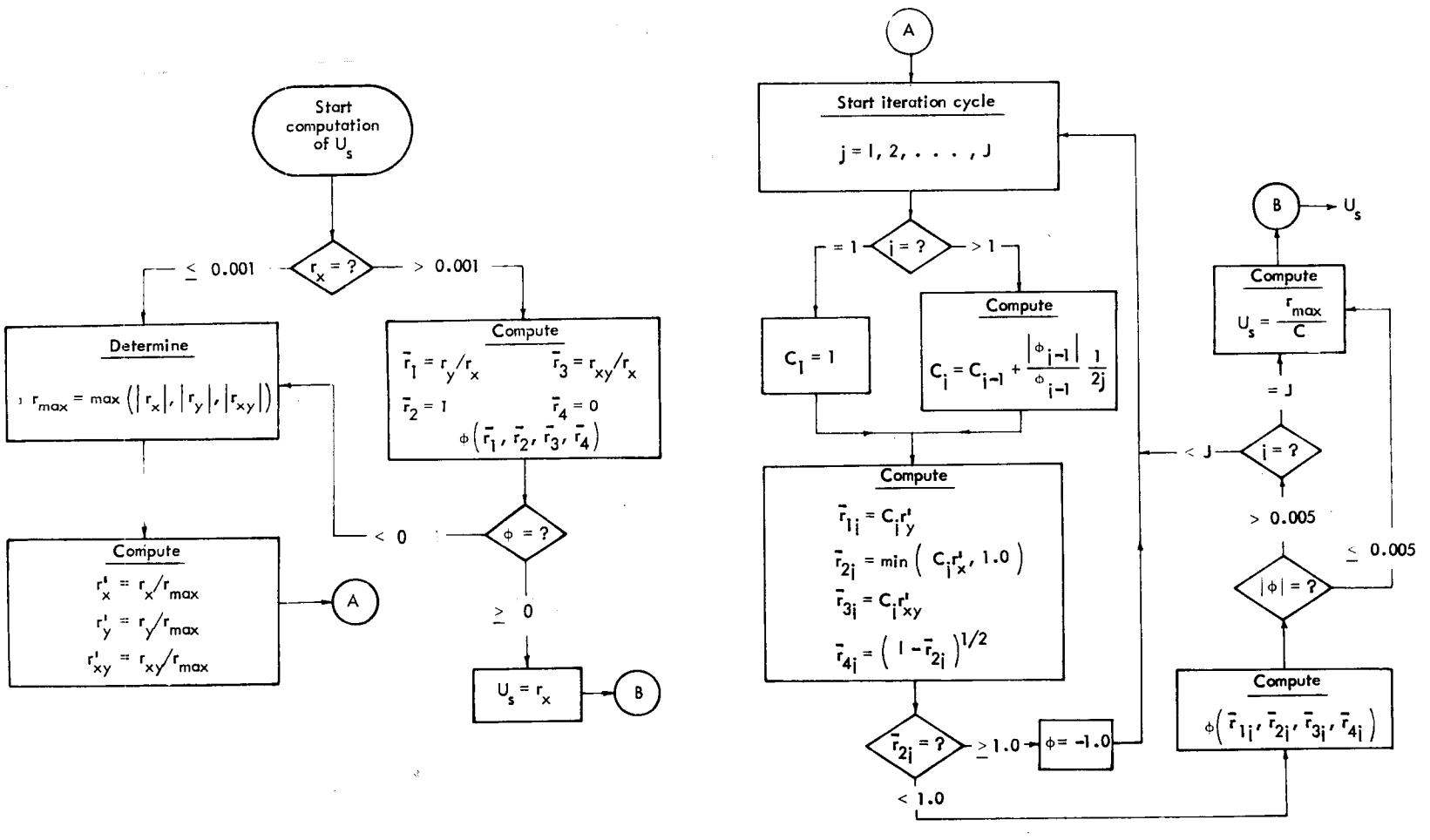

Figure 10-6. Procedure for computing utilization factor in analysis of local instability of faces of truss-core sandwich

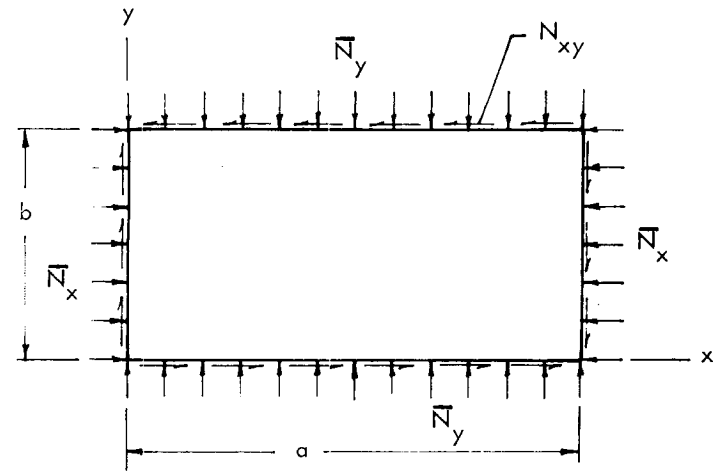

(a) Loading and dimensional notation

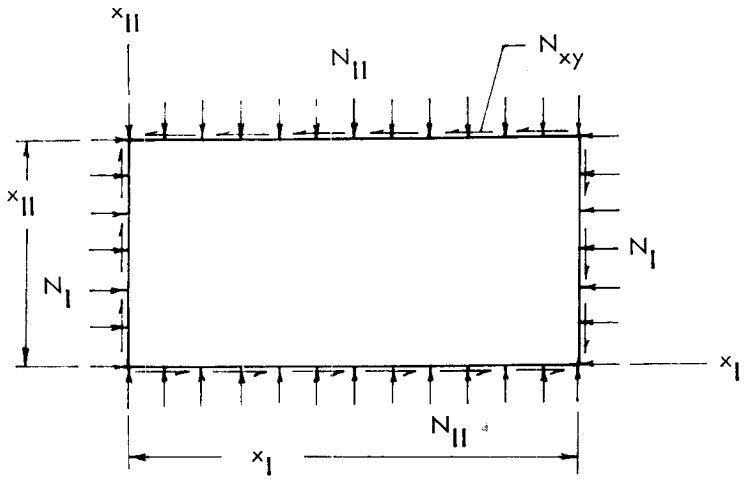

(b) Loading and dimensional notation as used in general instability equations

Figure 10-7. Notation of plate dimensions and loading for general instability analysis

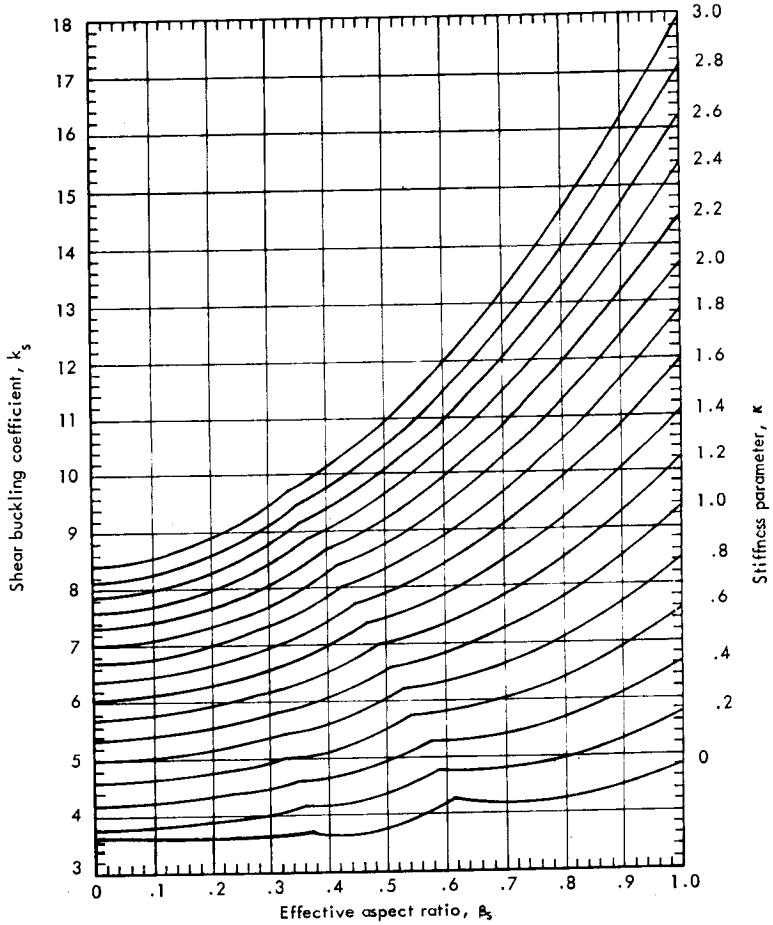

Figure 10-8. Shear buckling coeffieients of simply supported, orthotropic plates

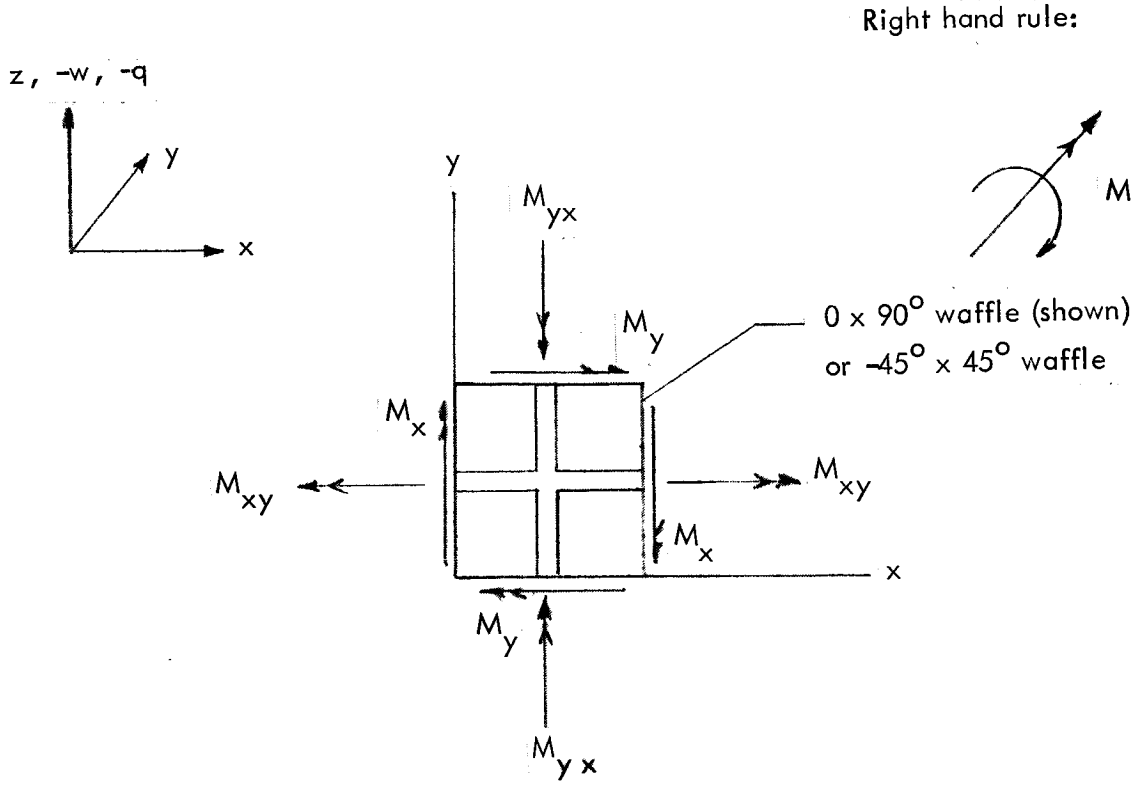

Expressions of curvature and twist:

$$\chi_x = -\frac{\partial^2 w}{\partial x^2} \qquad \chi_y = -\frac{\partial^2 w}{\partial y^2} \qquad \chi_{xy} = -\frac{\partial^2 w}{\partial x \partial y}$$

Figure 10-9. Sign convention of deflection, moments and pressure loading and expressions of curvatures and twist of waffle plate